DISS ETH NO. 24782

Downstream morphological effects of Sediment Bypass Tunnels

A thesis submitted to attain the degree of

DOCTOR OF SCIENCES of ETH ZURICH

(Dr. sc. ETH Zurich)

Presented by:

MATTEO FACCHINI

(M.D. Environmental and Land Engineering, University of Trento)

born on 11.02.1988

citizen of Italy

accepted on the recommendation of:

PROF. DR. ROBERT M. BOES [Examiner]

DR. ANNUNZIATO SIVIGLIA [Co-Examiner]

PROF. STEFANO LANZONI [Co-Examiner]

2017

You cannot step in the same river twice,
for the second time it is not the same river

- Heraclitus -

To Mum and Dad.
A Mamma e Papà.

Abstract

Sediment Bypass Tunnels (SBTs) are built with the main aim of routing sediment around or past dams. On the one hand, they avoid or reduce reservoir sedimentation, while on the other, they re-establish sediment and water connectivity with downstream reaches. There are few tens of SBTs in the world, but their number is likely to increase in the near future due to the current problem of reservoir sedimentation, thanks to water protection legislations aiming at re-establishing sediment continuity but also thanks to the likely decrease of their building and maintenance costs. While SBTs have a proven record of efficiently reducing reservoir sedimentation, less is known about their effects on the downstream reach. In the last ten years, some studies focused on ecological modifications in the downstream reach following SBT operations (i.e. opening of the SBT allowing for the transport of either water and sediment or just water), while less attention has been paid to their downstream morphological effects. As of today, there is a need of detailed monitoring downstream of SBTs as well as of objective and quantitative studies allowing for the assessment of possible future impacts of SBT operations. The main aim of this thesis is to quantify morphological effects of SBTs under different operational conditions. The problem tackled was tackled with a twofold approach: (i) quantification of morphological changes and displaced sediment volumes in a case study with in-field monitoring, taking advantage of state-of-art technologies such as bathymetric LiDAR (Light Detection And Ranging); (ii) identification of SBTs possible operational conditions quantifying water and sediment feed rates to the downstream reach and study of their downstream morphological effects via a large set of numerical simulations. Results show that: (i) in the case of the SBT built at the Solis dam on the Albula River (Canton of Grisons, Switzerland), about 6000 m^3 of sediment were released from the SBT during two consecutive operations in 2016 causing major morphological changes; (ii) river reaches subject to SBT operations might recover on a short-temporal scale from sediment starvation caused by river damming.

Sommario

I Tunnel di Bypass per Sedimenti (in inglese Sediment Bypass Tunnel, SBT) sono progettati allo scopo di trasportare i sedimenti oltre il corpo diga. Questa tecnica permette da un lato di ridurre l'interrimento dei serbatoi e dall'altro di ripristinare la continuità del flusso di sedimenti altrimenti interrotta dal corpo diga. Attualmente vi sono pochi SBT attivi al mondo, tuttavia l'utilizzo di tali bypass è in evoluzione per effetto di vari fattori, quali: il consolidamento della tecnologia con conseguente diminuzione dei costi di costruzione e manutenzione, la necessità di fronteggiare il problema dell'interrimento dei serbatoi esistenti, ed infine l'entrata in vigore di normative ambientali per il ripristino della continuità dei flussi di sedimenti nelle aste fluviali. L'efficacia degli SBT nel ridurre l'interrimento dei serbatoi è largamente comprovata, mentre lo studio degli effetti degli stessi sui tratti fluviali di valle resta invece tuttora inesplorato. Diversi studi negli ultimi dieci anni hanno preso in esame le alterazioni ecologiche legate alle operazioni di SBT (il rilascio di misture di materiale di fondo e acqua o solo acqua), ma poca attenzione è stata posta sugli effetti morfologici dei bypass sul tratto fluviale a valle degli impianti. Ad oggi quindi, si riscontra la necessità di monitorare gli effetti morfologici degli SBT e di sviluppare procedure specifiche per la valutazione e quantificazione gli impatti a medio e lungo termine delle operazioni di bypass. Lo scopo principale di questa tesi è quello di quantificare gli effetti morfologici dei bypass considerando diversi scenari operativi. Lo studio si sviluppa secondo due approcci: (i) la quantificazione dei cambiamenti morfologici in un determinato caso studio utilizzando tecnologie consolidate come la scansione batimetrica attraverso volo LiDAR (Light Detection And Ranging); (ii) l'individuazione di possibili scenari di utilizzo degli SBT e la quantificazione dei loro effetti morfologici attraverso simulazioni numeriche. Dai risultati si osserva che: (i) per il caso studio dell'SBT situato presso la diga Solis (sul fiume Albula, nel Cantone dei Grigioni, Svizzera), circa 6000 m^3 di sedimenti sono stati rilasciati a seguito di due operazioni di bypass nel 2016 ed importanti variazioni morfologiche si sono verificate di conseguenza; (ii) i deficit di sedimenti dei tratti fluviali a valle dei corpi diga potrebbero essere colmati in un arco temporale relativamente breve.

Acknowledgements

First and foremost I would like to express my gratitude to my supervisor, Dr. Annunziato Siviglia. To him, I would like to dedicate a quote by Butch Rovan:"Mentors can be pivotal people in your life. They show you something about yourself that you did not realize." I realized many things about myself during my PhD, mostly thanks to Nunzio. His continuous encouragement, his guidance and patience have driven me even in the toughest times. I also gratefully acknowledge Prof. Dr. Robert M. Boes for offering me the great opportunity to do this study at VAW and for supporting me during these four years.

I am grateful to the Federal Office for the Environment (FOEN) for the financial support to this research project in the scope of the "Sediment and Habitat Dynamics" project. My PhD project is also further affiliated to the Swiss Competence Center for Energy Research – Supply of Electricity (SCCER-SoE), towards which I would also like to express my gratitude. All of my colleagues who collaborated with me in the "Sediment and Habitat Dynamics" project are also gratefully acknowledge. In particular, I would like to thank Eduardo J. Martín for sharing with my ideas and hours of field-work. The Federal Office of Energy of Switzerland (SFOE) is also gratefully acknowledged for the financial support given to perform the bathymetric LiDAR surveys at the Albula River.

Furthermore I would like to extend my sincere thanks to the third member of the committee, Prof. Stefano Lanzoni, for taking his time to read my thesis and providing valuable feedbacks.

I would like to thank my colleagues at VAW, particularly the Numerics Team, for the fruitful discussions, the ideas we shared and the funny moments we had together at lunch and outside the university. In particular I would like to thank Dr. David Vetsch for offering me the opportunity to work with BASEMENT, to play with it, and to discuss about it. My office-mates Stephan and Lukas are also kindly acknowledged for being patient with me and for sharing the last (very hot) summers. Furthermore I would like to thank Sam for being always sincere to me and for the precious hints concerning the thesis layout, and Michelle for the hours spent discussing with me about anything concerning work and not and for sharing her precious bedload data with me.

A special thanks goes to Davide, Francesco, and Martín with whom I shared the joy

of music during my Swiss years. Music to me is something I share with my dearest friends and without which I could never be what I am. With them I would like to thank all the "Guete Abig" Italian gang and the "Wannabes" for the fun nights and weekends in Zürich. Grazie!

I also thank my friends in Trento who never stopped believing in me and that have always been close to me even with many kilometers dividing us. Your are many and you are my big wonderful family.

My family deserves a special thank because my parents and my brother Luca with his wife Chiara have never stopped supporting me, even when times were hard. Vi ringrazio per tutto quello che avete fatto e che continuate a fare per me perché in fondo se sono dove sono e se sono quello che sono è grazie a quello che siamo tutti assieme.

Last but not least, my girlfriend Eleonora: your curiosity towards everything that surrounds us, your gentle smile and your support are the fuel for everything I do.

Contents

List of Figures

List of Tables

1 Introduction

1.1 Motivation

Sediment Bypass Tunnels (SBTs) route sediments through or around reservoirs, reducing on the one hand reservoir sedimentation and re-establishing on the other water and sediment connectivity at dams. There are roughly 30 SBTs worldwide and their number is most likely to increase in the near future (i) thanks to water protection legislations requiring to re-establish nearly natural water and sediment fluxes in rivers, (ii) due to the need to mitigate reservoir sedimentation resulting in both operational restrictions (e.g. due to blockage of outlet structures) and safety issues at dams and reservoirs, and (iii) thanks to the decrease of life-cycle costs due to the advances in construction and material technology. As of today, the majority of SBTs is concentrated in Switzerland and Japan, which are the leading countries in construction technology and research about SBTs. Other examples of SBTs are present mostly in Taiwan, but also in France, Ecuador, Iran, Pakistan, United States, and the Republic of South Africa.

SBTs are operated during flood events on average less than 10 times per year. During SBT operations, the downstream river reach is subject to intense and impulsive water and sediment releases, which might cause great morphological modifications. Currently, the study of the impacts of SBT operations on the downstream reach is mainly focused on river ecology and is based on monitoring channel conditions with in-field measurements.

River reaches experiencing abrupt and intense bedload-laden water releases could undergo great morphological modifications during the events and are morphologically inactive for the rest of the year. The effects of intense modifications of water and sediment discharges have been studied in the last two decades with field studies, labora-

tory experiments and numerical simulations. Sediment released in form of pulses to a sediment-starved river system might disperse in situ or move downstream depending on the hydraulic conditions and on the pulse grain size and volume. If these events are repeated cyclically for a sufficiently long time, the river might adapt and reach an equilibrium state after which only the upstream part of it, i.e. close to the source of the disturbance, is subject to strong variations of riverbed level and grain-size composition.

SBT operations have the power to greatly modify the morphology of sediment-starved river reaches stretching below dams. Not much is known about the effects that SBT operations might have on the downstream reach, and while ecological effects are currently under investigation, morphological changes are still poorly investigated. Gaining a better understanding of the morphological processes induced by water and sediment released cyclically by SBTs poses a challenge both from a research and from a more practical point of view.

1.2 Main goal and research questions

The main aim of this work is to quantify the morphological changes and understand the underlying morphological processes induced by water and sediment released from SBTs. The problem is firstly tackled analyzing the morphological changes of the river reach downstream to the Solis SBT (Canton of Grisons, Switzerland) induced by recent SBT operations, and then through a more theoretical study based on numerical simulations. The research questions addressed are the following:

i) Which are the volumes mobilized by two years of SBT operations at the Solis SBT and how do they affect river morphology?

ii) How much sediment and water are released by SBTs to the downstream reach, under different operational conditions?

iii) Which are the morphological effects of repeated SBT operations on both short and long temporal scales from both a quantitative and qualitative perspective?

1.3 Thesis outline and main novelties

To answer the research questions, the thesis is subdivided in three main parts as sketched in Figure 1.1, where the sketch of the outline of the thesis is given.

i) After introducing the problem in Chapter 2 by presenting a background on river damming, SBTs and related research works, two years of SBT operations at the Solis SBT (Canton of Grisons, Switzerland) are analyzed in Chapter 3. To this end, two bathymetric LiDAR surveys were carried out allowing for a DEM (Digital Elevation Model) of Difference (DoD) analysis used to quantify the volumes of sediment released during SBT operations and describe the morphological changes occurring in the downstream river reach. Starting from two DEMs measured after two SBT operations in 2014 and 2016, the volumes mobilized by the SBT are calculated taking into account the uncertainties of the single survey and propagating them into the DoD with a statistical approach. The main novelties of this Chapter concern the technology used to survey the river reach under investigation, i.e. the bathymetric LiDAR, and the methodology used as a control on the measured points which allows for a better estimation of the sediment volume released by the SBT.

ii) In Chapter 4, the DoD analysis of Chapter 3 is used as a starting point to expand the study to SBTs in general, trying to describe the way they can be operated. To achieve this goal, the bedload transport in the upstream river reach is related to the one in the downstream reach, taking into account different SBT operational conditions (OCs). That is, depending on how the SBT is operated it might carry out (i) entirely what is transported upstream, (ii) alternatively bedload-laden water and just water, (iii) only the finest part or (iv) only part of the upstream bedload. In this Chapter, a framework to model sediment and water releases from the SBT is presented for the first time.

iii) In Chapter 5, the effects of repeated sediment and water releases are analyzed with a one dimensional numerical study using a simplified geometry inspired by the Albula river. The problem is investigated on different time scales, i.e. both from

the short- (50 SBT operations) and the long-term (10^4 SBT operations) perspective. The general framework presented in Chapter 4 is used to quantify reliable boundary conditions for the numerical study and to take into account different release conditions linked to real SBTs. The main novelty of this Chapter concerns the study of downstream morphological effects of SBT operations under different operational conditions.

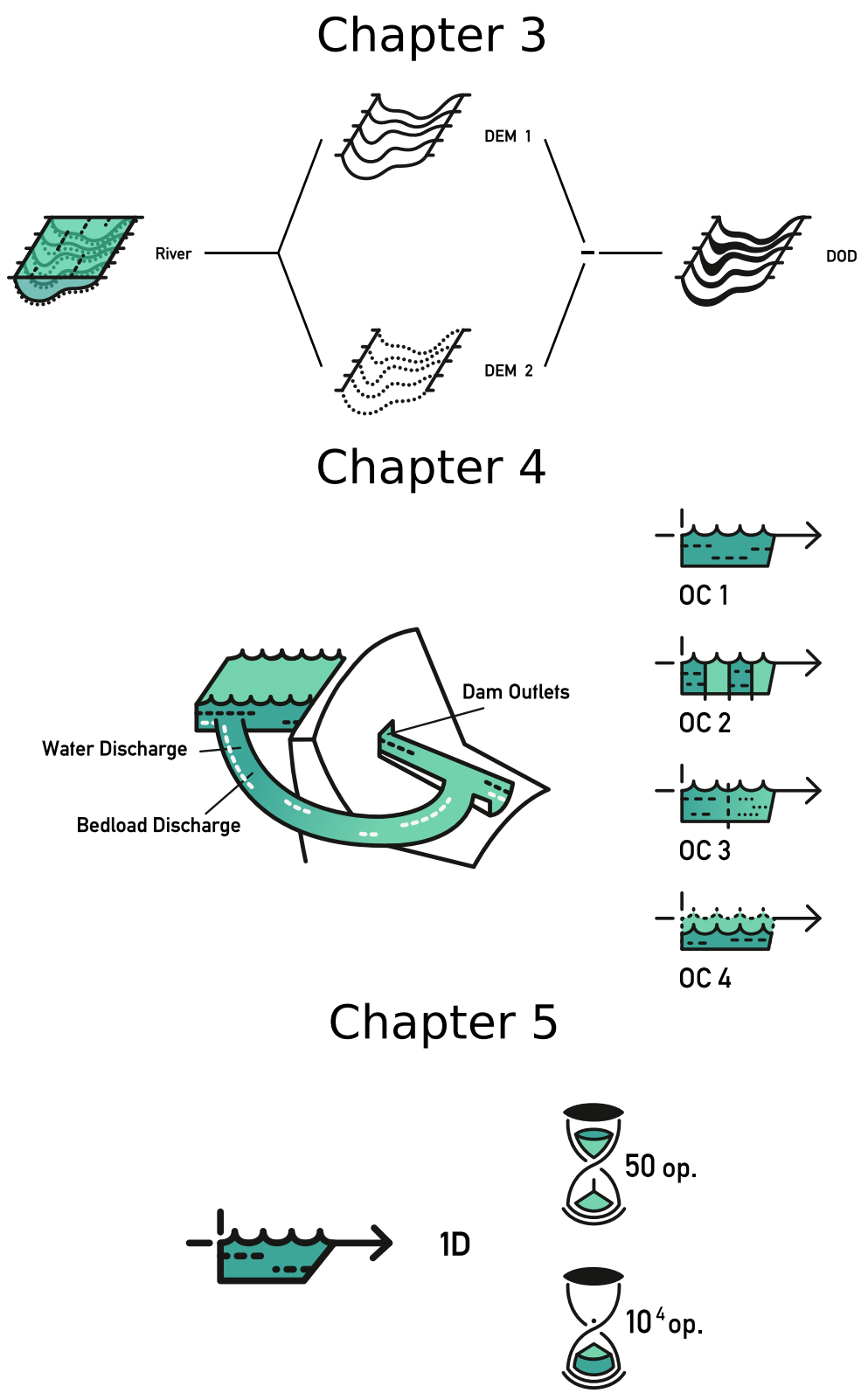

Figure 1.1: Graphical representation of the thesis outline, with DEM: Digital Elevation Model, DoD: DEM of Difference, OC: Operational Conditions, op.: SBT operations.

2 Sediment bypassing: a mean to reestablish natural sediment and water regimes in dammed rivers

Water flowing from the upstream river system to a reservoir carries sediment, both as bedload and suspended load. Once in the reservoir, they are deposited due to reduced flow velocities that cause reduced transport capacity (Morris and Fan, 1998). When Sediment Bypass Tunnels (SBTs) are operated they convey sediment-laden waters from the reservoir to the downstream reach. Under certain circumstances, water can be released through the dam outlets, i.e. bottom outlets and spillways. SBTs and bypass channels are an effective strategy to route sediments around or through reservoirs thereby avoiding or even removing accumulation (Vischer *et al.*, 1997; Sumi *et al.*, 2004; Boes, 2015; Sumi, 2017). In the last years, they have been considered as a possible mean to restore natural water and sediment regimes in the downstream reach, since they also reestablish sediment and water connectivity at dams (Martín *et al.*, 2017).

In the following, a short introduction about the effects of river damming, both on the upstream and on the downstream reach will be given. Afterwards, SBTs' typical design and operation will be presented together with some examples of existing SBTs in Switzerland and worldwide. Eventually, the results of recent research works concerning the effects of sediment augmentations and of artificial water releases on sediment-depleted rivers are presented and discussed.

2.1 Damming a river: eco-morphological consequences

Anthropogenic impacts have altered river systems worldwide with about 15% of the global annual river runoff stored in manmade reservoirs (Nilsson *et al.*, 2005). On the one hand, dams confine reservoirs, which provide several services to the community including: flood regulation, water supply for irrigation, human consumption, and industrial use, aquaculture, navigation, and hydropower (ICOLD, 2016). On the other hand, dams disrupt sediment and water flow connectivity, increase hazards due to aging of dams (Asmal *et al.*, 2000) and have several effects on the ecosystem. In particular, they may reduce biodiversity, deplete water quality, lower crop production, and decrease fish population (Petts, 1984).

In this chapter, ecological and morphological consequences of river damming occurring at different spatial scales, i.e. from the patch to the catchment scale, are presented and discussed.

2.1.1 Ecological consequences of river damming

Dams adversely impact the structure and functioning of river ecosystems in many ways (Petts, 1984), i.e. they alter the downstream flux of water and sediment, which modifies biogeochemical cycles as well as the structure of dynamics aquatic and riparian habitats (Petts, 1984; Bayley, 1995). A broad overview on river damming ecological effects is presented in Petts (1984).

Altered water flow regimes affect mainly the bioenergetic and vital rates of river organisms (Ward and Stanford, 1979; Muth *et al.*, 2000). On the one hand, long-term storage and nonseasonal releases of water can alter downstream food webs and aquatic productivity (Wootton *et al.*, 1996). On the other hand, hydropower operations may produce very intense daily flow variations (i.e. hydropeaking) that affect downstream habitat and aquatic productivity (Bruno *et al.*, 2010; Nagrodski *et al.*, 2012; Vanzo *et al.*, 2016). In addition to that, reservoirs release waters, e.g. from the bottom outlets, which are relatively warm in winter, and relatively cool in summer due to thermal stratification of the reservoir (Poff and Hart, 2002). Such altered thermal regime modifies the densities and kinds of species present (Zolezzi *et al.*, 2011) in the downstream reach. Fur-

thermore, dams interrupt the upstream-downstream movement of sediment, organisms and nutrients. On a larger scale, they modify the landscape and the extensive fragmentation of free-flowing rivers promotes ecosystem isolation and prevents the dispersal and persistence of inland species (Poff and Hart, 2002).

2.1.2 Morphological consequences of river damming

By interrupting natural water flow and sediment regimes, dams modify river morphology with different effects upstream and downstream of the barrage. Upstream, they confine reservoirs, which cause water flow velocity to decrease favoring sediment deposition. Thus, they cause the formation and development of an aggradation body inside the reservoir, which reduces the reservoir storage capacity (Morris and Fan, 1998). In the downstream reach, reduced water flow and interruption of sediment supply cause mainly channel narrowing and degradation (e.g. Surian and Rinaldi, 2003) together with coarsening of the armored riverbed (e.g. Williams and Wolman, 1984).

Upstream: reservoir sedimentation

When a river enters a reservoir and flow velocity decreases, sediment load transported by the flow starts to deposit (e.g. Annandale, 1987). Bedload and coarse fractions of suspended load are deposited close to the reservoir head and form an aggradation body. Fine sediment with lower settling velocities are transported deeper into the reservoir by either stratified or non-stratified flow (Morris and Fan, 1998). The simplest sediment deposition pattern is represented by a reservoir on a single stream with no major tributaries and operated at a nearly constant level. This presents a uniformly depositional environment, even if site-specific depositional patterns can occur, i.e. they depend on the reservoir (Morris and Fan, 1998). In reservoirs with fluctuating water levels or that are periodically emptied, previously deposited sediment may be extensively eroded and reworked. The presence of tributaries will add further complexity to the described system (Morris and Fan, 1998).

Most sediments are transported within reservoirs to points of deposition by three main physical processes: (i) transport of coarse material as bedload along the topset delta deposit, (ii) transport of fines in turbid density currents, and (iii) transport of fines as

non-stratified flow (Morris and Fan, 1998). Since typically reservoirs have long shorelines compared to their surface, erosion of shorelines and relative slope failure could occur at some sites. The resulting sediment deposition pattern is dependent on each of these processes and govern the rate at which sediment reservoir are filled.

Vörösmarty *et al.* (2003) extrapolated estimates from 85% of the world largest reservoirs (i.e. with a storage capacity grater than or equal to 0.5 km^2) to 44700 smaller reservoirs and concluded that more than 53% of the global sediment flux in regulated basins is potentially trapped in reservoirs. This means that in regulated rivers, which are 28% of all river basins in the world, the trapping rate is 4-5 billion tons of sediment per year (Vörösmarty *et al.*, 2003). Mean annual sedimentation rates (the percentage of the design reservoir storage capacity that yearly gets filled up with sediment) vary from 0.2 to some 2 to 3% with a global annual average rate of about 1%, and worldwide increase in sedimentation volume exceeds increase in reservoir capacity revealing a gross storage loss (ICOLD, 2009; Schleiss *et al.*, 2016). At the current rate the global storage capacity will be halved by 2050 (ICOLD, 2009). In Switzerland, sedimentation rate has been estimated to be around 0.2%. This means that by 2050 around 20% of total reservoir capacity in Switzerland will be lost (ICOLD, 2009; Schleiss *et al.*, 2010).

Downstream: channel incision and bed material coarsening

When rivers are dammed, they tend to be less dynamic because of the interruption of their connectivity, i.e. the reduction of sediment and eventually water discharge compared to natural regimes. This may reduce in turn river morphological complexity, i.e. reduces the river to an almost straight channel with no longitudinal slope variability (Williams and Wolman, 1984). The effects of river damming can be observed at different scales: (i) at patch scale (reaches-length comparable to river width), river damming affects the grain size distribution of riverbed; (ii) at reach scale (i.e. reaches-length that are several times the river width), it affects river longitudinal slope variability and cross-sectional shape; (iii) at catchment scale, it affects the river as a whole system, from the source to the mouth (Williams and Wolman, 1984; Kondolf, 1997). Insights on the effects at different scales are given hereafter.

At *patch scale*, riverbeds tend to react to sediment supply reduction with coarsen-

ing (Grant, 2012). Dams reduce intensity and frequency of high flows and released flows may not be able to transport grain sizes previously moved by higher flows. Therefore, flows released from dams can winnow finer materials from the bed, concentrating coarser fractions. The average particle size on the bed increases as bed degradation proceeds, eventually resulting in a surface armor of coarse particles alone (Williams and Wolman, 1984; Venditti *et al.*, 2012). The effect of dam closure on riverbed grain size distribution (GSD) is more intense close to the dam and stabilizes after few years after dam closure, i.e. when the dam is first put in operation (Williams and Wolman, 1984; Brandt, 2000).

At *reach scale*, rivers respond to sediment paucity with channel erosion and narrowing (e.g. Williams and Wolman, 1984). Brandt (2000) summarizes a large number of case studies around the world and identifies under which conditions either erosion or deposition are to be expected. Starting from a defined natural (i.e. predam) water discharge and the relative transport capacity in a given channel, he describes the outcomes of nine input scenarios varying water discharge and sediment supply. This analysis verifies that if sediment supply is below transport capacity, riverbed (riverbanks) will be eroded if the river is (not) confined and water discharge is constant. On the contrary, if sediment supply is higher than transport capacity, sediments are deposited on riverbed (riverbanks) if the river is (not) confined and water discharge is constant (Brandt, 2000). Surian and Rinaldi (2003) collected all available data and all published studies concerning main channel adjustments that occurred in Italian rivers in the last 100 years. They recognize two main types of adjustment, namely channel incision and channel narrowing. These alterations of the river topography are mainly due to human intervention, particularly sediment extraction, dam construction and channelization (Surian and Rinaldi, 2003). The aforementioned changes seem to be rapid at the early stages of water discharge and sediment supply disturbance occurring after dam closure. They tend to become slower after some years, and eventually asymptotic after many years (Brandt, 2000; Surian and Rinaldi, 2003).

At *catchment scale*, the influence of sediment scarcity can be also noticed on coastal regions, where sand-starved beaches have narrowed or disappeared, accelerating erosion of coastal areas (Syvitski *et al.*, 2009). Chen *et al.* (2012) report that 24 (out of 33)

world major deltas are sinking largely due to human impact, including reduced sediment supply. This will lead, in combination with an assumed 0.46 m rise in the sea levels by 2100, to a 50% increase of flooding in coastal areas (Chen *et al.*, 2012).

2.2 Re-establishment of sediment connectivity at dammed rivers

Reservoir sedimentation is a major consequence of river damming and has several effects on the reservoir itself, on the dam and the related structures and also on the downstream reach. Firstly, the decrease of the reservoir volume leads to a loss of energy production, water used for water supply and irrigation, and retention volume (Annandale, 2013). Secondly, it may lead to both an endangerment of operating safety due to blockage of outlet structures and an increased turbine abrasion due to increasing specific suspended sediment load concentrations. Eventually, the disruption of sediment fluxes causes morpho-ecological impacts on the river reach downstream of the dam (ICOLD, 2009). Therefore, sediment accumulating in reservoirs can be considered as a *"resource out of place"* (Kondolf *et al.*, 2014), because it is not needed in the reservoir, but it is needed downstream of the dam, both on a short spatial scale by the downstream river reach and on a longer one by coastal areas. Moreover, given the recent trends concerning energy production, which indicate a shift towards sustainable energy sources, and the relevance of hydropower production worldwide, it is of paramount importance to make hydroelectric production effective and sustainable (e.g. Dincer, 2000; Chu and Majumdar, 2012). For decades, several methods to counteract reservoir sedimentation have been developed and applied (see e.g. Kondolf *et al.*, 2014). Some of them simply solve the problem of reservoir sedimentation, others re-establish sediment and water flow connectivity at dams.

2.2.1 Sedimentation management strategies

Sedimentation management encompasses a large variety of strategies including flushing, sluicing and bypassing (e.g. Morris and Fan, 1998; Kondolf *et al.*, 2014; Auel *et al.*,

2016). Figure 2.1 shows an overview of the techniques applied to reduce reservoir sedimentation and their corresponding strategies: (i) sediment yield reduction, (ii) routing sediments around or through the reservoir, and (iii) recover volume by sediment removal or dam heightening. Furthermore, two more strategies may be added: (iv) dam removal and (v) no action.

New dams should be planned and designed including sediment management strategies, e.g. where possible by passing sediment around or through reservoirs (Kondolf *et al.*, 2014). Choices in the siting, design, and operation of dams determine their ability not to interrupt sediment connectivity. Siting decisions are irreversible and to adapt an existing structure by building sediment passing facilities afterwards is very expensive in the best cases and impossible in the worst ones (Kondolf *et al.*, 2014). For dams which are in the planning phase, Kondolf *et al.* (2014) recommend to revise plans, while for already existing dams, they suggest to assess several options to improve sediment management. The latter are listed in Figure 2.1 and discussed hereafter.

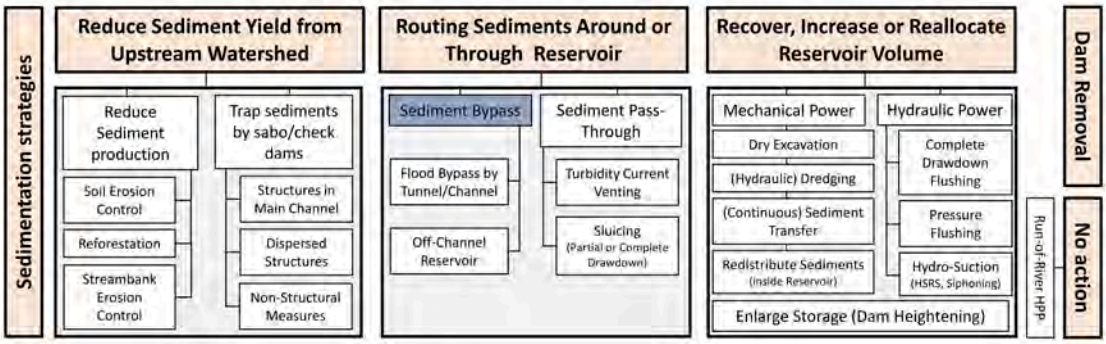

Figure 2.1: Classification of strategies for sediment management (Auel *et al.*, 2016).

Reduce sediment yield from upstream watershed

Various approaches have been employed, and are under development, to reduce the amount of sediment entering the reservoir from upstream. These approaches include reduction of sediment production through soil and stream-bank erosion control (e.g. by re-vegetating stream-banks). Structural measures, such as the construction of check-dams and sediment traps, could also be employed to reduce sediment load entering the reservoir. These methods have not been proven to be very effective in preventing reser-

voir sedimentation (Annandale, 2011) and are not re-establishing sediment connectivity at dams.

Routing sediments around or through reservoir

The routing of sediment around the reservoir to the tailwater can be achieved by means of several strategies: (i) sluicing of sediment through the reservoir outlet structure, (ii) venting of turbidity currents, and (iii) routing of sediment through sediment bypass tunnels and bypass channels. In the first two cases, sediments are routed without settling in the reservoir (Morris and Fan, 1998). The main differences between the first two methods are: (a) sluicing requires a partial reservoir drawdown, while turbidity currents flow to the bottom outlet autonomously; (b) sluicing allows for the routing of both suspended load and bedload, while turbidity currents are mainly composed by material being transported in suspension. Sluicing of sediment has the main disadvantage of requiring a special design for bottom outlets, since they are operated under high pressures. Moreover, the duration of a sluicing operation depends on the watershed size and the time scale of flood events (Kondolf *et al.*, 2014). In contrast to sluicing and venting of turbidity currents, sediment routing through a sediment bypass tunnel (SBT) or bypass channel is very effective (see e.g. Kantoush *et al.*, 2011; Auel *et al.*, 2016), as it allows the bypassing of both suspended sediment and bedload (Auel and Boes, 2011a; Sumi, 2015; Morris, 2015). SBTs are addressed separately in section 2.3.

Recover, increase or reallocate reservoir volume

To increase or recover the storage volume of the reservoir, it is possible to remove sediment from the deposition body. This could be achieved through either mechanical removal, i.e. excavation or dredging, or hydraulic excavation, i.e. drawdown flushing or pressure flushing. Moreover, sediment being mechanically extracted could also be redistributed or reallocated downstream of the dam or where needed, e.g. in the scope of sediment augmentation programs (Bunte, 2004). Drawdown flushing is an alternative to sluicing, but it aims at scouring and re-suspending sediments already present inside the reservoir and transport them downstream. Another key difference between sluicing and drawdown flushing is that the latter could deliver a lot of material during low-flow period

if performed during the nonflood season (Kondolf *et al.*, 2014). The main disadvantages of drawdown flushing are that it requires the complete emptying of the reservoir and that it is feasible just in narrow and long reservoirs, which allow for the establishment of river-like flow conditions inside the reservoir, therefore favoring sediment transport (e.g. Auel, 2014). Pressure flushing is effective in removing sediment just in front of the dam and therefore keeping intakes operational. The reservoir level is not lowered, but outlets are opened to remove sediment at a short distance upstream of the dam (Sumi, 2015).

As for drawdown flushing, mechanical removal of sediment by excavation requires the complete emptying of the reservoir, although it is less expensive than dredging, since the latter requires the use of hydraulic pumps for removing accumulated sediment by suction (Kondolf *et al.*, 2014).

2.3 Sediment Bypass Tunnels (SBTs): design, operation and worldwide examples

Compared to the other sediment management methods, SBTs have some advantages, namely: they bypass sediment generally without interfering with reservoir operations, can be built at already existing dams, and their operations do not require the complete drawdown of reservoirs with the consequent loss of storage capacity for a defined amount of time (Sumi *et al.*, 2004). On the other hand, SBTs have high construction costs and need to be optimized to lower the possibilities of damages to the structure (e.g. on the tunnel invert, Boes *et al.*, 2014; Baumer and Radogna, 2015; Mueller-Hagmann, 2018).

2.3.1 SBT design and operation

Sediment bypass tunnels are designed for being operated in supercritical open channel flow conditions to avoid undesirable outcomes due to choking and transition to pressurized flow (Auel, 2014). Supercritical flows ensure a sufficient sediment transport capacity and an advantageous dimensioning of the tunnel. Typically, SBTs consist of:

(i) a guiding structure to be built inside the reservoir, which guides sediment-laden flows into the tunnel, (ii) an intake structure including a gate, (iii) a short and steep acceleration segment, (iv) a long and less steep segment, and (v) an outlet structure (Auel, 2014) (see Figure 2.2).

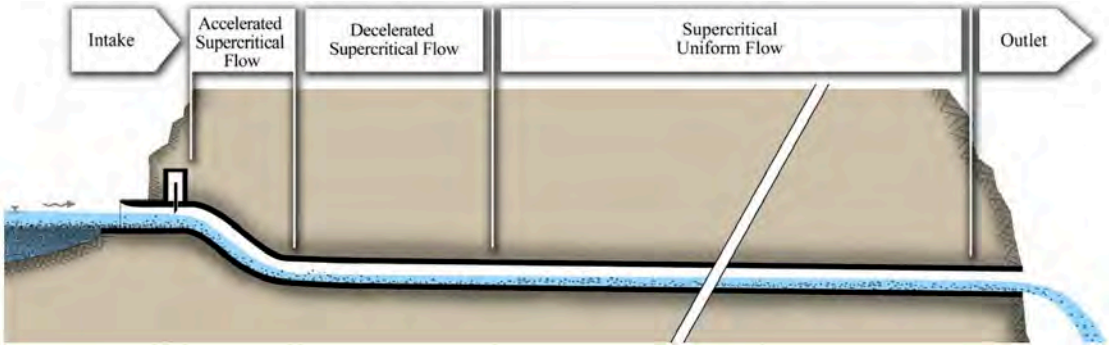

Figure 2.2: Longitudinal section of a SBT with intake structure, acceleration segment, long and smoothly sloped segment, and outlet structure (from Auel (2014)).

Two main types of SBT systems are distinguished, i.e. type A and B, depending on the position of the intake structure, as represented in Figure 2.3 (e.g. Mueller-Hagmann, 2018). In most of the cases, the intake structure is built at the upstream end of the reservoir and a weir regulates the flux of sediment-laden waters into the tunnel (SBT system of type A, Figure 2.3(a)). Once sediment concentration falls, water is allowed to flow into the reservoir again. Under certain circumstances, it is possible to build the tunnel intake downstream of the reservoir head (SBT system of type B, Figure 2.3(b)). In this case, the inflow will be under pressurized conditions (Auel and Boes, 2011a).

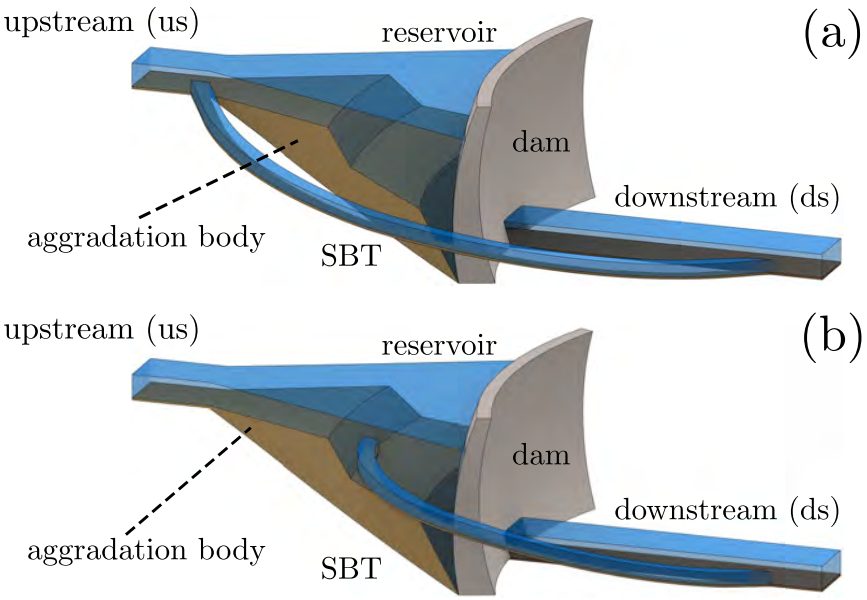

Figure 2.3: Sketch of SBT systems with upstream river reach (u), reservoir, aggradation body, SBT, dam and downstream reach (ds). (a) SBT system of type A: location of the tunnel intake at the reservoir head. (b) SBT system of type B: location of the tunnel intake downstream of the reservoir head.

On the one hand, locating the intake structure at the upstream end of the reservoir has mainly two advantages: (i) the entire reservoir is kept free from sediments, and (ii) the reservoir level is kept constant during SBT operations. However, this configuration has also some disadvantages: (i) depending on the topography of the system, there could be a long distance to cover from the reservoir head to the tailwater, which increases in turn the construction costs; (ii) the free surface flow conditions at the tunnel intake require a steep acceleration segment, which may provoke high abrasion at the tunnel invert. On the other hand, positioning the intake structure downstream of the reservoir head has some advantages compared to the other configuration: (i) a shorter distance between the tunnel intake and the tailwater; (ii) the pressurized flow at the intake makes an acceleration segment unnecessary. Also in this case, there are some disadvantages, namely: (i) the reservoir is kept free from sediment only downstream of the intake structure, and (ii) a partial reservoir drawdown is necessary to operate the tunnel.

In fact, depending on the tunnel intake location, the reservoir operation during sediment routing can be different. When the intake structure is positioned at the reser-

voir head, the gate is opened during flood events, and the tunnel routes the incoming sediment-laden flow in free surface flow conditions, with no reservoir drawdown needed. On the contrary, locating the intake structure downstream of the reservoir head, requires a drawdown of the reservoir prior to a flood event. This has several consequences on the way the SBT is operated. Firstly, the magnitude of the reservoir drawdown has to be related to the distance of tunnel intake from the reservoir head, i.e. the longer the distance, the more intense the drawdown. Secondly, it has to be ensured that the reservoir reach upstream of the intake structure is subjected to free surface flow conditions to let the incoming sediment-laden water flow towards the intake. Eventually, during SBT operations, the reservoir head has to be kept at a certain level to avoid interruption of the sediment transport (Auel, 2014). Moreover, the location of the intake structure affects the grain size distribution (GSD) of material entering the tunnel, considering that downstream sorting of material deposited inside the reservoir causes the aggradation body to be finer the further it is from the reservoir head (e.g. Berchtold *et al.*, 2008).

2.3.2 Examples of SBTs worldwide and in Switzerland

Worldwide, the number of SBTs is still limited due to high construction and maintenance costs. Most SBTs are located in mountainous regions with small ($<$ 1 million m^3) to medium–sized ($<$ 10 millions m^3) reservoirs where a considerable amount of coarse material (bedload) is entrained (Auel and Boes, 2011b; Boes *et al.*, 2014). However, new schemes include large reservoirs ($>$ 100 million m^3) and shift the focus on suspended sediment load bypassing (Boes, 2015; Sumi, 2017).

SBT should be considered as an adequate desilting measure rather for small to medium-sized reservoirs with capacity-inflow ratios (CIR), i.e. the ratio between the reservoir volume and the annual water inflow volume, of about CIR = 0.003 to 0.2 and with typical reservoir life values, i.e. the ratio between reservoir volume and mean annual sediment inflow volume, of up to some hundreds without countermeasures (Sumi and Kantoush, 2011). The prototype SBTs currently in service mainly in Switzerland and Japan underline this application range for which SBTs are most effective.

Although the worldwide number of SBTs at dam reservoirs currently only amounts to

a few dozens or so (see Tables 2.1 and 2.2), their number is likely to increase considerably in the near future in view of (i) water protection legislation requiring to re-establish sediment continuity in many countries (e.g. Swiss Federal Council, 1998; European Union, 2000), (ii) the growing problem of reservoir sedimentation, resulting in both operational restrictions and safety issues at dams and reservoirs, and (iii) improved design and better knowledge on abrasion-resistant materials (Mueller-Hagmann, 2018) which will limit maintenance and refurbishment cost. As to (ii), SBTs have a proven record to effectively reduce sediment accumulations. For instance, research on the two Japanese SBTs Asahi and Nunobiki showed that in average 77% and 94% of the incoming sediments are diverted to the downstream river reach, enlarging the estimated reservoir life to 450 and 1,200 years, respectively (Auel *et al.*, 2016). Whereas Asahi SBT has been in operation for almost 20 years, Nunobiki SBT in Kobe, Japan, has been successfully in service for 109 years (Sumi, 2017). The main characteristics of SBTs in the world are summarized in Tables 2.1 and 2.2.

Additional information about SBTs is given in Auel (2014), where it is reported that (i) uniform flow velocity values range between ca. 7 m s^{-1} and 15 m s^{-1}, corresponding always to supercritical flow conditions, to maximize the transport capacity in the tunnel; (ii) in most SBTs, uniform flow conditions are reached at the tunnel outlet; (iii) at the intake, discharge is conveyed under supercritical flow conditions; (iv) maximum flow velocities occur either at the end of the acceleration segment, just before the longer segment, downstream of the gate (in case of gate-controlled SBT), or at the tunnel outlet if the tunnel is neither gate-controlled nor has the acceleration segment; (v) the filling ratios (referred to the outlet flow depth) respect the limit to avoid chocking, except in the case of the Asahi SBT (Auel, 2014).

2.3.3 SBT-related research

As of today, since SBTs are mainly built to counteract reservoir sedimentation and the consequent loss of storage capacity (Annandale, 1987), only few works have focused on the downstream morphological effects of SBT releases. Ongoing projects mainly focus on the monitoring of morphological changes following SBT construction. Very few works attempted to couple field observations with numerical predictions. Among

Table 2.1: SBTs in Switzerland (CH), Japan (JP), and Taiwan (TWN); b_t and h_t (D_t): tunnel width and height (diameter), L and S: total length and general slope, $Q_{w,d}$: SBT design discharge. Adapted from Sumi (2017) and Mueller-Hagmann (2018).

Reservoir name	Country	Completion year	Cross-section shape	Intake position	b_t [m]	h_t or D_t [m]	L [m]	S [–]	$Q_{w,d}$ [$m^3\ s^{-1}$]	Target grain size [mm]	Run time [days/a]	Reservoir purpose*
Egshi	CH	1976	Circular**	Upst.	1.20	2.80	360	0.026	50	d_m: 60	3–10	P
Hintersand	CH	2001	Arch	Upst.	3.25	3.20	1050	0.012	38	d_m: 20	n.s.	P
Palagnedra	CH	1977	Horseshoe	Upst.	3.70	6.20	1760	0.02	250	d_m: 74	5	P
Pfaffensprung	CH	1922	Horseshoe	Upst.	4.70	5.23	282	0.03	220	d_m: 250	100–200	P
Rempen	CH	1986	Horseshoe	Upst.	3.45	3.42	450	0.04	80	d_m: 60	1–5	P
Runcahez	CH	1962	Arch$^+$	Upst.	3.80	4.27	572	0.014	110	d_m: 230	4	P
Serra	CH	1952	Horseshoe	Upst.	2.80	2.80	425	0.0157	40	d_m: 50	1–10	P
Solis	CH	2012	Arch	Midst.	4.40	4.68	968	0.019	170	d_m: 60	1	P
Ual da Mulin	CH	1962	Horseshoe	Upst.	2.50	3.70	268	0.043	n.s.	d_m: 40	> 15	P
Val d'Ambra	CH	1967	Circular**	Upst.	3.60	3.60	512	0.02	85	d_m: 60	2–3	P
Nunobiki – Gohonmatsu	JP	1908	Arch	Upst.	2.90	2.90	258	0.013	39	n.s.	n.s.	W
Tachigahata	JP	1905	n.s.	Upst.	n.s.	n.s.	n.s.	n.s.	n.s.	n.s.	n.s.	W
Miwa	JP	2005	Horseshoe	Midst.	7.80	7.00	4308	0.01	300	washload	1–2	F/P
Asahi	JP	1998	Arch	Upst.	3.80	3.80	2350	0.029	140	d_m: 50	16	P
Koshibu	JP	2016	Horseshoe	Upst.	5.50	7.90	3999	0.02	370	d_m: 10	n.s.	F/A/P
Matsukawa	JP	2016	Arch	Upst.	5.20	5.20	1417	0.04	200	d_m: 10	n.s.	F/W
Shihmen	TWN	i.p.	Arch	Midst.	9.00	9.00	3685	0.0286	600	d_m: 0.04	n.s.	F/W/A
Nanhua	TWN	2018	Horseshoe	Midst.	9.50	9.50	1287	0.0185	1000	d_m: 0.02	n.s.	F/W
Tsengwen	TWN	2017	Horseshoe	At dam	9.50	9.50	1235	0.0532	995	d_m: 0.005	n.s.	F/W/A

i.p.: in planning phase; n.s.: not specified

*: F: flood control; A: agriculture; W: water supply; P: hydropower production

**: circular shape with plain invert; $^+$: slightly concave invert

Table 2.2: SBTs in France (FR), Ecuador (ECU), Iran (IRN), Pakistan (PAK), United States (USA), and Republic of South Africa (ZAF); b_t and h_t (D_t): tunnel width and height (diameter), L and S: total length and general slope, $Q_{w,d}$: SBT design discharge. Adapted from Sumi (2017) and Mueller-Hagmann (2018).

Reservoir name	Country	Commission-ing year	Cross-section shape	Intake position	b_t [m]	h_t or D_t [m]	L [m]	S [–]	$Q_{w,d}$ [m^3 s^{-1}]	Target grain size [mm]	Run time [days/a]	Reservoir purpose*
Jotty	FR	1949	n.s.	n.s.	n.s.	n.s.	118	0.006	n.s.	n.s.	n.s.	n.s.
Rizzanese	FR	2012	n.s.	n.s.	n.s.	n.s.	133	0.069	100	d_m: 0–18	n.s.	n.s.
Chespí – Palma Real	ECU	i.p.	n.s.	n.s.	n.s.	n.s.	2200	0.017	n.s.	n.s.	n.s.	n.s.
Delsitanisagua	ECU	u.c.	n.s.	n.s.	n.s.	n.s.	880	0.02	200	n.s.	n.s.	n.s.
Dez	IRN	i.p.	n.s.	n.s.	n.s.	n.s.	n.s.	n.s.	n.s.	n.s.	n.s.	n.s.
Patrind	PAK	2017	Arch	Midst.	7.50	8.50	180	0.0112	340	n.s.	n.s.	n.s.
Mud Mountain	USA	1940	Horseshoe	At dam	2.74	n.s.	505	0.0194	120	d_{50}: 62	~ 80	n.s.
Nagle Dam	ZAF	1950	n.s.	n.s.	n.s.	n.s.	n.s.	n.s.	n.s.	n.s.	n.s.	n.s.

i.p.: in planning phase; u.c.: under construction; n.s.: not specified

*: F: flood control; A: agriculture; W: water supply; P: hydropower production

them the work by Fukuda *et al.* (2012) is worth mentioning, who show that at the Asahi Dam in Japan, the pre-dam riffle-pool morphology and GSD of the downstream reach has recovered following more than 15 years of SBT operations. More attention has been paid to describe and quantify ecological effects of SBT operations through regular monitoring after each SBT operatio (Sumi *et al.*, 2012; Auel *et al.*, 2017; Martín *et al.*, 2017) of the downstream reach. From these studies emerge that SBT operations act as sudden floods (Martín *et al.*, 2017) affecting river ecology both on the short-term (Sumi *et al.*, 2012; Martín *et al.*, 2017) and on the long-term (Auel *et al.*, 2017). SBT operational effects concern microhabitat (Auel *et al.*, 2017), sediment respiration (i.e. organic matter processing), periphyton biomass and macroinvertebrate density and richness (Martín *et al.*, 2017) as well as fish habitat suitability (Sumi *et al.*, 2012). Moreover, ecological effects of SBT operations are strongly dependent on the frequency of the events, where positive effects are noticed if SBTs are operated seasonally in harmony with flood seasonality (Martín *et al.*, 2017).

In addition to that, in the past 15 years, growing recognition of how severely and extensively past river engineering has altered rivers has in turn contributed to the growth of river restoration, which has become in the last two decades one of the most prominent areas of applied water-resources science (Bunte, 2004; Wohl *et al.*, 2005; Dufour and Piégay, 2009; Wohl *et al.*, 2015). A thorough definition of river restoration has been given by Wohl *et al.* (2005), who define it as a variety of modifications that share the common aim of "assisting the establishment of improved hydrologic, geomorphic, and ecological processes in a degraded watershed system and replacing lost, damaged, or compromised elements of the natural system." Re-establishing sediment connectivity at dams is one of the modifications used to accomplish river restoration (Wohl *et al.*, 2015). In this framework, SBTs can be considered as a tool for river restoration. In fact, where SBTs have been constructed, tailwaters undergo a series of seasonal, and therefore intermittent, inputs of sediment-laden water (Facchini *et al.*, 2015; Martín *et al.*, 2017). Water and sediment supply rates change seasonally, ranging during the year between a maximum during SBT operations and a minimum during non operational times, when the downstream reach might be considered as morphologically inactive. In Figure 2.4 a sketch of the functioning of SBTs is given, where the SBT and dam releases are con-

sidered as the source of water and sediment feeding the downstream reach. Sediments are conveyed in the reservoir from the upstream river reach (us), shaping the aggradational body. SBT can carry both water and sediment to the downstream reach (ds). Blue and red arrows indicate possible bypassing operation, with water (blue) and sediment (red) being carried out by the SBT, and water being also possibly released from the dam outlets. Intermittent sediments and water released during SBT operations, result in hydrograph and sedimentograph feeding the downstream reach Even though SBT operations act as short-term disturbances, they may potentially enhance natural sediment regimes downstream of dams in the long term (Martín *et al.*, 2017).

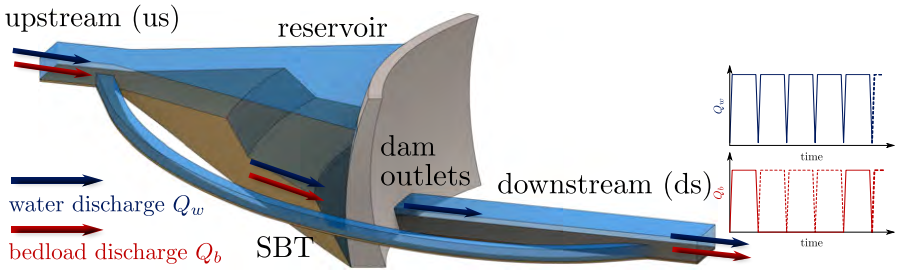

Figure 2.4: Sketch of SBT systems with upstream river reach (us), reservoir, aggradation body, SBT, dam and downstream reach (ds). Blue and red arrows indicate possible bypassing operation, with water (blue) and sediment (red) being carried by the SBT, and water being also released from the dam outlets. On the right, ideal hydrograph and sedimentograph feeding the downstream reach.

This notwithstanding, the study of SBTs as a mean for river restoration is still in its infancy mainly due to the combined effect of (i) the relative small number of SBTs present around the world and (ii) the only recent interest in perceiving SBTs as a mean for river restoration.

2.4 Morphological response of sediment-depleted rivers to sediment augmentations and water inputs

Water and sediment are released from the dam outlets and the SBT in form of water and sediment pulses (see Figure 2.4). That is, when the SBT is put in operation, it releases high volumes of water and sediment (i.e. well above the downstream trans-

port capacity) in a relative short amount of time. Thus, SBTs might restore natural sediment and water regimes, but during non-operational times the river can be considered as morphologically inactive. In the last decades, sediment fluxes and management aimed at restoring natural sediment regimes have been widely discussed by the scientific community. Many techniques have been studied and implemented to restore natural sediment regimes in sediment-depleted river reaches, whereby sediments are: (i) artificially added downstream of dams (e.g. Bunte, 2004), (ii) mobilized by induced side erosion caused by mechanical channel reconfiguration (e.g. Die Moran *et al.*, 2013), (iii) mobilized with artificial floods (e.g. Kondolf and Wilcock, 1996), or (iv) routed around or through reservoirs (e.g. Sumi *et al.*, 2012). As to (i), sediment artificially added to sediment-depleted river reaches are flushed by flowing water and behave like sediment pulses (see Figure 2.5(a)). The latter have been defined by Humphries *et al.* (2012) as "a body of sediment introduced to a channel, the zone of pronounced bed material transport that it causes, and the sediment wave that may form in the channel from the additional sediment supply, which can include input sediment and bed material". Similarly, concerning (iii), water releases are used as an alternative to reactivate sediment transport (e.g. Junk *et al.*, 1989; Poff *et al.*, 1997; Tockner *et al.*, 2000; Robinson *et al.*, 2003, 2004), where hydrographs with different shape and intensity are used to mobilize even armored riverbeds (see Figure 2.5(b)). The dynamic of combined non-stationary sediment and water releases (see Figure 2.5(c)) is complicated by the interplay between water and sediment and it has been poorly investigated so far. Hereafter, research findings concerning sediment augmentations, artificial floods and combinations of these two are discussed.

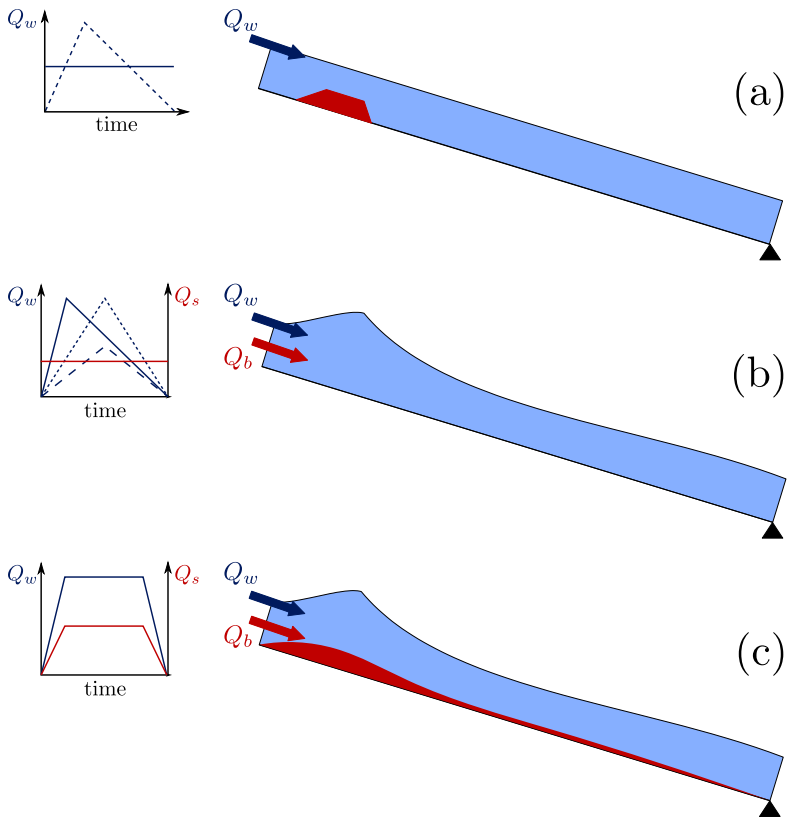

Figure 2.5: Sketch of a simplified river channel (a) with a sediment augmentation body being washed by flowing water, (b) receiving a hydrograph and constant sediment supply as input, and (c) receiving non-stationary water and sediment feedings.

2.4.1 River morphology modifications due to sediment pulses

The morphodynamic response of a river subject to sediment pulses (Figure 2.5a) is mainly dependent on four factors: (i) pulse volumes compared to the channel dimensions, (ii) pulse GSD compared to the riverbed one, (iii) the hydraulic conditions under which they are washed, i.e. either with constant discharge or an unsteady hydrograph, and (iv) the Froude number. Sediment being washed from the aggraded body, i.e. the pulse's body, has been noticed either to translate downstream as a sediment wave, or to disperse *in situ*, depending on the aforementioned characteristics (see e.g. Humphries *et al.*, 2012). In the last 15 years, many researchers have focused on this twofold behavior, analyzing field studies (Madej, 2001; Sutherland *et al.*, 2002; Zunka *et al.*, 2015; Nelson and Dubé, 2016; Pace *et al.*, 2017), performing flume experiments (Cui *et al.*,

2003a; Sklar *et al.*, 2009; Venditti *et al.*, 2010; Humphries *et al.*, 2012; Podolak and Wilcock, 2013), and numerical modeling (Lisle *et al.*, 2001; Cui *et al.*, 2003b; Cui and Parker, 2005; Blair Greimann *et al.*, 2006; Viparelli *et al.*, 2011; Maturana *et al.*, 2014; Gran and Czuba, 2017). The main outcomes of these studies are that: (i) a small (large) volume of sediment favors translation (dispersion), (ii) finer (coarser) sediment accelerate (slow down) the dynamic of morphological processes, therefore favoring sediment pulse translation (dispersion), (iii) impulsive hydrographs (constant discharge) favor(s) translation (dispersion) of sediment, while (iv) low (high) Froude numbers favor dispersion (translation). As to (iv), Pace *et al.* (2017) assert that the Froude number is the most reliable metric to predict the behavior of sediment pulses in real case scenarios.

2.4.2 The effect of repeated hydrographs on sediment-depleted river reaches

Much of the work concerning the effects of flood hydrographs shape, duration and intensity (Figure 2.5b) has been conducted to study the hysteretic effects of sediment transport rate and texture during hydrographs, i.e. the effect of past conditions on the actual situation (Hassan *et al.*, 2006; Mao, 2012; Humphries *et al.*, 2012; Martin and Jerolmack, 2013; Waters and Curran, 2015). Many researchers have found that antecedent bed-surface textures have an influence on sediment transport rates in unsteady flow events. Guney *et al.* (2013) found that sediment yield during unsteady flow stages was lower, the higher the degree of coarsening of the pre-hydrograph bed was. Reid *et al.* (1985) reported a strengthening of the bed framework caused by long periods of low flow between floods. These low flow periods enhance particle interlocking and infiltration of fine material below the surface. A similar effect was described by Waters and Curran (2015), who found that long duration of low flow periods contribute to consolidate and stabilize the bed. This prevents in turn particle entrainment in the flow. Similar results have also been obtained by Ferrer-Boix and Hassan (2015). They introduced very sharp hydrographs (i.e. rectangular hydrographs) repeatedly in a flume, which is fed with a constant sediment discharge throughout the whole experiment; the feed size distribution is also kept constant during the runs. Their results show a downstream fining tendency of bed-surface texture. This process is affected by the duration of low

flow periods, i.e. the longer they are the greater the downstream fining. Since bedload transport is itself influenced by sediment sorting, the evolution of bedload transport is affected by the frequency of water pulses: short interpulse duration reduces the time over which fine sediment can be entrained and transported as bedload (Ferrer-Boix and Hassan, 2015).

Differently, Parker *et al.* (2007) found that downstream of a short region changes in riverbed level and surface grain size distribution are absorbed by bedload. In their numerical runs, they seek for the equilibrium configuration of a simplified 1D channel undergoing a cycled hydrograph and constant sediment supply rate and GSD. Their results show that bed elevation and bed slope fluctuations are confined in a short inlet transition region, which they call *hydrograph boundary layer (HBL)*, while gravel transport rate and GSD remain nearly equal to the feed ones. Downstream of this region, bed elevation and bed slope do not fluctuate, while gravel transport rate and GSD do (Parker *et al.*, 2007). That is, the higher transport flows support a higher transport rate of coarser material and the lower flows support a lower transport rate of finer material (Parker *et al.*, 2007). This implies that rivers subject to repeated hydrographs can evolve so that neither surface GSD, nor mean bed elevation change much with the hydrograph, since all the variations are absorbed by the bedload (Parker *et al.*, 2007). However, the presence and extension of a boundary layer might be influenced by the interaction between sediment mixtures and hydrograph shape (Wong and Parker, 2006). More recently, An *et al.* (2017a) proved that if the feeding material is characterized by a wide GSD the concept of the HBL breaks down due to the persistence of forced low-amplitude (i.e. grain-scale) oscillations of the riverbed level and composition, i.e. sorting waves (Stecca *et al.*, 2014), over the entire reach.

2.4.3 Sediment-laden waters released from SBTs

Differently from the dynamics described in the works reviewed so far, the dynamic induced by SBT operations (Figure 2.5(c)) is influenced by water and sediment being released together at a time-dependent rate. This difference originates from the interplay between the pre-operation river characteristics (i.e. width, slope and riverbed GSD) and the sediment-laden water release. The released water is usually heavily loaded with a

strongly heterogeneous bedload material (Hagmann *et al.*, 2015), i.e. the feed to the tailwater has a wide GSD. Despite the number of studies concerning design, building and operation of SBTs, to date there has been almost no process-based study of the geomorphic response of a river to a shift in water and sediment supply regime caused by SBT operations. However, the physical processes that follow an alteration of water and sediment supply regime are similar to the ones described in the previous subsections. Recently, An *et al.* (2017b) described the effects of pulsed sediment supplies fed in the middle of the studied reach in addition to a constant sediment supply at the upstream end. Results indicate that after the domain reaches a mobile-bed equilibrium, two distinct regions are present in the domain, where riverbed elevation and composition vary periodically in time. The first one is at the upstream end and it is the one described also by Wong and Parker (2006) and Parker *et al.* (2007), the second is just downstream of the cross-section where sediment is fed at a time-dependent rate. Outside these two regions, riverbed level and composition are only perturbed by low-amplitude oscillations (An *et al.*, 2017a), i.e. sorting waves (Stecca *et al.*, 2014).

As outlined in this section, previous work on pulse morphodynamics has mostly been focusing on the deformation process of a single pulse either moving downstream, dispersing in site or evolving following a combination of these two. The physical processes triggered by releases of sediment-laden waters from Sediment Bypass Tunnels might show some analogies with what has already been described in the literature concerning sediment and water pulses. However, the effects of combined and repeated water and sediment inputs (pulses) have received less attention to date.

3 Analysis of the effects of two years of SBT operations at Solis

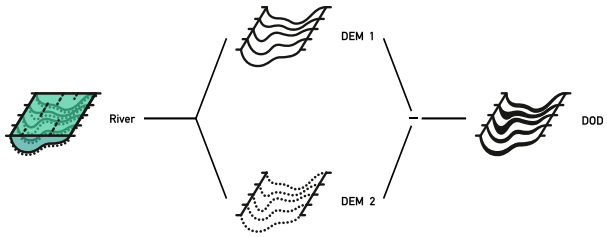

In the last few years, several studies have been carried out to describe and quantify downstream ecological effects of SBT operations through regular monitoring after each SBT operation (Sumi *et al.*, 2012; Auel *et al.*, 2017; Martín *et al.*, 2017). The few studies concerning also river morphology are mostly relative to grain size distribution (GSD) changes following SBT operations (Auel *et al.*, 2017; Martín *et al.*, 2017). Differently, Fukuda *et al.* (2012) use both in-field cross-sections monitoring, and numerical simulations to define the morphological changes occurring in the downstream reach following the construction of a SBT.

Similarly, in this work, the river reach downstream of an existing SBT was surveyed to assess the actual changes induced by two years of SBT operation and to quantify the volume of mobilized sediment. This analysis relies on state-of-the-art survey and data-validation methods. First, the study site is described, i.e. some details are given concerning the Albula River and its basin and the Solis reservoir and SBT. Second, the SBT operations at the Solis SBT since its construction are described. Third, the monitoring activities performed by third parties in the river reach under investigation are summarized. Fourth, the monitoring activities performed in the scope of this work,

i.e. both the surveys and the procedure to process and validate the collected data, are described. Eventually, the results of the analysis are presented.

3.1 Study site

The field activities described hereafter refer to the reach of the Albula River downstream of the Solis SBT near Alvaschein, canton of Grisons, Switzerland (see Figure 3.1). Hereafter, the characteristics of the SBT, the reservoir at which it is constructed, and the downstream reach under investigation are described.

Figure 3.1: Solis SBT during operation (photo by A. Schlumpf, VAW, ETH Zurich) and map of Switzerland to locate it.

3.1.1 Albula River and catchment

The Albula River flows from the Albula pass to the Hinterrhine, draining a 950 km^2 basin, with a total length of almost 40 km. The reach of the Albula under investigation stretches from the SBT outlet to the river mouth into the Hinterrhine for about 8 km in a narrow valley (the Schin canyon, see Figure 3.2). The main tributary of the Albula upstream of the Solis reservoir is the Julia River (not shown in Figure 3.2 since its confluence to the Albula is a few hundreds meters upstream of the gravel quarry), but the main input (about 95%) of bedload particles to the Solis reservoir stems from the Albula since two artificial lakes (hydropower reservoirs) limit the Julia River contribution of coarse sediment into the Solis reservoir (Martín *et al.*, 2017; Rickenmann *et al.*, 2017). Downstream of the dam, three tributaries enter the main reach of the Albula (Rain Digl Lai, Grossbach, and Prodavosbach), providing additional flow and potentially sediment (see Figure 3.2).

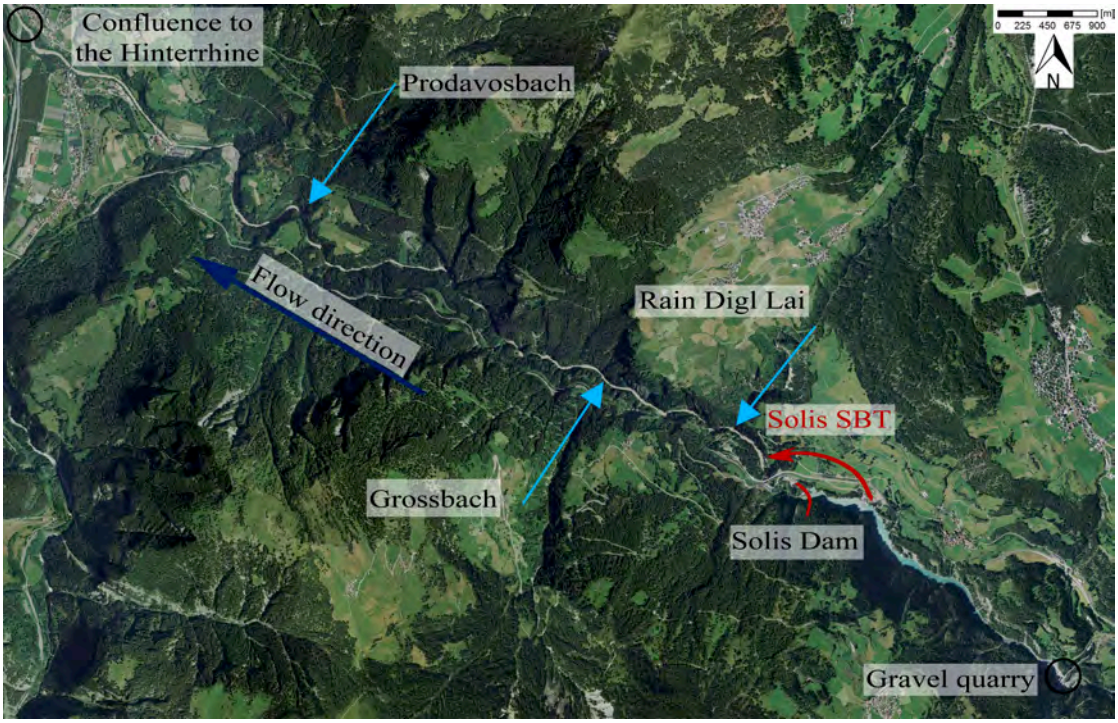

Figure 3.2: Aerial picture of the Albula from the Solis Reservoir to the confluence with the Hinterrhine.

The canyon is accessible only at three spots: close to the SBT, in the middle of the reach and close to the confluence of the Prodavosbach. The stream is primarily single-thread flowing through an active channel 5 to 25 m wide. This channel is composed primarily of bare gravel, with some areas where the bedrock emerges. Point bars are present mostly due to changes in the river width and bends (see Figure 3.3(a)), while some reaches of the Albula inside the Schin canyon are confined by rock (see Figure 3.3(b)).

Figure 3.3: (a) Photo looking downstream of a reach of the Albula inside the Schin canyon, where a point bar is present. (b) Photo looking downstream of a reach of the Albula inside the Schin canyon, where the stream is confined (Photos M. Facchini).

3.1.2 Solis reservoir and SBT

The Solis dam is located along the Albula River, just downstream of Tiefencastel in the canton of Grisons (see Figure 3.2). It is operated by the electric power company of Zurich (Elektrizitätswerk der Stadt Zürich, ewz) and was built in 1986. It is a 61 m high arch dam with a crest length of 75 m. The catchment area at the dam amounts to 900 km^2. The original reservoir capacity was about 4.1 million m^3 (Auel *et al.*, 2010). From surveys of the sediment deposited in the reservoir, the annual sediment delivery of the Albula has been estimated at 80'000 to 100'000 m^3 (Rickenmann *et al.*, 2017).

However, about 30'000 m^3/a of gravel are mined at a quarry located at the reservoir inlet (see Figures 3.2 and 3.4(a)) (Auel *et al.*, 2010).

Figure 3.4: Aerial pictures representing: (a) gravel quarry at the upstream end of the reservoir, (b) intake structure of Solis SBT with submerged guiding structure in the reservoir, (c) Solis Dam and SBT outlet structure, and (d) confluence of the Albula to the Hinterrhine.

The significant sediment transport from the upstream reach resulted in a progressive reduction of the reservoir volume. Moreover, the deposit poses a threat to the safety of the dam infrastructures by potentially blocking its outlets. In Figure 3.5, the progression of the deposition front inside the Solis reservoir from dam construction in 1986 to SBT commissioning in 2012 is shown.

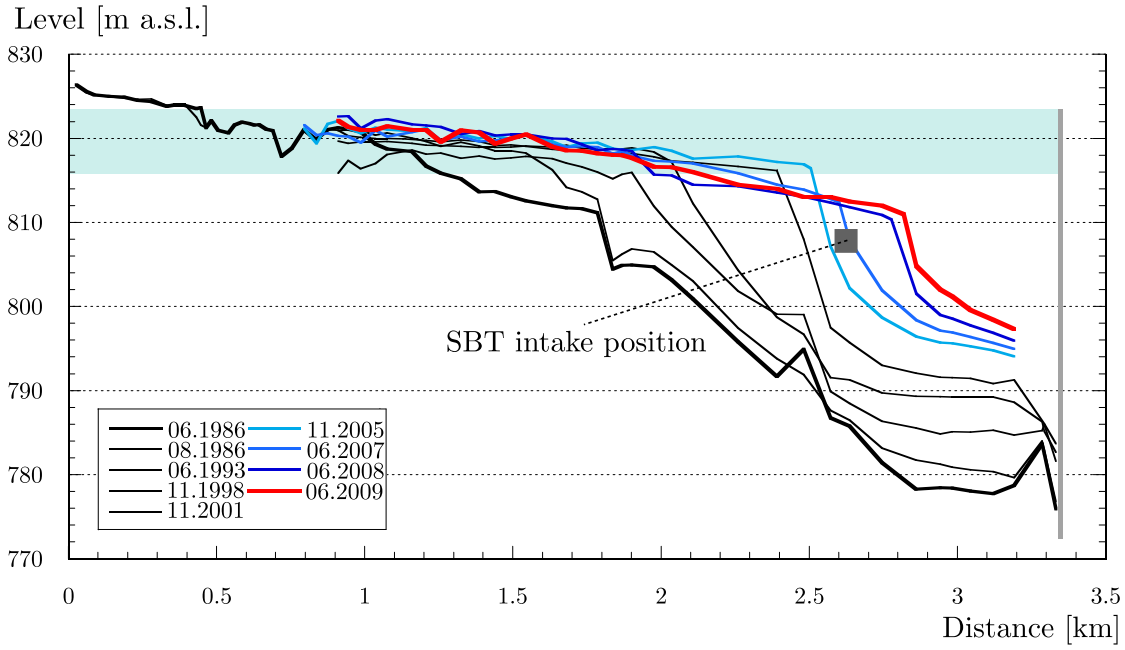

Figure 3.5: Downstream progression of the aggradation body since dam construction in 1986 (adapted from (Auel *et al.*, 2010)).

To solve the problem of reservoir sedimentation, the Solis SBT was built in 2012. Its intake structure is on the right-hand side shore of the lake (see Figure 3.4(b)), and the outlet structure downstream of the concrete dam (see Figure 3.4(c) and Figure 3.6) is ca. 10 m above the riverbed level. The Solis SBT was designed with a capacity $Q_{w,d,SBT}$ = 170 $m^3 s^{-1}$ corresponding to a five-year return period flood. The total length of the bypass tunnel is 968 m with a slope of 1.9%, except for the inflow section, which is 50 m long with a slope of 1%. The tunnel cross section has an archway shape with a width of 4.40 m and a height of 4.68 m (see Figure 3.6). More details about the Solis SBT can be found in Auel *et al.* (2010), Oertli and Auel (2015), and Mueller-Hagmann (2018).

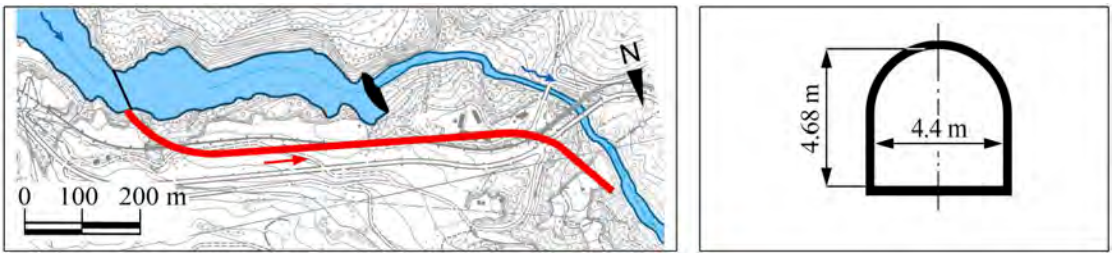

Figure 3.6: Top view of the Solis reservoir, dam, and SBT, and cross-section of the tunnel (courtesy of M. Müller-Hagmann, VAW, ETH Zurich).

3.2 Solis SBT operations since 2012

The Solis SBT is in operation, i.e. it is used to release either bedload-free or bedload-laden water, since 2012. To estimate suspended sediment and bedload transport, turbidimeters and Swiss Impact Plates (e.g. Rickenmann *et al.*, 2014) have been installed at the bottom outlet of the SBT (Mueller-Hagmann, 2018). The SBT is operated on average two times per year, i.e. as of today once in 2013, three times in 2014, twice in 2015 and three times in 2016 (see Figure 3.7). Among these operations, the SBT transported bedload sediment only during the last operation in 2014 (August 13) and the first two in 2016 (June 11 and 16). The duration of the SBT operations at Solis goes from 5.5 to 24 hours with mean water discharge being released by the SBT during these operations ranging between 58 and 153 m^3s^{-1}. Before, during and after SBT operations, water can be released from the dam outlets, i.e. the two bottom outlets. If the reservoir level exceeds the full supply level, water can also be released via the dam spillway. The hydrograph representing the water discharge being released from the Solis dam and SBT from January 2014 to January 2017 is represented by the black line in Figure 3.7, where red lines and full stars indicate the SBT operations with bedload transport (August 2014 and June 2016) and blue lines and empty stars indicate the SBT operations without bedload transport (May and June 2014 and 2015, and July 2016).

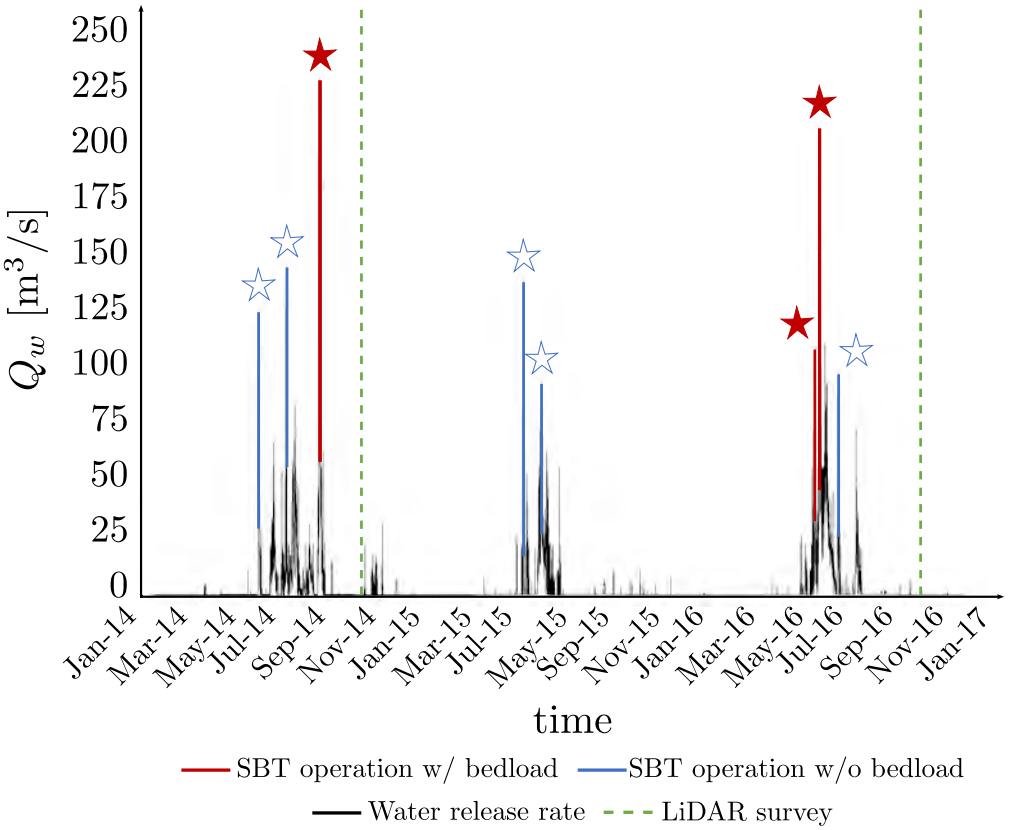

Figure 3.7: Water released from Solis dam and SBT between January 2014 and January 2017, SBT operations are marked with colored lines and stars over the hydrohraph and LiDAR surveys are indicated with green dashed lines. Full stars indicate bedload-laden water releases and empty stars releases of water.

Detailed hydrographs concerning the bedload-laden SBT operations are given in Figure 3.8, where (a) is the hydrograph relative to the operation of August 13, 2014, (b) the one relative to the operation of June 11, 2016, and (c) the one relative to the operations of June 16 and 17, 2016. The solid line represents the hydrograph relative to the SBT alone, while the dashed line is relative to the water discharge being released to the downstream reach. The peaks of the three hydrographs presented in Figure 3.8(a), (b), and (c) are relative to a 30, 2, and 10 years return period flood, respectively.

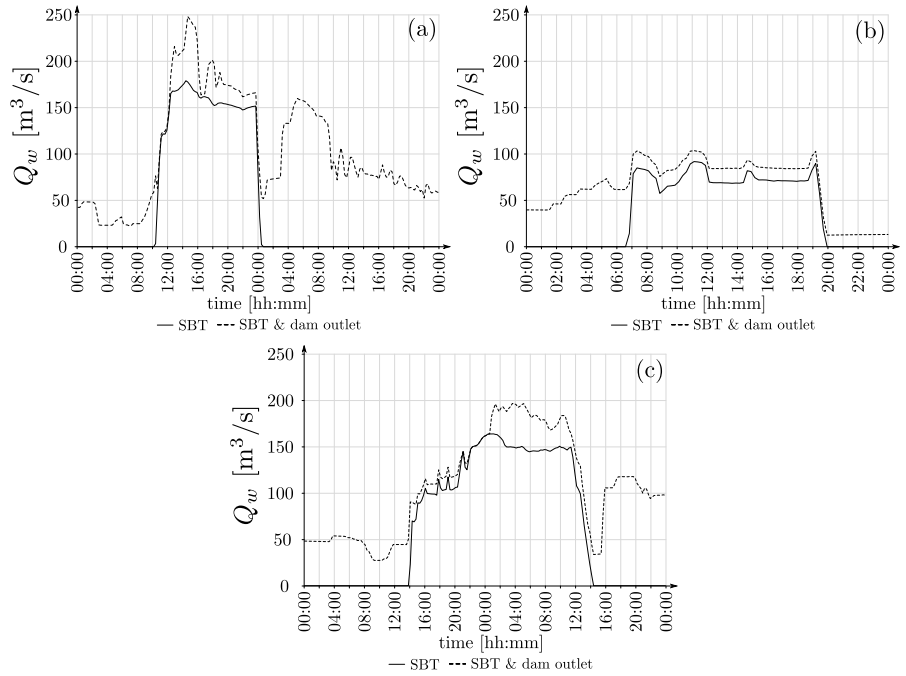

Figure 3.8: Hydrographs relative to SBT operations carrying bedload-laden water to the downstream reach: (a) relative to the operation on August 13, 2014, (b) to the operation on June 11, 2016, and (c) to the operation between June 16 and June 17, 2016. Solid lines refer to the water discharge through the SBT, dashed lines to the total water discharge being delivered to the downstream reach, i.e. from the SBT and from the dam outlets.

3.3 Monitoring activities carried out by third parties in the downstream reach

Field measurements in the reach below the SBT outlet structure are carried out every year and are commissioned by the electric power company of Zurich (Elektrizitätswerk der Stadt Zürich, ewz) to Meisser Vermessung AG and ecowert GmbH, which are in charge of morphological and ecological monitoring, respectively. Morphological monitoring activities are focused in three zones of the river reach (black empty circles in Figure 3.9), where for each site three cross-sections are measured every year. Locations are denoted as the number of kilometers downstream from the SBT outlet structure traced along the river centerline. Moreover, the Swiss Federal Institute of Aquatic Science

and Technology (eawag) monitored the reach in two areas along the river reach, which are represented by the green full dots in Figure 3.9. They measured physico-chemical properties, sediment respiration, periphyton biomass and chlorophyll-a, and macroinvertebrate assemblages at each site after each SBT operation (Martín *et al.*, 2017).

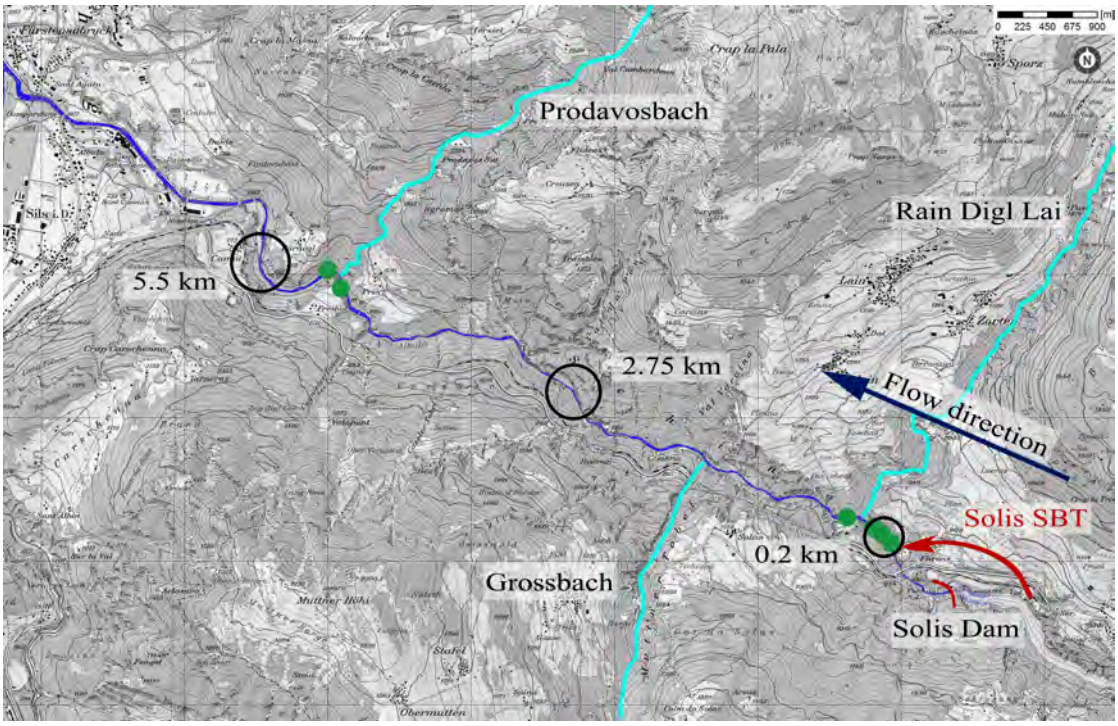

Figure 3.9: River reach under investigation: black circles indicate where morphological and ecological monitoring are performed every year by Meisser Vermessung AG and ecowert GmbH, respectively, as commissioned by the electric power company of Zurich (Elektrizitätswerk der Stadt Zürich, ewz); green dots indicate locations where the Swiss Federal Institute of Aquatic Science and Technology (eawag) performed ecological monitoring in the scope of E.J. Martín's (former eawag) PhD project (Martín *et al.*, 2017). Locations are denoted as the number of kilometers downstream from the SBT outlet structure traced along the river centerline.

3.4 Bathymetric LiDAR surveys at the Albula River

A detailed description of the topography of the valley bottom is needed to assess more accurately the morphological changes occurring after SBT operations. This is a stringent requirement for running reliable numerical simulations and obtaining detailed in-

formation about the amount of sediment volume mobilized during SBT operations. Six cross-sections have been monitored every year since SBT commissioning in 2012, but they are localized at three reaches far from one another, which makes it impossible to estimate the changes between the reaches. Moreover, the conventional cross-section monitoring approach to estimate volumes and patterns of scoured and filled sediments has been proven to result in major inaccuracies in the estimation of morphological changes at the cross-section spacings typically used (i.e. ca. 10 m) (Lane *et al.*, 1994; Brewer and Passmore, 2002). On the contrary, the information supplied from terrain models, which can be acquired rapidly when using e.g. modern laser scanning techniques, allows for accurate estimation of the volumes of sediment mobilized for example during unconventional events such as SBT operations.

Nowadays, there is a growing need of detailed and accurate representation of river channel geometry at high resolutions, which allows for the study of fluvial environments. Specifically, detailed channel geometry is useful for: (i) describing flow hydraulics (e.g. Mandlburger *et al.*, 2009, 2015), (ii) flood protection purposes (e.g. Khosronejad *et al.*, 2016), (iii) sediment transport estimation (e.g. Croke *et al.*, 2013; Pace *et al.*, 2017; Bezak *et al.*, 2017), (iv) aquatic habitat assessment and monitoring of geomorphic change (e.g. Lane *et al.*, 1994; Mandlburger *et al.*, 2015), and (v) numerical modeling of river morphodynamics (e.g. Bates *et al.*, 2003; Khosronejad *et al.*, 2016). Modern survey techniques, such as Light Detection And Ranging (LiDAR) surveys, have significantly increased the potential accuracy and extent, both in space and time, of morphologically-based sediment transport estimates and have recently been used, e.g. to quantify sediment transport in rivers (Croke *et al.*, 2013; Anderson and Pitlick, 2014; Brestolani *et al.*, 2015; Cavalli *et al.*, 2017).

LiDAR surveys can be of three types, namely: (i) terrestrial, (ii) aerial, and (iii) bathymetric (Milan, 2012). The first two are similar, the only difference being that the hardware used for aerial LiDAR surveys is mounted on an aircraft or helicopter and the instruments used are designed for surveying objects on a large range (Milan, 2012). Differently from aerial and terrestrial LiDAR, bathymetric LiDAR allows for the measurement of points that are under the water surface. In the last decade, bathymetric LiDAR has been proven to be a reliable technique for accurately representing

riverbed topography (Kinzel *et al.*, 2007; Hilldale and Raff, 2008; Bailly *et al.*, 2010; Mandlburger *et al.*, 2015). Applications of LiDAR to fluvial systems have increased in number since 2000, partly due to wider availability of hardware and the introduction of terrestrial LiDAR, which reduces the cost of surveys as compared to aerial LiDAR. Nowadays, LiDAR are not only research tools, but are also widespread as commercial tools.

During bathymetric LiDAR surveys, the distance to an object is determined by measuring the time of flight of laser pulses from the sensor (usually mounted on an aircraft) to the object and back, i.e. measuring the range (a variable distance) to the ground. Hence, after the georeferencing of the measured points, LiDAR delivers a point cloud of varying elevation values that identify the top of buildings, tree canopy, power-lines, and other types of features. The unprocessed point cloud detected during a LiDAR survey identifies the Digital Surface Model (DSM) of the Earth. Moreover, during bathymetric LiDAR surveys, laser light in the blue-green wavelength (532 nm) can penetrate the water surface and measure points that are e.g. on the riverbed. Signals reflected by the riverbed reach high-sensitive receivers on the aircraft, where laser pulse signal and echoes are recorded. Received echo signals hold information about objects that have modified the signal inside the water (e.g. waves, turbidity, obstacles). Signal digitalization and full waveform analysis are used to interpret the resulting echo pulses shape and discern what causes them (Steinbacher *et al.*, 2010).

The resulting point cloud representing the DSM needs to be georeferenced using reference points on the ground, and then classified to discern between points that have been reflected by e.g. trees, buildings, or water surface. Afterwards, from the water surface the riverbed can be extrapolated taking into account the index of refraction of the water.

3.4.1 2014 and 2016 bathymetric LiDAR surveys at the Albula

Two bathymetric LiDAR surveys were performed in collaboration with AirborneHyroMapping (AHM) GmbH from Innsbruck, Austria, one in October 2014 and one in October 2016, after the SBT operations of August 2014 and June 2016, respectively (see the green dotted lines in Figure 3.7). Surveys were performed during a minimum flow

Table 3.1: Technical details of the 2014 and 2016 LiDAR surveys at the Albula River. λ_{pts} is the point density, ε_{ALS} is the accuracy of the ALS system, ε_{geo} is the georeferencing error, and ε_{aln} is the stripes alignment error.

Year	Operator	Flight Date	ALS[a] System	Stripes	λ_{pts} [pts/m^2]	ε_{ALS} [cm]	ε_{geo} [cm]	ε_{aln} [cm]
2014	AHM[b]	Oct. 18	VQ820-G	16	20-30	2.5[c]	5	6
2016	AHM[b]	Oct. 17	VQ880-G	16	50-60	2.5[d]	5	8

[a]Airborne Laser Scanning, [b] AirborneHyroMapping GmbH, [c] at 1 Secchi depth, [d] at 1.5 Secchi depths.

period with no releases from either the dam outlets or the SBT. Therefore, water depth was in an acceptable range for LiDAR surveys (e.g. Milan, 2012). The valley was flown over several times and points to obtain more stripes of points (16 in 2014 and 2016) which have been aligned to obtain a single point cloud. For both the 2014 and 2016 survey, the wavelength of the laser used is in the blue-green range (532 nm), which allows for measuring points below the water surface. The device used for the 2014 survey was the VQ820-G by Riegl Laser Measurement Systems (LSM), which measures with an accuracy of 25 mm until 1 Secchi depth (e.g. Preisendorfer, 1986). For the 2016 survey, a different device was used, i.e. the VQ880-G by Riegl LSM, which measures with an accuracy of 25 mm until 1.5 Secchi depths. Therefore, if the turbidity of the water is too high, points below the water surface result to be less detectable. The point density of the measurements is ca. 20-30 pts/m^2 for the 2014 survey, and ca. 50-60 pts/m^2 for the 2016 one. The technical details of the two LiDAR surveys are summarized in Table 3.1, where the year, the operator, the flight date, the ALS system used, the number of stripes, the point density λ_{pts}, the ALS system accuracy ε_{ALS}, the georeferencing error ε_{geo}, and the stripes-alignment error ε_{aln} are given.

The procedure for obtaining a DEM from the measured point cloud is composed by seven steps following the flight: (i) alignment of the stripes, (ii) georeferentiation of the point cloud, (iii) automatic classification of the point cloud, (iv) manual correction of the classified point cloud, (v) refraction for the riverbed points, (vi) interpolation of the riverbed, and (vii) building of the DEM. The stripes have been aligned and geo-

referenced by the AHM operators using some control points available on-line on the website of the Swiss Federal Office of Topography siwsstopo and ground points measured by Steinbacher Consult GmbH, with an estimated alignment error of 6 and 8 cm for the 2014 and 2016 survey, respectively, and georeferencing error equal to 5 cm. The points have been projected into the World Geodetic System 1984 Universal Transverse Mercator coordinates (zone 32N). The point clouds have been then automatically preproccessed with HydroVISH, a software developed by AHM GmbH in collaboration with the University of Innsbruck, based on the VISH visualization shell (Benger *et al.*, 2007) (see Figure 3.10). In this phase, the points relative to high objects have been filtered out from the Digital Surface Model (DSM) and a model of the ground has been extrapolated from the point cloud, which describes the ground and the water surface. Afterwards, points belonging to the water surface that were not detected during the automatic classification have been manually detected to allow for the correction of the refraction due to water and extrapolation of the riverbed (e.g. Dobler *et al.*, 2014). The final result of the point-cloud pre- and post-processing is a model of the elevations of the points representing the ground of dry areas and the riverbed, i.e. a Digital Elevation Model (DEM) of the river reach with cell size equal to 1 m^2 both for the 2014 and 2016 DEMs.

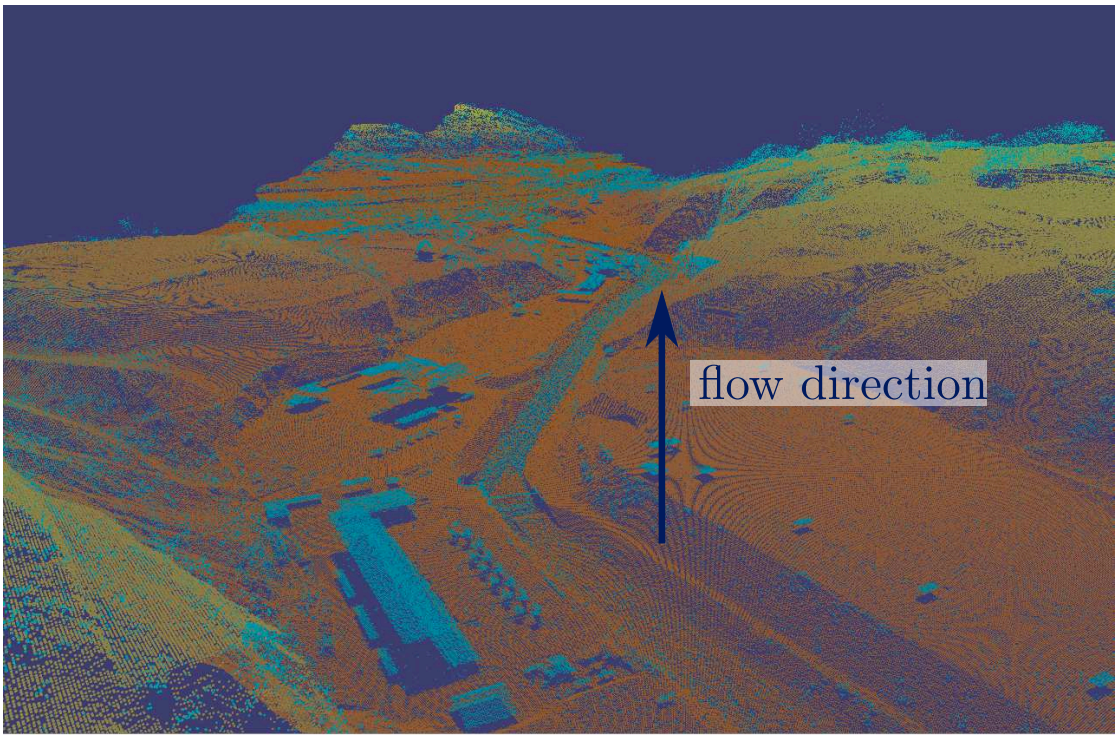

Figure 3.10: 3D representation of the downstream reach of the Albula close to a power-plant in Sils im Domleschg, Canton of Grisons, Switzerland. Buildings (e.g. bottom-left), tree canopy (e.g. top right), and water surface (e.g. middle) are visible in this representation of the pre-processed point cloud. Colors are also representative of the classification (e.g. cyan for high objects).

3.4.2 Validation of the 2014 and 2016 LiDAR data with cross-sections

In a first phase, to validate the DEM derived from the two LiDAR surveys, six cross-sections measured in field by Meisser Vermessung AG, three at the 0.2 km station and three at the 5.5 km station (see Figure 3.9), were used. The ones measured at the 2.75 km station are georefernced with a local reference system and therefore do not match with any point belonging to the LiDAR dataset. Cross-sections from the 2014 LiDAR survey show a good agreement with the ones measured with the total station, with indices of correlation R^2 ranging between 0.73 and 0.97 (Figure 3.11). Most of the scatter concerns the points on the river banks.

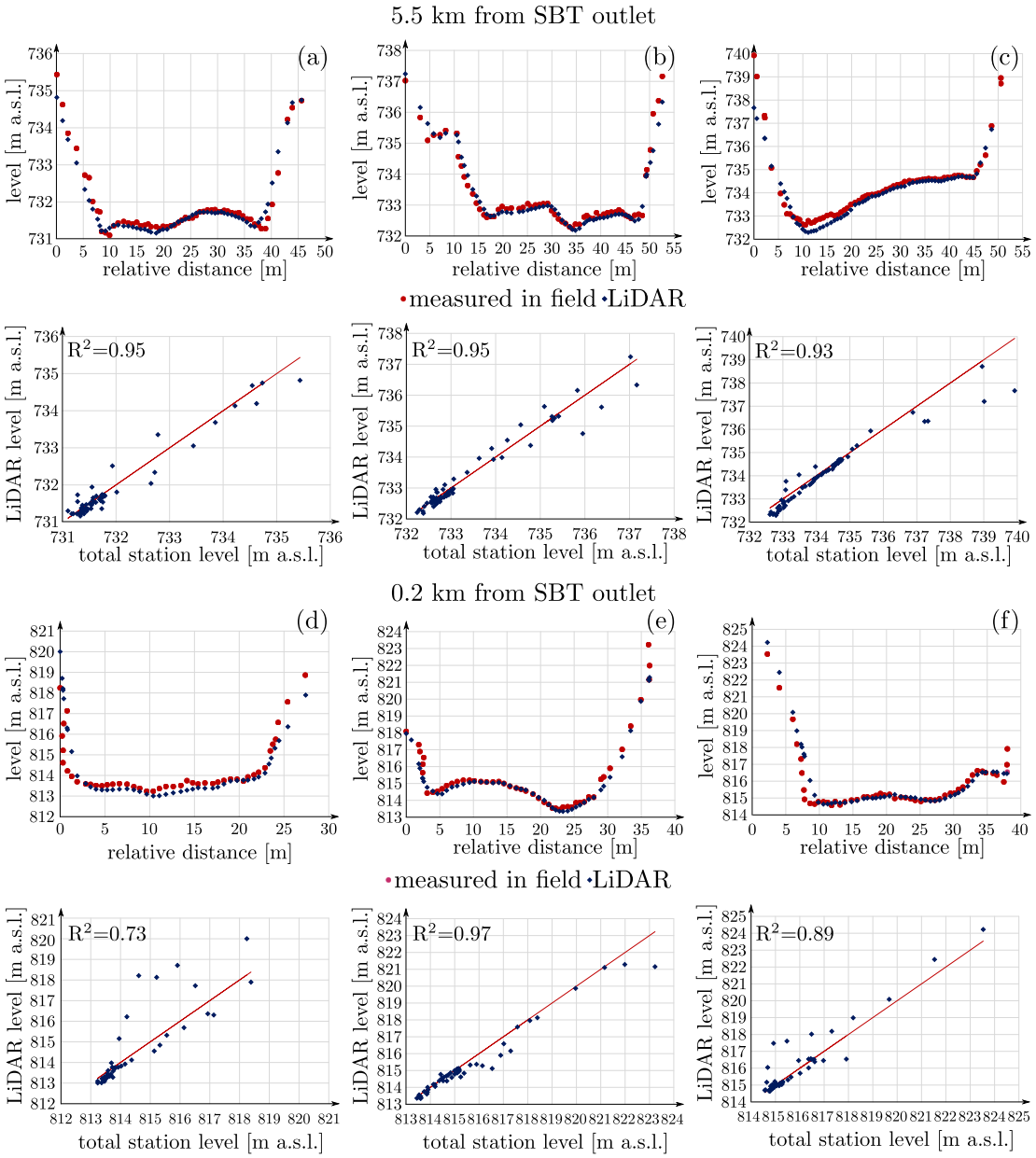

Figure 3.11: Cross-sections extrapolated from the 2014 LiDAR survey (blue diamonds) plotted against the ones measured in field by Meisser Vermessung AG (red dots and lines).

During the 2016 survey, although the water level was very low, the turbidity of the water was high. Therefore, data collected in 2016 have been first validated against cross-sections without taking into account points measured under water. Results of this validation are plotted in Figure 3.12 and show that LiDAR points are mostly in good

agreement with the ones measured in the field ($R^2 = 0.59 \div 0.98$). However, many riverbed points are missing (see e.g. cross-sections (c) and (d) in Figure 3.12).

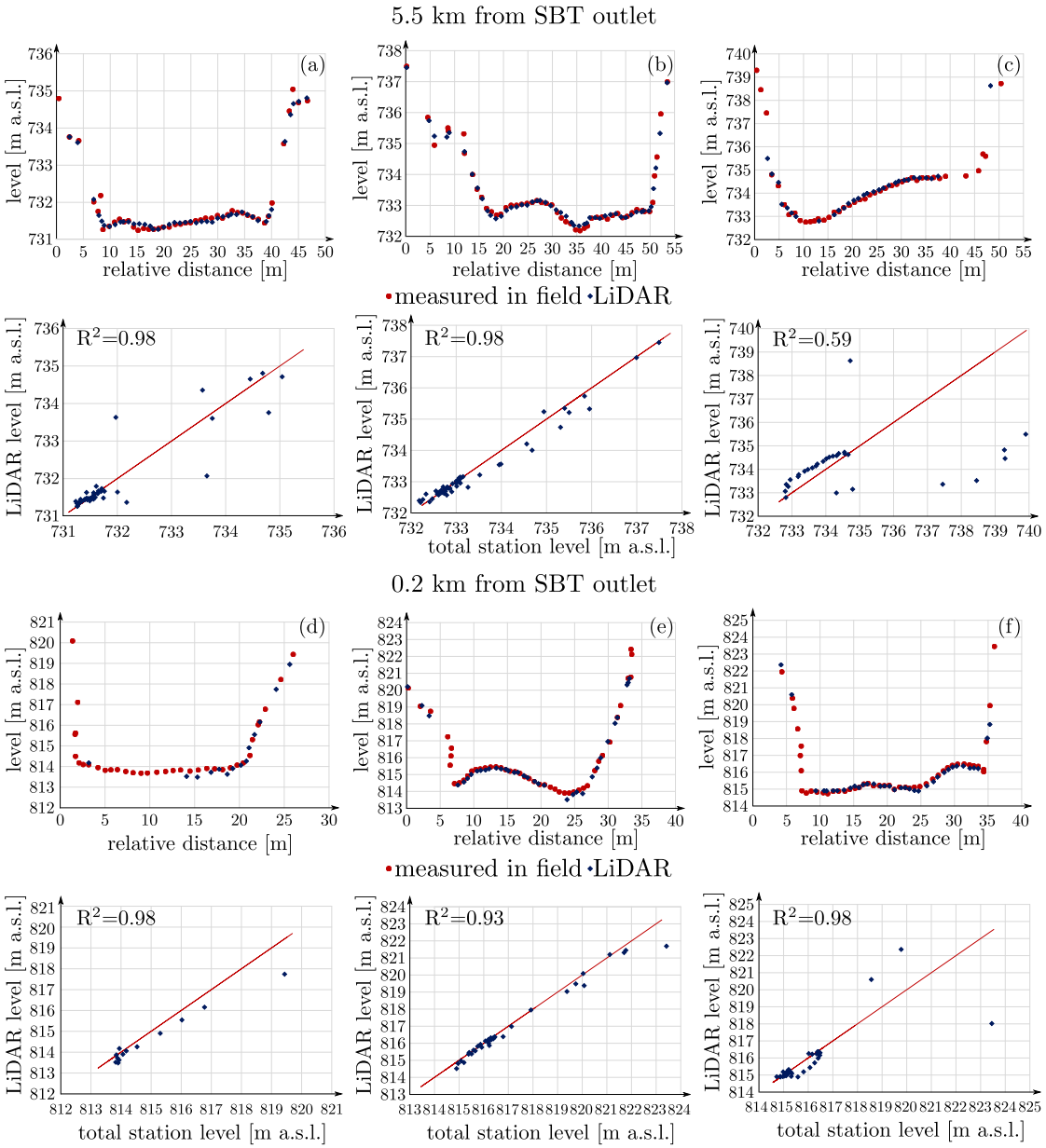

Figure 3.12: Cross-sections extrapolated from the 2016 LiDAR survey, without interpolated points below the water surface, plotted against the ones measured in field by Meisser Vermessung AG (red dots and lines).

Therefore, the missing data have been interpolated by building a triangular mesh in

the areas where no points were available. Results presented in Figure 3.13 show that points measured with the LiDAR survey and then interpolated are in good agreement with the one measured in the field, with indices of correlation R^2 ranging between 0.61 and 0.98.

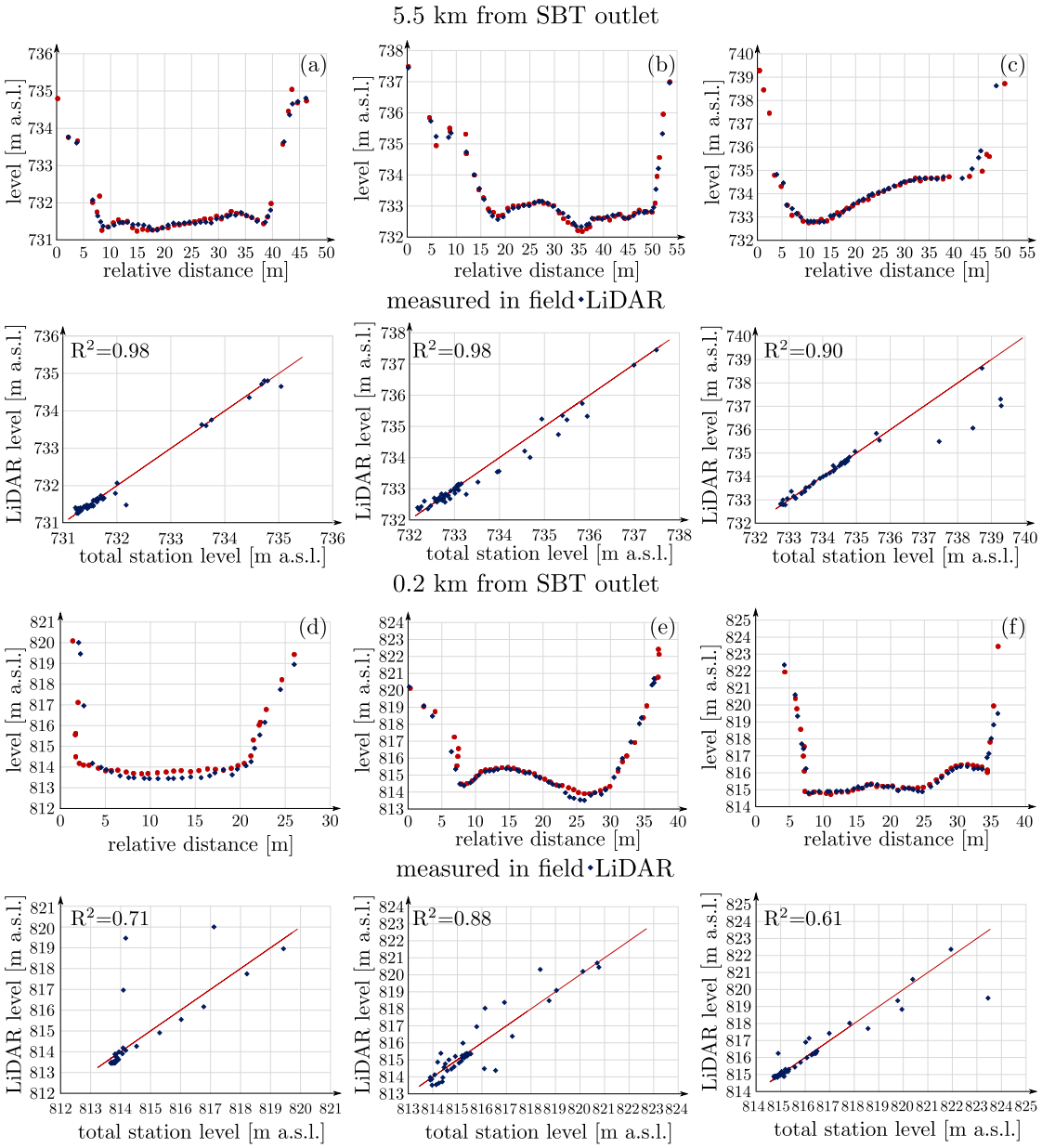

Figure 3.13: Cross-sections extrapolated from the 2016 LiDAR survey (blue diamonds), with interpolation for points below the water surface, plotted against the ones measured in field by Meisser Vermessung AG (red dots and lines).

3.4.3 New validation procedure for bathymetric LiDAR data

The interpolated data of the 2016 LiDAR survey seem to be reliable at the locations where cross-sections have been measured in the field. However, these are representative of only two short reaches that cover less than 5% of the total reach length. Therefore, a new validation procedure for bathymetric LiDAR data is applied, based on two-dimensional (2D) hydraulic modeling and raw LiDAR data analysis to verify if the few points measured under the water surface belong to the riverbed or not. The new validation procedure consists of combining the information given by the 2D hydrodynamic modeling with the information given by the LiDAR raw data analysis. Deep-water areas are defined using the results of the modeling, and the quality of the points measured in these areas is assessed using a combination of the intensity and return numbers of the LiDAR point cloud to distinguish between points measured inside the water column or on the riverbed. To allow for this new procedure, a numerical mesh is first built using the 2014 DEM. Second, the model is calibrated with water depth h, flow velocity u, and wetted area A_w data collected in the field in December 2014 over three long reaches at the same locations where cross-sections are monitored (black circles in Figure 3.9). At the end of the calibration process, a set of parameters is selected to define from which run the distribution of the water depth along the reach under investigation can be estimated. Eventually, intensity and return numbers of the LiDAR points that were under the water surface and were actually measured are checked to assess their reliability.

Numerical meshing using a DEM

To generate the mesh using the DEM derived from the LiDAR point clouds, BASEmesh is used, a free tool for the generation of computational meshes for numerical simulations available at `www.basement.ethz.ch/download/tools/basemesh`. BASEmesh is developed at VAW (ETH Zurich) and is available as python plugin for QGIS, a free and open source geographic information system used worldwide, published under GNU GPL and available under `www.qgis.org`. The resulting mesh is an unstructured 2D-mesh composed of triangular elements of variable size. Two different computational domains are built having 36001 (coarse mesh) and 80115 (fine mesh) elements, i.e. a mean cell area equal to 13.5 m^2 and 6.1 m^2, respectively. The nodes of

the elements generated by BASEmesh are then interpolated with the 2014 DEM surface, since the 2016 DEM surface has not enough data relative to the riverbed in areas of deep water allowing for interpolation.

Calibration of the roughness

Hydraulic simulations have been conducted with BASEMENT (Vetsch *et al.*, 2017a), i.e. with BASEplane, its underlying unsteady 2D shallow water numerical model. In BASEplane, a robust wet-and-dry algorithm is implemented, allowing the correct simulation of emerging topographies. The two-dimensional non-conservative hyperbolic system of PDEs which is numerically solved in BASEMENT is presented hereafter:

$$\begin{cases} \dfrac{\partial h}{\partial t} + \dfrac{\partial q_{wx}}{\partial x} + \dfrac{\partial q_{wy}}{\partial y} = 0 \\ \dfrac{\partial q_{wx}}{\partial t} + \dfrac{\partial}{\partial x}\left(\dfrac{q_{wx}^2}{h} + \dfrac{1}{2}gh^2\right) + \dfrac{\partial}{\partial y}\left(\dfrac{q_{wx}q_{wy}}{h}\right) + gh\dfrac{\partial \eta}{\partial x} = -ghS_{fx} \\ \dfrac{\partial q_{wy}}{\partial t} + \dfrac{\partial}{\partial x}\left(\dfrac{q_{wy}q_{wx}}{h}\right) + \dfrac{\partial}{\partial y}\left(\dfrac{q_{wy}^2}{h} + \dfrac{1}{2}gh^2\right) + gh\dfrac{\partial \eta}{\partial y} = -ghS_{fy} \end{cases} \tag{3.1}$$

where h denotes flow depth, $\vec{q}_w = (q_{wx}, q_{wy})$ is the vector of the flow discharge per unit width, g is the acceleration due to gravity, and η is the riverbed elevation. Furthermore, $\vec{S}_f = \left(S_{fx}, S_{fy}\right)$ is the vector of the dimensionless friction slope, which can be written as

$$S_{fx} = \frac{|q_{wx}|q_{wx}}{h^{10/3}k_s^2}, \qquad S_{fy} = \frac{|q_{wy}|q_{wy}}{h^{10/3}k_s^2} \tag{3.2}$$

where k_s is the Gauckler-Strickler coefficient measured in $[\mathrm{m}^{1/3}\mathrm{s}^{-1}]$ and equal to the inverse of the Manning coefficient. The Gauckler-Strickler coefficient k_s is assumed to be constant and it is calculated with the empirical formula

$$k_s = \frac{21.1}{d_{90}^{1/6}} \tag{3.3}$$

where d_{90} is the grain size such that 90% of the grains are finer. Alternatively, the friction slope $\vec{S}_f$ in the momentum equation in (3.1) can be evaluated by the Chezy

friction law as

$$S_{fx} = \frac{|q_{wx}|q_{wx}}{gC_h^2h^3}, \qquad S_{fy} = \frac{|q_{wy}|q_{wy}}{gC_h^2h^3} \tag{3.4}$$

where C_h is the dimensionless Chezy coefficient that can be assumed as a constant, typically ranging between 10 and 20, or evaluated with a logarithmic law in the form

$$C_h = 6 + 2.5 \ln\left(\frac{h}{k_{C_h} d_m}\right) \tag{3.5}$$

where k_{C_h} is a constant (usually $k_{C_h} = 2.5$) and d_m is the median grain size of the riverbed GSD. Bezzola (2002) proposed an extension of the Chezy friction law for low submergence which reads

$$\begin{cases} C_h = 2.5\sqrt{1-\dfrac{h}{h_R}}\ln\left(10.9\dfrac{h}{h_R}\right) & \dfrac{h}{h_R} > 2 \\ C_h = 1.25\sqrt{\dfrac{h}{h_R}}\ln\left(10.9\dfrac{h}{h_R}\right) & 0.5 < \dfrac{h}{h_R} \leq 2 \\ C_h = 1.5 & \dfrac{h}{h_R} \leq 0.5 \end{cases} \tag{3.6}$$

where h_R is the height of the roughness sublayer, which for rivers is usually equal to the surface size d_{90}. For high submergence ($h/h_R > 2$), eq. 3.6 converges to eq. 3.5. More details on how the two-dimensional system of equations is solved in BASEMENT are given in the software system manual (Vetsch *et al.*, 2017a).

The roughness is calibrated using two different closure relations over the two meshes, i.e. Bezzola and Strickler, and seven different values for the riverbed surface grain size d_{90}, which is used to calculate k_s and C_h, i.e. the Strickler parameter and Chezy coefficient, respectively. The seven d_{90} chosen here are taken as representative of the river reach under investigation and cover a range of values spanning from the finest to the coarsest d_{90} measured in the reach between 2012 and 2016. Values of d_{90} and k_s used as input to the numerical runs are summarized in Table 3.2. Values of C_h are dependent on the level of submergence, i.e. the ratio of water depth h to the d_{90}, therefore the input to the numerical runs is the d_{90}.

For each combination of mesh and closure relation for the roughness seven simulations are performed, for a total of 28 simulations. Simulations are performed with a

Table 3.2: Riverbed surface grain size d_{90} values and calculated Strickler coefficients k_s used as input to the numerical runs.

d_{90} [mm]	120	175	230	285	340	500	1000
k_s [$m^{1/3}$ s^{-1}]	30	28	27	26	25	24	21

fixed bed configuration, imposing a constant inflow discharge at the upstream boundary and uniform flow at the downstream boundary. The inflow water discharge fed at the upstream end of the domain corresponds to the minimum flow released from the Solis dam during the period when the field measurements have been carried out (December 2014), i.e. $Q_w = 0.36$ $m^3 s^{-1}$. Each run reached the steady state after a few hours of simulated time, which corresponds to less than 10 minutes of computational time.

To calibrate the roughness, three reaches have been surveyed, i.e. the ones identified by black circles in Figure 3.9, during a period of low flow in December 2014, to measure water depth h, flow velocity u and wetted areas A_w. First, wetted areas have been defined at the three chosen sites within the stream using a rangefinder (TruPulse 360B, Laser Technology, Inc., Continental, CO, USA), a pocket PC (rugged Algiz 10X, Handheld, Lidköping, Sweden), ArcPAD software (ESRI, Redlands, CA, USA), and GPS positioning. During the survey, the offset points of the wetted areas are collected using the rangefinder (with a range accuracy of $\pm$ 10-30 cm and an inclination accuracy of $\pm$ 0.1-0.25°) and are saved on georeferenced aerial pictures using the pocket PC and the ArcPAD software. For each surveyed area, between 60 and 150 measurements are taken of water depth and flow velocity, using a portable electromagnetic flowmeter (Marsh-McBirney Flo-Mate, Hach Company, Loveland, CO, USA). For each surveyed area, minimum, maximum and average values as well as the standard deviation of the distribution for each measured variable are compared. Results of the calibration using the water depth are presented in Tables 3.3, where h_{max} is the maximum, and $\bar{h}$ the mean, while σ_h is the standard deviation. The same applies to Tables 3.4 and 3.5, where results of the calibration using the flow velocity u and the wetted area A_w are presented, respectively. Moreover, in Tables 3.3 to 3.5: **u**, **m**, and **d** refer to the three reaches that

are 0.2, 2.75, and 5.5 km downstream of the SBT outlet structure, respectively; coarse and fine mesh refer to the two meshes derived from the 2014 DEM having 36'001 and 80'115 elements, respectively; Bezzola and Strickler refer to the two closure relations used to evaluate the dimensionless friction slope $\vec{S}_f$, where the different values of d_{90} are used to calculate C_h and k_s, respectively. Results presented in Tables 3.3, 3.4 and 3.5 are not influenced by the choice of the roughness relation or by the choice of the d_{90}. Simulated values relative to the water depth h and the flow velocity u are slightly different from the ones measured in the field. Differently, simulated values relative to the wetted area A_w are similar to the one measured in the field. Given the small difference between the computational time using the coarse rather than the fine mesh, the latter is preferred. Concerning the closure relation and the roughness parameter, the Bezzola closure relation seem to be the more reasonable choice since it has been developed for low-submergence conditions. The same applies to the chosen d_{90} = 175 mm which is a good estimation of the d_{90} measured in the field in the years following the SBT commission.

Return number and intensity of the LiDAR points

To filter and assess the quality of the few points measured under water, return numbers and the intensity of the points are used as control. First, water depth data resulting from the numerical simulations are used to see where deep-water areas are most likely to be. Second, return numbers are used to consider only the points that are in deep-water areas and have return numbers larger than 1. Third, in areas of shallow water, the values of the intensity of the first and last returns are used to double check the under-water points, since the water surface has a higher intensity than the riverbed. For example, if in an area of shallow water there is a point with return numbers 1 and high intensity and one with a return numbers >1 and lower intensity, the second is assumed as belonging to the riverbed. Examples of the application of this filtering system are given in Figures 3.14, 3.15, and 3.16. In Figure 3.14, a river bar is defined by a black thick line. At the border of the river bar and on its south-east side the water is shallow and both points with return numbers 1 and >1 are present (Figure 3.14(b) and (c)). However, these points have different intensity, as one can notice by comparing (d) and (e) in the same Figure.

Table 3.3: Results of the roughness calibration using measured water depths (field) as a reference, both on the **coarse** and **fine mesh**, using the roughness closure relations by Bezzola and Strickler; **u**, **m**, and **d** refer to 0.2, 2.75, and 5.5 km reaches in Figure 3.9, respectively. The results relative to the chosen set of parameters are highlighted in red.

Coarse mesh

		field	Bezzola							Strickler						
			120mm	175mm	230mm	285mm	340mm	500mm	1000mm	120mm	175mm	230mm	285mm	340mm	500mm	1000mm
u	h_{max}	1.70	1.25	1.24	1.26	1.26	1.27	1.26	1.28	1.48	1.48	1.48	1.48	1.48	1.48	1.49
	$\bar{h}$	0.72	0.38	0.37	0.38	0.38	0.38	0.38	0.39	0.52	0.52	0.52	0.52	0.52	0.52	0.52
	σ_h	0.36	0.31	0.31	0.31	0.31	0.31	0.31	0.32	0.33	0.33	0.33	0.33	0.33	0.33	0.33
m	h_{max}	1.48	1.39	1.39	1.38	1.40	1.40	1.41	1.43	1.44	1.44	1.44	1.44	1.44	1.44	1.45
	$\bar{h}$	0.53	0.41	0.41	0.41	0.41	0.41	0.42	0.43	0.32	0.32	0.32	0.32	0.32	0.32	0.32
	σ_h	0.32	0.34	0.34	0.34	0.34	0.34	0.35	0.35	0.27	0.27	0.27	0.27	0.27	0.27	0.27
d	h_{max}	1.48	1.14	1.15	1.16	1.18	1.19	1.21	1.23	1.12	1.12	1.12	1.12	1.12	1.12	1.13
	$\bar{h}$	0.42	0.21	0.22	0.22	0.23	0.23	0.24	0.25	0.20	0.20	0.20	0.20	0.20	0.20	0.21
	σ_h	0.29	0.19	0.19	0.20	0.20	0.20	0.20	0.21	0.19	0.19	0.19	0.19	0.19	0.19	0.19

Fine mesh

		field	Bezzola							Strickler						
			120mm	175mm	230mm	285mm	340mm	500mm	1000mm	120mm	175mm	230mm	285mm	340mm	500mm	1000mm
u	h_{max}	1.48	1.74	1.75	1.76	1.76	1.77	1.78	1.80	1.73	1.73	1.73	1.73	1.73	1.73	1.74
	$\bar{h}$	0.42	0.44	0.45	0.44	0.45	0.45	0.46	0.47	0.44	0.44	0.45	0.45	0.45	0.44	0.45
	σ_h	0.29	0.41	0.41	0.41	0.41	0.41	0.41	0.42	0.41	0.41	0.41	0.41	0.41	0.41	0.41
m	h_{max}	1.48	1.98	1.99	1.99	1.99	1.99	2.00	2.02	1.98	1.98	1.98	1.98	1.98	1.99	1.99
	$\bar{h}$	0.53	0.43	0.44	0.44	0.44	0.45	0.46	0.47	0.43	0.43	0.43	0.43	0.43	0.43	0.43
	σ_h	0.32	0.38	0.39	0.39	0.39	0.39	0.39	0.40	0.38	0.38	0.38	0.38	0.38	0.38	0.38
d	h_{max}	1.70	2.18	2.19	2.20	2.21	2.22	2.24	2.28	2.18	2.19	2.19	2.19	2.18	2.19	2.18
	$\bar{h}$	0.72	0.41	0.42	0.42	0.43	0.43	0.44	0.44	0.42	0.41	0.42	0.42	0.42	0.41	0.41
	σ_h	0.36	0.36	0.37	0.37	0.37	0.37	0.38	0.38	0.36	0.36	0.36	0.36	0.36	0.36	0.36

h_{max}: maximum water depth, $\bar{h}$: mean water depth, and σ_h: standard deviation.

Table 3.4: Results of the roughness calibration using measured flow velocities (field) as a reference, both on the **coarse** and **fine mesh**, using the roughness closure relations by Bezzola and Strickler; **u**, **m**, and **d** refer to 0.2, 2.75, and 5.5 km reaches in Figure 3.9, respectively. The results relative to the chosen set of parameters are highlighted in red.

			Coarse mesh													
		field	Bezzola							Strickler						
			120mm	175mm	230mm	285mm	340mm	500mm	1000mm	120mm	175mm	230mm	285mm	340mm	500mm	1000mm
u	u_{max}	1.18	0.75	0.66	0.67	0.66	0.59	0.58	0.51	1.89	1.82	2.01	2.00	1.82	2.08	2.06
	$\bar{u}$	0.26	0.15	0.14	0.13	0.12	0.12	0.11	0.11	0.14	0.13	0.14	0.14	0.13	0.17	0.16
	σ_u	0.26	0.17	0.15	0.14	0.13	0.12	0.11	0.10	0.29	0.28	0.30	0.30	0.27	0.32	0.32
m	u_{max}	1.87	2.76	2.31	2.70	2.61	2.22	2.30	2.03	2.36	2.41	2.48	2.48	2.18	2.63	2.51
	$\bar{u}$	0.46	0.21	0.19	0.19	0.18	0.17	0.16	0.15	0.21	0.21	0.22	0.22	0.21	0.21	0.21
	σ_u	0.42	0.31	0.27	0.28	0.26	0.24	0.23	0.22	0.29	0.28	0.30	0.30	0.27	0.30	0.29
d	u_{max}	1.47	2.76	1.19	1.20	1.17	1.09	0.88	0.84	1.29	1.29	1.29	1.29	1.28	1.28	1.26
	$\bar{u}$	0.49	0.21	0.15	0.15	0.15	0.14	0.14	0.13	0.20	0.20	0.19	0.19	0.19	0.19	0.18
	σ_u	0.32	0.31	0.16	0.16	0.15	0.14	0.13	0.13	0.20	0.20	0.20	0.20	0.19	0.20	0.19
			Fine mesh													
		field	Bezzola							Strickler						
			120mm	175mm	230mm	285mm	340mm	500mm	1000mm	120mm	175mm	230mm	285mm	340mm	500mm	1000mm
u	u_{max}	1.18	1.18	0.74	0.71	0.71	0.72	0.71	0.65	1.48	1.45	1.42	1.40	1.38	1.34	1.27
	$\bar{u}$	0.26	0.13	0.13	0.12	0.12	0.12	0.11	0.10	0.15	0.15	0.15	0.15	0.15	0.15	0.14
	σ_u	0.26	0.15	0.14	0.13	0.13	0.12	0.11	0.10	0.18	0.18	0.18	0.17	0.17	0.17	0.16
m	u_{max}	1.87	1.46	1.41	1.44	1.41	1.38	1.26	2.91	1.43	1.49	1.49	1.42	1.43	1.46	1.47
	$\bar{u}$	0.46	0.15	0.14	0.13	0.13	0.12	0.12	0.12	0.16	0.16	0.16	0.16	0.16	0.16	0.16
	σ_u	0.42	0.19	0.18	0.17	0.16	0.15	0.14	0.15	0.22	0.21	0.21	0.21	0.21	0.21	0.20
d	u_{max}	1.47	2.13	1.96	1.89	1.84	1.84	1.67	1.58	2.26	2.25	2.25	2.24	2.20	2.19	2.09
	$\bar{u}$	0.49	0.16	0.15	0.15	0.14	0.14	0.13	0.12	0.18	0.18	0.18	0.18	0.18	0.17	0.17
	σ_u	0.32	0.20	0.19	0.18	0.17	0.16	0.15	0.14	0.23	0.23	0.23	0.23	0.22	0.22	0.21

u_{max}: maximum flow velocity, $\bar{u}$: mean flow velocity, and σ_u: standard deviation.

Table 3.5: Results of the roughness calibration using measuredwetted areas (field) as a reference, both on the **coarse** and **fine mesh**, using the roughness closure relations by Bezzola and Strickler; **u**, **m**, and **d** refer to 0.2, 2.75, and 5.5 km reaches in Figure 3.9, respectively. The results relative to the chosen set of parameters are highlighted in red.

			Coarse mesh													
		field	Bezzola							Strickler						
			120mm	175mm	230mm	285mm	340mm	500mm	1000mm	120mm	175mm	230mm	285mm	340mm	500mm	1000mm
u	A_w	2234	2858	2884	2885	2919	2943	2920	2992	2801	2796	2796	2796	2796	2815	2811
m	A_w	5213	5071	5107	5172	5197	5182	5279	5277	4948	4932	4957	4931	4949	5001	5050
d	A_w	6232	7184	7255	7491	7644	7679	7828	7980	6941	6911	6919	6943	6928	6949	7003
			Fine mesh													
		field	Bezzola							Strickler						
			120mm	175mm	230mm	285mm	340mm	500mm	1000mm	120mm	175mm	230mm	285mm	340mm	500mm	1000mm
u	A_w	2234	2787	2812	2829	2834	2830	2880	2901	2773	2762	2766	2769	2769	2771	2777
m	A_w	5213	5052	5109	5135	5171	5182	5239	5276	4942	4943	4955	4941	4971	4950	4964
d	A_w	6232	6409	6625	6717	6866	6934	7121	7258	5978	5999	6035	6045	6057	6104	6143

A_w: wetted area

Therefore, only the points that have return numbers >1 and high intensity are assumed to belong to the riverbed surface. Differently, in the areas of deep water (the one colored in blue in Figure 3.14(a)) only points with return numbers >1 and high intensity are considered as riverbed points. The same applies to the shallow-water regions at different locations, such as the ones represented in Figures 3.15 and 3.16.

By using this new validation procedure, it is possible to (i) identify the areas of deep-water (i.e. with h larger than a certain threshold) where the LiDAR measurement is less accurate by means of a 2D hydrodynamic modeling approach; (ii) assess the quality of the points measured in those areas by analyzing the associated values of return numbers and intensity. With this approach, even the points measured in deep water under critical conditions (e.g. high water turbidity) can be evaluated and the quality of the measured dataset can be assessed.

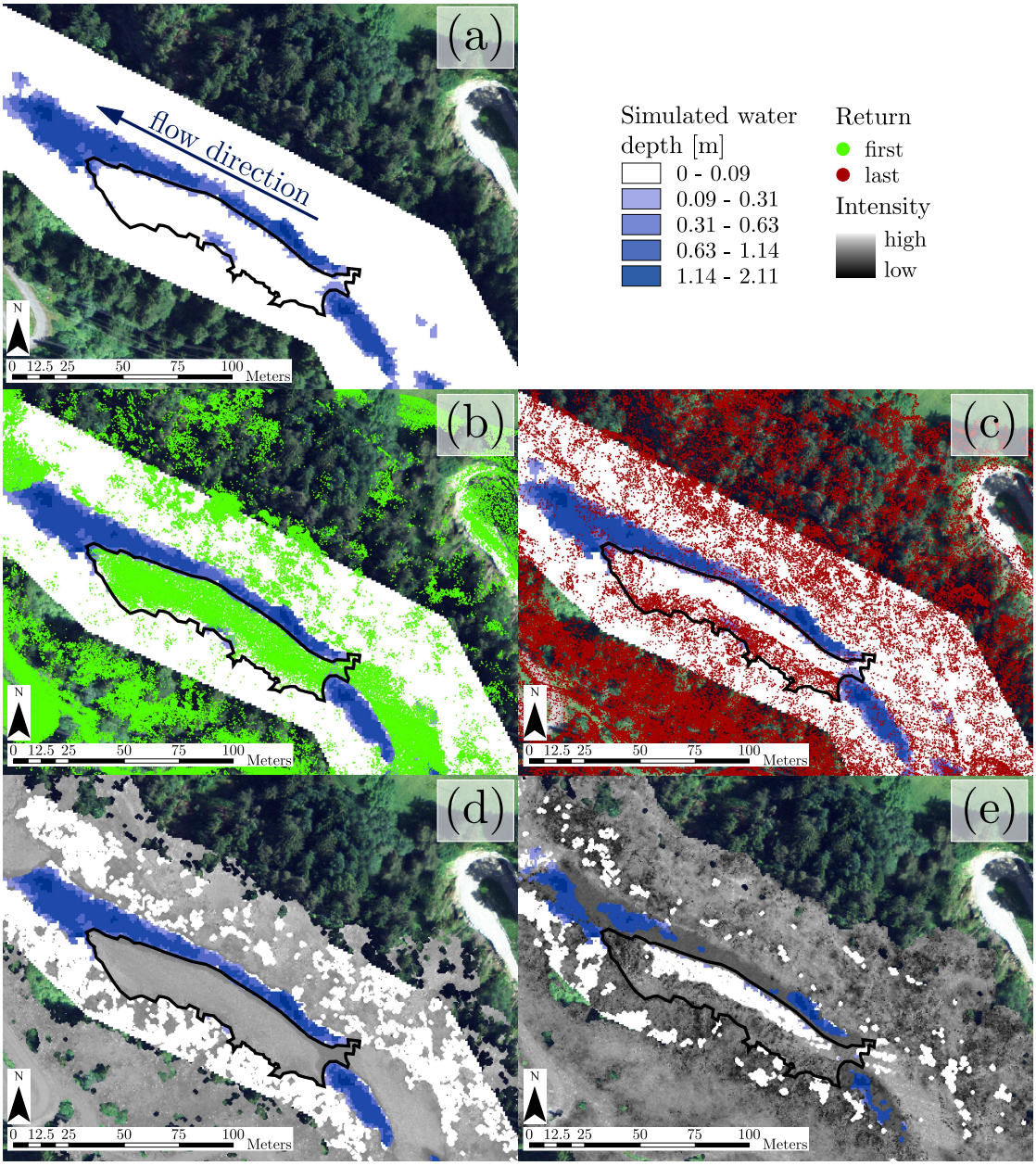

Figure 3.14: Example of LiDAR data filtering procedure at a reach 0.2 km downstream of the SBT outlet structure (see Figure 3.9). In (a), the result of the numerical run is represented in terms of water depth, where white represents the dry areas, and blue the wet areas. (b) Represents the LiDAR measured points with return numbers equal to 1, (c) the ones with return numbers larger than 1, (d) the intensity map for the first return points, and (e) the intensity map for the last return points.

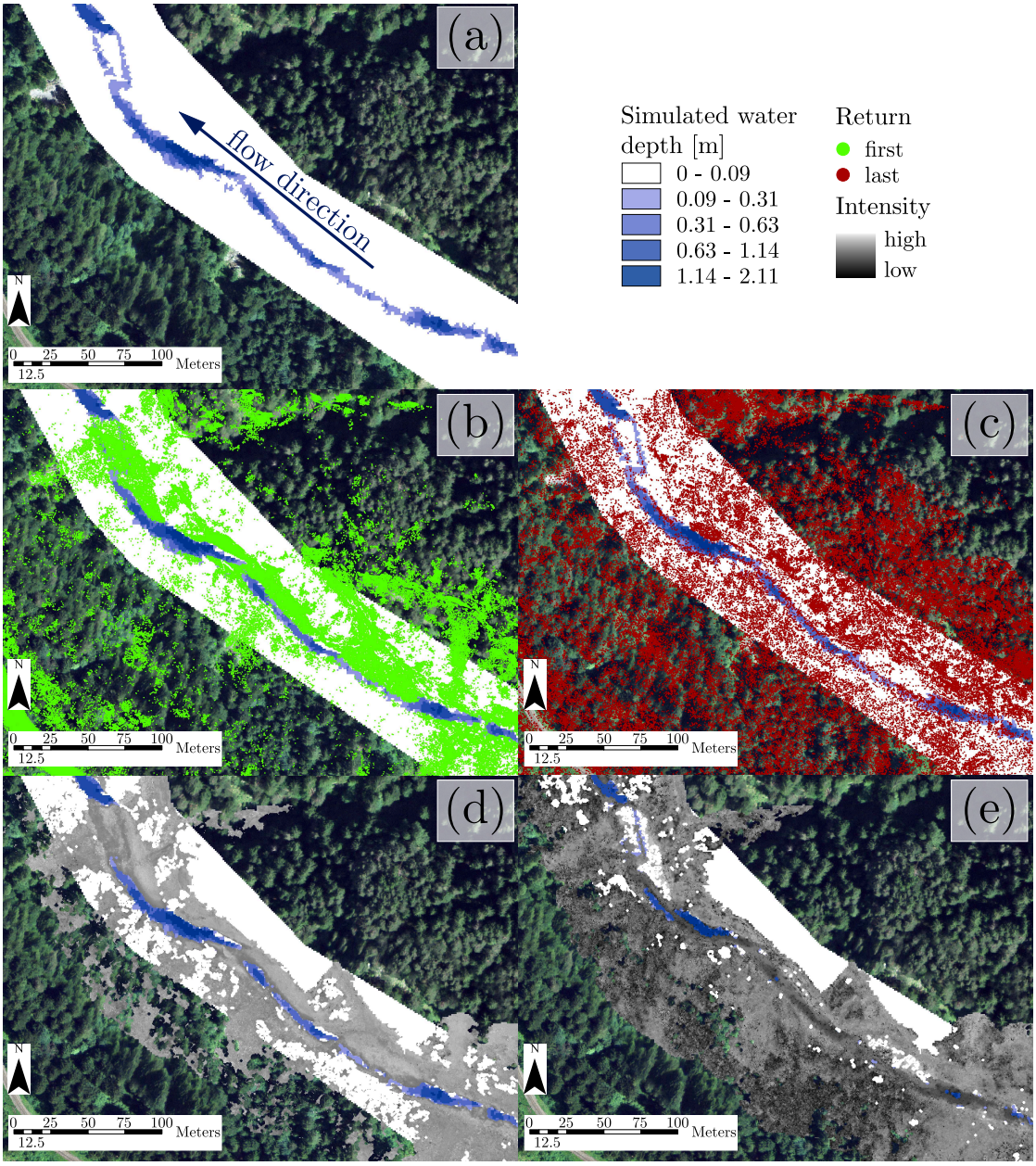

Figure 3.15: Example of LiDAR data filtering procedure at a reach 2.75 km downstream of the SBT outlet structure (see Figure 3.9). In (a), the result of the numerical run is represented in terms of water depth, where white represents the dry areas, and blue the wet areas. (b) Represents the LiDAR measured points with return numbers equal to 1, (c) the ones with return numbers larger than 1, (d) the intensity map for the first return points, and (e) the intensity map for the last return points.

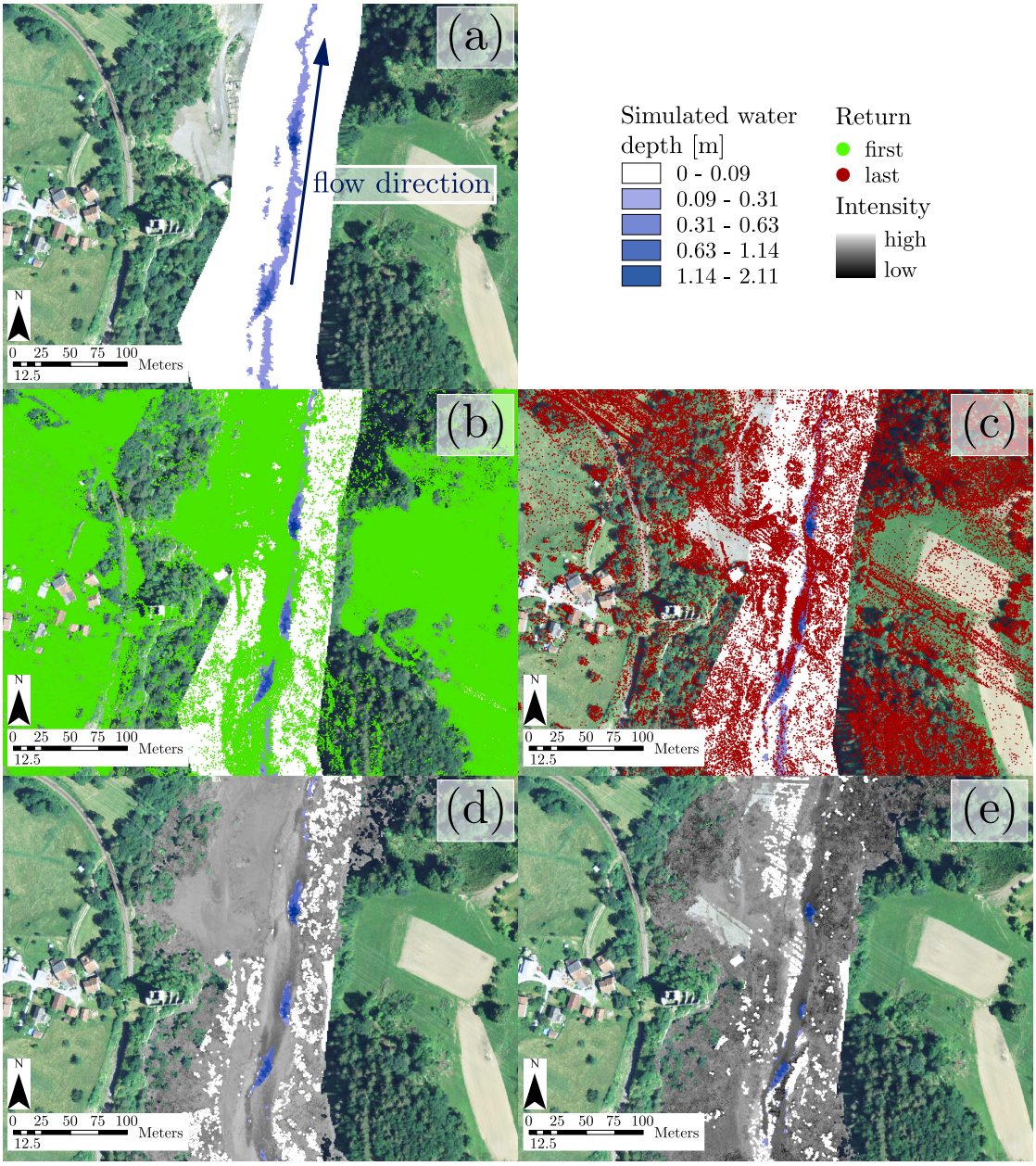

Figure 3.16: Example of LiDAR data filtering procedure at a reach 5.5 km downstream of the SBT outlet structure (see Figure 3.9). In (a), the result of the numerical run is represented in terms of water depth, where white represents the dry areas, and blue the wet areas. (b) Represents the LiDAR measured points with return numbers equal to 1, (c) the ones with return numbers larger than 1, (d) the intensity map for the first return points, and (e) the intensity map for the last return points.

3.5 Repeat LiDAR surveys and DEM of Difference (DoD)

Repeat surveys of river reaches are often conducted to establish both the spatial patterns of erosion and deposition and changes in volumes (scour and fill). When successive DEMs are subtracted from one another, a DEM of Difference (DoD) is produced, that highlights areas of scour and fill (e.g. Lane *et al.*, 1994). For more than two decades, the spatial distribution of geomorphically-based survey data has been demonstrated to be an undoubted improvement on previous cross-section interpolation techniques (Lane *et al.*, 1994; Brewer and Passmore, 2002). Parallel to this, researchers focused on the estimation of uncertainties in DoD application to distinguish real geomorphic changes from noise produced by the uncertainty inherent in individual DEMs (e.g. Brasington *et al.*, 2000; Lane *et al.*, 2003). Despite the knowledge about DEM uncertainties being a function of DEM quality (e.g. Wechsler and Kroll, 2006), most past estimates of DEM uncertainties in DoDs assume either that errors are spatially uniform (Brasington *et al.*, 2000) or that they vary spatially on the basis of wet and dry areas (Lane *et al.*, 2003). Consequently, quantified uncertainties are sometimes either overestimating the error in areas where the morphologic change can be really small (e.g. smooth flood plain surfaces) or underestimating it in areas where changes magnitude is high (e.g. eroding banks) (Wheaton *et al.*, 2010). The most commonly adopted procedure for managing spatially uniform or varying DEM uncertainties involves specifying a minimum level of detection (minLoD) to distinguish the actual surface changes from the inherent noise (Fuller *et al.*, 2003). Determination of the minLoD requires both a theory of change detection and a metric of DEM quality (Brasington *et al.*, 2000; Lane *et al.*, 2003).

More recently, the need for high reliability of scour and fill estimates derived from DoD has motivated researchers to develop accurate models accounting for spatially dependent uncertainties in DEMs from repeat topographic surveys (e.g. Wheaton *et al.*, 2010; Milan *et al.*, 2011). In this work, the Wheaton *et al.* (2010) technique is adopted to estimate DEM quality and its influence on sediment budgets, i.e. the balances between sediment added to and removed from the river system, derived from DEM differencing. This technique is divided into three steps, which are analyzed hereafter: (i) quantifying

DEM uncertainties for single surveys, (ii) propagating the identified uncertainties into the DoD, and (iii) assessing the significance of propagated uncertainties.

3.5.1 Quantifying DEM uncertainties

Approaches for approximating vertical errors related to DEM uncertainties (i.e. $\delta\eta$) range from adopting a manufacturer reported instrument precision to attempts at composing complete error budgets (Lichti *et al.*, 2005). Manufacturer reported instrument precision is only one of the components of $\delta\eta$, which include also measurement errors, sampling biases due to point density and sampling patterns, and interpolation methods. Therefore, the estimation of $\delta\eta$ requires information beyond topographic data itself (Wheaton, 2008). However, $\delta\eta$ tends to exhibit patterns in its spatial variability that are coherent and predictable, i.e. areas that are steep have low survey point density and high surface roughness (e.g. cobbles and boulders), whereas areas that are flat have high survey point density and low surface roughness (Wheaton, 2008). Thus, the first have very high elevation uncertainty while the second have low elevation uncertainty. However, the various components of elevation uncertainty are collinear variables which do not exhibit a simple monotonic relationship to elevation uncertainty and thus a deterministic model cannot be unambiguously constructed. Fore these reasons, Wheaton *et al.* (2010) attempted to build a more heuristic approach based on fuzzy models, which require very few assumptions and can be applied when relatively little is known about the uncertainty (Klir and Yuan, 1995). One of the tools of fuzzy logic, which is itself a subset of fuzzy models, are fuzzy inference systems (FIS). FIS are convenient frameworks for geomorphological surveys where the precise magnitude of elevation uncertainty in each component of the error budget might be unknown (Wheaton *et al.*, 2010). In this case, the little information that are always known about survey sampling (e.g. point density and in some cases point quality) and river morphology (e.g. slope and in some cases roughness) are sufficient to produce a reliable estimate of $\delta\eta$. The FIS developed by Wheaton *et al.* (2010) consists of four components: (i) specification of FIS type, fuzzy operation methods, rule implication method (and vs. or), aggregation method for the applied rules (min vs. max), and defuzzification method (if applicable); (ii) definition of fuzzy membership functions for the inputs; (iii) definition of rules relating inputs to

outputs; (iv) definition of fuzzy membership function for the output.

3.5.2 Propagating uncertainties into DoD

Since DoD can be considered as a cell-wise subtraction of two DEMs, propagation of errors into DoD can be treated with standard error theory, given that both inputs can be treated as independent (e.g. Kirchner, 2001). That is, for addition and subtraction errors propagate in quadrature, i.e. with the square root of the sum of the squares of each element, namely

$$\delta\eta_{DoD} = \sqrt{(\delta\eta_{new})^2 + (\delta\eta_{old})^2} \tag{3.7}$$

where $\delta\eta_{DoD}$ is the propagated error in the DoD, and $\delta\eta_{new}$ and $\delta\eta_{old}$ are the individual errors in the last DEM and in the first DEM, respectively. This method assumes that errors in each DEM cell are random and independent. If $\delta\eta_{new}$ and $\delta\eta_{old}$ are invariant in space, i.e. each cell of the DEM has the same error, $\delta\eta_{DoD}$ is uniform in space. Otherwise, $\delta\eta_{DoD}$ can be calculated on a cell-by-cell basis (Wheaton *et al.*, 2010).

3.5.3 Assessing the significance of DoD uncertainties

The significance of DoD uncertainties can be assessed mainly in two ways, both relying on thresholding the DoD and discarding or applying a lower weight to elevation changes below some detection limit. In the first simple approach, one can simply propagate the error using eq. 3.7 and e.g. for surveys having single error $\delta\eta_{new} = \delta\eta_{old}$ = 18 cm, the resulting $\delta\eta_{DoD}$ is ca. 26 cm. Therefore, the more uncertain the DEMs, the higher the threshold value and the more information is lost from the budget. The second approach relies on probabilistic thresholding carried out with a user-defined confidence interval (Brasington *et al.*, 2003; Lane *et al.*, 2003). If the estimate $\delta\eta$ is a reasonable approximation of the standard deviation of error σ_E, eq. 3.7 can be recast as

$$H_{crit} = t\left(\sqrt{(\sigma_{E,new})^2 + (\sigma_{E,old})^2}\right) \tag{3.8}$$

where H_{crit} is the critical threshold error, based on a critical student's t-value at a chosen confidence interval where

$$t = \frac{|\eta_{new} - \eta_{old}|}{\delta\eta_{DoD}} \tag{3.9}$$

where $|\eta_{new} - \eta_{old}|$ is the absolute value of the DoD. The probability of a DoD predicted elevation change occurring due to errors can be calculated by relating the t-statistics to its cumulative distribution function and choosing a confidence interval.

3.5.4 The Spatial Contiguity Index (SCI) and Bayesian Update of the uncertainties

Spatially coherent erosion and deposition units can be identified to assign to each level variation $\delta\eta$ a probability of being true. That is, elevation changes occurring within areas of contiguous and coherent changes could be assigned a higher probability of being true, whereas changes in areas without structured patterns of scour and fill could be assigned to a lower probability. To this end, Wheaton *et al.* (2010) defined (i) a technique for adjusting probability estimates accounting for spatial information concerning areas of contiguous and coherent change and (ii) a method for segmenting structured patterns of change, from those taken to be random. As for (i), a moving window (convolution filter) is run around the DoD counting the number of cells in the window that are erosional or depositional and giving as a result an index of spatial contiguity for the cell in the center of the window. For instance, a depositional (erosional) cell surrounded entirely or primarily by depositional (erosional) cells will be assigned a high spatial contiguity index for deposition (erosion) and a low contiguity index for erosion (deposition). After the contiguity indices (one for deposition and one for erosion) are calculated for each cell of the DoD, in any cell only one index is used, i.e. the one relative to the predicted elevation change. A simple linear transform function is used to relate the spatial contiguity index to the conditional probability of the jth cell of being erosional $p(A|E_j)$ or depositional $p(A|D_j)$. On a $n \times n$ cell window, the elevation change of one cell can be in agreement with maximum n^2 cells, i.e. all cells belong to the same class, while the choice of the lower threshold in Wheaton *et al.* (2010) is left to the user and therefore

the probability varies between 0 and 1 and is calculated as

$$p(A|E_j) = \frac{\left(\sum_{i=1}^{n^2} x_i\right) - x_{min}}{x_{max} - x_{min}} \qquad p(A|D_j) = \frac{\left(\sum_{i=1}^{n^2} x_i\right) - x_{min}}{x_{max} - x_{min}} \tag{3.10}$$

where x_i is a unit vector being -1 for erosional cells and +1 for depositional ones, x_{max} = n^2, and x_{min} is the lower threshold. Therefore, if a given cell is calculated to be erosional but the magnitude of the elevation change falls beneath the minLoD for that cell, it would normally be discarded. With the introduction of a spatial contiguity index, if the low-magnitude erosional cell is surrounded by all or primarily (depending on x_{min}) erosional cells, than it is likely that the previously discarded elevation change is real.

Eventually, the probability that an elevation change is true based on a spatial variable estimate of the elevation change error $\delta\eta$ and the spatial reliability measure performed on a moving window can be conjoined using Bayes Theorem. That is, the existing prior probability is updated using additional information to calculate a conditional probability incorporating both measures. Therefore, if $p(E_j)$ is defined as the a priori probability of the elevation change in the jth cell to be significant (i.e. above the threshold) and $p(A|E_j)$ as the probability revealed from its spatial index analysis, the posterior updated probability $p(E_j|A)$ that a vertical elevation difference is significant can be calculated as follows

$$p(E_j|A) = \frac{p(A|E_j)p(E_j)}{p(A)} \tag{3.11}$$

where $p(A)$ is the conditional probability that the cell is erosional, given its spatial context within an area of erosion and it is defined as

$$p(A) = p(A|E_j)p(E_j) + p(A|E_i)p(E_i) \tag{3.12}$$

where subscripts j and i refer to the probability that a change is significant or insignificant, respectively. Equations (3.11) and (3.12), presented here for the erosional case (E_j), can be used for the depositional case (D_j) just by changing the probabilities accordingly.

More details about DoD uncertainties propagation can be found in the original refer-

ence (Wheaton *et al.*, 2010) and in Wheaton's PhD thesis (Wheaton, 2008).

3.6 DoD applied to a SBT-affected gravel-bed river: the case of the Albula River

Given the heterogeneity in quality and accuracy of the two available DEMs and the morphological complexity of the study area, a robust approach for the assessment of the geomorphic change as well as the estimation of scour and fill volumes is necessary to discriminate the actual changes from noise. To generate the DoD subtracting the 2014 DEM from the 2016 DEM, the Geomorphic Change Detection (GCD) Software developed by Joe Wheaton (Utah State University, Department of Watershed Sciences) and James Brasington (Queen Mary University) was used. The software is provided at `gcd.joewheaton.org` and it is licensed under a Creative Commons Attribution-NonCommercial-ShareAlike 4.0 International License. It implements the methods described in Section 3.5 and is available as an ArcGIS Add-In.

The GCD software allows for morphological sediment budgeting in rivers following three fundamental steps (described in Section 3.5): (i) estimation of single DEM uncertainties, (ii) propagating them into the DoD, and (iii) assessing the significance of propagated uncertainties. Furthermore, the GCD software also provides ways for segregating the best estimates of change spatially using different types of masks.

The DoD technique developed by Wheaton *et al.* (2010) have already been successfully applied to case studies similar to the one of this work (Heckmann *et al.*, 2017; Pace *et al.*, 2017; Cavalli *et al.*, 2017; Bezak *et al.*, 2017). In the following, its application to a SBT-affected gravel-bed river is described.

Estimation of single DEM uncertainties

To avoid additional noise, since this study is mainly concerned with topographic changes associated with channelized processes (sediment and water released from a SBT), the DoD analysis is restricted to an automatically delineated terrain perimeter. The latter was drawn by means of a filter that calculates for each input cell the mini-

mum elevation within a specified neighborhood around it, i.e. on 250 m^2 areas. The surface of the movable used window was estimated as to always include the whole river width. Then, such surface is subtracted from the original DEM to have a detrended map of elevations, which contains elevation values relative to the lowest point of each 250 m^2 window. Eventually, all the points that are more than 4 m above the reference point belonging to each window are identified and eliminated from the DEM. As a final result, two DEMs are obtained (i.e. for the 2014 and 2016 LiDAR survey, respectively) composed by all the measured points that are less than 4 m above the lowest point on 250 m^2 windows, i.e. the lowest point of the thalweg. The resulting DEMs are verified against orthophotos and slope maps to verify that the perimeter of each DEM corresponds with the perimeter of the river.

To estimate the error surfaces proper of each single DEM, two approaches are used. First, a uniform threshold for the DEM uncertainty is assumed, i.e. the conservative value proposed by Wheaton *et al.* (2010) for bathymetric LiDAR (18 cm) is used, which overestimates the actual error occurring during the 2014 and 2016 surveys. Second, one of the Fuzzy Inference Systems (FIS) proposed by Wheaton *et al.* (2010) is used, which is based on two main parameters: one related to the topography (i.e. the local slope) and one related to the survey properties (i.e. point density). The rules used by the applied FIS are described in Figure 3.17 and Table 3.6. A FIS is created by first defining membership functions (MFs) μ for the input variables and identify some classes to evaluate them (i.e. Low, Medium, High) and setting a range of values for each class (Figure 3.17). Second, rules must be defined to relate the inputs to the output (Table 3.6). Eventually, a MF for the output (i.e. elevation uncertainty $\delta\eta$) must be defined. This is obtained in this case by defining four classes (Low, Average, High, Extreme) with the relative ranges of values (Figure 3.17). The FIS applied here is available in the FIS DEM Error Repository by Philip Bailey (North Arrow Research) at `bitbucket.org/pipbailey/fis-dem-error-repository`.

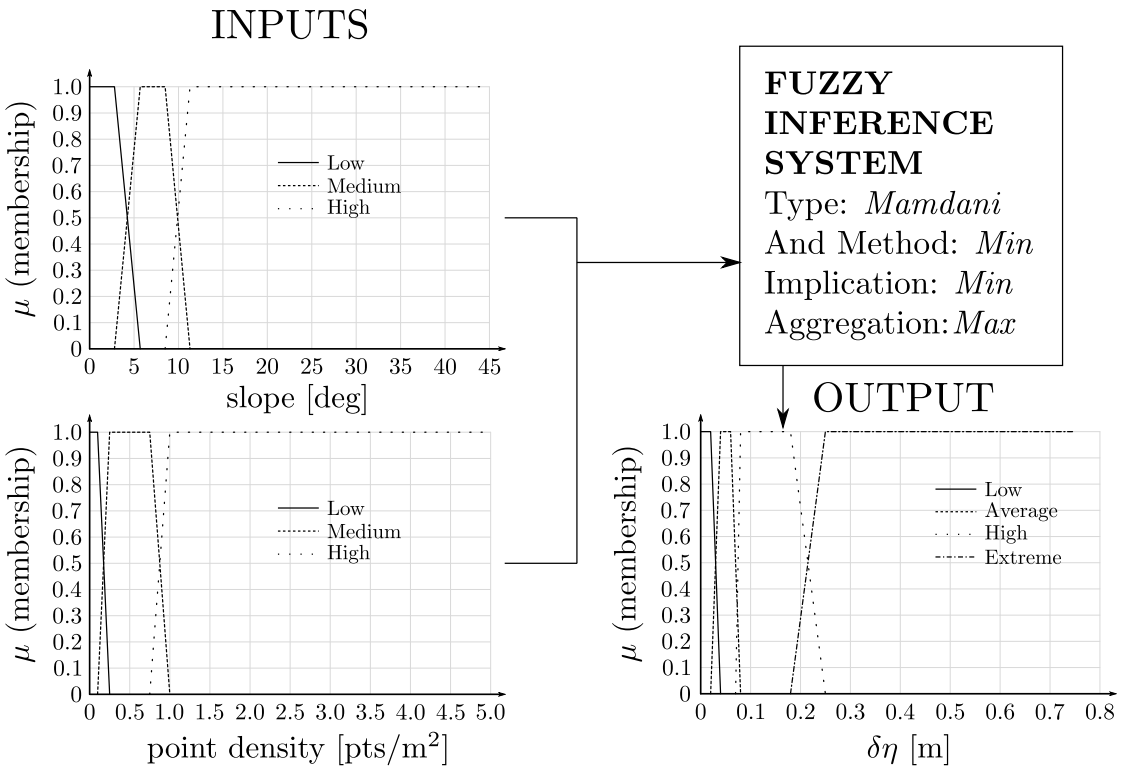

Figure 3.17: Inputs (slope [deg] and point density [pts/m^2]) and output (elevation uncertainty $\delta\eta$ [m]) fuzzy membership functions used in the present study.

Table 3.6: Rules definition scheme for the two-input FIS used to evaluate geomorphic changes in this study.

Rule	Input		Output
	Slope [deg]	Points density [pts/m^2]	$\delta\eta$ [m]
1	Low	Low	Average
2	Low	Medium	Low
3	Low	High	Low
4	Medium	Low	High
5	Medium	Medium	High
6	Medium	High	Average
7	High	Low	Extreme
8	High	Medium	High
9	High	High	High

An example of inputs and output rasters for the 2014 and 2016 surveys is given in Figures 3.18. Note that the 2016 DEM has few points since in the wetted areas almost no points were measured. Moreover, the uncertainty for the 2016 survey is high (i.e. >1 m) in areas close to the water (e.g. bar edges).

Propagation of DEM uncertainties into the DoD and significance assessment

Given the complexity of this study, several different approaches are used to propagate the single DEM uncertainties into the DoD and assess the significance of the resulting uncertainties. First, both the uniform and the FIS estimated uncertainties of each DEM are propagated into the DoD with a simple approach for error propagation following equation (3.7)) and each elevation change falling inside the threshold interval, i.e. falling beneath the minimum level of detection (minLoD) $\delta\eta_{DoD}$, is not considered. Second, a probabilistic representation of uncertainty is applied, which is thresholded at

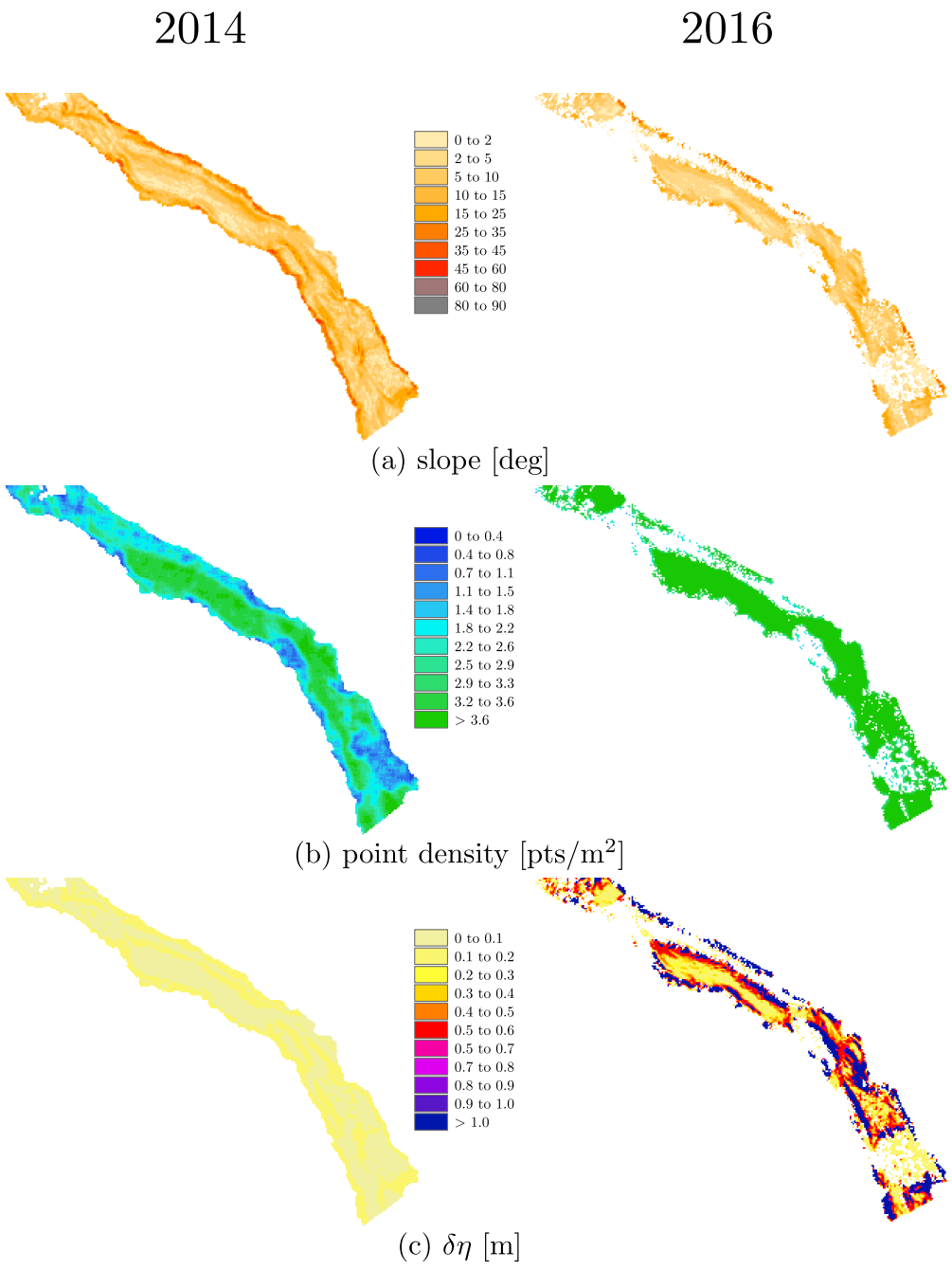

(a) slope [deg]

(b) point density [pts/m^2]

(c) $\delta\eta$ [m]

Figure 3.18: Example (reach 0.2 km downstream of the SBT, see Figure 3.9) of input surfaces and output of the FIS.

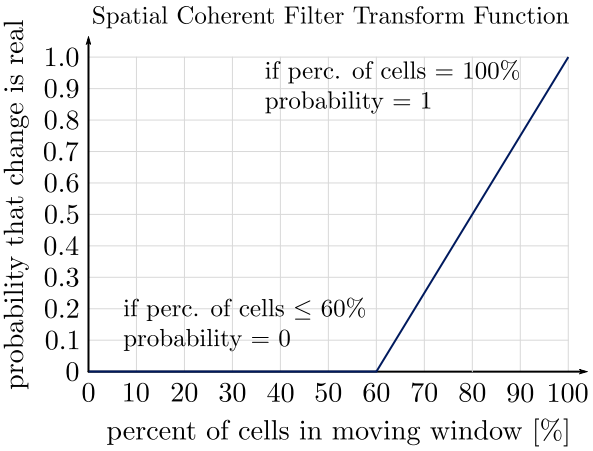

Figure 3.19: Transformation function to calculate contiguity indices for each cell, e.g. if more than 60% of the surrounding cells are showing the same trend (either depositional or erosional) as the interested cell the index will be between 0 and 1.

a conservative 95% confidence interval following equation (3.8)). Finally, the Spatial Contiguity Index (SCI) approach is used for the case where DEM uncertainties have been estimated with the FIS and have been propagated into the DoD applying the probabilistic thresholding. To do this, a 5x5 cells window and a probability function as described in Figure 3.19 are used. In the following, the results relative to these different approaches are compared.

3.6.1 Estimation of geomorphic changes and scour and fill volumes

The different approaches used to estimate the uncertainties of single DEMs and propagate them into the DoD are summarized in Table 3.7.

Results presented in Table 3.8 show that both the DEM uncertainty estimation, and the approach for uncertainty propagation into the DoD play a role in the quantification of scour and fill volumes and related erosion and deposition heights. In particular, using a spatial heterogeneous uncertainty estimation for the single DEMs (i.e. a FIS) has the advantage of recovering data that would have been lost when using a more conservative approach. In fact, the eroded, deposited and net volumes estimated with the FIS and the probabilistic propagation of DEM uncertainties into the DoD (U2P2) are very close to the raw data. When using a spatial heterogeneous uncertainty estimation for the single

Table 3.7: Summary of different DoD analysis performed with the GCD tool by Wheaton *et al.* (2010); U stands for DEM uncertainties and 1 indicates uniform error while 2 the use of a Fuzzy Inference System (FIS). P stands for DoD propagation of DEM uncertainties and 1 indicates a simple error propagation, while 2 the use of a probabilistic thresholding with a 95% confidence interval (CI). SCI stands for Spatial Contiguity Index.

Name	DEM uncertainties	DoD propagation	SCI
raw	none	none	No
U1P1	uniform error	simple minLoD	No
U2P1	FIS	simple minLoD	No
U1P2	uniform error	CI 95%	No
U2P2	FIS	CI 95%	No
U2P2SCI	FIS	CI 95%	Yes

DEMs, the uncertainty in a single cell is estimated considering e.g. topographic and and survey-related features. For example, cells belonging to areas where the points density is high and the slope is not might be characterized by lower uncertainty values than the ones estimated using a uniform error. Moreover, using a statistic approach to propagate the error into the DoD produces a DoD that does not discard changes below a minimum level of detection, but rather views them as statistically improbable. On the contrary, neglecting small elevation changes, i.e. using a uniform error estimation for the DEMs and propagating it following equation (3.7)), has the effect of removing a large part of the eroded and deposited volumes. This means that most of the volumetric changes are relative to small elevation changes. From the most (U2P1) to the least conservative method (U2P2SCI) the net volume estimation goes from 2355 m^3 to 5804 m^3, which is very similar to the raw estimate (5823 m^3). In the case of U2P2SCI, the use of the SCI allows for the recovery of data belonging to erosional (depositional) cells that would be discarded due to the applied FIS rules, but are surrounded by at least 60% of erosional (depositional) cells over a 5x5 cells window and are therefore taken into account. This result, together with the estimate of the sediment volume released during the 2016 SBT operations (June 11 and 16), measured with the Swiss Impact

Table 3.8: Volumes and elevation changes estimated with different DoD analysis.

	raw	U1P1	U2P1	U1P2	U2P2	U2P2SCI
Eroded V [m^3]	6593	3085	5171	1103	3373	6182
Deposited V [m^3]	12416	5959	10552	3458	8138	11985
Net V [m^3]	**5823**	**2874**	**5381**	**2355**	**4765**	**5804**
Average erosion depth [m]	0.15	0.42	0.23	0.70	0.28	0.15
Average deposition depth [m]	0.17	0.53	0.24	0.90	0.28	0.17

Plates (SIPs) at the downstream end of the SBT (Mueller-Hagmann, 2018), will concur to reliably quantify the volume of sediment that can be released during SBT operations. The estimate of the bedload volume carried during the two SBT operations of June 2016 measured with the SIPs is 1100 m^3 (Mueller-Hagmann, 2018). DoD volumes resulting from the different approaches presented here are generally larger than the SIPs estimate, but both are of the same order of magnitude. Moreover, DoD analysis takes into account morphological variations caused by a wide range of processes including e.g. sediment being delivered by the tributaries and bank collapses. Furthermore, given the long time-span between the two LiDAR surveys (2 years), the DoD is also able to account for sediment being carried outside of the domain (i.e. sediment output) due to intra-event sediment transport, caused e.g. by water releases from the dam outlets and the SBT.

The distribution of elevation differences is also affected by the choice of different approaches as shown in Figure 3.20 and by the values of average erosion and deposition depths in Table 3.8. That is, using a FIS and a confidence interval on propagated uncertainties updated with a SCI (U2P2SCI analysis, Figure 3.20(e)) helps in recovering information that would have been neglected e.g. in the case of the U1P1 analysis (Figure 3.20(a)). That is, areas of small elevation changes can be taken into account in the estimation of scoured and filled volumes only if the DEM uncertainties are not spatially uniform and possibly if a SCI is used. In fact, for the most (least) conservative approach, i.e. U1P2 (U2P2SCI), the average erosion and deposition depths are the largest (smallest), since all the small elevation changes are neglected (taken into

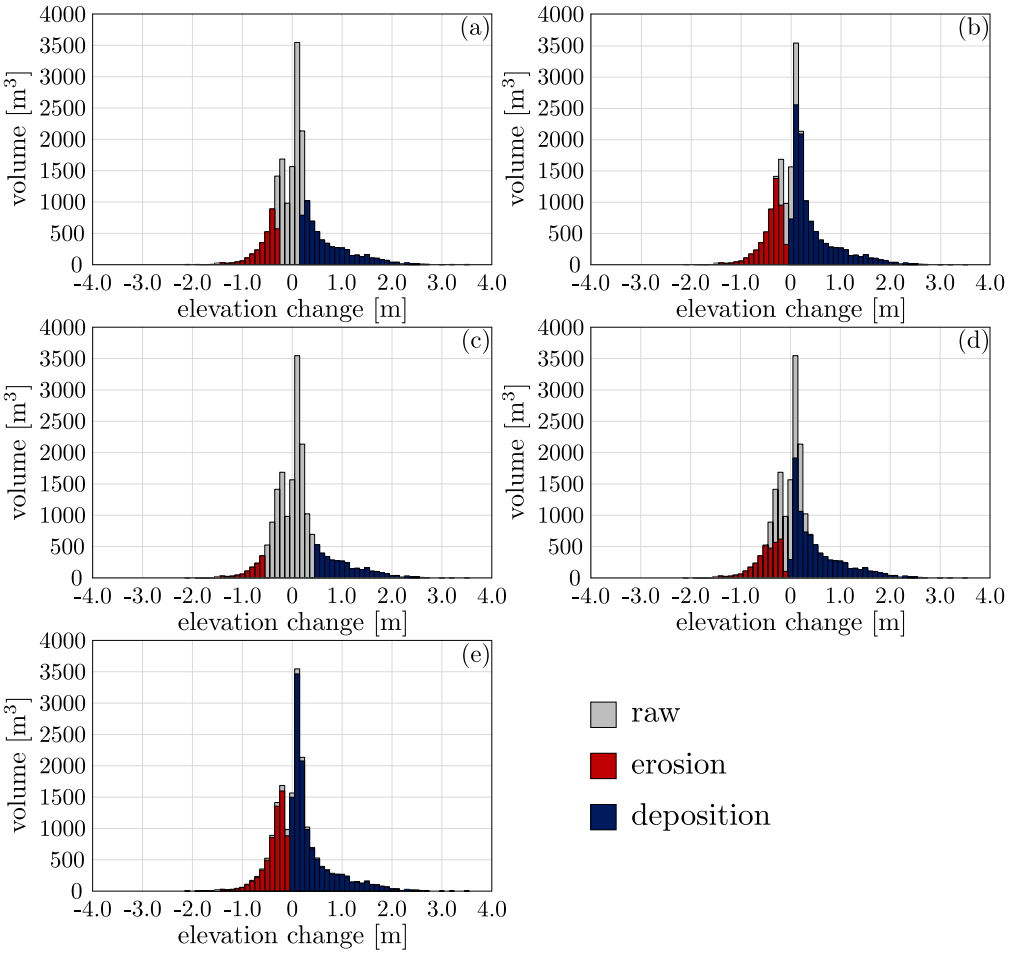

Figure 3.20: Volumetric distribution over elevation changes estimated with: (a) U1P1, (b) U2P1, (c) U1P2, (d) U2P2, and (e) U2P2SCI. Grey bars refer to the gross unthresholded DoD (raw).

account). Moreover, while being more conservative, using a uniform error estimate for a DEM has been proven to provide less realistic error estimates e.g. along bank edges (Bangen *et al.*, 2016). Therefore, given the diversity of the two LiDAR surveys and the complexity of the topography of the reach under investigation, to calculate scour and fill volumes with the U2P2SCI analysis and recover as much data as possible seems to be the wisest choice.

To understand the spatial trends of volume variation, the chosen sediment budgeting analysis have been segregated spatially using different masks, which subdivide the domain into 200 m long river reaches and eliminate from them the areas where the sim-

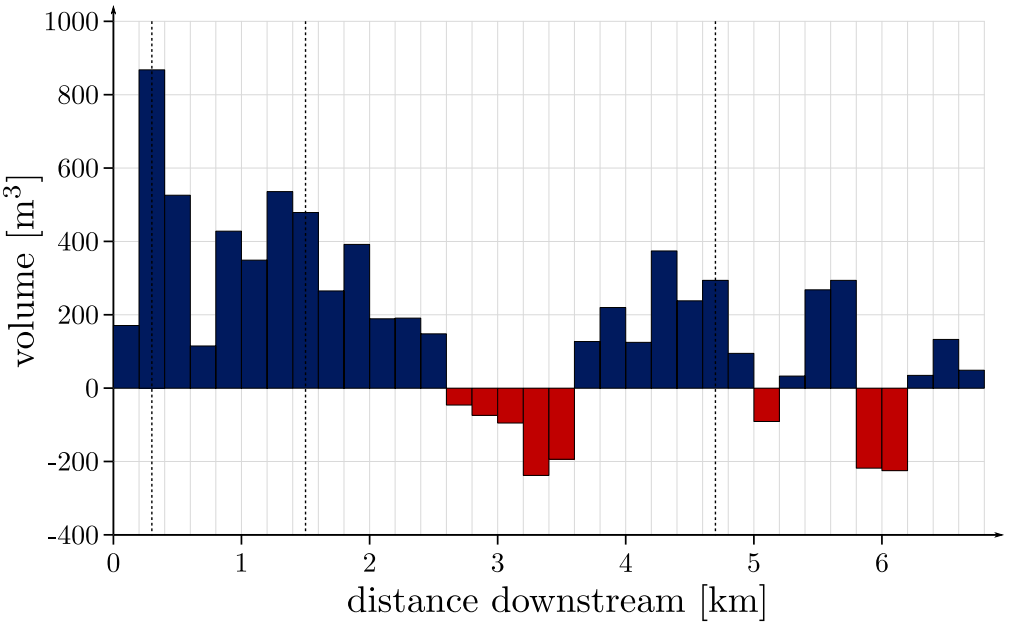

Figure 3.21: Budget segregation over 200 m reaches for the U2P2SCI DoD analysis. Positive values (blue bars) refer to deposition, negative values (red bars) to erosion, and the dashed lines indicate the tributaries confluences.

ulated water depth is higher than 60 cm, 80 cm and 100 cm. Results are identical to the ones presented in Figure 3.20, showing that the few under-water points available in the 2016 DEM do not play any role in the volume change estimation. Results of the budget segregation analysis performed using the mask including also deep-water areas are given in Figure 3.21 where the downstream distance to the SBT outlet structure is shown on the x-axis. The results on the y-axis are presented in terms of scour (negative) and fill (positive) volume.

Based on the results shown in Figure 3.21, four main reaches can be defined: (i) a depositional reach from 0 km to 2.6 km, (ii) an erosional reach from 2.6 km to 3.6 km followed by (iii) another reach where deposition is favored, i.e. from 3.6 km to 5 km. (iv) From 5 km to 6.8 km, a reach where the behavior is mixed can be identified. If only the effect of SBT operations is considered, a possible explanation for the formation of the alternate trend in the first three reaches is that sediments being released during the two SBT operations evolved like two sediment pulses not interacting with one another. Note that the 2014 LiDAR survey was carried out after the large SBT operation of

August 13, 2014, where the SBT was operational for 14 hours during which it conveyed bedload-laden water to the downstream reach. Moreover, in 2015 bedload-free water was released from the SBT during two operations (see Figure 3.7). Therefore, sediment being released during the 2014 SBT operation might have behaved as a sediment pulse, therefore dispersing close to the SBT during the 2014 operation due to coarse pulse grain size and large pulse size (e.g. Pace *et al.*, 2017). Afterwards, during the bedload-free water releases of 2015, sediment deposited close to the SBT in 2014 could have been transported downstream due to the absence of additional sediment inputs from the SBT and relative high water discharges (e.g. Pace *et al.*, 2017). Eventually, during the 2016 SBT operation, sediment released might have as well dispersed close to the SBT, while the one being released in 2014 could have been transported further downstream.

The effect of the main tributaries has been neglected here, since the LiDAR surveys have been performed at the reach scale and not at the basin scale. Therefore, it is difficult to assess the sediment volume mobilized by the tributaries. On the one hand, however, the pre-SBT state of the river reach was most likely close to a post dam-closure sediment-starvation equilibrium. In fact, as reported in other studies, 30 years of disruption of sediment continuum (the Solis dam was built in 1986) might be enough to greatly modify the river morphology (e.g. Surian and Rinaldi, 2003). In the light of this, disturbances coming from the tributaries should not affect greatly the channel morphology, while the newly introduced water and sediment released from the SBT might act as major disturbance. On the other hand, totally neglecting possible sudden sediment inputs to the reach under investigation coming from the tributaries might be an oversimplification, since during high-magnitude hydrological events streams might react with sudden and extreme morphological changes causing unusual peaks in sediment transport (e.g. Croke *et al.*, 2013; Rinaldi *et al.*, 2016; Bezak *et al.*, 2017). However, the tributaries might be considerd as either acting sympathetically with the SBT in case of sudden response to extreme event or not contrasting with the disturbance caused by SBT operations. Either way, the SBT exerts undoubtedly a strong control on water and sediment being release to the downstream reach, the morphological effects of which should be magnified by the tributaries. Moreover, the conservative estimate of bedload volume released with the two SBT operations of June 2016, i.e. 1100 m^3 (Mueller-Hagmann,

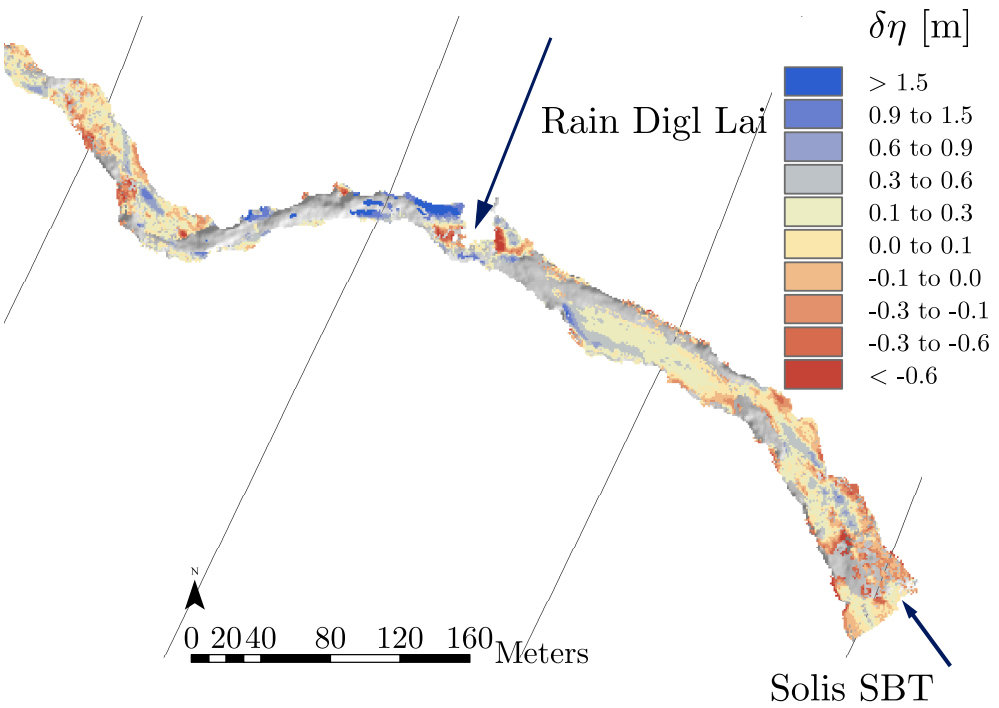

Figure 3.22: Erosion and deposition trends in the first 600 m downstream of the SBT outlet structure. SBT outlet structure and the first tributary are indicated by the two arrows, black thin lines indicate the subdivision into 200 m long reaches. The DEM relative to the 2014 LiDAR survey is used as a background (green-brown areas).

2018), seems to confirm that a large part of the mobilized volume of sediment estimated with the DoD analysis stems from the SBT.

On a smaller spatial-scale, the first 300 m downstream of the SBT outlet down to the Rain Digl Lai tributary (Figure 3.9) are most likely prone to sediment pulse advection, due to the mild slope favoring low Froude numbers. The Froude numbers in the first 300 m downstream of the Solis SBT have been proven to be subcritical over a wide range of water discharges. Pace *et al.* (2017) have identified the Froude number as the main indicator of pulse behavior for field studies. In the case of the Albula river downstream of the Solis SBT, a significant change of the slope occurs downstream of the first tributary (see Figure 3.23). This might be due to topographic reasons, or to the impact of the Rain Digl Lai Stream which could transport large amounts of sediment material. Either way, the large deposition occurring right downstream of the confluence of the Rain Digl Lai (see Figure 3.21) might be a combined effect of the gentle slope

Table 3.9: Scour and fill volumes estimated with different DoD analysis without the effect of the first tributary.

	raw	U1P1	U2P1	U1P2	U2P2	U2P2SCI
Eroded V [m^3]	6593	3085	5171	1103	3373	6182
Deposited V [m^3]	11816	5359	9952	2858	7538	11385
Net V [m^3]	**5223**	**2274**	**4781**	**1755**	**4165**	**5204**

of the first 300 m downstream of the SBT outlet structure and of large sediment inputs from the tributary. The erosion and deposition patterns in the first 600 m downstream of the outlet structure of the Solis SBT are shown in Figure 3.22, where the SBT and the confluence of the Rain Digl Lai are represented with two arrows, and the 200 m reaches division is indicated with diagonal black thin lines. A diffused deposition trend can be located in the first 300 m, i.e upstream of the confluence of the Rain Digl Lai, while immediately downstream of it the elevation variations between 2014 and 2016 are larger than 2.5 m. The volume deposited immediately downstream of the Rain Digl Lai in the dark blue area right downstream of the arrow in Figure 3.22 amounts to roughly 600 m^3. This influences the total estimation of the net volumes presented in Table 3.8 since it is ca. 10% and 40% of the least conservative and of the most conservative bedload volume estimates (U2P2SCI), respectively.

In Table 3.9, the volume estimations relative to different DoD analysis are presented, without taking into account the deposition immediately downstream of the first tributary. Results show that even though the effect of the first tributary is remarkable, the range between the minimum (1755 m^3) and maximum (5204 m^3) estimated volumes remains similar to the previous one.

The scoured volume in the erosional reach between 2.6 and 3.6 km is mostly due to a diffuse in-channel erosion, as indicated by the scour and fill trends represented on the DoD map in Figure 3.24. This trend might be a possible explanation for the 2014 sediment pulse advection. In fact, if it is assumed that sediments released during the 2014 SBT operation were transported downstream during the 2015 SBT operations and

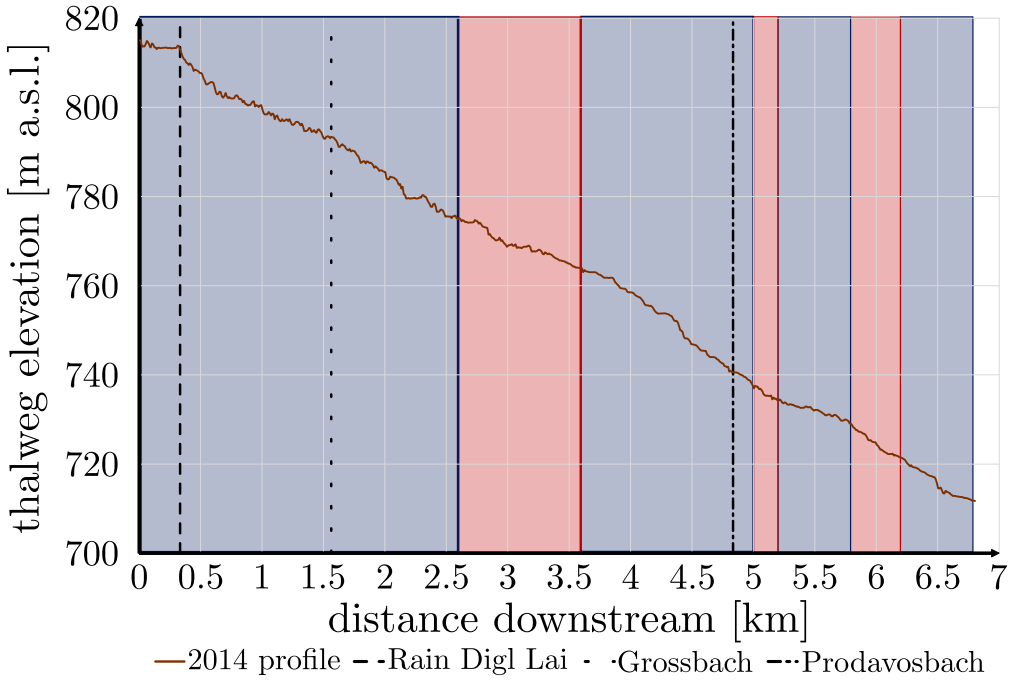

Figure 3.23: Thalweg profile of the Albula River downstream of the Solis SBT extrapolated from the 2014 DEM. The tributaries are indicated with vertical lines, and colored background areas indicate the erosion and deposition trends as indicated in Figure 3.21.

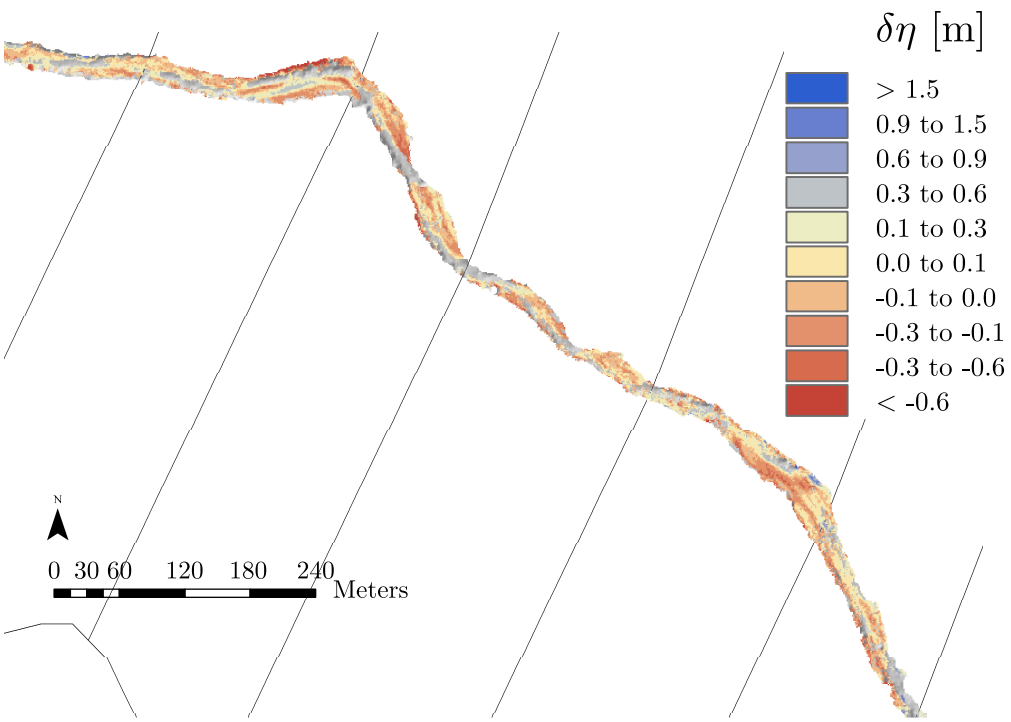

Figure 3.24: Erosion and deposition trends between 2.6 km and 3.6 km downstream of the SBT outlet structure. Black thin lines indicate the subdivision into 200 m long reaches. The DEM relative to the 2014 LiDAR survey is used as a background (green-brown areas).

further downstream in 2016, the reach represented in Figure 3.24 would represent the gap between the 2014 and 2016 sediment pulses.

The erosion and deposition trends in the reach going from 3.6 to 5 km downstream of the SBT outlet structure are given in Figure 3.25, where diffused erosion and deposition areas and some spots of large elevation changes are represented. These are most likely due to local topographic features such as channel width variations.

Eventually, the alternate erosion and deposition trend occurring between 5.4 km and 6.2 km is represented in Figure 3.26, where both fill (reach from 5.4 km to 5.8 km circled with a blue line) and scour (reach from 5.8 km to 6.2 km circled with a red line) are results of diffuse in-channel processes.

To summarize, the Solis SBT was operated seven times between January 2014 and January 2017. Among these, the SBT released bedload-laden water to the downstream river reach only in August 2014 and June 2016 (see Figure 3.7). Sediments released

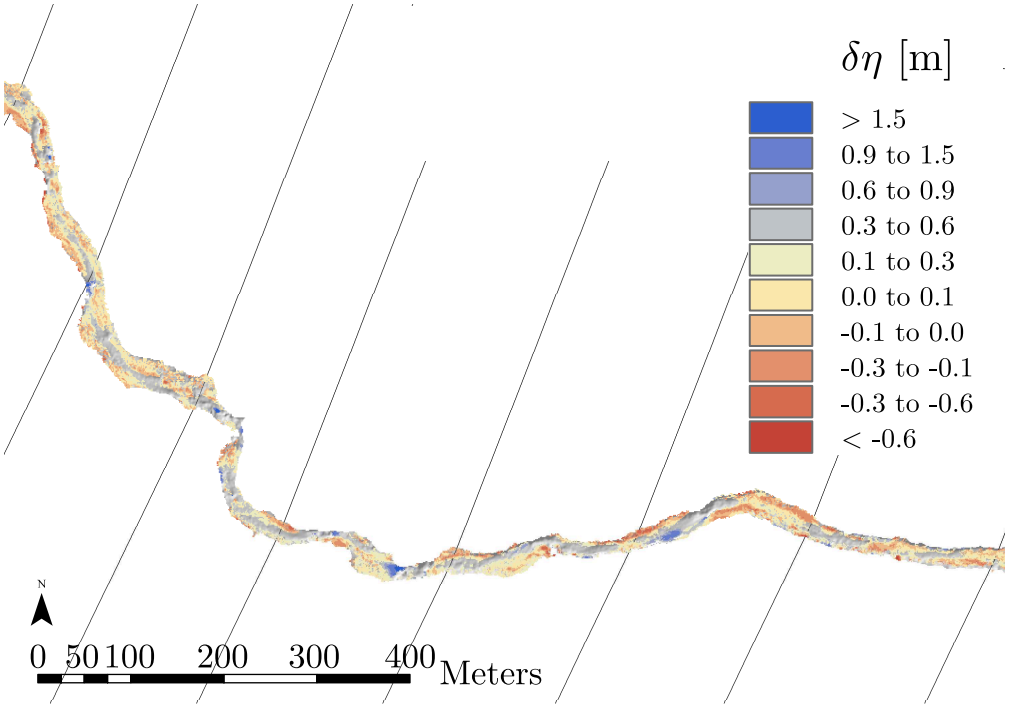

Figure 3.25: Erosion and deposition trends between 3.6 km and 5 km downstream of the SBT outlet structure. Black thin lines indicate the subdivision into 200 m long reaches. The DEM relative to the 2014 LiDAR survey is used as a background (hillshade).

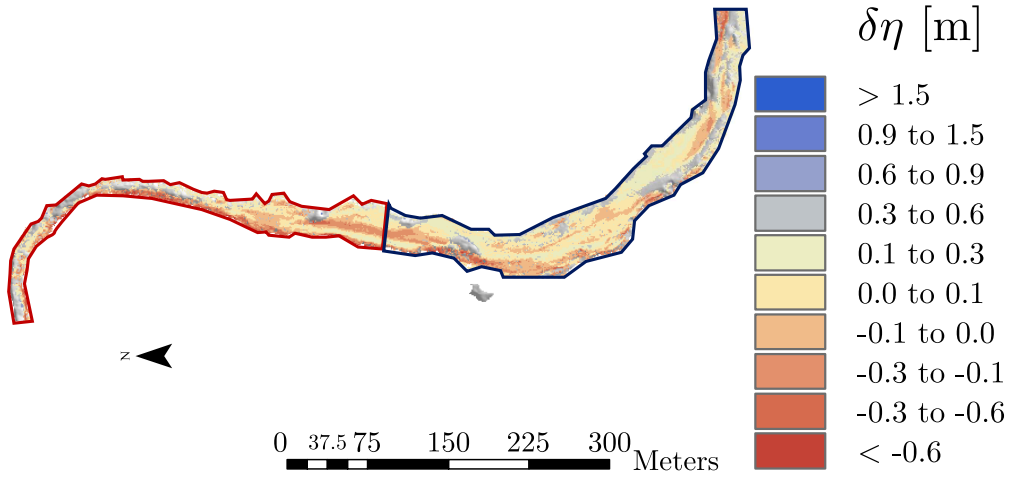

Figure 3.26: Erosion and deposition trends between 5.4 km and 6.2 km downstream of the SBT outlet structure. The reaches where deposition or erosion are prevailing are circled in blue and red, respectively. The DEM relative to the 2014 LiDAR survey is used as a background (green areas).

during these SBT operations seem to behave like two distinct sediment pulses not interacting with one another. DEMs of the reach of the Albula River downstream of the Solis SBT have been built following two bathymetric LiDAR surveys in October 2014 and 2016, respectively. While the 2014 survey was fully successful, during the 2016 one the water turbidity was high and many points under the water surface have not been detected. Therefore, a new technique to filter and assess the quality of points measured with bathymetric LiDAR was developed, involving the use of two-dimensional hydrodynamic modeling to detect the areas of deep water. Afterwards, points belonging to deep-water areas have been considered as belonging to the riverbed only if their return numbers was larger than 1 and if their intensity was lower than the one of points with return numbers equal to 1, i.e. belonging to the water surface. Given the complexity of the topography of the river reach under investigation, and the problem that occurred during the 2016 LiDAR survey, DEM uncertainties have been estimated using a Fuzzy Inference System (FIS) to take into account that errors in DEMs might not be uniformly distributed, but are usually a function of topographic features (such as the local slope) and of survey properties (such as point density). From the two DEMs, a DEM of Difference (DoD) has been calculated. DEM uncertainties have been propagated into the DoD using a probabilistic representation of uncertainty thresholded at a conservative 95% confidence interval and probabilities of elevation changes to be real have been then updated by means of a Spatial Index of Contiguity (SCI). From the results, three subreaches have been defined in the river reach under investigation: (i) a depositional one in the first 2.6 km downstream of the SBT, followed by (ii) a 1 km long erosional reach, (iii) a 1.4 km long depositional reach, and (iv) a 1.8 km long mixed behavior reach. The trend in the first three reaches might be influenced mainly by the SBT, from which two distinct sediment pulses have been released, in 2014 and 2016, respectively. In 2014, the first pulse might have evolved mainly due to dispersion caused by the high volume of coarse sediment (bedload) released. In 2015, two bedload-free water SBT operations have been carried out at the Solis SBT, probably causing the 2014 pulse to move downstream due to advection caused by high water discharges and no further sediment input. Finally, the 2016 SBT operation carrying out bedload-laden water might have caused further advection of the 2014 SBT pulse and dispersion close to the SBT of the 2016

pulse. In this analysis, the effect of the tributaries, which might introduce large volumes of sediment into the system, is neglected. In fact, the thalweg profile of the river reach under investigation shows a significant change of slope and the analysis of the DoD reveals a very high deposited volume right downstream of the first tributary (Rain Digl Lai, see Figure 3.23), both of which might be effects of the tributary itself. Without a basin-scale LiDAR survey, it is difficult to say whether the main source of sediments in the river reach under investigation is the SBT or the tributaries. However, given the size of the basin, the tributary should transport large volumes of water and sediments during flood period, i.e. when the SBT is usually operated, acting as magnifiers of the effects of SBT operations.

4 General framework for SBT release scenarios

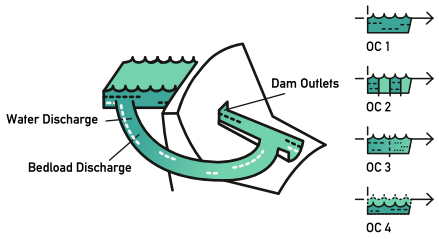

SBTs exert a strong control on water and sediment supply rates being released to the downstream reach. To properly model the morphological changes occurring in a river reach subject to SBT operations in terms of riverbed slope and composition (see Figure 4.1(b)), the operational conditions, i.e. the release patterns concerning water and sediment, need to be properly understood. Possible SBT-release scenarios (or SBT operations) shall be defined in terms of water and sediment discharge being conveyed through the SBT and the dam to the downstream reach (see Figure 4.1(a)) identifying as main variables water supply rate and sediment supply rate and composition. The analysis reported in this chapter allows for the quantification of reliable upstream boundary conditions to be used for numerical simulations and as a reference for real case studies.

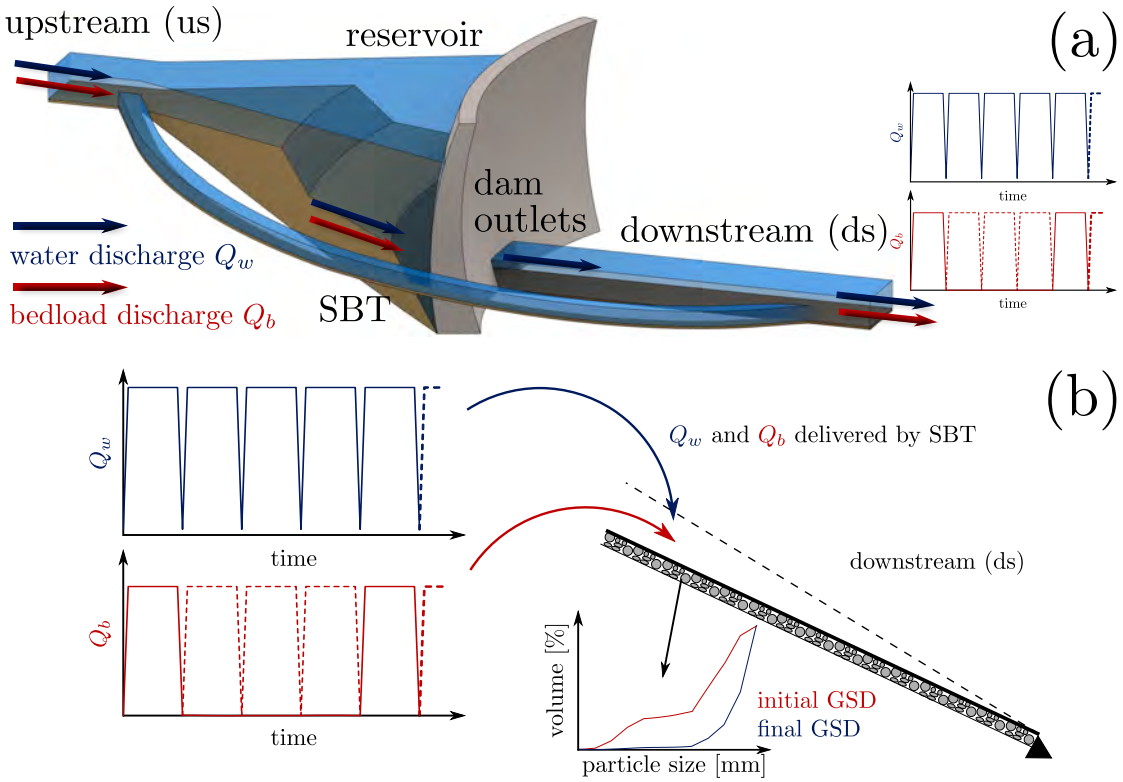

Figure 4.1: Functioning scheme of a SBT-dam system (a) for the quantification of boundary conditions used for numerical modeling (b).

4.1 SBT release scenarios

Possible SBT-release scenarios are obtained starting from the observation that, to properly fulfill its task, a SBT must have a higher sediment transport capacity than the upstream river reach. In fact, SBTs are designed to have high slopes and low friction values at the bottom (e.g. Auel and Boes, 2011b). In the following, the functioning scheme represented in Figure 4.1(a) is adopted, i.e. water and sediment transported in the upstream reach (us) are conveyed through the SBT to the downstream reach (ds) and water might as well be conveyed through the dam outlets. The combination of water and bedload discharges being transported through the dam and the SBT results in the water and bedload supply rates released to the downstream reach.

4.1.1 Bedload Rating Curves

Given the slope and the GSD of the upstream river reach, the relationship between the water discharge Q_w and the bedload transport rate Q_b (i.e. the bedload rating curve, BRC) can be calculated for the upstream river reach (BRC_{us}) and the SBT (BRC_{SBT}), corresponding in Figures 4.2(b), 4.3(b), 4.4(b), 4.5(b), and 4.6 to the solid red and blue lines, respectively.

In most of the cases, SBTs are located in mountainous regions where a considerable amount of coarse material (bedload) is entrained (Auel and Boes, 2011b; Boes *et al.*, 2014). Usually, in such gravel-bed rivers, both bedload and riverbed surface are likely composed of an admixture of sand and gravel. To take into account the effect that sand has on coarser grains, the BRC_{us} is computed adopting the Wilcock and Crowe (2003) sediment transport formula, while for BRC_{SBT} the Smart and Jaeggi (1984) formula is adopted as suggested in the literature (Albayrak *et al.*, 2016; Boes *et al.*, 2017). The Wilcock and Crowe (2003) transport formula predicts a dimensionless bedload transport rate W_k^* for the kth grain class, related to the volume transport rate per unit width $q_{b,k}$ as

$$q_{b,k} = F_{a,k} \frac{u_*^3}{(s-1)\,g} W_k^* \tag{4.1}$$

To compute the dimensionless bedload transport rate W_k^* it is necessary to know (i) the shear velocity $u_* = \sqrt{\tau_b/\rho}$, (ii) the ratio of the sediment density to the water density $s = \rho_s/\rho_w$, (iii) the active layer grain sizes d_k and fractions $F_{a,k}$, (iv) the surface geometrical mean size d_g, and (v) the fraction of sand F_s in the surface layer, both of which can be computed from d_k and $F_{a,k}$. Details about the Wilcock and Crowe (2003) bedload transport relation are given in the original reference, in Parker (2004) and in Chapter 5 in this thesis.

Differently, the Smart and Jaeggi (1984) transport formula predicts the total bedload discharge in [m^3 s^{-1}] as follows

$$Q_b = \alpha \frac{\sqrt{g\,(s-1)\,d_m^3}}{1-\lambda_p} \left(\frac{d_{90}}{d_{30}}\right)^{0.2} S^{0.6} \theta^{0.5} \max\left((\theta - \theta_c), 0\right)^{\beta} \left(\frac{u}{u_*}\right) \tag{4.2}$$

where α and β are dimensionless constant parameters, θ_c is the critical Shields stress,

λ_p is the bed porosity, d_{30} and d_{90} are the diameters relative to the sizes of the riverbed surface GSD such that 30% and 90% of the sediment is finer, respectively, S is the riverbed slope, u is the flow velocity, and u_* is the shear velocity. Throughout this work it is considered that $\alpha = 8$, $\beta = 3/2$, $\theta_c = 0.047$, and $\lambda_p = 0.4$.

4.1.2 Release scenarios and operational conditions

SBTs are designed according to a given water discharge value $Q_{w,d,SBT}$. Referring to Figures 4.2 to 4.6, $Q_{w,d,SBT}$ identifies, on the BRC_{SBT} curve, the maximum bedload discharge that can be carried by the SBT ($Q_{b,M,SBT}$), i.e. the maximum bedload transport capacity of the SBT. The Q_w needed for carrying the maximum sediment discharge $Q_{b,M,SBT}$ in the upstream reach is $Q_{w,M}$. On the BRC_{SBT} curve, it is also possible to identify the minimum value of Q_w for which the SBT is first put in operation ($Q_{w,m,SBT}$), together with the corresponding minimum bedload discharge transported by the tunnel ($Q_{b,m,SBT}$). Then, four possible scenarios can be identified in terms of water and sediment discharges released by the SBT to the downstream river reach. SBT-release scenarios are presented hereafter.

Scenario I – very small events

In the case of very small events generating a water discharge $Q_{w,us}$ not exceeding the minimum one needed to open the SBT, i.e. $Q_{w,us} < Q_{w,m,SBT}$ (Figure 4.2(b)), the SBT is not operated and sediments carried by the upstream river, once the threshold of motion is exceeded, are all deposited in the reservoir (see Figure 4.2(a)). Water might as well be stored in the reservoir or it might be conveyed through the dam outlets. Water supply rate values to the downstream reach, i.e. possible SBT operations, are identified by points lying on the x-axis for $Q_w < Q_{w,m,SBT}$.

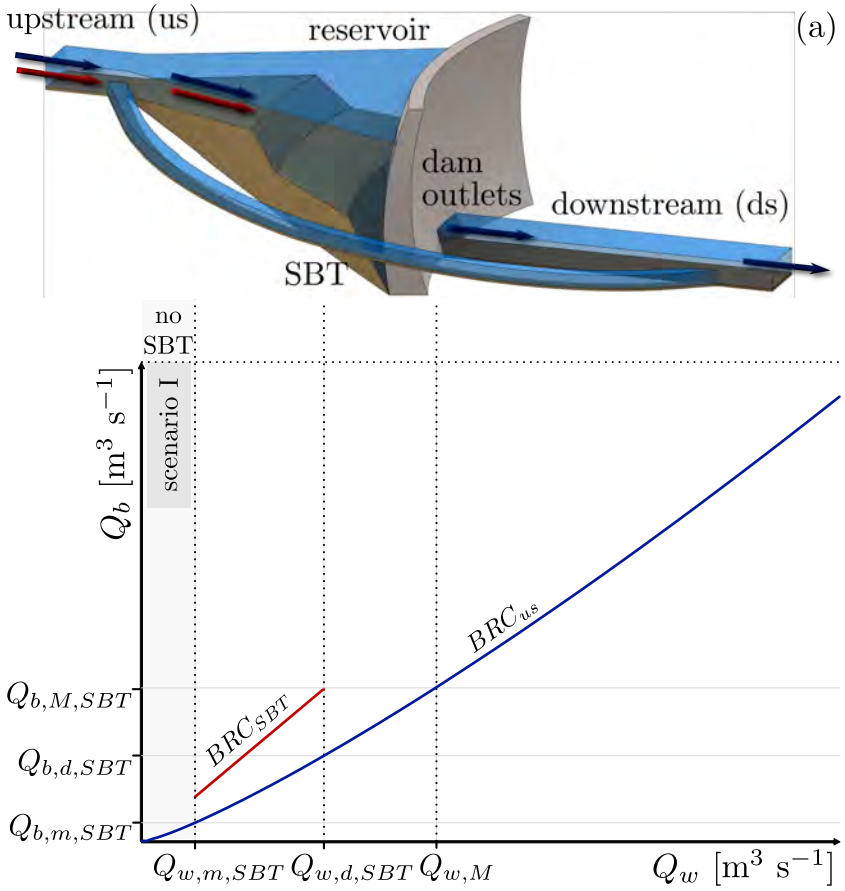

Figure 4.2: SBT release scenario I: (a) sketch of a SBT-dam system with water and sediment discharges represented as blue and red arrows, respectively, and (b) Bedload Rating Curves for the upstream reach (BRC_{us}, blue solid line) and for the SBT (BRC_{SBT}, red solid line).

Scenario II – design range

If the SBT is operated for water discharges in its design range, i.e. $Q_{w,m,SBT} < Q_{w,us} < Q_{w,d,SBT}$ (Figure 4.3(b)), the entire amount of sediment coming from upstream is diverted downstream by the SBT (see Figure 4.3(a)). Water and sediment supply rate values to the downstream reach, i.e. possible SBT operations, are identified by points lying on the BRC_{us} curve.

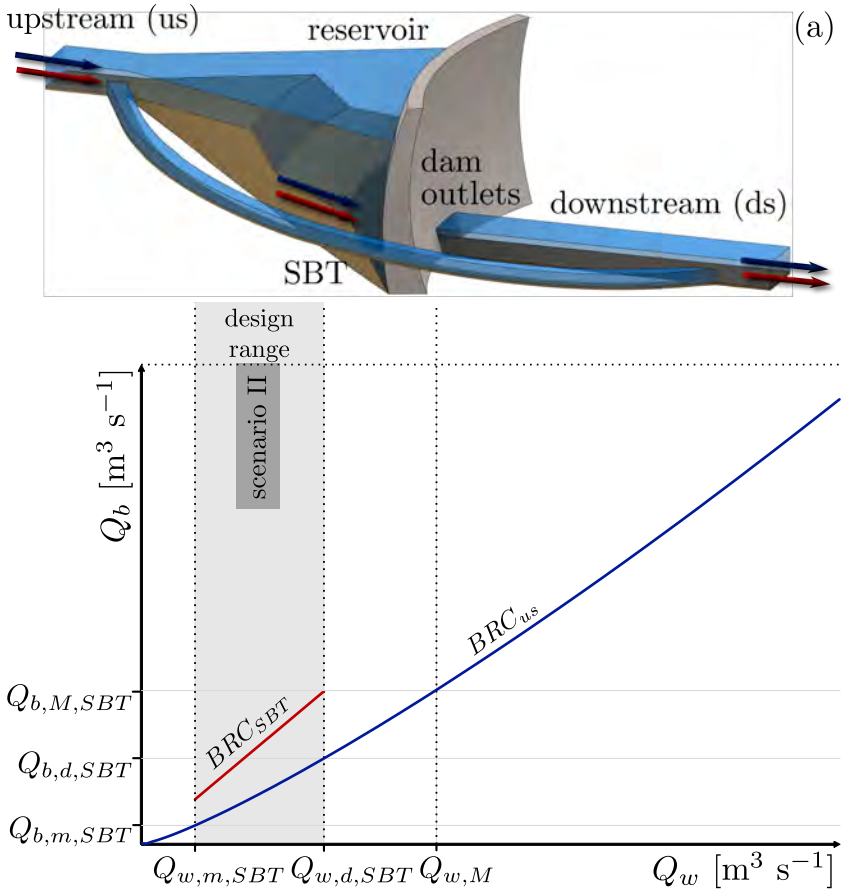

Figure 4.3: SBT release scenario II: (a) sketch of a SBT-dam system with water and sediment discharges represented as blue and red arrows, respectively, and (b) Bedload Rating Curves for the upstream reach (BRC_{us}, blue solid line) and for the SBT (BRC_{SBT}, red solid line).

Scenario III – large floods

During large floods, i.e. $Q_{w,d,SBT} < Q_{w,us} < Q_{w,M}$ (Figure 4.4(b)), the water and sediment discharges being delivered to the downstream reach range between the SBT design discharges (i.e. $Q_{w,d,SBT}$ and $Q_{b,d,SBT}$) and the maximum discharges possible (i.e. $Q_{w,M}$ and $Q_{b,M,SBT}$). This gives rise to two extreme situations: the first occurs when the water discharge fed to the downstream reach is kept constant (i.e. $Q_{w,ds} = Q_{w,d,SBT}$) and the water surplus (i.e. $Q_{w,us} - Q_{w,d,SBT}$) is stored inside the reservoir, while the sediment discharge ranges between the design and the maximum

one, i.e. $Q_{b,d,SBT} < Q_{b,ds} < Q_{b,M,SBT}$ (points on the left cathetus of the green triangle in Figure 4.4(b)). The second occurs when water and sediment discharges fed to the downstream reach range both between the design and the maximum value, i.e. $Q_{w,d,SBT} < Q_{w,ds} < Q_{w,M}$ and $Q_{b,d,SBT} < Q_{b,ds} < Q_{b,M,SBT}$ (points on the hypotenuse of the green triangle, i.e. on BRC_{us} in Figure 4.4). Between these two situations a number of other release conditions is possible, i.e. all the points lying inside the green triangle in Figure 4.4;

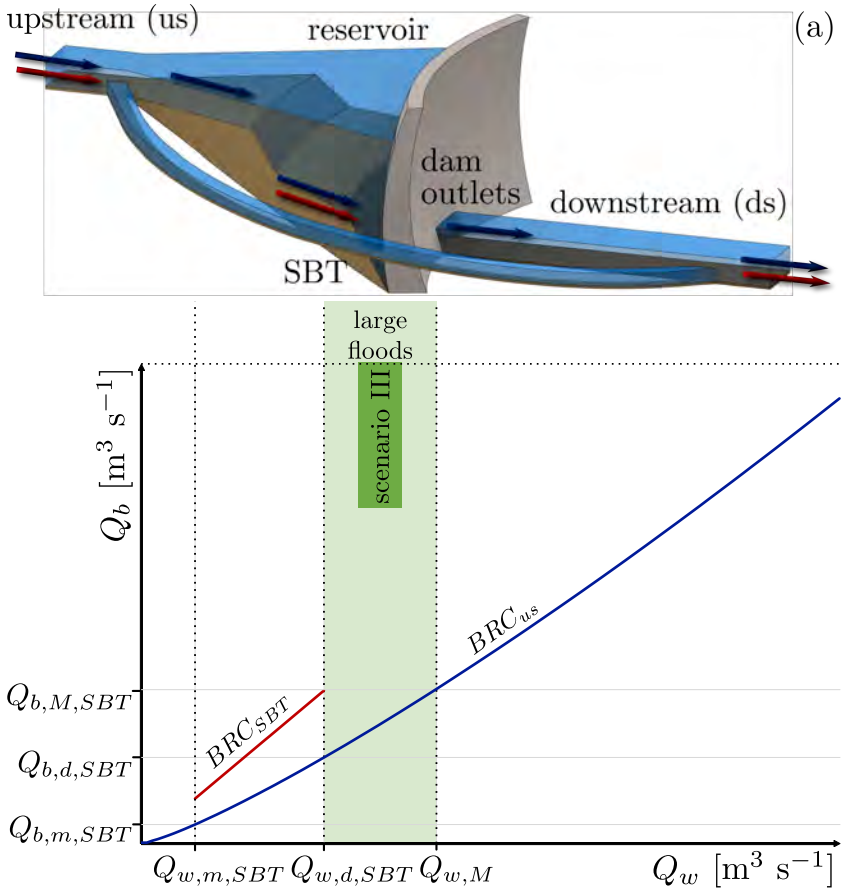

Figure 4.4: SBT release scenario III: (a) sketch of a SBT-dam system with water and sediment discharges represented as blue and red arrows, respectively, and (b) Bedload Rating Curves for the upstream reach (BRC_{us}, blue solid line) and for the SBT (BRC_{SBT}, red solid line), and green triangle identifying a number of possible release conditions.

Scenario IV – very large floods

During very large floods, i.e. $Q_{w,us} > Q_{w,M}$ (Figure 4.5(b)), the sediment discharge fed to the downstream reach is constant and equal to the maximum transport capacity of the SBT (i.e. $Q_{b,M,SBT}$) and the water discharge increases above the maximum one (i.e. $Q_{w,M}$), since extra water not flowing through the SBT is released from the dam (see Figure 4.5(a)).

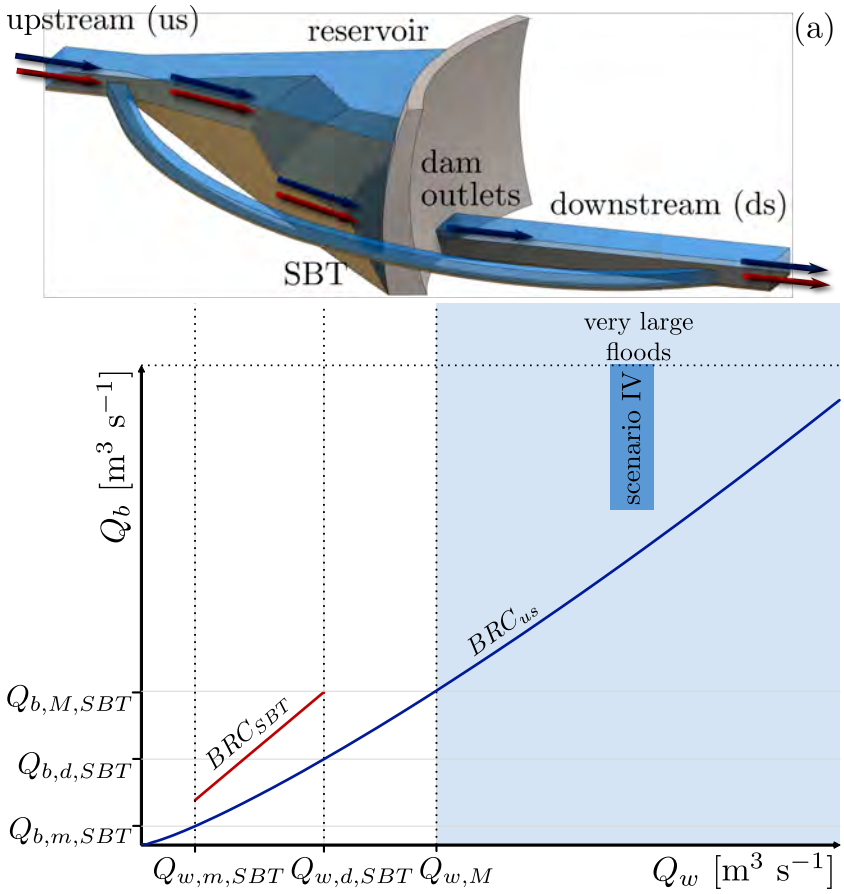

Figure 4.5: SBT release scenario IV: (a) sketch of a SBT-dam system with water and sediment discharges represented as blue and red arrows, respectively, and (b) Bedload Rating Curves for the upstream reach (BRC_{us}, blue solid line) and for the SBT (BRC_{SBT}, red solid line).

4.1.3 Operational Spaces (OS_{SBT}) and Operational Conditions (OCs)

Points relative to each scenario identify couples of water and sediment supply rates, which depend on the upstream reach and SBT transport capacity. These points can be (i) on the x-axis (scenario I), (ii) on the BRC_{us} (scenario II), (iii) inside a space defined by the BRC_{us}, a vertical line going from $Q_{b,d,SBT}$ to $Q_{b,M,SBT}$ and a horizontal line going from $Q_{w,d,SBT}$ to $Q_{w,M}$ (scenario III), or (iv) on a horizontal line at $Q_b = Q_{b,M,SBT}$ for $Q_w > Q_{w,M}$ (scenario IV). The totality of these points defines a SBT operational space (OS_{SBT}), i.e. a geometrical space where points defining water and sediment supply rates can be identified.

Furthermore, for each scenario the four different Operational Conditions (OCs) described hereafter can be considered.

OC1: bypassing efficiency equal to 1

OC1 is relative to the ideal conditions under which the SBT releases the same amount of water and sediment being carried out in the upstream reach. Therefore, OC1 are defined as the conditions where the SBT has a bypassing efficiency $e_{SBT} = 1$.

OC2: alternate bedload-laden and bedload-free water pulses

So far, sediments have been considered to be released from the SBT to the downstream reach at a rate being influenced only by the transport capacity of the upstream reach and of the SBT. Differently, SBTs might release bedload-free water (Mueller-Hagmann, 2018). This holds particularly for SBTs of type B (Mueller-Hagmann, 2018) with intake within the reservoir. To describe the case of bedload-free water releases, different release patterns for the bedload supply rate are defined, i.e. while water is released at each SBT operation, bedload material might be released every other operation, or even less frequently. In this case, the OS_{SBT} is the same one identified by the four release scenarios presented above, but between two bedload and water releases, a series of bedload-free water releases is carried out (see the solid red line in the sedimentograph of Figure 4.1(b)). Here, the case of bedload-free water being released every other (OC2a),

every two (OC2b) and every three (OC2c) bedload-laden water release is considered.

OC3: gravel-mining and coarse material extraction to avoid SBT-invert abrasion

Gravel can be extracted upstream of the SBT intake structure either for being used e.g. as construction aggregate (i.e. gravel-mining (e.g. Kondolf, 1997)), or to reduce the abrasion at the invert caused by coarse and very coarse gravel, cobbles and boulders (e.g. Baumer and Radogna, 2015). This is the case for most Japanese SBTs, where to avoid SBT invert abrasion and to sell coarse sediment as construction aggregate, coarse material is trapped and mined upstream of the SBT inlet structure (Sumi, 2017). In this case, not only the sediment volume conveyed to the SBT is reduced, but also the GSD of the transported sediment is deprived of its coarsest part. The OS_{SBT} relative to these conditions is the one represented with a dashed orange line in Figure 4.6.

OC4: reduced bypassing efficiency

The scenarios described in Subsection 4.1.2 define an OS_{SBT} obtained assuming that SBTs always work with a bypassing efficiency (e_{SBT}) of 1.0. That is, sediments being transported in the upstream reach are conveyed entirely through the SBT.

Literature studies suggest that SBTs usually do not carry all the bedload material coming from upstream, i.e. SBTs are generally characterized by an e_{SBT}<1.0, and it comes across that e_{SBT} may decrease with increasing incoming water discharge (e.g. De Cesare *et al.*, 2015). Auel *et al.* (2016) report mean e_{SBT}-values of 0.77 and 0.94 for the Japanese SBTs Asahi and Nunobiki, respectively, where total sediment flows are considered. For Nunobiki SBT, all coarse sediments enter the SBT even for floods with $Q_w > Q_{w,d,SBT}$ (Auel *et al.*, 2016), i.e. $e_{SBT} \rightarrow 1$ regarding bedload. However, in addition to fully efficient SBTs, reduced e_{SBT}-values are also considered, i.e. the bedload discharge Q_b being carried through the SBT is halved considering e_{SBT}=0.5 (see dashed red line in Figure 4.6).

Summary of SBT operational conditions (OCs)

To summarize, four different SBT operational conditions (OCs) are defined: (i) OC1, where SBT bypassing efficiency e_{SBT}=1.0, (ii) OC2, where the bedload release pattern

is different from the water release one, (iii) OC3, where the coarser part of the incoming sediment GSD is mined, i.e. there is a reduction of the GSD (GSD_{red}), and (iv) OC4, where SBT bypassing efficiency e_{SBT}=0.5. These OCs define three different OS_{SBT}, represented with dashed lines in Figure 4.6.

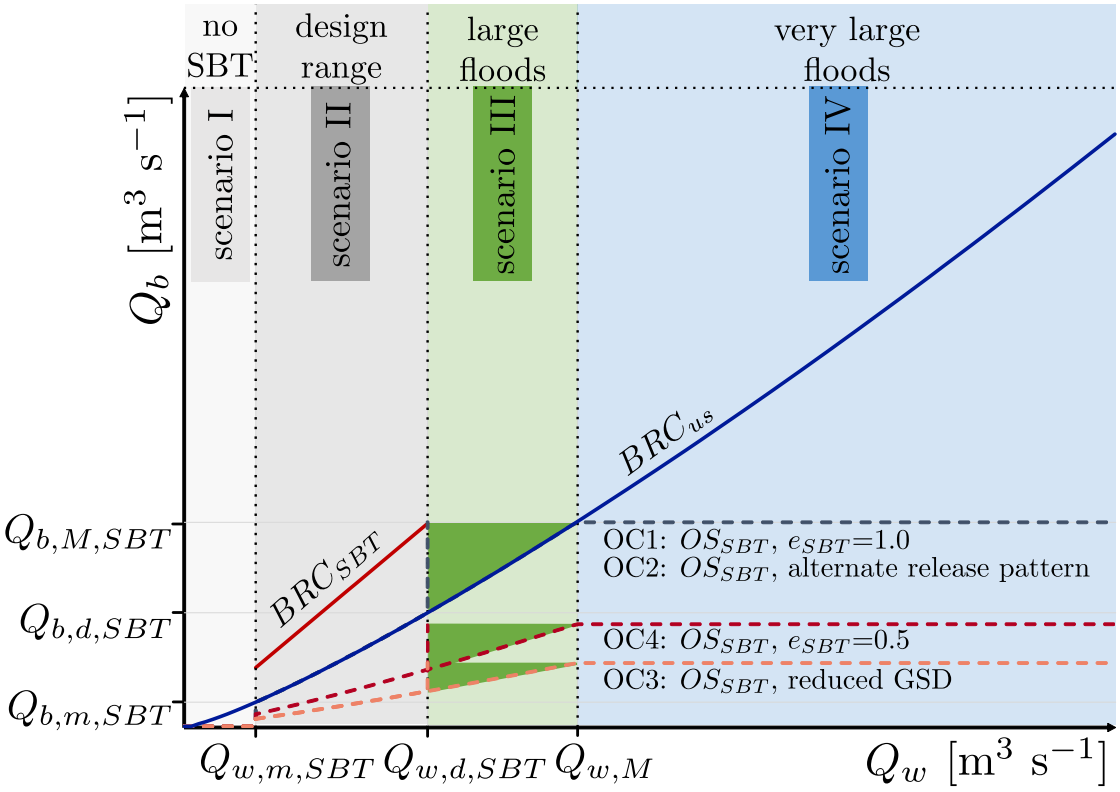

Figure 4.6: SBT release scenarios: Bedload Rating Curves for the upstream reach (BRC_{us}, blue solid line) and for the SBT (BRC_{SBT}, red solid line), Operational Spaces of the SBT (OS_{SBT}) considering SBT bypassing efficiency e_{SBT}=1.0 both with continuous and alternate sediment release patterns (Operational Conditions (OC) 1 and 2, gray dashed line), reduced sediment supply GSD (OC3, orange dashed line), and e_{SBT}=0.5 (OC4, red dashed line).

5 1D numerical modeling of riverbed evolution in a gravel-bed river subject to SBT operations

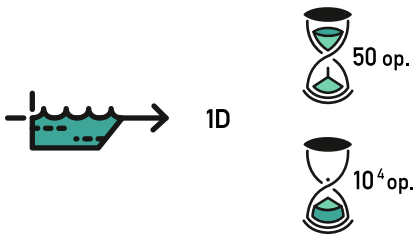

SBT operations act as sudden floods affecting river morphology both on the short-term and on the long-term. SBTs exert a strong control on water and sediment discharges and on the feeding GSD. To gain a better understanding of morphological processes triggered by SBT operations, time-dependent water and sediment supply rates and variable sediment supply GSD must be taken into account. Therefore, following the definition of a general framework to describe SBT release scenarios presented in Chapter 4, the results of a 1D numerical study of morphological effects of SBT operations at different time-scales are presented hereafter.

5.1 Numerical modeling of river morphodynamics with sediment mixtures

The interplay between different grain size classes, i.e. sediment sorting, is of paramount importance for describing morphological changes induced by SBT operations. From a

mathematical point of view, these effects can be accounted for using the active layer approach proposed by Hirano (1971, 1972), which is implemented in many numerical models (e.g. Delft3D (Sloff *et al.*, 2001) and BASEMENT (Vetsch *et al.*, 2017a)).

The software used for numerical simulations in this work is BASEMENT (Basic Simulation Environment for Computation of Environmental Flow and Natural Hazard Simulation) (Vetsch *et al.*, 2017b), which is a freeware software developed at the Laboratory of Hydraulics, Hydrology and Glaciology (VAW) of the Swiss Federal Institute of Technology (ETH) in Zurich, Switzerland.

The model considers the free-surface flow as hydrostatic and describes the hydrodynamics by the Saint-Venant equations. Friction exerted by flow over a cohesionless bottom composed of mixed sediment induces sediment transport, which is assumed to occur only as bedload. Grain-size distribution of the riverbed surface and the development of size stratification are described by using the active-layer approach of Hirano (Hirano, 1971, 1972). This schematization results to be accurate in the description of streamwise sorting and its interplay with bed elevation (Siviglia *et al.*, 2017).

5.1.1 Hydrodynamics

The evolution of the hydraulic characteristics is described by the one-dimensional Saint-Venant equation system. This includes equations for conservation of water mass (the continuity equation),

$$\frac{\partial h}{\partial t} + \frac{\partial q_w}{\partial x} = 0, \tag{5.1}$$

and for the momentum principle for the water phase,

$$\frac{\partial q_w}{\partial t} + \frac{\partial}{\partial x}\left(\frac{q_w^2}{h} + \frac{1}{2}gh^2\right) + gh\frac{\partial \eta}{\partial x} = -ghS_f, \tag{5.2}$$

where $h(x,t)$ [m] denotes flow depth, $q_w(x,t)$ [m^2 s^{-1}] flow discharge per unit width, $g = 9.81$ [m s^{-2}] is the acceleration due to gravity, η [m] is the riverbed elevation, and $S_f(x,t)$ [-] is the dimensionless friction slope. The friction slope S_f in the momentum equation (5.2) can be evaluated by the Gauckler-Strickler relation as

$$S_f = \frac{|q_w| q_w}{h^{10/3} k_s^2} \tag{5.3}$$

where k_s is the Gauckler-Strickler coefficient measured in [$m^{1/3}s^{-1}$] and equal to the inverse of the Manning coefficient. Here k_s is assumed to be constant and it is calculated like follows

$$k_s = \frac{21.1}{(d_{90})^{1/6}} \tag{5.4}$$

5.1.2 Morphodynamics

The time evolution of riverbed level changes is described using the Exner equation:

$$(1-\lambda_p)\frac{\partial \eta}{\partial t} + \frac{\partial q_b}{\partial x} = 0, \tag{5.5}$$

where λ_p is bed porosity, $\eta(x,t)$ [m] is the riverbed elevation, and q_b [m^2 s^{-1}] is the total sediment discharge per unit width.

To deal with mixed sediment, the model adopts (i) a representation of the sediment mixture using discrete fractions, i.e. grain size classes, (ii) a vertical discretization of the riverbed, and (iii) a grain size specific sediment continuity model (Stecca *et al.*, 2014). The GSD of the sediment mixture is discretized using N_{gc} classes, each one characterized by one representative grain diameter d_k, where k is an index spanning the range from 1 to N_{gc}.

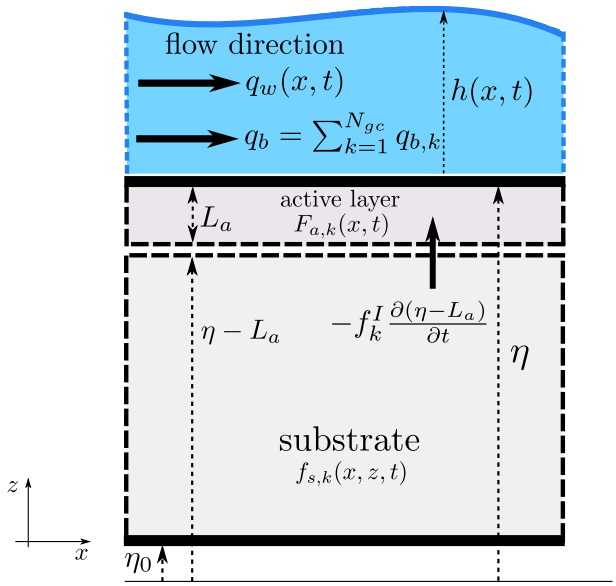

Figure 5.1: Sketch and notation of riverbed vertical discretization and sediment fluxes for the active layer approach.

To discretize in vertical direction the riverbed stratification, two layers are considered: the active layer and a substrate layer (Hirano, 1971, 1972), as sketched in Figure 5.1. The active layer (riverbed surface layer, exchange layer) is a vertically mixed moving volume located immediately under the bed surface (Church and Haschenburger, 2017). Throughout this work, the active layer is considered to have constant (not time dependent) thickness L_a [m], being an order-one multiple of the surface size d_{90} [m] such that 90% of the sediment is finer:

$$L_a = n_a d_{90} \tag{5.6}$$

where n_a is an order-one parameter, here equal to 2. Below the active layer, the substrate is found, and the interface between the active layer and the substrate is located at elevation $\eta(x,t) - L_a(x)$. Each grain class-k is represented in the active layer by an averaged volume fraction $F_{a,k}(x,t)$ and in the substrate, which is not vertically mixed, by a fraction content denoted with $f_{s,k}(x,z,t)$. The following constraints over the sediment fraction values hold:

$$0 \leq F_{a,k} \leq 1, \qquad 0 \leq f_{s,k} \leq 1 \qquad \text{for} \quad 1 \leq k \leq N_{gc} \tag{5.7}$$

and

$$\sum_{k=0}^{N_{gc}} F_{a,k} = 1, \qquad \sum_{k=0}^{N_{gc}} f_{s,k} = 1 \tag{5.8}$$

For each grain class a mass conservation law must be defined. To this end, two sets of conserved variables, i.e. variables for which physically meaningful balance laws can be established (e.g. Stecca *et al.*, 2014), must be defined:

$$M_{a,k} = F_{a,k} L_a, \qquad M_{s,k} = \int_{\eta_0}^{\eta - L_a} f_{s,k}(z) dz \tag{5.9}$$

where η_0 is a constant reference elevation, i.e. a reference bottom level (see Figure 5.1). $M_{a,k}$ and $M_{s,k}$ have the dimension of lengths [m] and represent the sediment mass per surface area of the kth fraction, respectively in the active layer and in the substrate, divided by the constant sediment density ρ_s [kg m^{-3}]. Rewriting (5.8) leads to:

$$\sum_{k=0}^{N_{gc}} M_{a,k} = L_a, \qquad \sum_{k=0}^{N_{gc}} M_{s,k} = \eta - L_a - \eta_0 \tag{5.10}$$

While the active layer provides a source of sediment to be entrained in the flow and transported with a grain size specific discharge $q_{b,k}$ [m^2 s^{-1}], the substrate does not contribute to sediment transport, but exchanges sediment with the active layer. This exchange occurs only by degradation and aggradation at the interface between the two layers, and results in a vertical flux of sediment. In the light of this, the mass conservation principle in the active layer and in the substrate can be applied, leading to two mass conservation laws that if L_a is assumed to be constant in time read as:

$$\frac{\partial M_{a,k}}{\partial t} = -f_k^I \frac{\partial \eta}{\partial t} - \frac{\partial q_{b,k}}{\partial x}, \tag{5.11}$$

and

$$\frac{\partial M_{s,k}}{\partial t} = f_k^I \frac{\partial \eta}{\partial x}, \tag{5.12}$$

where $f_k^I(x,t)$ denotes the volume content of the kth fraction at the interface between the

active layer and the substrate. Since at that location a discontinuity is allowed, following Toro-Escobar *et al.* (1996) the value of $f_k^I(x,t)$ at the interface is evaluated as:

$$f_k^I = \begin{cases} f_{s,k}\big|_{z=\eta-L_a}, & \frac{\partial \eta}{\partial t} < 0 \\ \alpha F_{a,k} + (1-\alpha)\, p_{b,k}, & \frac{\partial \eta}{\partial t} \geq 0 \end{cases} \tag{5.13}$$

where α is a specified parameter ranging between 0 and 1 (Toro-Escobar *et al.*, 1996) and $p_{b,k}$ is defined as the volume fraction of bedload in the kth grain class and is denoted as

$$p_{b,k} = \frac{q_{b,k}}{q_b} \tag{5.14}$$

where q_b, the total sediment discharge to be used in (5.5), is given by

$$\sum_{k=0}^{N_{gc}} q_{b,k} = q_b \tag{5.15}$$

By definition (5.13) and the constraints (5.7), the interface fraction content is in turn subject to the constraints:

$$0 \leq f_k^I \leq 1, \qquad \sum_{k=0}^{N_{gc}} f_k^I = 1 \qquad \text{for} \quad 1 \leq k \leq N_{gc} \tag{5.16}$$

By constraint (5.8) and assuming that L_a is constant, only $N_{gc}-1$ independent active layer and substrate equations can be set. This leads to a system of $2N_{gc}+1$ equations, consisting of two equations for the hydraulics, the Exner equation and $2\,(N_{gc}-1)$ sediment continuity equations. Moreover, equation (5.15) and constraints (5.8) must be considered. It is worth mentioning that if $k = 1$, i.e. if one characteristic grain size is considered, the system automatically reduces to the Saint-Venant – Exner system of equations.

5.1.3 Bedload transport relations

The numerical study presented in this Chapter is restricted to the case of bedload transport of gravel with some admixtures of sand. Thus, a surface-based bedload transport

formulation is needed to estimate bedload transport and to compute the evolution of the active layer fractions $F_{a,k}$ for each kth fraction as the bed evolves. This should link the transport rate of the kth size range to its availability in the surface layer. To account for the effect that sand (i.e. $0.063 < d_k < 2$ mm) has on coarser grains, these calculations are performed with the Wilcock and Crowe (2003) transport formula, which predicts a dimensionless bedload transport rate W_k^* for the kth grain size range, related to the volume transport rate per unit width $q_{b,k}$ as

$$q_{b,k} = F_{a,k} \frac{u_*^3}{(s-1)\,g} W_k^* \tag{5.17}$$

To compute the dimensionless bedload transport rate W_k^* it is necessary to know (i) the shear velocity u_*, (ii) the submerged specific gravity of the sediment Δ, (iii) the active layer grain sizes d_k and fractions $F_{a,k}$, (iv) the surface geometrical mean size d_g, and (v) the fraction of sand F_s in the surface layer, both of which can be computed from d_k and $F_{a,k}$. The dimensionless bedload transport rate W_k^* is described by a discontinuous function

$$W_k^* = G(\phi_k) = \begin{cases} 0.002\phi_k^{7.5} & \phi_k < 1.35 \\ 14\left(1 - \dfrac{0.894}{\phi_k^{0.5}}\right)^{4.5} & \phi_k \geq 1.35 \end{cases} \tag{5.18}$$

where ϕ_k is the ratio of the shear stress to the reference shear stress of size fraction k:

$$\phi_k = \frac{\theta_{s,g}}{\theta_{ssr,g}} \left(\frac{d_k}{d_g}\right)^{-b_k} \tag{5.19}$$

where $\theta_{s,g}$ is the shear stress relative to the mean geometric size d_g, $\theta_{ssr,g}$ is the reference Shields number for the surface geometric mean size, and b_k is a coefficient depending on the grain sizes d_k. These three coefficients can be calculated as follows

$$\theta_{s,g} = \frac{u_*^2}{\Delta g d_g} \quad \theta_{ssr,g} = 0.021 + 0.015 exp(-F_s) \quad b_k = \frac{0.67}{1 + exp(1.5 - d_k/d_g)} \tag{5.20}$$

To analyze the sensitivity of the model to the bedload transport formula, the results

obtained using the Wilcock and Crowe (2003) formula are tested against results obtained using the Meyer-Peter and Müller (1948) formula in conjunction with the hiding-exposure correction of Egiazaroff (1965) to account for grainsize selectivity, which reads

$$Q_b = \alpha \frac{\sqrt{g\,(s-1)\,d_k^3}}{1-\lambda_p} \max\left(\left(\theta_k - \xi_k \theta_c\right), 0\right)^{\beta} \tag{5.21}$$

where λ_p (constant) is the bed porosity, α and β are dimensionless constant parameters, and θ_c is the critical shear stress, and are assumed to be $\lambda_p = 0.4$, $\alpha = 8$ and $\beta = 1.5$, and $\theta_c = 0.047$. Furthermore, the ratio of the sediment density to the water density $s = \rho_s/\rho_w = 2.65$, and d_k are the sediment diameters of the grain size distribution. In eq. 5.21, θ_k represents the Shields stress relative to the kth sediment fraction defined as

$$\theta_k = \frac{u_*}{g\,(s-1)\,d_k} \tag{5.22}$$

Finally in eq. 5.21, ξ_k is the hiding factor for the kth fraction, which reads

$$\xi_k = \left(\frac{\log_{10} 19}{\log_{10}\left(19 \frac{d_k}{d_m}\right)} \right)^2 \tag{5.23}$$

where d_m is the mean sediment diameter in the active layer, defined as

$$d_m = \sum_{k=1}^{N_{gc}} d_k F_{a,k} \tag{5.24}$$

Details of the relations of Meyer-Peter and Müller (1948) and Wilcock and Crowe (2003) can be found in the original reference and in Parker (2004).

5.1.4 Prediction of the static armor composition

The static armor is defined here as the layer that forms by selective erosion as a result of the action of clear water. Therefore, static armor composition is obtained in the limit of vanishing sediment transport, under the constraint that bedload and surface size

distribution are identical. A similar prediction is presented by Parker and Sutherland (1990), where good agreement between measured and calculated GSD is shown. While Parker and Sutherland (1990) predict the composition of the static armor layer with the Canterbury and the Oak Creek models of the transport of non-uniform sediment, in this work it is calculated with the Wilcock and Crowe (2003) formula. This definition will turn out to be relevant in the interpretation of the results and in the definition of the initial conditions for the numerical study.

The Wilcock and Crowe formula can be inverted to calculate the surface size fractions $F_{a,k}$ as a function of the bedload size fractions $p_{b,k}$. Given the hydraulic conditions, i.e. $u_* > 0$, and assuming vanishing bedload due to the presence on the riverbed surface of a static armor, i.e. $q_b \to 0$, $\phi_k \to 0$ may be assumed as well, i.e. $\phi_k < 1.35$ in equation (5.18). Then, the inverted Wilcock and Crowe (2003) formula can be used to predict the size composition of the static armor:

$$F_{a,k} = \frac{p_{b,k}\delta_k^{7.5b_k}}{\sum_{k=1}^{N_{gc}} p_{b,k}\delta_k^{7.5b_k}} \tag{5.25}$$

where

$$\delta_k = \frac{d_k}{d_g} \tag{5.26}$$

5.1.5 Discretization of GSD to N_{gc} grain classes

Each grain size distribution needs to be reduced from grain sizes to grain classes to be used for numerical simulations using the Saint-Venant – Hirano numerical model. In fact, the Hirano model refers to grain classes, which are characterized by a volume fraction in the active layer $F_{a,k}$, or in the bedload transport $p_{b,k}$, and a grain size d_k. To give an example of the reduction to grain classes from grain sizes, the approach proposed by Parker (2004) is followed hereafter and the grain class fractions are indicated as f_k and the grain class sizes as d_k. Therefore, each class is defined by two fractions, i.e. $f_{k-1/2}$ and $f_{k+1/2}$, and two sizes, i.e. $d_{k-1/2}$ and $d_{k+1/2}$ (see Figure 5.2).

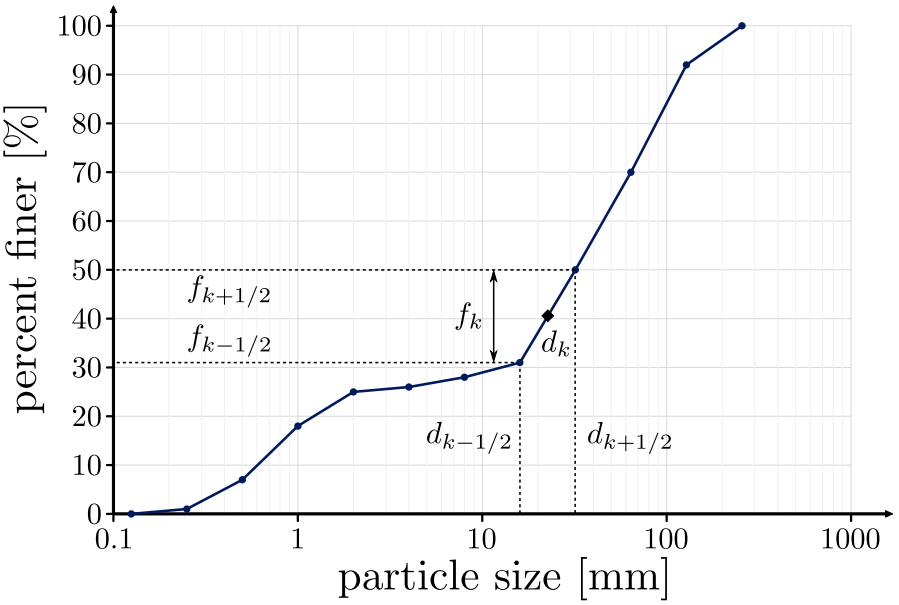

Figure 5.2: GSD discretization in grain classes.

The mean sediment diameter of the grain size distribution d_m can be calculated with eq. 5.24, while the mean geometric size d_g is calculated specifying each grain size in terms of a base-2 logarithmic scale (phi scale or psi scale), as follows

$$d_g = 2^{\psi_m} \qquad \psi_m = \sum_{k=1}^{N_{gc}} \psi_k f_k \qquad \psi_k = \log_2 d_k \tag{5.27}$$

where ψ_m is the mean size in the psi scale. Moreover the standard deviation of the GSD on psi scale can be calculated as

$$\sigma = \sqrt{\sum_{k=1}^{N_{gc}} (\psi_k - \psi_m)^2 f_k} \tag{5.28}$$

and the geometric standard deviation is $\sigma_g = 2^{\sigma}$.

N_{gs} grain sizes (bounds) define $N_{gc} = N_{gs} - 1$ grain classes, and f_k and d_k calculated based on $f_{k\pm1/2}$ and $d_{k\pm1/2}$ using the following formulas

$$f_k = f_{k+1/2} - f_{k-1/2}, \qquad d_k = \left(d_{k+1/2} d_{k-1/2}\right)^{1/2} \tag{5.29}$$

5.1.6 Mathematical behavior of the Saint–Venant - Hirano model for sediment mixtures

The mathematical behavior of the active layer approach was firstly studied by Ribberink (1987), who developed approximations to the speed of sediment waves forming and traveling in the active layer. In addition to Ribberink's (1987) work, Stecca *et al.* (2014) considered grain size selectivity, i.e. they considered the riverbed grain size distribution as a mixture of different grain classes. Each equation related to each grain class considered gives rise to an additional wave in the active layer. Stecca *et al.* (2014) define these waves arising from the Exner equation and the Hirano equations, respectively, as "bed" wave and "sorting" waves. Furthermore, they define sorting waves as the waves having a prominent role in advecting changes in the GSD of the active layer and also a broader effect, as they also convey changes in bed elevation and hydraulic variables that are determined by the changes in the grain size distribution.

Stecca *et al.* (2014) analyzed the problem in partial and high sediment transport conditions (i.e. all fractions are being transported) under different Froude regimes. When all fractions are being transported, $N_{gc} - 1$ bed waves travel downstream at different speed. In condition of partial mobility, achieved by suppressing some of the Hirano equations, some grain classes are not moving, i.e. there is a number of steady waves equal to the number of suppressed equations (Stecca *et al.*, 2014). Moreover, localized perturbations in the active layer grain size distribution are always advected downstream and the resulting unbalance in total bedload triggers downstream-traveling bed perturbations. Furthermore, perturbations in grain size distribution, and the associated riverbed elevation disturbances, are traveling at higher pace than the one of the "bed" wave predicted by the Exner equation in single-grain models (Stecca *et al.*, 2014). Moreover, under supercritical conditions, the mixed-sediment model introduces a novel downstream-propagating wave, in addition to the upstream-propagating one, which was already predicted by the unisize-sediment model (Ribberink, 1987).

Stecca *et al.* (2014) also analyzed the hyperbolicity domain of the problem solutions, and they found that until the active layer degrades into a coarser substrate the problem solutions remain in the domain of hyperbolicity. On the contrary, if the active layer degrades into a finer substrate, the problem becomes elliptic, and it is therefore not

suitable for morphodynamic predictions.

Finally, it can be assumed that N_{gc} grain size classes generate $N_{gc} - 1$ sorting waves. This means that the number of waves propagating in the active layer depends on the number of grain classes that are used to discretize the grain size distribution.

5.1.7 Numerical solution of the one dimensional Sain-Venant – Hirano model

In the 1D module of BASEMENT, i.e. BASEchain, the one-dimensional non-conservative hyperbolic system of PDEs that comprises equations (5.1), (5.2), (5.5), (5.11), and (5.12) is numerically solved. The solution of the system is uncoupled, i.e. hydraulics and riverbed elevation and composition are updated following an asynchronous solution procedure (e.g. Cao *et al.*, 2002). Moreover, the Shallow Water Equations (SWE) (5.1) and (5.2) are solved using the approximated Roe Riemann Solver (Toro, 2009), while the Exner–Hirano equations (5.5), (5.11), and (5.12) are solved using an explicit finite difference approach. More details on how the system of equations is solved in BASEMENT are given in the software system manual (Vetsch *et al.*, 2017a). Finally, the bookkeeping procedure for the administration of size stratification and its vertical storage in BASEMENT is implemented dividing the substrate into different sublayers having different height. For the bookkeeping procedure, two cases are defined, i.e. erosion and deposition. In the first case, the volume fractions in the active layer are updated with the ones of the underlying layers weighted with the single layer width. In Figure 5.3, a sketch of the riverbed vertical discretization with the notation relative to the bookkeeping procedure in case of erosion is presented.

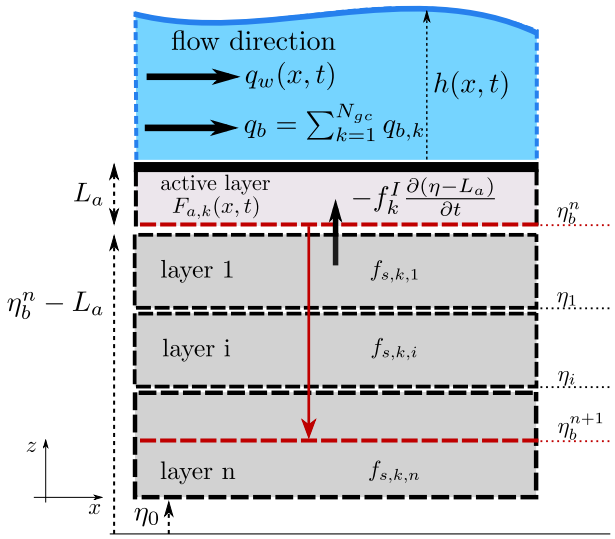

Figure 5.3: Sketch and notation of riverbed vertical discretization and sediment fluxes for the bookkeeping procedure in case of erosion.

When the active layer is mined into the substrate with the riverbed level going from η_b^n to η_b^{n+1}, the new composition of the active layer is determined according to equation (5.13), and the single substrate fractions $f_{s,k,i}$ are weighted due to the width of the sublayer as follows

$$F_{a,k} = \frac{1}{\eta_b^n - \eta_b^{n+1}} \sum_{i=1}^{n_{sub}} \left[f_{s,k,i} \left(\eta_{i-1} - max\left(\eta_j, \eta_b^{n+1} \right) \right) \right] \tag{5.30}$$

where the notation adopted refers to the one used in Figure 5.3. In the case that deposition occurs, the active layer moves upwards and as soon as the deposition height reaches a defined value a new sublayer is generated having the composition determined following equation (5.13) for depositional cases. Further details can be found in the reference manual of the software (Vetsch *et al.*, 2017b).

5.2 1D numerical modeling of repeated SBT operations

According to the data reported in Tables 2.1 and 2.2, SBTs are operating less than 10 times per year and for the rest of the year the downstream reach is fed with the minimum flow (Martín *et al.*, 2017). Therefore, the river is assumed to be morphologically

inactive if the SBT is not operated and the focus of this work is on the morphological evolution of the river reach during and following repeated hydrographs and sedimentographs. Responses in channel geometry and surface grain size distribution (GSD) that accommodate perturbations in the water and sediment supply regimes happen on different time scales (Buffington, 2012). On the one hand, on a long time scale, only the dynamics of stream gradient due to aggradation/incision on a reach-scale can be observed. On the other hand, changes on smaller spatial scale occur during a shorter time-scale going from minutes to decades (Buffington, 2012). Furthermore, channel responses on large scales reflect the cumulative action of smaller-scale processes. Thus, a progression of spatial scales of response can be conceived, as the one represented in Figure 5.4.

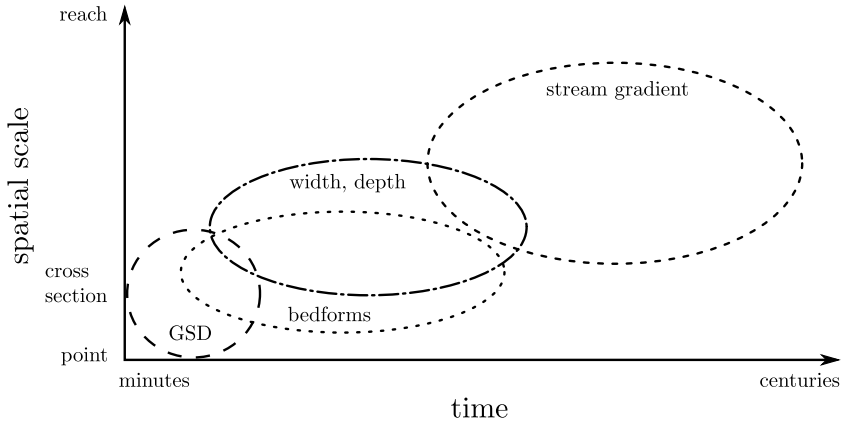

Figure 5.4: Spatial and temporal scales of response in alluvial rivers: grain size (individual grains to textural patches), width, depth (cross-sectional to reach changes), bedforms (from e.g. ripples to bars), and stream gradient (reach-scale channel aggradation/erosion). Adapted from Buffington (2012).

Therefore, the problem is studied on two different time scales. First, the effects of SBT operations at mobile-bed equilibrium, i.e. the state reached after sustaining a defined configuration for a sufficiently long time (e.g. Parker *et al.*, 2007), are analyzed. The equilibrium configuration relative to different release scenarios is characterized in terms of (i) the active layer composition (described by the geometric mean diameter of the active layer GSD d_g), and (ii) the riverbed slope S. In this case, there is no need to distinguish between different initial conditions since the equilibrium does not depend

on them. In fact, after a sufficiently long time the system converges to a configuration where its characteristics depend only on the boundary conditions (e.g. Parker *et al.*, 2007). Second, the effects of few tens of SBT operations are analyzed, which are representative of a more realistic time-span, i.e. a human time-scale (e.g. Buffington, 2012). To this end, proper initial conditions need to be defined. Thus, two extreme situations are chosen: (i) when the downstream reach is in the same conditions as the upstream reach (blue line in Figure 5.7) and (ii) when the downstream reach has a lower slope and a static armor on the river surface (red line in Figure 5.7). These can be linked to two real situations, namely: (i) the construction of a SBT parallel to a dam construction, as it is suggested nowadays to avoid reservoir sedimentation (Kondolf *et al.*, 2014) and (ii) the construction of a SBT as it has been done in the past decades, i.e. at rivers that suffer already the consequences of river damming.

5.2.1 Hydrograph shape, duration and maximum discharge

Water and sediment are fed to the channel in form of repeated hydrographs and sedimentographs, the shape and duration of which recall the SBT operation that occurred at the Solis SBT on August 13, 2014 (Facchini *et al.*, 2015). Therefore, they have a trapezoidal shape with steep rising and falling limbs. In this study, a single SBT operation lasts 12 hours with 1-hour rising and falling limbs (see Figure 5.5).

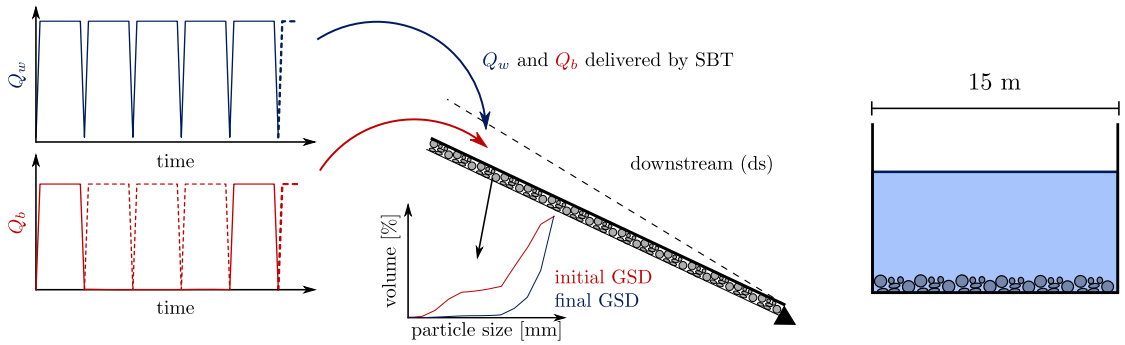

Figure 5.5: Representation of the simulations scheme: hydrograph (blue) and sedimentograph (red) fed to the channel, channel degrees of freedom (riverbed slope and composition), and channel cross-section used for one-dimensional numerical study.

To define the hydrograph and sedimentograph magnitudes (i.e. the peak values of

the hydrograph and sedimentograph), the general framework to describe SBT release scenarios presented in Chapter 4 is taken as a reference. Here, BRC_{us} and BRC_{SBT} have been calculated using as a reference the characteristics of the reach of the Albula River upstream of Solis Reservoir and Solis SBT, respectively (Rickenmann *et al.*, 2017; Oertli and Auel, 2015). The first is considered to have a 1.5% slope, a 15 m-wide channel and a Gauckler-Strickler parameter k_s=32 $m^{1/3}s^{-1}$, while the Solis SBT is considered to have a 1.9% slope, a 4.4 m channel-width, and a Gauckler-Strickler parameter k_s=65 $m^{1/3}s^{-1}$.

As described in Chapter 4, several bedload release patterns (OC1 and OC2) are considered, i.e. bedload might be released (OC1) or not (OC2) during one single SBT operation. In both cases, the sedimentograph varies sympathetically with the hydrograph, but while under OC1 sediments are always released, under OC2 they are released every other (OC2a), two (OC2b) or three (OC2c) SBT operations. The four different sediment release patterns used in this work are summarized in Figure 5.6.

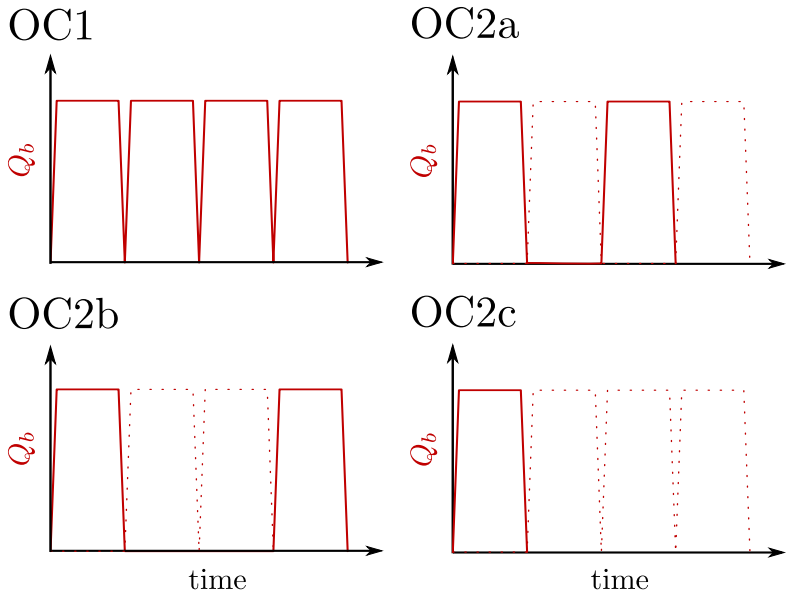

Figure 5.6: Representation of sediment release patterns: continuous sediment release as for OC1, sediment released every other SBT-operation for OC2a, sediment release interrupted for two consecutive SBT-operations for OC2b, and sediment release interrupted for three consecutive SBT-operations for OC2c.

5.2.2 Feeding grain size distributions

Sediment being transported in the upstream reach and through the tunnel is considered to be characterized by a bimodal mixture with geometric mean size d_g=16.22 mm and geometric standard deviation σ_g = 7.37 mm, composed by a 25% sand-mode (d <2 mm), and a 75% gravel-mode ($d \geq$2 mm), and represented by the blue line and dots in Figure 5.7. The gravel-mode resembles the GSD of samples collected inside the Solis Reservoir to which the sand-mode is added since great majority of gravel-bed reaches usually show varying degrees of bimodality (e.g. Shaw and Kellerhals, 1982). That is, in the simplified dam-SBT system represented in (Figure 4.1 on page 83 it is assumed that the upstream reach is likely to transport an admixture of sand and gravel.

diameter [mm]	fraction [%]		
	ref. GSD	red. GSD	s.a. GSD
0.125	0	0	0
0.25	1	19.35	0
0.5	6	35.48	0
1	11	22.59	0
2	7	3.22	0
4	1	6.45	0
8	2	9.68	0
16	3	3.23	0
32	19	0	0
64	20	0	0.08
128	22	0	6.82
256	8	0	93.1

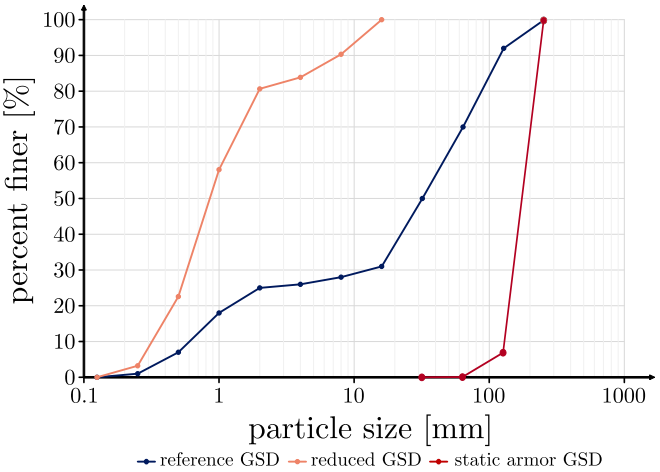

Figure 5.7: Hypothesized grain size distribution (GSD) of the upstream river reach (blue line and dots), reduced GSD due to gravel-mining or sediment extraction to avoid SBT-invert abrasion (orange line and dots), and static armor GSD prediction (red line and dots).

Moreover, gravel can be extracted upstream of the SBT intake structure either for being used e.g. as construction aggregate (i.e. gravel-mining (e.g. Kondolf, 1997)), or to reduce the abrasion at the invert caused by coarse and very coarse gravel, cobbles and boulders (e.g. Baumer and Radogna, 2015). Therefore, it is supposed hereafter that under certain circumstances grains coarser than 16 mm are extracted (see Figure 5.7). In this case, not only the sediment volume conveyed to the SBT will be reduced by a factor of 3, but also the GSD of the sediment will be deprived of its coarsest part. The GSD of the delivered material is the one represented with an orange line in Figure 5.7.

5.3 Numerical simulations setup

Numerical runs are performed for cycled hydrograph and sedimentograph both having trapezoidal shape, with a total duration of 12 hours, and a rising- and falling-limb duration of one hour. The base discharge per unit width for the hydrograph is 0.33 m^2s^{-1}, and the base sediment discharge is 0 m^2s^{-1}. Hydrographs and sedimentographs are repeated one after the other since if the SBT is not in operation the river is supposed to be morphologically inactive. According to what is described in Chapter 4, four different SBT operational conditions (OCs) are considered: (i) OC1, where SBT bypassing efficiency e_{SBT}=1.0, (ii) OC2, where sediments are released every other (OC2a), every two (OC2b) and every three (OC2c) hydrographs (iii) OC3, where the coarser part of the incoming sediment GSD is mined, i.e. there is a reduction of the GSD (GSD_{red}), and (iv) OC4, where SBT bypassing efficiency e_{SBT}=0.5. These OCs define four different OS_{SBT}, represented with dashed lines in Figure 5.8. For each OC, 12 runs are defined with different maximum water and sediment discharge, i.e. hydrograph and sedimentograph peaks, as defined in Table 5.1.

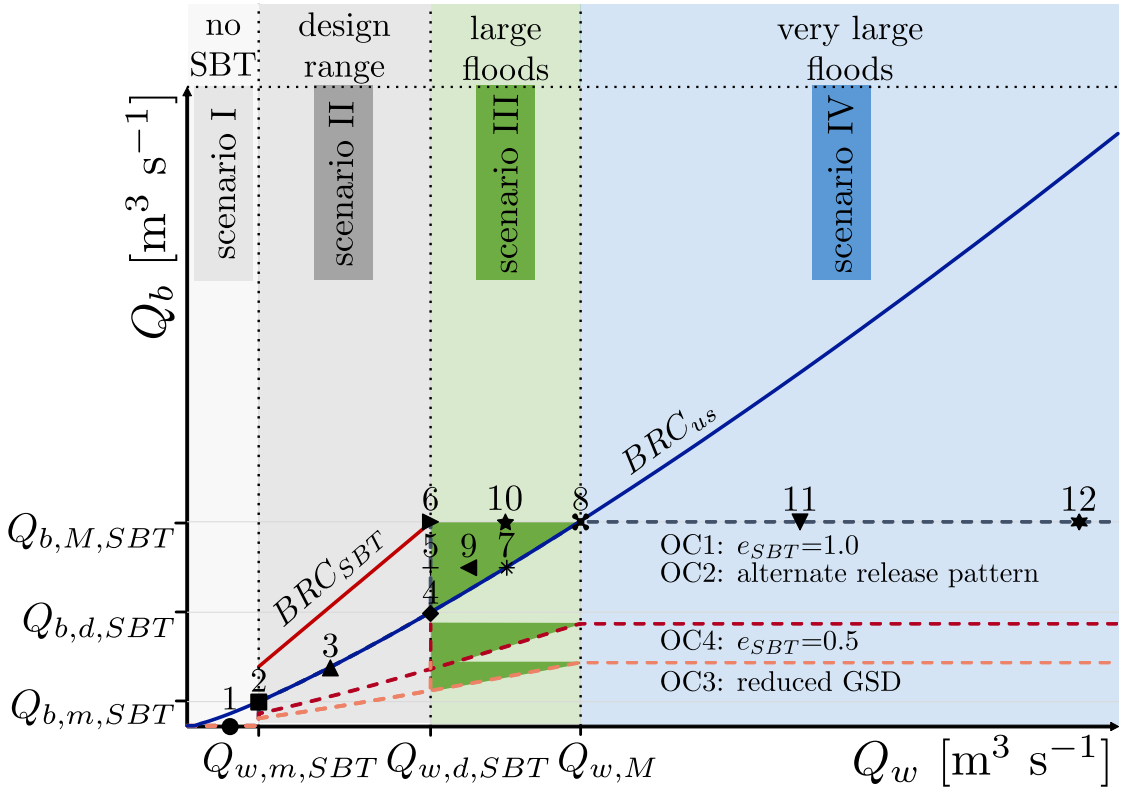

Figure 5.8: SBT release scenarios: Bedload Rating Curves for the upstream reach (BRC_{us}, blue solid line) and for the SBT (BRC_{SBT}, red solid line), Operational Spaces of the SBT (OS_{SBT}) considering SBT bypassing efficiencies e_{SBT} = 1.0 and both continuous and alternate sediment releases (Operational Condition (OC) 1 and 2, gray dashed line), reduced sediment supply GSD (OC3, orange dashed line), and e_{SBT} = 0.5 (OC4, red dashed line). Black symbols represent the values of hydrogrpah and sedimentograph peaks used as input to the numerical runs under OC1 and OC2: to each run a specific symbol is given.

Table 5.1: Q_w and Q_b values used as input for numerical runs with different configurations. Colored row refer to different OCs as defined in Figure 5.8: gray for OC1 and OC2, orange for OC3, and red for OC4. Values relative to OC1 and OC2 are the quantification of black dots in Figure 5.8.

run #	1	2	3	4	5	6	7	8	9	10	11	12
Q_w $[m^3/s]$	30	50	100	170	170	170	223	275	197	222	428	623
Q_b $[m^3/s]$	0	0.23	0.55	1.06	1.49	1.92	1.49	1.92	1.49	1.92	1.92	1.92
Q_b $[m^3/s]$	0	0.07	0.17	0.33	0.46	0.60	0.46	0.60	0.46	0.60	0.60	0.60
Q_b $[m^3/s]$	0	0.12	0.28	0.53	0.74	0.96	0.74	0.96	0.74	0.96	0.96	0.96

The sediment feed is taken to be the bimodal feed of gravel and sand represented by a blue line in Figure 5.7 under OC1, OC2, and OC4, and the one represented by an orange line in Figure 5.7 under OC3. The surface layer composition is (i) the same as the feeding one (blue line in Figure 5.7) for the runs with unarmored initial conditions, and (ii) the static armor GSD (red line in Figure 5.7) for the runs with static armor initial conditions. The substrate size distribution is the same as the feeding GSD under all circumstances (blue line in Figure 5.7). Depending on the active layer GSD the active layer thickness is changing since it is defined as $L_a = 2d_{90}$ (as specified in equation (5.6) on page 96). Details about grain sizes and fractions are given in the Table in Figure 5.7.

Finally, in all numerical simulations, the total length of the domain is 10000 m discretized using 101 cross-sections, so that the distance between each cross-section is 100 m, and the cross-section width is 15 m and it is constant for each run.

5.4 Results

In the following, the morphological effects of bedload-laden and bedload-free water releases to the downstream reach are investigated taking into account different operational conditions (OCs) as defined in Chapter 4. SBTs exert a strong control on water and sediment being released to the downstream reach and have the potential to greatly modify riverbed level and composition both on the short- and on the long-term.

A total of 72 numerical simulations were performed for mobile-bed equilibrium (12 under OC1, OC3, and OC4 and 36 under OC2 to encompass 3 different release patterns

as described in Figure 5.6(b), (c), and (d)) and 144 simulations for the short-term study (12 under OC1, OC3, and OC4 and 36 under OC2 starting both from unarmored initial conditions and from static armor initial conditions).

5.4.1 Mobile-bed equilibrium (long-term effects)

The mobile-bed equilibrium is generally reached after thousands to tens of thousands cycled hydrographs and sedimentographs, depending on the OCs and scenarios. Numerical results at mobile-bed equilibrium are given in Figure 5.9, where a non-dimensional water discharge relative to the SBT design discharge, i.e. $Q_w^* = Q_w/Q_{w,d,SBT}$, is shown on the x-axis in the left and middle panels. The results on the y-axis are presented (i) on the left in terms of non-dimensional riverbed slope $S^* = S/S_{ref}$, where S and S_{ref} are the downstream riverbed slope at mobile-bed equilibrium and the reference riverbed slope, i.e. the one of the upstream reach, respectively; (ii) on the right in terms of non-dimensional geometric mean size of the riverbed surface $d_g^* = d_g/d_{g,f}$, where d_g and $d_{g,f}$ are the geometric mean sizes at mobile-bed equilibrium and of the feeding, respectively. In the right panel, resulting GSD at equilibrium for each run are given. The reference values chosen for d_g^* and S^*, i.e. $d_{g,f}$ and S_{ref}, represent the target values used to evaluate the rehabilitation potential (Dufour and Piégay, 2009) for each SBT operation. In other words, the effectiveness of SBT operations is evaluated in terms of their ability to shift the state of a degraded river reach, such as a dammed river reach, closer to a more natural state, such as the one of the river reach upstream of the reservoir. Moreover, the closer the riverbed surface GSD is to the feeding one (i.e. the closer d_g^* is to 1.0), the less armored the riverbed surface results (Parker and Sutherland, 1990). In fact, bedload and feeding have the same GSD at mobile-bed equilibrium and due to the strong form of equal-mobility described in Parker and Klingeman (1982) and in Parker *et al.* (1982), substrate and bedload can be assumed to have the same GSD as well (Parker and Toro-Escobar, 2002). Therefore, at mobile-bed equilibrium, substrate and feeding have the same GSD and thus the non-dimensional geometric mean size of the riverbed surface d_g^* is a surrogate of the armoring ratio described for instance by Hassan *et al.* (2006).

Results in Figure 5.9 show that when the SBT is not operated (scenario I), if water is released from the dam outlets it causes the equilibrium riverbed slope to be lower

than the reference one (i.e. S^*<1.0) and the riverbed surface to be greatly armored (i.e. d_g^*=6.2). However, a static armor is not present on the riverbed surface at mobile-bed equilibrium, since for static armor d_g^*=10.7. Moreover, irrespective of the OC, there is a high variability of the equilibrium riverbed slope S^* going from scenario II to scenario IV, whereas d_g^* does not show large variations either with increasing Q_w^*, or with changing feeding rate (compare for instance points relative to runs 4, 5, and 6 at different OCs in Figure 5.9).

Effects of SBT operations on riverbed slope

First, S^* shows a common trend among the four different OCs, that is for increasing released Q_w at constant released Q_b (dashed blue lines in the left panel of Figure 5.9) S^* decreases. However, under OC1 (i.e. e_{SBT}=1.0) the slope of the downstream reach is higher than the reference one under all circumstances (i.e. S^*>1.0), while reducing the delivered sediment volume due to either pulsating sediment releases (OC2a, alternate sediment releases), sediment extraction (OC3, GSD_{red}), or reduced bypassing efficiency (OC4, e_{SBT}=0.5) causes a decrease of the equilibrium slopes. On the one hand, there are intense reductions of S^* for very large floods under OC2a and OC4 at mobile-bed equilibrium (e.g. runs 11 and 12 in the middle panel of Figure 5.9), and the reduction of the released sediment volume occurring with pulsating sediment releases (OC2a) or with reduced bypassing efficiency (OC4) produces the same values of S^* at mobile-bed equilibrium regardless of how the released sediment volume is reduced. That is, both under OC2a and OC4 the released sediment volume is reduced by a factor 2 compared to OC1, in the first case by releasing alternate bedload-laden and bedload-free water, in the second case by halving each sedimentograph, and the mobile-bed equilibrium results relative to these OCs are identical. On the other hand, if the volume reduction is combined with the selective extraction of the coarser grains, the equilibrium slope will always be less than half of the reference one, i.e. $S \leq 0.5\, S_{ref}$.

Effects of SBT operations on riverbed composition

Second, the general trend of the results concerning the riverbed surface composition at equilibrium does not change much with changing OC. In fact, the armoring degree

for scenarios II, III, and IV is always lower than 2.0, except for run 2 under OC2a and OC4, for which d_g^* is slightly larger than 2.0 (see the middle panel of Figure 5.9). Differently from the results relative to the riverbed slope presented before, there are small differences that are noticeable when comparing OC2a and OC4. These are due to the fact that the results are plotted for OC2a at the end of a release of bedload-free water and for OC4 at the end of a release of bedload-laden water. In the case of OC3, the armoring degree is almost 1.0 under all circumstances, meaning that at mobile-bed equilibrium, if only fine material is fed to the channel, nearly unarmored conditions are reached. That is, the GSD of the riverbed surface at the equilibrium results to be almost the same as the one of the feeding, which has d_g=1.08 mm. This value, representative of the equilibrium GSDs in the bottom-right panel of Figure 5.9, is typical of sand-bed rivers (e.g Shaw and Kellerhals, 1982), same as the resulting slopes. Therefore, these results suggest that if the feeding is deprived of most of its gravel-mode and mostly sand is fed to the downstream channel, this becomes a sand-bed river (e.g. Goudie, 2004). Note that the physical model used to describe sediment transport is not ideal for describing the transport of GSD without gravel-mode, where suspension might be dominant. In fact, no transport in suspension is taken into account since the focus of this work is to study the effect of SBT operations on bedload-dominated rivers. Moreover, while it is true that the Wilcock and Crowe (2003) formula takes into account the effect of sand on the transport of gravel, it cannot describe transport in suspension. Therefore, results relative to OC3 are used to comment on what is the effect of SBT operations of very fine material, and point out the dramatic change of riverbed slope and GSD they can cause.

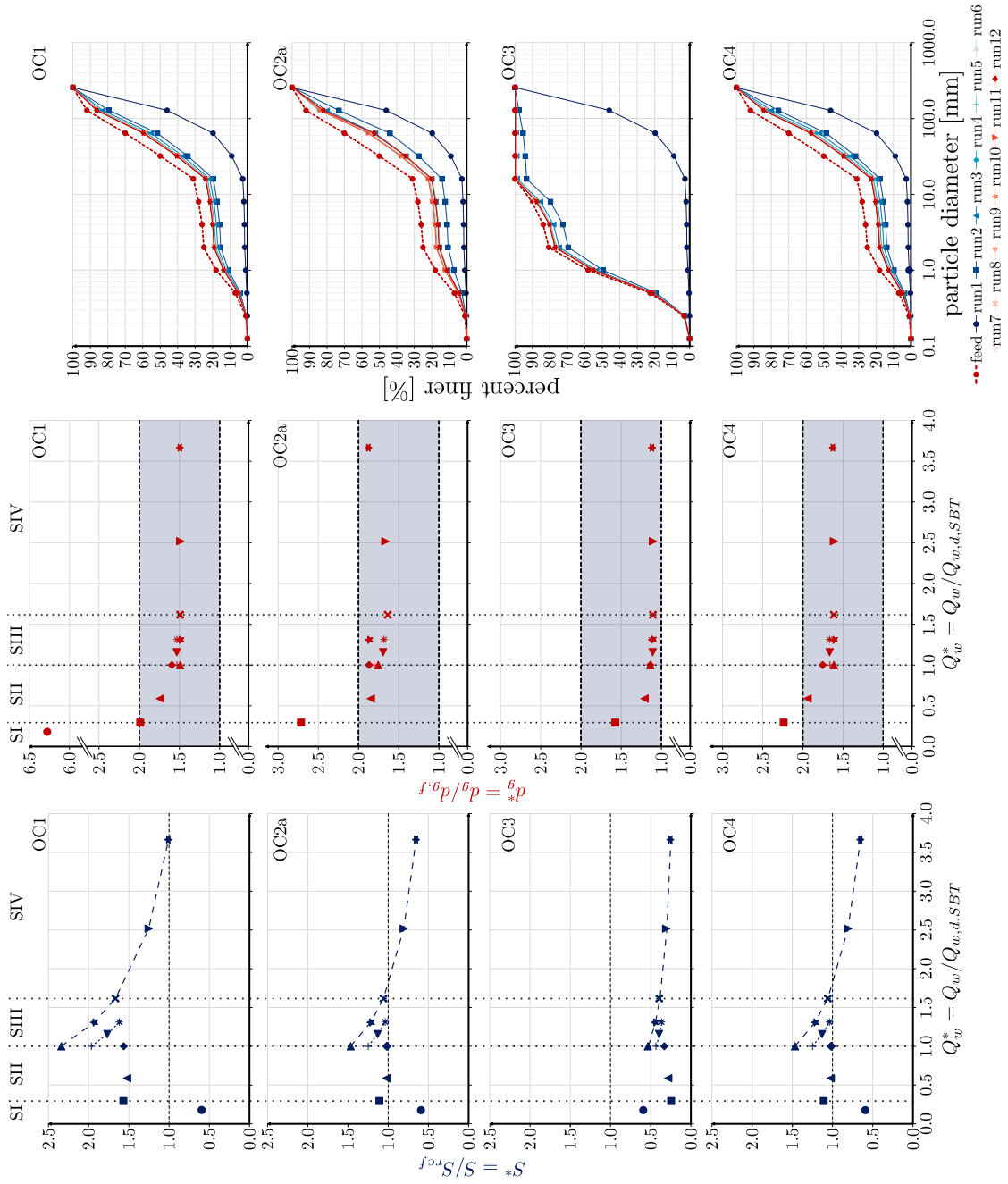

Figure 5.9: Non-dimensional riverbed slope (left) and composition (middle) at mobile-bed equilibrium considering four different SBT operational conditions, i.e. OC1, OC2a, OC3, and OC4, plotted against a non-dimensional water discharge relative to the SBT design discharge, i.e. $Q_w^* = Q_w/Q_{w,d,SBT}$. Dotted lines separate different scenarios and in the left panel dashed lines connect results concerning runs with the same bedload release rate. On the right, GSD curves for each run under different OCs are presented.

Effects of SBT operations on hydrograph boundary layer formation and length

A SBT acts as a boundary condition to the downstream reach, forcing water and sediment feed rates to fluctuate depending on how the SBT is operated. Therefore, the mobile-bed equilibrium developed after sustaining certain SBT OCs for a sufficient amount of time is a fluctuating equilibrium, which consists of a state in which the same cycle is repeated over and over, i.e. the bed degrades and coarsens at high flow stages and aggrades and becomes finer at the low flow stages. This behavior is realized only in a relatively short region, i.e. a *Hydrograph Boundary Layer (HBL)* (e.g. Parker *et al.*, 2007), downstream of the feed point. Downstream of the HBL, the cycling is transferred to the bedload transport rate and GSD (Parker *et al.*, 2007). The results of the one-dimensional numerical study presented by Parker *et al.* (2007) are also confirmed with laboratory experiment by Wong and Parker (2006). More recent studies by An *et al.* (2017b,a) confirm the observations that a HBL is forming if the water discharge is fluctuating and the sediment feed rate is kept constant. Moreover, An *et al.* (2017a) infer that the idea of a HBL breaks down due to the presence of low-amplitude perturbations of the riverbed level and composition, i.e. sorting waves (e.g. Stecca *et al.*, 2014), if the released sediments are poorly sorted. Eventually, if sediment is supplied in form of sediment pulses somewhere downstream of the feeding point in addition to a constant sediment feed from upstream, a *Sedimentograph Boundary Layer (SBL)* might form as well (An *et al.*, 2017b). Results presented in Figures 5.10 to 5.12 confirm the existence of a region where riverbed level and composition cycle in time due to the nonstationarity of the water discharge released by the SBT. Results concerning the maximum and minimum amplitudes of the HBL related to different release scenarios and bedload-free water releases (i.e. under OC1, OC2a, b, and c) are presented in Figure 5.10, where a non-dimensional water discharge relative to the SBT design discharge, i.e. $Q_w^* = Q_w/Q_{w,d,SBT}$, is shown on the x-axis. On the y-axis, the results are presented in terms of the ratio of the amplitude of the HBL A_{HBL} to the d_{90}. Red empty symbols in Figure 5.10 refer to the maximum amplitude due to erosion, while blue symbols refer to the maximum amplitude due to deposition. Under OC1 the amplitude of the fluctuations of the riverbed level inside the HBL reagion is smaller than the d_{90}, while for OC2a, b, and c it is always larger than 7.5 times the d_{90}. Moreover, the more bedload-free water

is released between two bedload-laden water releases (i.e. OC2c), the larger the HBL amplitude is.

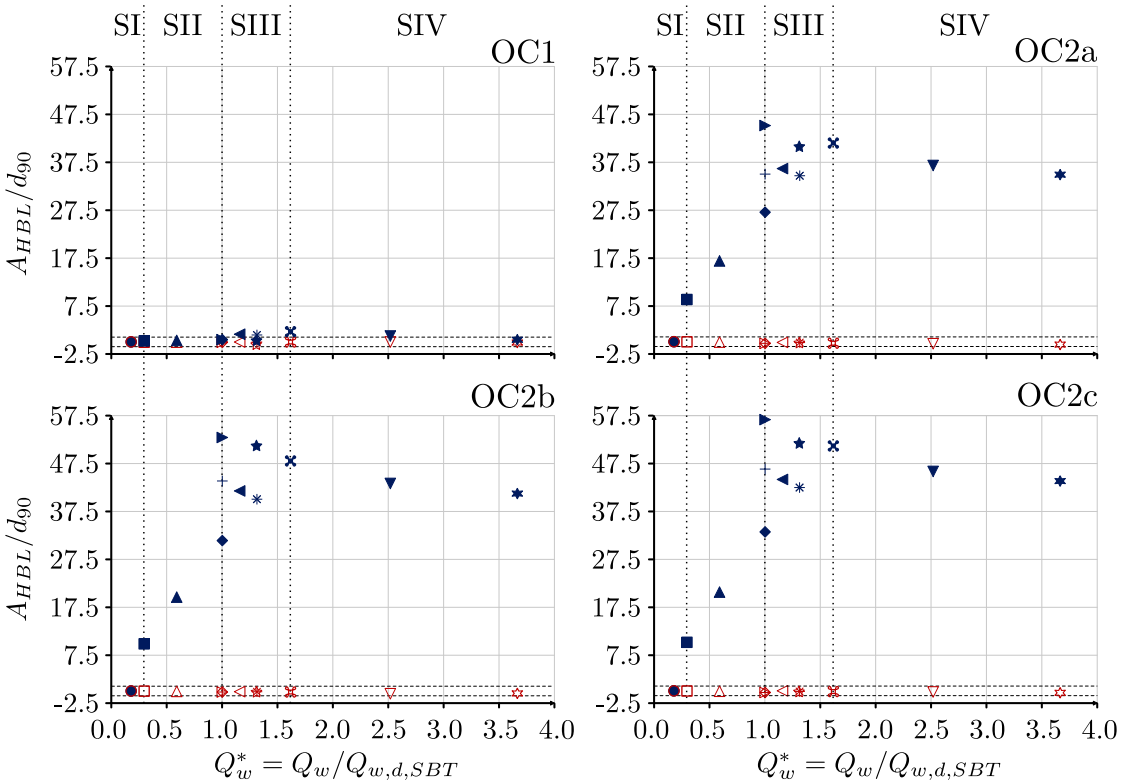

Figure 5.10: Non-dimensional HBL amplitudes at mobile-bed equilibrium considering four different SBT operational conditions, i.e. OC1, OC2a, OC2b, and OC2c, plotted against a non-dimensional water discharge relative to the SBT design discharge, i.e. $Q_w^* = Q_w/Q_{w,d,SBT}$. Red empty symbols are relative to the minimum elevation difference (i.e. to the maximum erosion), blue symbols are relative to the maximum elevation difference (i.e. to the maximum deposition).

The main cause of the large aggradation occurring during alternate bedload-laden – bedload-free water releases (i.e. under OC2a, b, and c) is the discrepancy between the transport capacity and the feeding rate (Parker *et al.*, 2007). That is, the riverbed undergoes erosion and coarsening when the transport capacity due to the water discharge is larger than the constant sediment feed rate, while it undergoes aggradation and fining when the transport capacity is smaller than the feed rate. This effect is evaluated over a single release pattern, i.e. over one SBT operation under OC1, and over two, three, and four SBT operations under OC2a, b, and c, respectively. Under OC1, the same

volume of sediment is released at each SBT operation. On the contrary, under OC2a, b, and c, the sediment volume relative to the transport capacity is greater than the released one. Therefore, under OC2, the riverbed aggrades during the releases of sediment-laden water, and the aggraded material is transported downstream during the following clear-water releases, going back to the equilibrium state at the end of each release pattern. The presence of a HBL under OC1 and the magnitude of riverbed level oscillations can be assessed analyzing the trends of the deviatoric riverbed level (elevation difference) $\Delta\eta$ and of the derivative of $\Delta\eta$ in the longitudinal direction x given in Figure 5.11. Here, the trends of the elevation difference and its derivative in the longitudinal direction x (Figure 5.11(a)) and the discrepancy between the transport capacity and the sediment feed (Figure 5.11(b)) are given. The elevation difference is calculated as follows

$$\Delta\eta(x,t) = \eta\left(x, n_{op} > 10^4\right) - \eta\left(x, t = 0\ s\right) \tag{5.31}$$

where n_{op} is the number of SBT operations. In Figure 5.11(a), two different thresholds are defined, one for $\Delta\eta$ and one for $\partial\Delta\eta/\partial x$, to detect significant riverbed level and small-amplitude oscillations, respectively. For the elevation difference $\Delta\eta$, the d_{90} is considered as the threshold value, while for $\partial\Delta\eta/\partial x$ the 5% of its maximum value is used as threshold. Results in Figure 5.11(a) show that oscillations of the elevation difference $\Delta\eta$ do not exceed the threshold, while $\partial\Delta\eta/\partial x$ does. Therefore, a surrogate of the HBL related to small-amplitude perturbations can be defined. In this case, oscillations are mainly due to the fact that the transport capacity does not vary in parallel with the water discharge. That is, the trapezoidal sedimentographs fed to the domain are not distributed in time as the transport capacity caused by the hydrographs. The different time distribution of sediment transport is represented in Figure 5.11(b), where the feed rate and the transport capacity in the first cross-section during a single SBT-operation are represented with a red dashed and solid line, respectively.

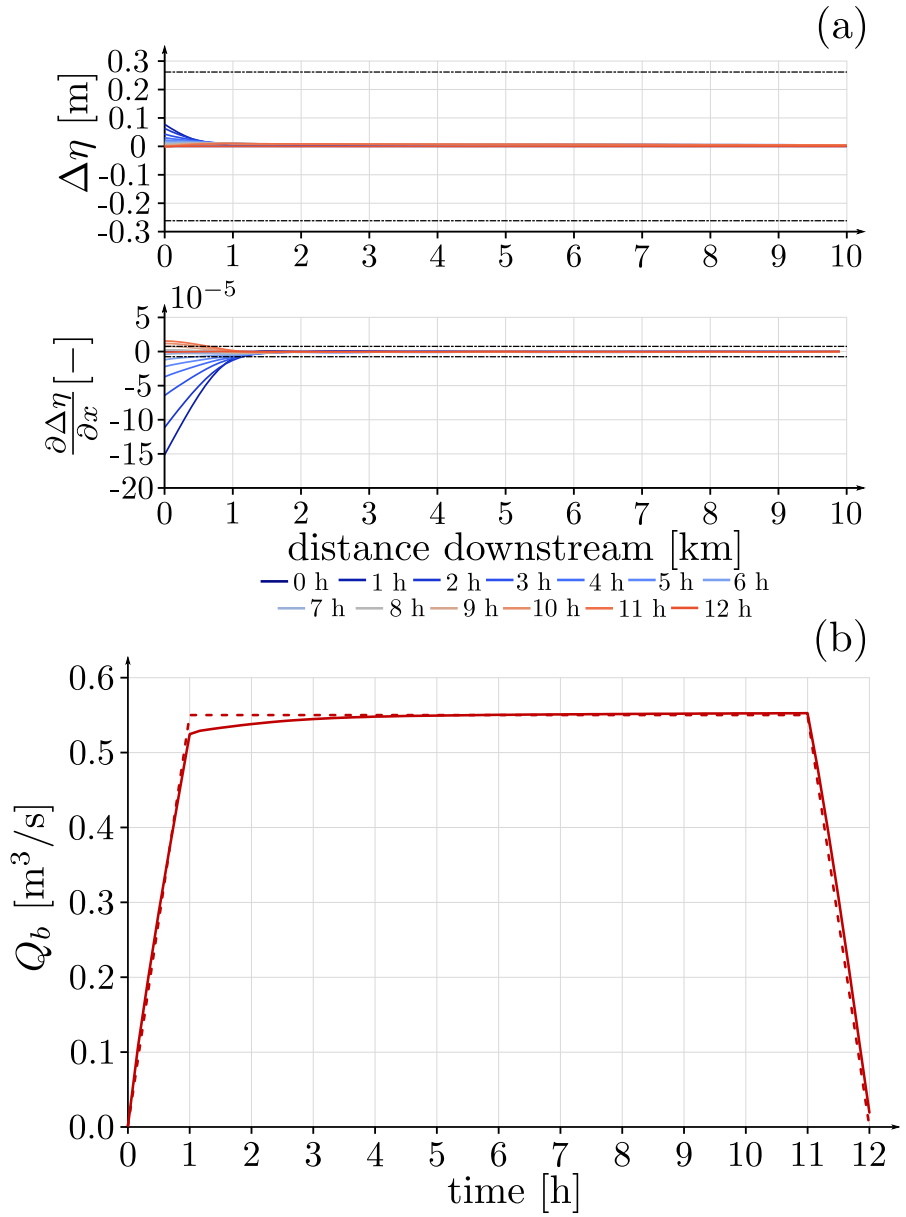

Figure 5.11: (a) Oscillation of the riverbed level due to low-amplitude riverbed perturbations: in the upper panel the threshold is the d_{90} (i.e. half of the active layer thickness L_a) of the riverbed GSD averaged over the hydrograph and over the cross-sections, while in the lower panel the threshold is 5% of the maximum value of the derivative of the elevation difference to x. (b) Discrepancy between the time distribution of the sediment feeding rate (red dashed line) and sediment transport capacity at the first cross-section during a SBT-operation after mobile-bed equilibrium has been reached (red solid line).

Results concerning the length of the HBL for runs under OC1 and OC2a, b and c are presented in Figure 5.12, where a non-dimensional water discharge relative to the SBT design discharge, i.e. $Q_w^* = Q_w/Q_{w,d,SBT}$, is shown on the x-axis. On the y-axis, the results are presented in terms of the ratio of the length of the HBL L_{HBL} to the total length of the domain L_{tot}. Results in Figure 5.12 show that significant perturbations of the riverbed level developing under OC2a, b, and c shaping the HBL are always confined in the first 1.5 to 2.0 km, regardless of the release pattern and the more water is released, the longer the HBL results, while the increases of sediment feeding rate do not play a major role. Differently, a short HBL is forming under OC1 only for few runs belonging to scenario III.

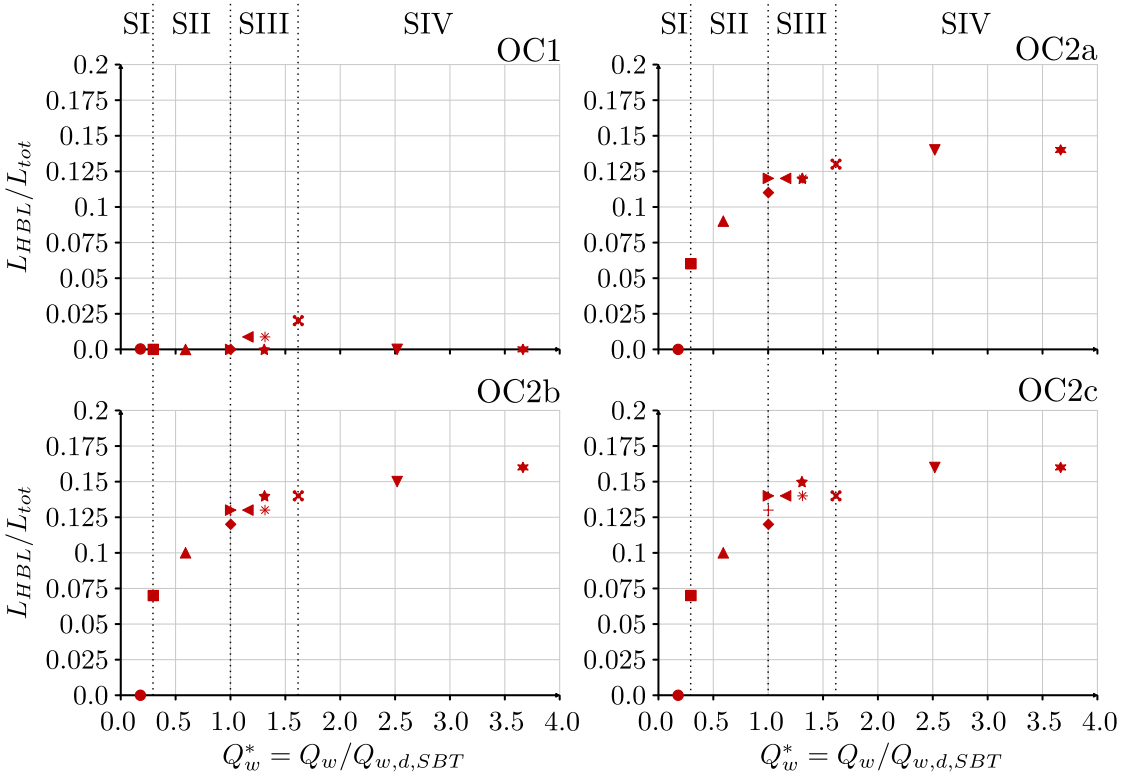

Figure 5.12: Non-dimensional HBL lengths at mobile-bed equilibrium considering four different SBT operational conditions, i.e. OC1, OC2a, OC2b, and OC2c, plotted against a non-dimensional water discharge relative to the SBT design discharge, i.e. $Q_w^* = Q_w/Q_{w,d,SBT}$. Red symbols are relative to the length of the HBL calculated considering the d_{90} as the threshold for the elevation difference.

Summary of results at mobile-bed equilibrium

To summarize, there are common trends in riverbed slope and GSD changes caused by different SBT-release scenarios under different operational conditions (OCs). However, all else being equal, a reduction of the released sediment volume causes major changes to the equilibrium riverbed slope, whereas the armoring degree of the riverbed is less affected. Nevertheless, if the reduction of the released sediment volume is combined with an extraction of the coarser grains from the material being conveyed by the SBT, major changes in the riverbed GSD are noticeable, i.e. a dramatic fining occurs (right panel of Figure 5.9). A mobile-bed equilibrium developed under the superimposition of fluctuating water discharges does not consist of a constant state, but of a state in which exactly the same cycle is repeated over and over. This brings to the formation of a hydrograph boundary layer, the significance of which depends on the discrepancy between sediment feed and transport capacity. If water and sediment are released in parallel (OC1), the perturbations defining the HBL have similar magnitudes as low-amplitude riverbed perturbations, i.e. sorting waves. On the contrary, if bedload material is released every other, two or three bedload-free water releases (OC2a, b, and c, respectively), riverbed fluctuations in the HBL become larger due to the larger distance between the sediment feed and the transport capacity.

5.4.2 Short-term effects of SBT operations

Except for a couple of cases, SBTs are operational less than 10 times per year (e.g. Sumi, 2017), i.e. the mobile-bed equilibrium in rivers subject to SBT operations would be reached after hundreds to thousands of years. While this is a useful benchmark for understanding the morphological trajectory followed by a river approaching equilibrium, effects on a shorter-term, i.e. on an engineering or human time-scale, are of interest to understand how the river reacts to SBT-related disturbances on a short-term and how it reaches mobile-bed equilibrium (Buffington, 2012). Furthermore, on the short-term, the effects of the initial conditions can be appreciated, while at mobile-bed equilibrium they do not play any role. In this section, it is first discussed how far from the equilibrium state riverbed level and composition are after 50 SBT operations under

different OCs. Second, the pulses-like behavior of SBT-released sediment is discussed, for sediment material introduced to the downstream reach during sediment-laden water releases at event-scale under each OC. Eventually, the effect of the initial composition of the riverbed is discussed with a focus on how the disturbances of the riverbed composition propagate downstream.

Evolution of riverbed level and composition under different OCs

Numerical results after 50 SBT operations under OC1 starting from an unarmored riverbed surface (i.e. the GSD of the riverbed surface is the same as the one of the substrate and of the feeding) are given in Figure 5.13, where a non-dimensional water discharge relative to the SBT design discharge, i.e. $Q_w^* = Q_w/Q_{w,d,SBT}$, is shown on the x-axis. OC1 is chosen here as a reference and results concerning other OCs will be compared with the ones relative to OC1 in the following. The effect of the initial composition of the riverbed will be discussed in the next section. The results on the y-axis are presented (i) in the left panel in terms of non-dimensional deviatoric riverbed level variations $\Delta\eta/\Delta\eta_{eq}$, i.e. the ratio of the elevation difference $\Delta\eta$ after 50 SBT operations (n_{op} = 50) defined as

$$\Delta\eta(x,t) = \eta(x = x^*, n_{op} = 50) - \eta\,(x = x^*, t = 0\ s) \tag{5.32}$$

where x^* is the downstream distance at the selected locations, to the equilibrium one defined as in equation (5.31); (ii) in the right panel, in terms of non-dimensional geometric mean grain size of the active layer, i.e. the ratio of the mean grain size of the active layer d_g after 50 SBT operations to the equilibrium one $d_{g,eq}$. In the left panel, positive values (scenarios II, III, and IV) are relative to a depositional equilibrium ($S^* > 0$ in Figure 5.9), while negative values (scenario I) are relative to an erosional equilibrium ($S^* < 0$ in Figure 5.9). In Figure 5.13, results are relative to four different cross-sections that are 0.2 km, 1 km, 5 km, and 10 km downstream of the upstream end.

Results in Figure 5.13 show that the riverbed level (left panel in Figure 5.13) evolves towards mobile-bed equilibrium more slowly than the riverbed composition (right panel in Figure 5.13). In fact, the ratio of riverbed level to the equilibrium one is below 0.5

under all circumstances, while the active layer composition is closer to the equilibrium one, with values of the ratio of $d_g/d_{g,eq}$ being larger than 0.8 in most of the cases. Moreover, from the diagrams in Figure 5.13, the effect of the distance from the upstream end can be observed, which is evident for both riverbed level and composition, being both farther from equilibrium with increasing distance from the upstream end (going from the top to the bottom panels in Figure 5.13). However, for scenario IV this reduction is smaller than for other scenarios. This is most likely due to the fact that in this case more water is released from the dam and the SBT to the downstream reach, which accelerates morphological changes.

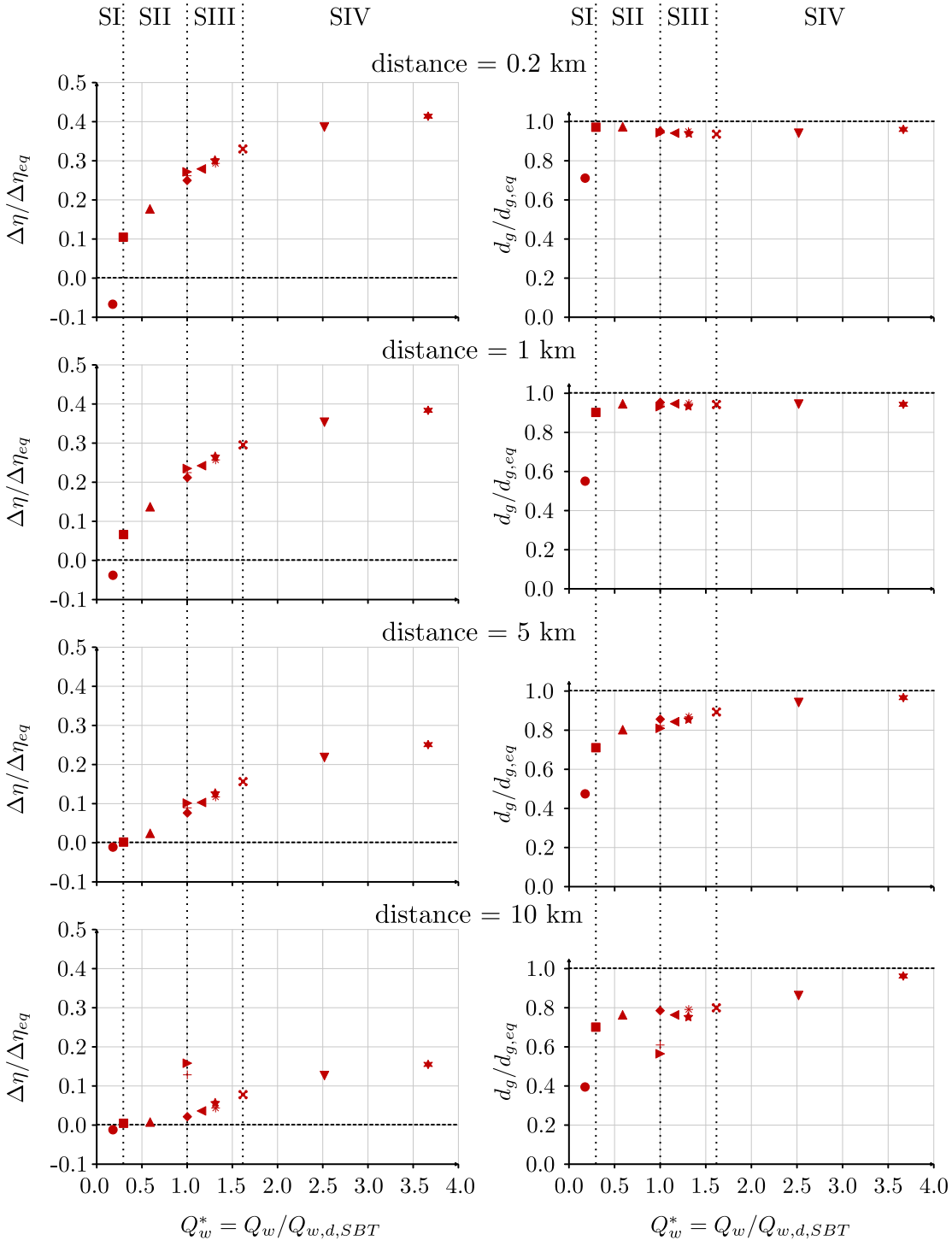

Figure 5.13: Non-dimensional deviatoric riverbed level variations $\Delta\eta/\Delta\eta_{eq}$ and geometric mean size $d_g/d_{g,eq}$ plotted against a non-dimensional water discharge relative to the SBT design discharge, i.e. $Q_w^* = Q_w/Q_{w,d,SBT}$. Plots are relative to all runs under OC1 and unarmored initial conditions at different cross-sections along the modeled reach.

It is hypothesized that the evolution trends of riverbed level and composition should not change with changing OCs. This hypothesis is tested running the same numerical simulations already presented but under different OCs. The results of these simulations are presented in Figures 5.14, 5.15, and 5.17, where results relative to OC4, OC2a, and OC3, respectively, are represented by blue empty symbols and results relative to OC1 are represented by red full symbols. Results concerning riverbed level generally confirm the assumption made. However, while the trend towards the equilibrium configuration is similar under different OCs in all scenarios, the equilibrium itself might be different. That is, with reduced feeding GSD (OC3) or reduced released sediment volume (OC2a and OC4) the river might evolve towards an erosional equilibrium (see Figure 5.9). For example, under OC2a, runs 11 and 12 (represented by a downward-pointing triangle and a six-pointed star, respectively) reach an equilibrium slope which is lower than the reference one, while their counterpart under OC1 reach a slope which is almost the same as the reference one (see Figure 5.9). However, results presented in Figures 5.14, 5.15, and 5.17 show that under different OCs, the domain approaches the equilibrium in a similar way. That is, the riverbed level evolves slower than the riverbed composition, and the distance from the mobile-bed equilibrium of $\Delta\eta$ and d_g after 50 SBT operations is more or less similar regardless of the OC. This holds particularly for results relative to scenario IV, where the morphodynamics is faster due to large released water discharges. Concerning $d_g/d_{g,eq}$, results in Figure 5.14 show that far from the upstream end, a reduced released volume of sediments combined with continuous bedload-laden water releases (OC4) produces values of $d_g/d_{g,eq}$ that are closer to the equilibrium, i.e. to mobile-armor conditions. Everywhere else in the domain, the volume of released sediments does not affect $d_g/d_{g,eq}$ much. OC2a and OC4 show similar values of S^* and d_g^* at mobile-bed equilibrium (see Figure 5.9), i.e. regardless of the way the released sediment volume is reduced, riverbed slope and composition result to be similar. This does not hold completely for results after 50 SBT operations, mainly due to the fact that under OC2a both riverbed level and composition are fluctuating due to alternate bedload-laden and bedload-free water releases. The equilibrium results for OC2a relative to the riverbed level and composition configurations after a bedload-laden water release is presented in Figure 5.15. Results relative to the end of

a bedload-free water release divided by the relative equilibrium state are presented in Figure 5.16 where the riverbed level and the riverbed composition are farther from the equilibrium as compared to their counterparts in Figure 5.15.

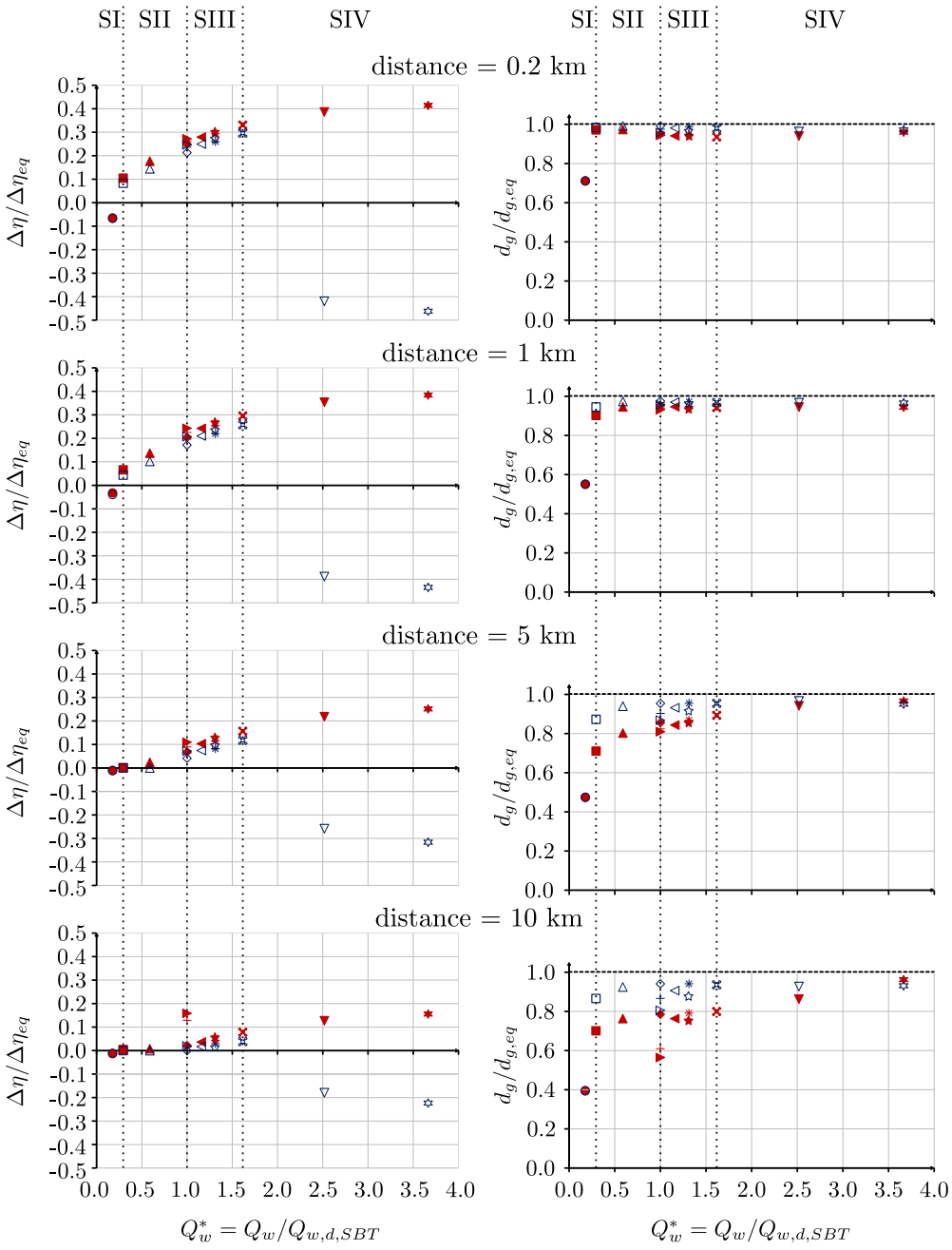

Figure 5.14: Non-dimensional deviatoric riverbed level variations $\Delta\eta/\Delta\eta_{eq}$ and geometric mean size $d_g/d_{g,eq}$ plotted against a non-dimensional water discharge relative to the SBT design discharge, i.e. $Q_w^* = Q_w/Q_{w,d,SBT}$. Results refer to different cross-sections along the modeled reach. Blue empty symbols refer to runs under OC4, red symbols refer to runs under OC1, both starting from unarmored initial conditions. Positive and negative values of $\Delta\eta/\Delta\eta_{eq}$ indicate that mobile-bed equilibrium is depositional or erosional, respectively.

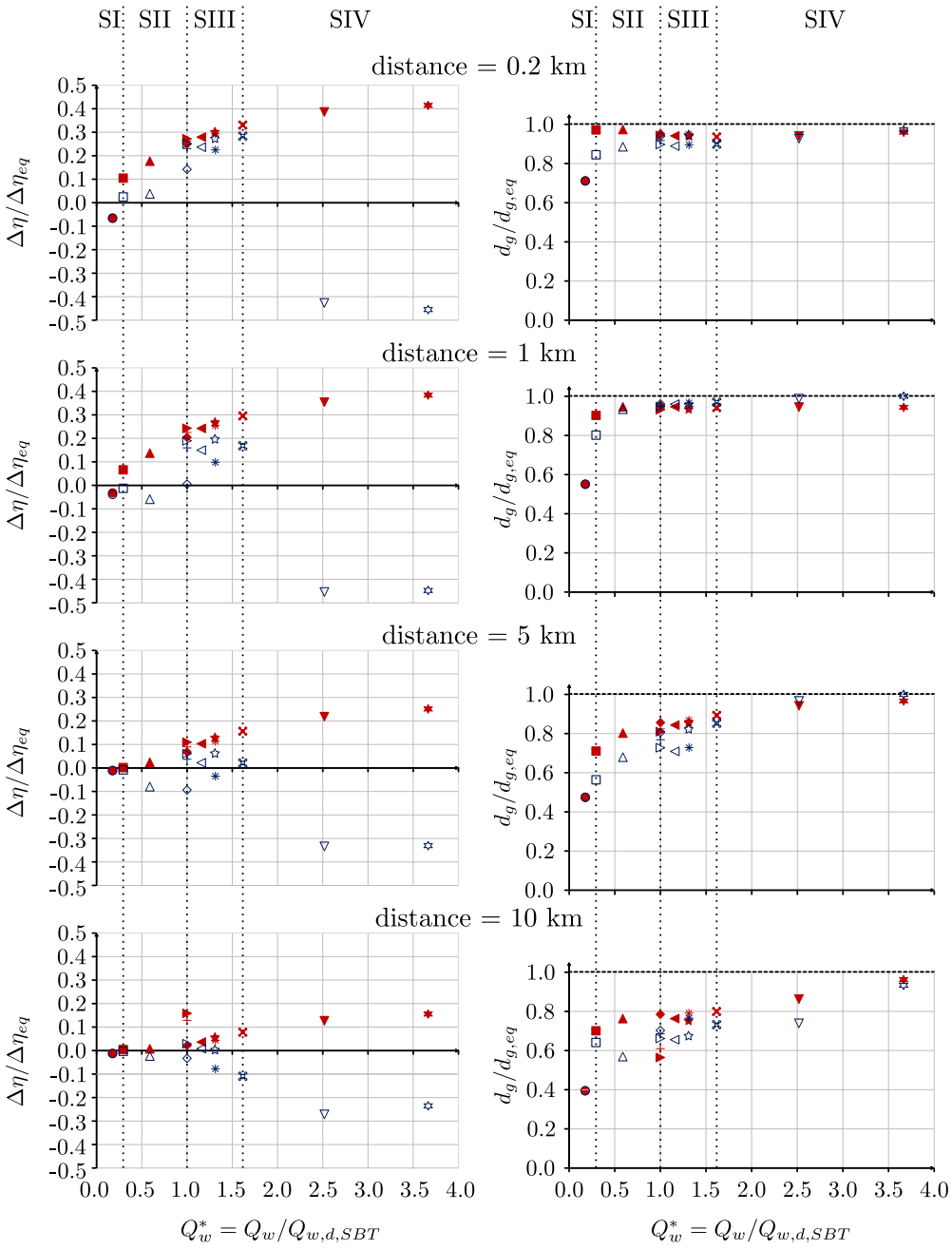

Figure 5.15: Non-dimensional deviatoric riverbed level variations $\Delta\eta/\Delta\eta_{eq}$ and geometric mean size $d_g/d_{g,eq}$ plotted against a non-dimensional water discharge relative to the SBT design discharge, i.e. $Q_w^* = Q_w/Q_{w,d,SBT}$. Results refer to different cross-sections along the modeled reach. Blue empty symbols refer to runs under OC2a after a release of bedload-laden water, red symbols refer to runs under OC1, both starting from unarmored initial conditions. Positive and negative values of $\Delta\eta/\Delta\eta_{eq}$ indicate that mobile-bed equilibrium is depositional or erosional, respectively.

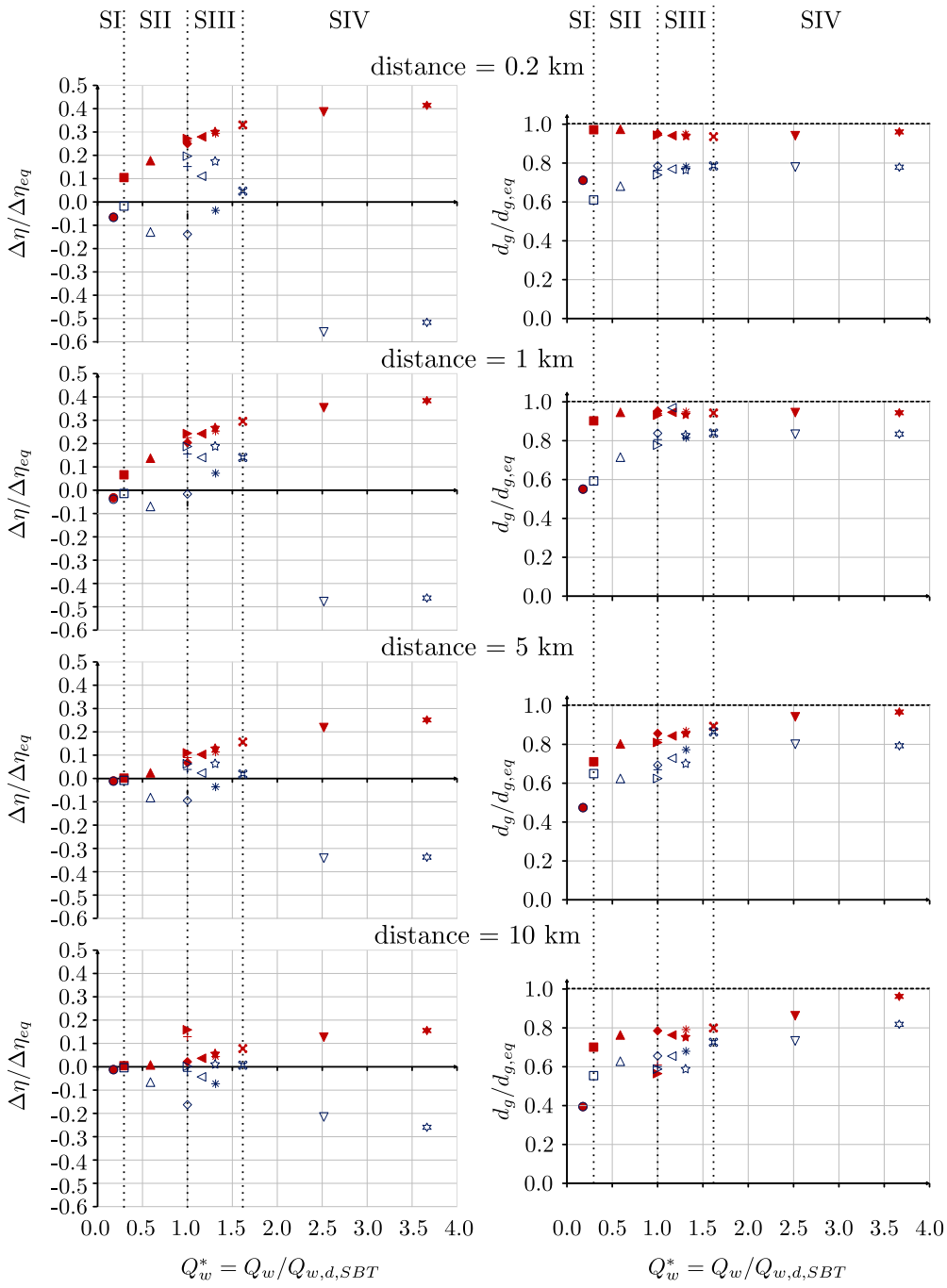

Figure 5.16: Non-dimensional deviatoric riverbed level variations $\Delta\eta/\Delta\eta_{eq}$ and geometric mean size $d_g/d_{g,eq}$ plotted against a non-dimensional water discharge relative to the SBT design discharge, i.e. $Q_w^* = Q_w/Q_{w,d,SBT}$. Results refer to different cross-sections along the modeled reach. Blue empty symbols refer to runs under OC2a after a water release, red symbols refer to runs under OC1, both starting from unarmored initial conditions. Positive and negative values of $\Delta\eta/\Delta\eta_{eq}$ indicate that mobile-bed equilibrium is depositional or erosional, respectively.

Results in Figure 5.17 show that under OC3, $d_g/d_{g,eq}$ behaves differently than under OC1, OC2, or OC4, because of the absence of the coarsest grains in the feeding GSD. As a consequence, the initial riverbed composition is much coarser than the equilibrium one and the values of $d_g/d_{g,eq}$ are still far from 1 after 50 SBT operations, especially for scenarios II and III where the magnitude of the released water discharge is small, and for cross-sections that are far from the upstream end (see Figure 5.17). That is, the change in the riverbed surface composition is traveling more slowly under OC3 than under OC1, OC2 and OC4. This might be both due the fact that (i) the initial condition is more far from the equilibrium (initial $d_g/d_{g,eq}$ is ca. 13 under OC3, and ca. 0.5 under OC1 and OC2), and that (ii) coarse particles present on the riverbed surface at the beginning are more difficult to entrain and transport and therefore are slowly substituted by fines, which compose the greatest part of the equilibrium GSD under OC3.

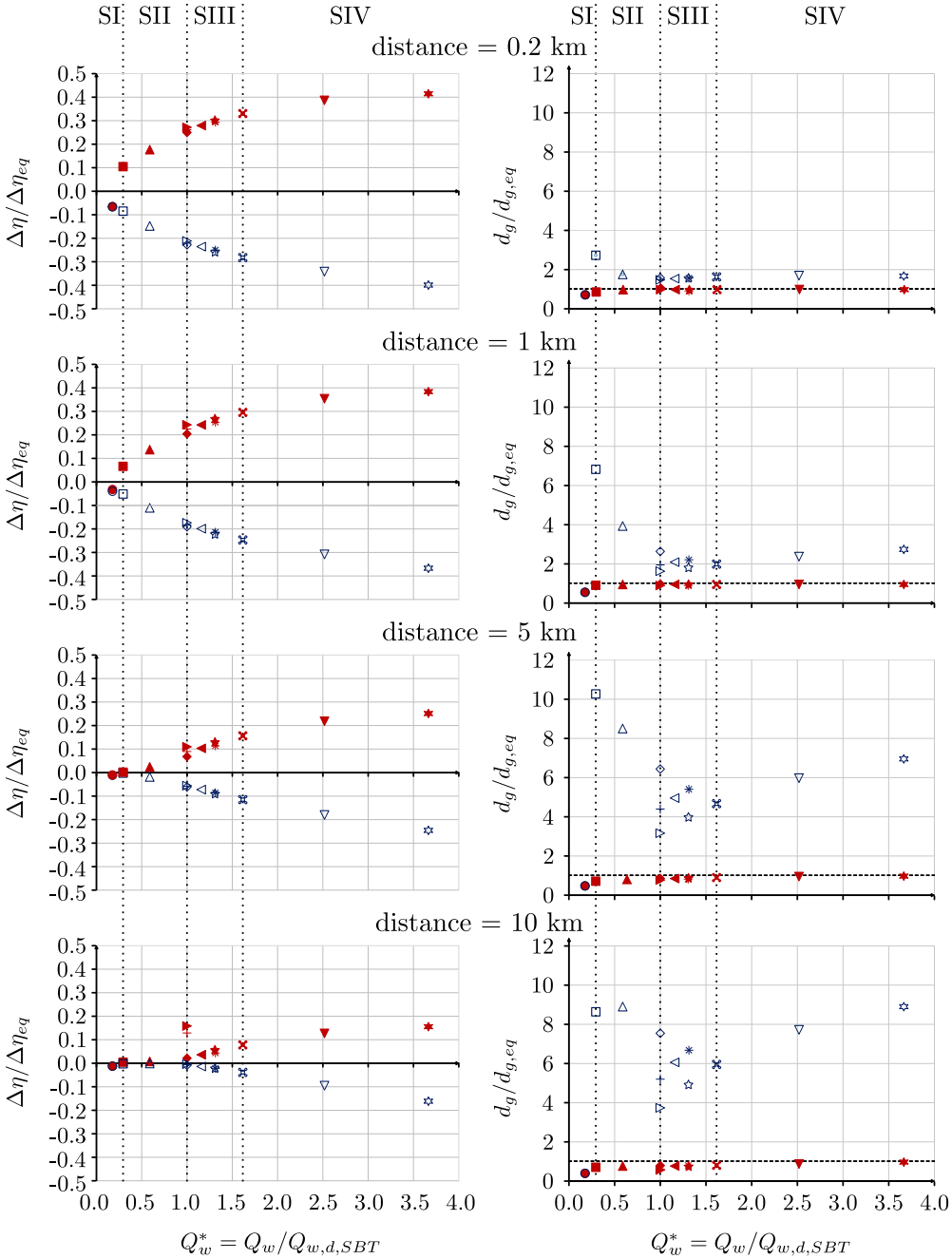

Figure 5.17: Non-dimensional deviatoric riverbed level variations $\Delta\eta/\Delta\eta_{eq}$ and geometric mean size $d_g/d_{g,eq}$ plotted against a non-dimensional water discharge relative to the SBT design discharge, i.e. $Q_w^* = Q_w/Q_{w,d,SBT}$. Results refer to different cross-sections along the modeled reach. Blue empty symbols refer to runs under OC3, red symbols refer to runs under OC1, both starting from unarmored initial conditions. Positive and negative values of $\Delta\eta/\Delta\eta_{eq}$ indicate that mobile-bed equilibrium is depositional or erosional, respectively.

Memory of the initial conditions

From the results presented in the previous section, it seems that after 50 SBT operations the riverbed composition does not depend on the initial conditions anymore since the active layer has already been almost completely reworked (i.e. its GSD has changed dramatically) and its composition is already very close to the mobile-bed equilibrium. To study the effect of the initial conditions, the same numerical simulations discussed before have been run, but starting from a very coarse riverbed surface (a static armored layer defined as described in section 5.1.4). Results in Figure 5.18 prove that after 50 SBT operations (events) riverbed level and composition do not depend on the initial riverbed composition anymore, which confirms the hypothesis about the memory of initial conditions.

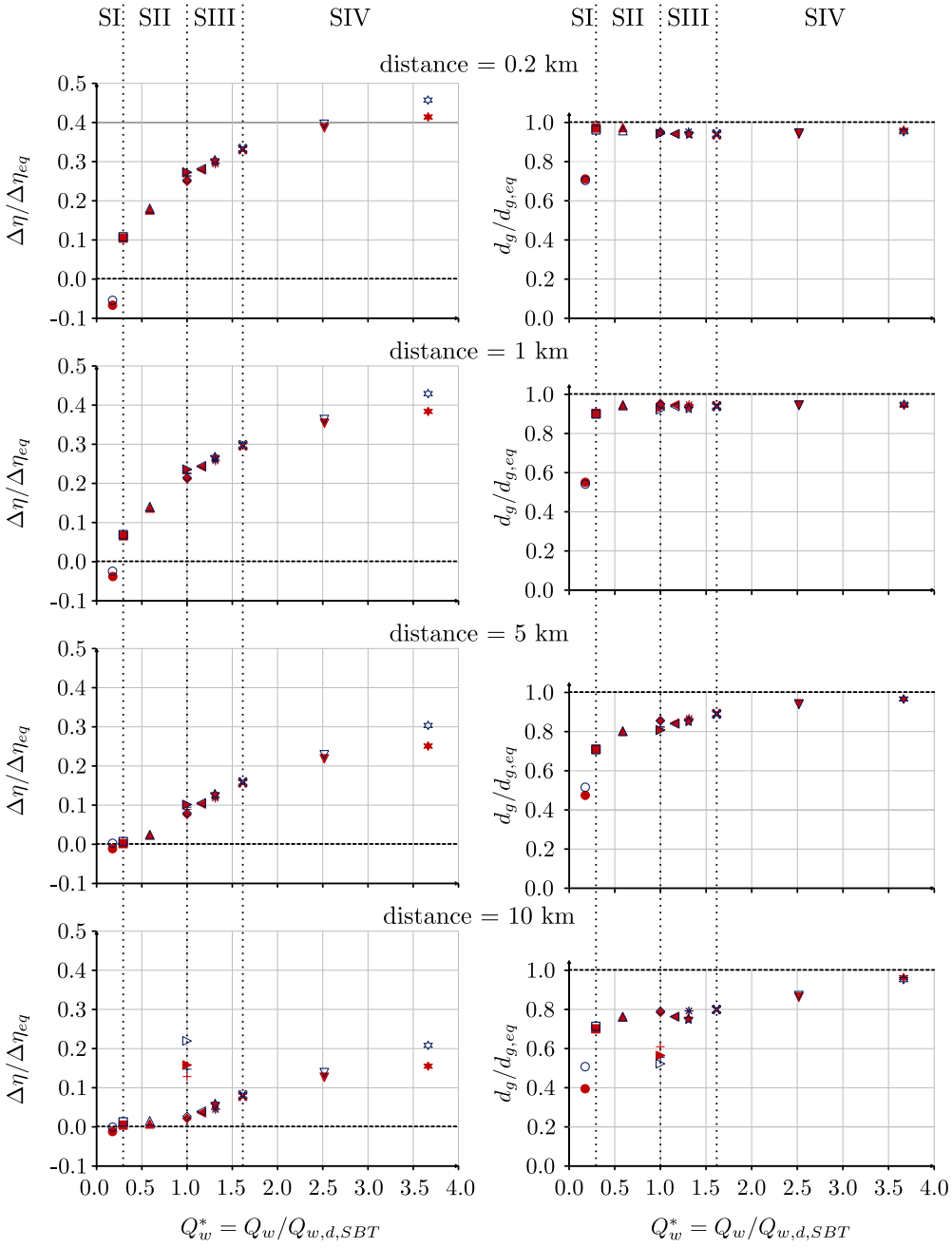

Figure 5.18: Non-dimensional deviatoric riverbed level variations $\Delta\eta/\Delta\eta_{eq}$ and geometric mean size $d_g/d_{g,eq}$ plotted against a non-dimensional water discharge relative to the SBT design discharge, i.e. $Q_w^* = Q_w/Q_{w,d,SBT}$. Results refer to different cross-sections along the modeled reach. Blue empty symbols refer to runs starting from a static armored surface, red symbols refer to runs starting from an unarmored surface, both under OC1.

To understand how long the initial conditions are affecting the GSD of the riverbed, the effects of the first few SBT operations starting from different initial conditions is studied. Results presented in Figure 5.19 show the evolution of the riverbed GSD during the first five SBT operations for three runs (3, 7, and 11) belonging to three different release scenarios (II, III, and IV, respectively) under OC1 starting from different initial conditions. Results are presented for four different cross-sections that are 0.2 km, 1 km, 5 km, and 10 km downstream of the inlet. In Figure 5.19, GSD trends are analyzed using three main indexes: the surface sizes d_{16} and d_{84} such that 16% and 84% of the sediment is finer, respectively, and the surface geometric mean size d_g. These indicate the trends of the fine part, of the coarse part, and the general trend of the active layer GSD, respectively. Initial conditions have a great impact on results on a very short time scale. That is, after a short initial phase (lasting less than five SBT operations) in which coarse sediment are transported downstream, the GSD oscillations in the static armor case (middle panel in Figure 5.19) resemble the ones in the unarmored one (left panel in Figure 5.19).

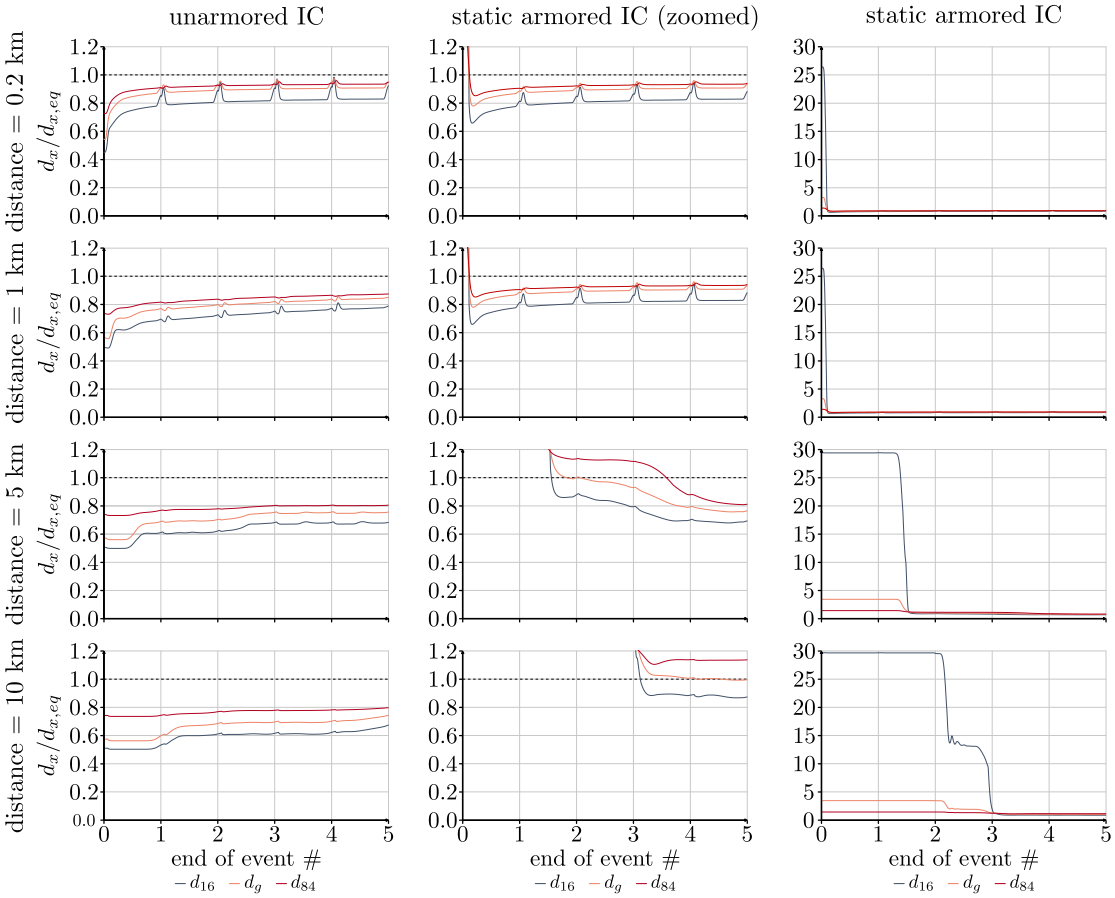

Figure 5.19: Non-dimensional diameter ratios ($d_x/d_{x,eq}$) relative to the sizes of the riverbed surface GSD such that 16% (blue-gray line) and 84% (red line) of the sediment is finer (d_{16} and d_{84}, respectively), and geometric mean size d_g of the riverbed surface GSD (pink-orange line), plotted against the SBT operation number. Plots are relative to run 3, scenario II, under OC1 with unarmored (left) and static armored (middle and right) initial conditions at different cross-sections along the modeled reach.

The oscillations in the riverbed GSD shown e.g. in the left panel in Figure 5.19 are triggered by sorting waves, which are defined in Section 5.1.6 on page 103. These waves advect changes in the GSD of the active layer at each SBT operation in downstream direction. This trend can be detected more clearly in Figure 5.20: disregarding the intensity, every change in the active layer GSD propagates downstream as shown by the peaks of the curves that e.g. start at the beginning of the first SBT operation at 0.2 km (upper panels of Figure 5.20) and reach the end of the domain at 10 km (lower panels of Figure 5.20) during the peak of the first event, i.e. after few hours.

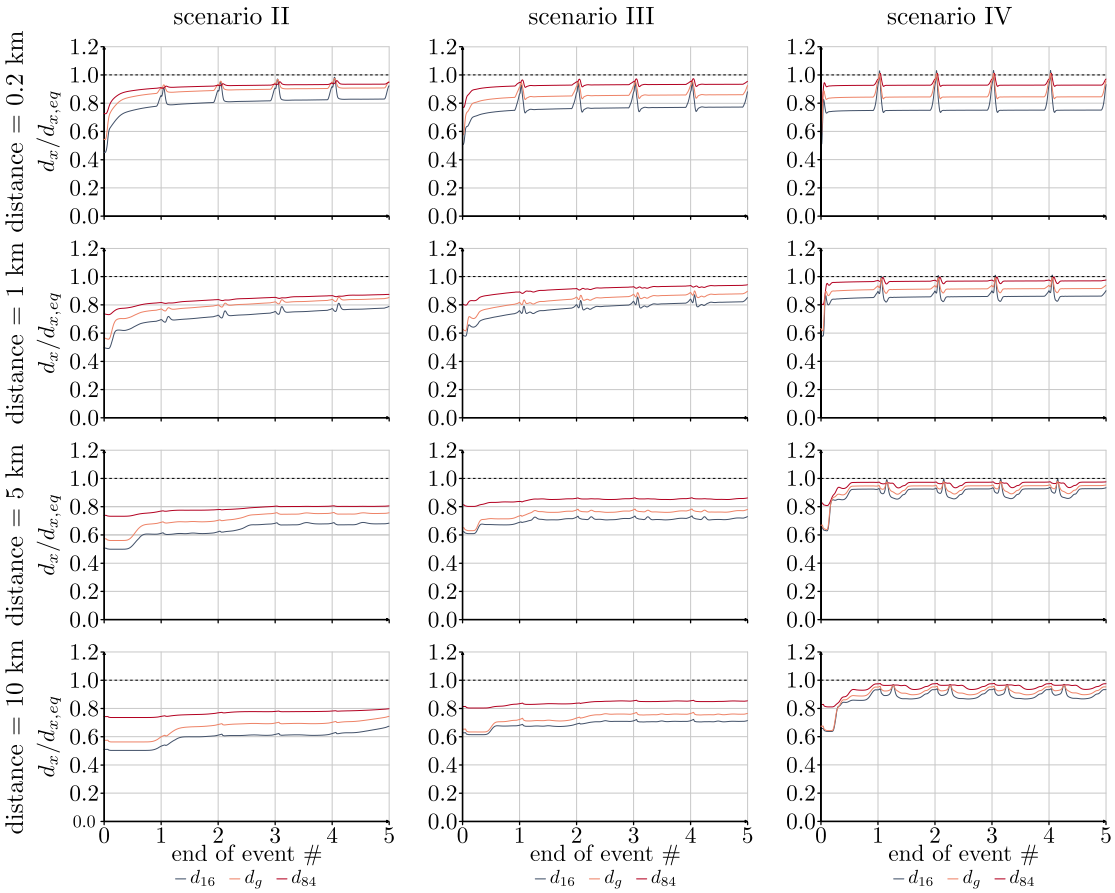

Figure 5.20: Non-dimensional diameter ratios ($d_x/d_{x,eq}$) relative to the sizes of the riverbed surface GSD such that 16% (blue-gray line) and 84% (red line) of the sediment is finer (d_{16} and d_{84}, respectively), and geometric geometric mean size d_g of the riverbed surface GSD (pink-orange line), plotted against the SBT operation number. Plots are relative to three runs (3, 7, and 11) belonging to three different scenarios (II, III, and IV, respectively) under OC1 and unarmored initial conditions at different cross-sections along the modeled reach.

Ribberink (1987) proposes an expression to calculate the propagation celerity of such perturbations in the average diameter of the mixture, i.e. the speed of the so-called *sorting wave*, which is:

$$\lambda^* = \frac{q_b}{u L_a} \tag{5.33}$$

where λ^* is the non-dimensional wave celerity, q_b is the total sediment transport per unit width, u is the mean flow velocity, and L_a is the active layer thickness. Therefore, in the case presented here, sorting waves should become slower for smaller sediment

supply rate (going from scenario IV to scenario II in Figure 4.6), higher flow velocity (going from scenario II to scenario IV in Figure 4.6), and thicker active layer. The first two hypotheses have been tested comparing results of simulations with the same active layer thickness and different water or sediment supply, i.e. the parameters over which SBTs exert a strong control, in Figure 5.20. Results show that sorting waves move at comparable speeds for every scenario, the main reason for that being the parallel water discharge (i.e. flow velocity) and sediment discharge increase when going from scenario II to scenario IV.

Moreover, diagrams in Figure 5.20 show that the active layer GSD is changing during each event, i.e. each SBT operation has the power to change the active layer composition, and results concerning scenario IV show that at the end of each event after the first one, the active layer composition returns almost the same as at the beginning. These fluctuations are more clearly represented in Figure 5.21, where the hysteretic cycle of the ratio of the geometric mean size to the equilibrium one $d_g/d_{g,eq}$ is represented against the ratio of the bedload discharge to the peak one $Q_b/Q_{b,peak}$. The diagrams represent the variations of active layer composition during the 50^{th} SBT operation, which have similar magnitude to the ones represented in Figure 5.20 for the first 5 SBT operations, but are closer to the equilibrium. They are relative to OC1, 1 km (Figures 5.21(a), (c), and (e)) and 10 km (Figures 5.21(b), (d), and (f)) downstream of the inlet for scenario II, III, and IV (Figures 5.21(a) and (b), (c) and (d), and (e) and (f), respectively). Results in Figure 5.21 show a common trend for each scenario, i.e. a coarsening followed by a fining during the rising limb and a coarsening during the falling limb. This clockwise hysteresis trend of the riverbed composition is in line with the one relative to bedload rate during flood events (e.g. Mao, 2012; Martin and Jerolmack, 2013), that is during the rising limb transport capacity increases together with the capacity of entraining coarse particles and transport as bedload, leaving finer particles on the riverbed surface. On the contrary, during the falling limb coarse particles are deposited first, causing the coarsening of the riverbed. The initial coarsening during the first stages of the rising limb is due to the addition of the coarse particles of the feeding, which at the beginning cannot be transported by the flow and are therefore deposited. Moreover, for scenario II (Figure 5.21(a)) the dynamic is slower since less water is released from the dam and the

SBT and therefore the active layer composition still adapts during the peak to the water and sediment input from upstream, i.e. at the end of the rising limb $d_g/d_{g,eq}$ is higher than at the beginning of the falling limb and the cycle is not closed. At the cross-section located 10 km downstream of the inlet, the hysteretic cycle seem to disappear and the oscillations have a smaller magnitude.

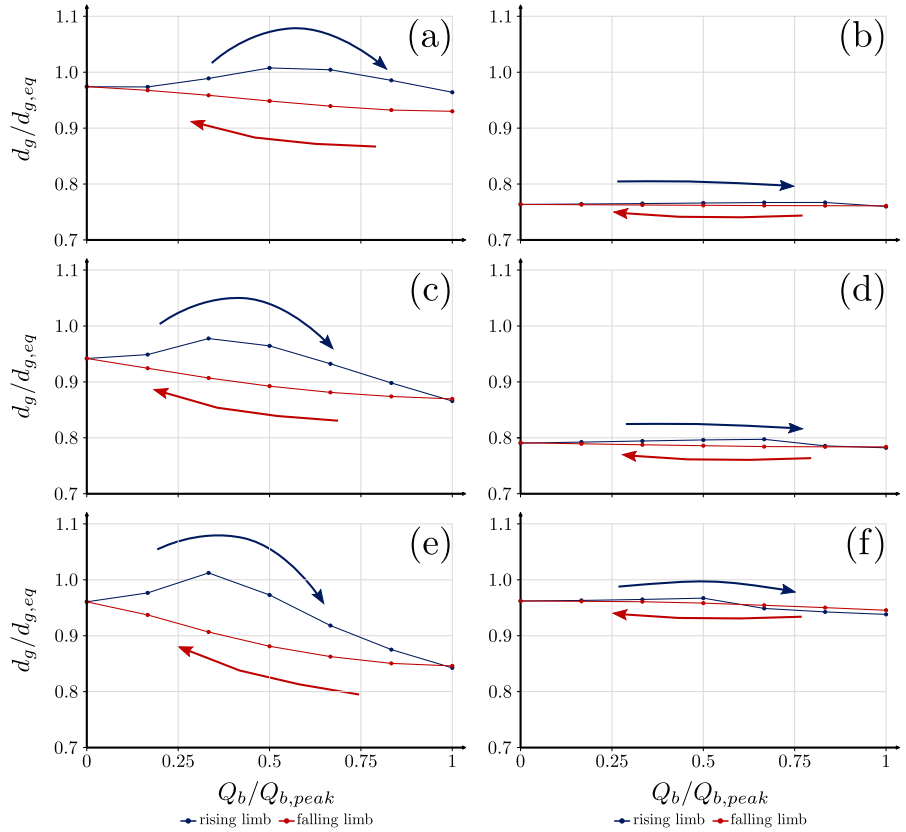

Figure 5.21: Evolution of active layer composition during the 5^{th} SBT operation under OC1, 1 km ((a), (c), and (e)) and 10 km ((b), (d), and (f)) downstream of the inlet for (a) and (b) scenario II (run 3), (c) and (d) scenario III (run 7), and (e) and (f) scenario IV (run 11). Both the variation of the riverbed composition during the rising (blue line and dots) and the falling (red line and dots) limbs of the hydrograph and sedimentograph are represented.

SBT-induced sediment pulse dynamics

From the comparison between Figures 5.15 and 5.16, it results that the situation of a river subject to alternate bedload-laden and bedload-free water releases in terms of

riverbed level and composition might be different if it is observed at the end of a bedload-laden water release (see Figure 5.15) or at the end of a bedload-free water release (see Figure 5.16). In fact, both riverbed level and composition are closer to the equilibrium in the first case than in the second. Oscillations of the riverbed composition have been discussed in the previous section in relation to the effect of sorting waves. Similarly, oscillations of the riverbed level are discussed hereafter in relation to the dynamics of sediment pulses. So far, only the trends of erosion and deposition after 50 SBT operations have been discussed related to the distance of riverbed level and composition to the equilibrium. These trends provide some indications also of how the sediment pulse introduced to the river during SBT-operations evolves, but for themselves these observations are inadequate to define if the pulse evolves due to advection, dispersion, or a mix of these two. Sklar *et al.* (2009) introduced a metric useful to assess whether a sediment pulse is advective or dispersive. They define a purely advective pulse as one where the leading and trailing edges, wave apex and center of mass, advance downstream and the pulse length remains the same. On the contrary, a purely dispersive sediment pulse is one where the wave apex and trailing edge do not migrate downstream and the pulse length grows. Since these characteristics are difficult to assess by only looking at the deviatoric riverbed level variations (i.e. elevation difference) $\Delta\eta$, Sklar *et al.* (2009) recommend using the cumulative elevation difference (CED) normalized by the maximum CED. After defining the elevation difference $\Delta\eta$ as

$$\Delta\eta\left(x,t=t^*\right)=\eta\left(x,t=t^*\right)-\eta\left(x,t=0\ s\right) \tag{5.34}$$

where t^* is the time at the end of each SBT operation, the CED is calculated as follows

$$CED\left(t=t^*\right)=\int_{\chi=0}^{\chi=L_{tot}}\Delta\eta\left(x,t=t^*\right)dx \tag{5.35}$$

where L_{tot} is the total length of the domain, and eventually the normalized CED is defined as

$$nCED\left(t=t^*\right)=\frac{CED\left(t=t^*\right)}{max\left(CED(t)\right)} \tag{5.36}$$

Figure 5.22 shows hypothetical $\Delta\eta$ and nCED curves for purely advective (Fig-

ure 5.22(a)), purely dispersive (Figure 5.22(b)) and mixed behavior (Figure 5.22(c)) sediment pulses. For purely advective pulses the slope of the nCED curves do not change and the leading and trailing edges translate downstream. Differently, the slope for a purely dispersive pulse rotates about the origin in a clockwise direction.

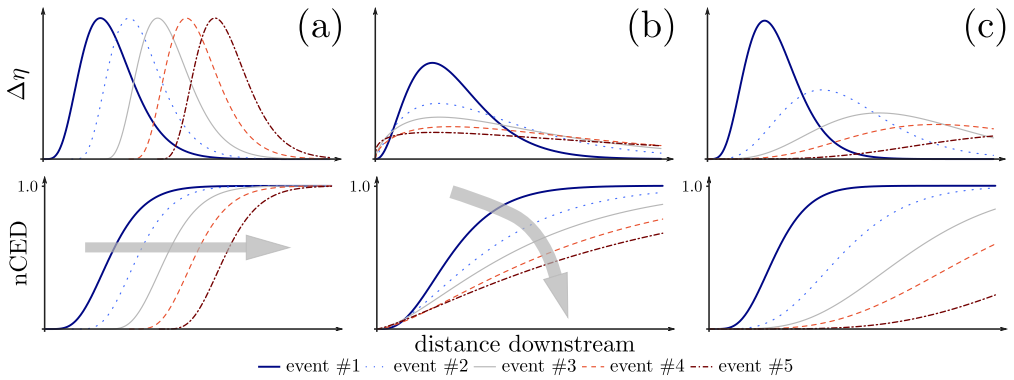

Figure 5.22: Elevation difference $\Delta\eta$ and normalized cumulative elevation difference nCED curves for hypothetical sediment pulses that (a) are purely advective, (b) are purely dispersive, and (c) have mixed behavior. The nCED curves are the summation of all elevation differences moving downstream, normalized by the maximum CED (adapted from Sklar *et al.* (2009)).

The pulses-like behavior of sediment introduced to the river reach by bedload-laden water releases is analyzed focusing on the first 5 SBT operations under OC1, OC2, and OC3. Note that the case of OC4 is not represented here, since it produces similar results to the case of OC1. Results are presented in Figure 5.23 where: (i) sediment release patterns are presented for each OC in the left panel, (ii) the deviatoric riverbed levels $\Delta\eta$, and (iii) the nCED for each of the 5 SBT operations over the whole domain length are presented in the mid and in the right panel, respectively. Concerning $\Delta\eta$ (mid panel of Figure 5.23), results show that increasing the number of bedload-free water releases between two consecutive releases of bedload-laden water (OC2a, b and c) increases the upstream erosion: under OC1 the domain only experiences aggradation, while under OC2a the domain experiences almost symmetrical erosion and deposition and under OC2b and c the erosion-deposition balance is shifted towards erosion. Similarly to the aggradation dynamics shown by $\Delta\eta$ under OC1, under OC3 the domain only experiences erosion due to upstream sediment mining which has the twofold effect of reducing both the released sediment volume (by a factor of 3 here) and composition.

Under OC1 and OC3, nCED diagrams (Figures 5.23(b) and (d)) indicate that the pulse evolves mostly due to dispersion, i.e. it remains confined in an upstream region and its apex and center of mass are only slightly moving downstream. Under OC2a, b, and c on the contrary, the body of sediment released and dispersed during the first SBT operation is advected downstream during the following water release(s). Diagrams concerning nCED under OC2a, b, and c (Figures 5.23(f), (h), and (j)) indicate the evolution of the pulse due to a mix of dispersion and advection, with the first prevailing during bedload-laden water releases and the second being promoted by bedload-free water releases.

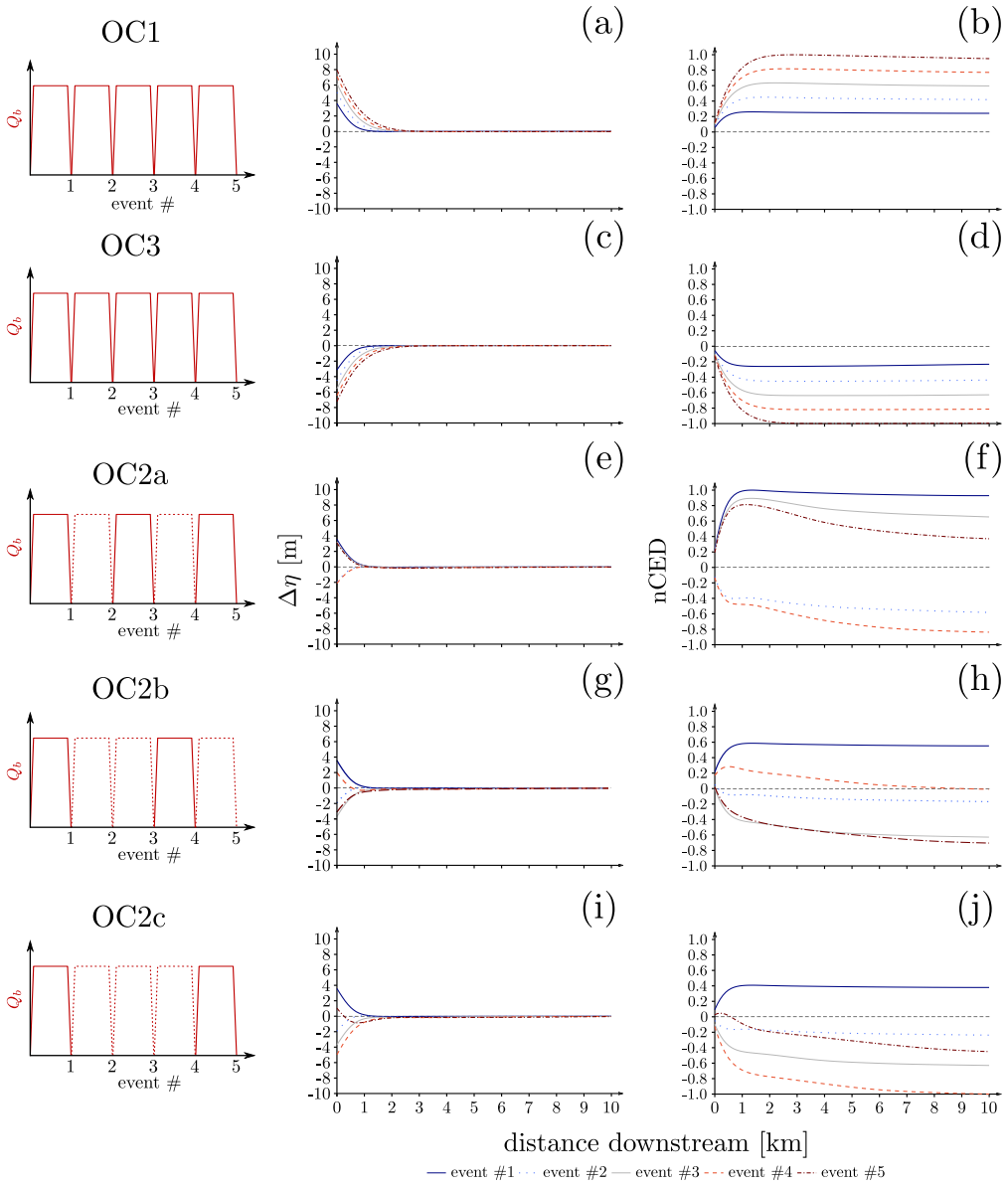

Figure 5.23: Deviatoric riverbed level variations (i.e. elevation difference $\Delta\eta$) and normalized cumulative elevation difference (nCED) (Sklar *et al.*, 2009) plotted against the downstream distance from the water and sediment input. Results refer to scenario II (run 3) with unarmored initial conditions. Sediments are fed to the domain following five different strategies, i.e. with zero (OC1 and OC3), one (OC2a), two (OC2b) and three (OC2c) bedload-free water releases between two consecutive bedload-laden water releases. Colors from blue to red indicate the marching of time going from SBT operation 1 to SBT operation 5. In the left panel, sedimentographs representing the bedload feeding rate for the 5 SBT operations are represented, with solid lines indicating the release of bedload-laden water and dashed lines indicating the release of water.

5.5 Discussion

Numerical results reveal that rivers affected by SBT operations undergo great modifications of riverbed surface level and composition, both on a short and on a long timescale. Four different operational conditions (OCs) for SBTs can be defined, namely: (i) OC1, where SBT bypassing efficiency e_{SBT} = 1.0, (ii) OC2, where sediment are released every other (OC2a), every two (OC2b) or every three SBT-operations (OC2c), (iii) OC3, where the coarser part of the incoming sediment GSD is mined upstream of the SBT intake structure, and (iv) OC4, where SBT bypassing efficiency e_{SBT} = 0.5. Moreover, four different release scenarios are defined that, depending on how a SBT is operated, identify different water and sediment discharge magnitudes being conveyed to the downstream reach. Scenario I is characterized by non-operating SBT; scenario II is defined as the design range of the SBT; scenario III and IV identify how a SBT is operated when large and very large floods approach the reservoir, respectively. However, the values considered for the bedload feeding rates only encompass a small range of sediment supply rates. That is, sediment discharges fed to the channel in this study vary between 4.67E-3 m^2 s^{-1} ($Q_{b,m,SBT}$ in OC3) and 1.28E-1 m^2 s^{-1} ($Q_{b,M,SBT}$ in OC1), while Parker *et al.* (2007) show that changes of order of magnitude in sediment supply rate are needed to cause substantial changes in the riverbed surface composition (see Figure 5.24). On the contrary, the range of bedload supply rates considered here is large enough to include a large range of slopes variability.

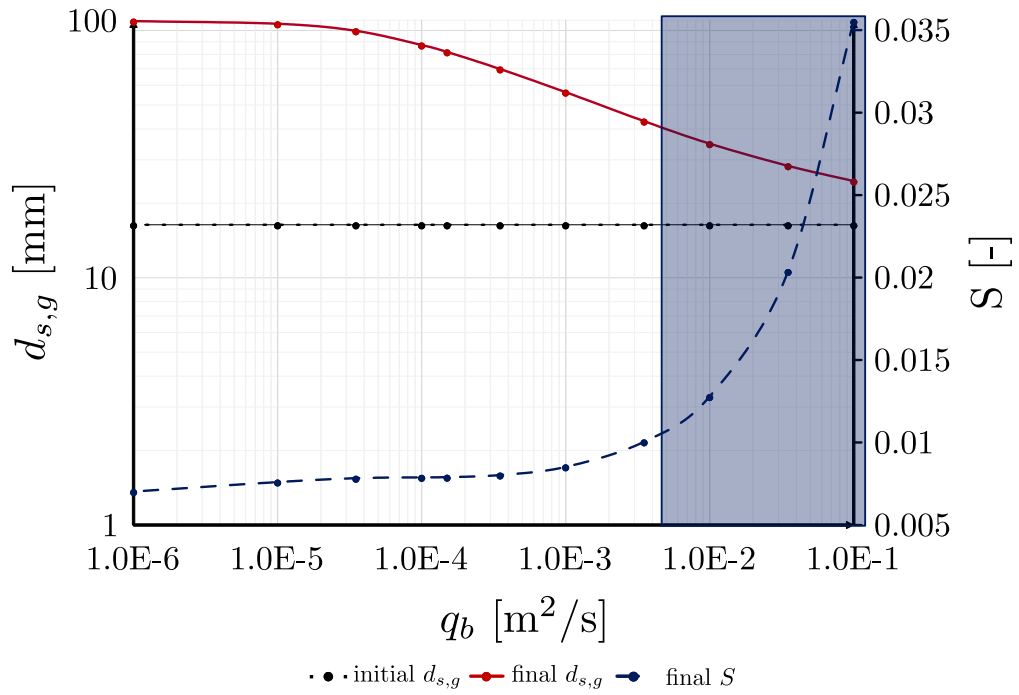

Figure 5.24: Plot of surface geometric mean size $d_{s,g}$ and bed slope S as functions of the bedload feed rate per unit width q_b at mobile-bed equilibrium (adapted from Parker *et al.* (2007)). The colored area indicates the range of sediment feed rates used in this study.

On the one hand, depending on the OCs, the reach downstream of a SBT can experience either an increase or a decrease of riverbed level, i.e. slope. In both cases, the downstream river reach approaches mobile-bed equilibrium conditions slowly, with riverbed level values after 50 SBT operations that are smaller than half of the equilibrium ones. Being able to distinguish which OC might cause aggradation or deposition is of paramount importance to evaluate the effectiveness of a SBT in counteracting river damming morphological effects, such as channel incision (e.g. Williams and Wolman, 1984; Brandt, 2000), and therefore to evaluate its effectiveness as river restoration measure (e.g. Wohl *et al.*, 2015). The results of this work show that if the SBT transports entirely the bedload coming from upstream, i.e. its bypassing efficiency is 1.0 (OC1), it might counteract channel incision below the dam effectively. On the contrary, if the coarsest part of the bedload material transported upstream is mined before entering the SBT, i.e. the GSD of the material fed to the downstream reach is reduced of its coarse

part (OC3), SBT operations worsen channel incision. In the case of alternate sediment releases, the SBT acts as a countermeasure to channel incision only after a release of bedload-laden water. On the contrary, riverbed results incised if the channel state after a release of water is considered. Eventually, if only a part of the incoming bedload is conveyed through the SBT to the downstream reach, i.e. the bypassing efficiency of the SBT is below 1.0 (OC4), the SBT is still acceptably effective as a countermeasure to channel incision, since only during very large floods (which have also a longer period of return) it will cause erosion downstream.

On the other hand, one can evaluate the effectiveness of SBT operations as river restoration measure also by evaluating their effectiveness in counteracting riverbed armoring (e.g. Dietrich *et al.*, 1989; Wohl *et al.*, 2015). Moreover, improved sediment mobility and the presence of gravel and cobbles on the riverbed have tremendous ecological importance as habitat for benthic macroinvertebrates and fish (Kondolf and Wolman, 1993). Results show that, regardless of the OCs, the riverbed surface of the downstream reach is always reworked ending in mobile-armor to nearly unarmored conditions. Furthermore, riverbed composition changes occur, almost in all cases, at the event-scale and are not greatly affected by the initial state of riverbed surface, the only exception being the cases when the SBT is operated under OC3 and delivers only fines. However, even in this case, after 50 SBT operations the composition of the riverbed surface is far from static armor conditions.

SBT operations might in most of the cases mitigate channel incision and riverbed armoring caused by dam closure and restore natural geomorphic processes in the downstream reach. However, SBTs are operating only few times a year and are therefore unable to restore the natural hydrologic processes (e.g. Wohl *et al.*, 2015). In fact, they reestablish hydrologic connectivity only during floods and when they are not operated only the minimum flow is generally flowing in the downstream reach (e.g. Martín *et al.*, 2017). Moreover, extreme magnitudes or frequencies of SBT operations could have sever consequences on the river ecosystem (Martín *et al.*, 2017). Therefore, a permanent renaturalization of geomorphic and hydrologic processes by means of SBT operations would take several years of adaptive management operations combined with extensive monitoring programs, similarly to experimental or artificial floods (Robinson, 2012).

5.6 Sensitivity Analysis

In the analysis presented before, the active layer thickness L_a and the Gauckler-Strickler roughness coefficient k_s have been considered to be constant in time and have been calculated with eq. 5.6 considering $n_a = 2$ and eq. 5.4 considering the d_{90} of the feeding material. Moreover, the numerical modeling of the effects of SBT operations on different time scales have been performed only using the Wilcock and Crowe (2003) formula. To analyze the effect of these parameters on the results, a sensitivity analysis have been performed considering: (i) a thinner active layer, i.e. $n_a = 1$ in eq. 5.6, (ii) a thicker active layer, i.e. $n_a = 5$ in eq. 5.6, (iii) a time-dependent Gauckler-Strickler roughness coefficient k_s varying in time with the d_{90} of the riverbed surface, and (iv) the Meyer-Peter and Müller (1948) formula as closure relation for the estimation of bedload transport. The characteristics of four sensitivity analyses performed, which are named (i) SA1, (ii) SA2, (iii) SA3, and (iv) SA4, respectively, are summarized in Table 5.2. The effects of the active layer thickness, of a time-dependent Gauckler-Strickler roughness coefficient, and of the formula for the estimation of the bedload transport have been tested for the results on different time-scales under two OCs, i.e. OC1 and OC2a. These have been chosen as the most representative ones, since the trends of the results under OC3 and OC4, and OC2b and OC2c recall the ones of the results under OC1 and OC2a, respectively. Among the 12 runs performed under each OC, runs 3, 7, and 11 (represented by an upward-pointing triangle, an asterisk and a downward-pointing triangle, respectively) have been chosen to represent the trends of scenarios II, III, and IV, respectively.

Table 5.2: Characteristics of the Sensitivity Analysis performed, with different active layer thickness L_a, Gauckler-Strickler roughness parameter k_s, and transport formula.

Name	L_a [m]	k_s [$m^{1/3}/s$]	bedload transport formula
reference	$2d_{90}$	32	Wilcock and Crowe (2003)
SA1	$1d_{90}$	32	Wilcock and Crowe (2003)
SA2	$5d_{90}$	32	Wilcock and Crowe (2003)
SA3	$2d_{90}$	$k_s(d_{90}(t))$	Wilcock and Crowe (2003)
SA4	$2d_{90}$	32	Meyer-Peter and Müller (1948)

The results of the sensitivity analysis for the results at mobile-bed equilibrium under OC1 and OC2a concerning both the relative change RC of the riverbed slope S and mean geometric size of the riverbed surface composition d_g are given in Table 5.3. The relative change of a generic variable Φ is calculated as follows

$$RC(\Phi) = \left| \frac{\Phi_{tested} - \Phi_{reference}}{\Phi_{reference}} \right| \tag{5.37}$$

where Φ is used to indicate both S and d_g, $reference$ refers to the values presented in Section 5.4.1, and $tested$ to the ones calculated in the scope of the sensitivity analysis (e.g. Ferrer-Boix *et al.*, 2014).

Table 5.3: Results of the sensitivity analysis concerning the relative change of the riverbed slope S and of the mean geometric size of the riverbed surface composition d_g at mobile-bed equilibrium for (i) a thinner active layer (SA1), (ii) a thicker active layer (SA2), (iii) a time-dependent Gauckler-Strickler parameter (SA3), and (iv) a different bedload transport formula (SA4).

		OC1			OC2a		
		SII	SIII	SIV	SII	SIII	SIV
SA1	$RC(S)$	0.003	0.006	0.005	0.001	0.008	0.001
	$RC(d_g)$	0.008	0.018	0.020	0.11	0.030	0.040
SA2	$RC(S)$	0.003	0.006	0.005	0.001	0.008	0.012
	$RC(d_g)$	0.006	0.008	0.010	0.070	0.030	0.094
SA3	$RC(S)$	0.003	0.006	0.005	0.015	0.016	0.012
	$RC(d_g)$	0.000	0.000	0.000	0.000	0.000	0.000
SA4	$RC(S)$	0.110	0.026	0.001	0.150	0.078	0.063
	$RC(d_g)$	0.330	0.300	0.280	0.310	0.330	0.330

Similar to the results presented in Table 5.3, the relative change of the hydrograph boundary layer (HBL) length L_{HBL} and of the amplitude A_{HBL} concerning numerical runs performed under OC2a is given in Table 5.4. Note that the results concerning the HBL for OC1 are not discussed here since a HBL is only forming when bedload-laden and bedload-free water releases are alternating (i.e. under OC2).

Table 5.4: Results of the sensitivity analysis concerning the relative change of the hydrograph boundary layer (HBL) length L_{HBL} and of the amplitude A_{HBL} at mobile-bed equilibrium for (i) a thinner active layer (SA1), (ii) a thicker active layer (SA2), (iii) a time-dependent Gauckler-Strickler parameter (SA3), and (iv) a different bedload transport formula (SA4).

		OC2a		
		SII	SIII	SIV
SA1	$RC(A_{HBL})$	0.002	0.009	0.001
	$RC(L_{HBL})$	0.110	0.000	0.070
SA2	$RC(A_{HBL})$	0.013	0.003	0.002
	$RC(L_{HBL})$	0.000	0.000	0.000
SA3	$RC(A_{HBL})$	0.000	0.000	0.000
	$RC(L_{HBL})$	0.110	0.000	0.000
SA4	$RC(A_{HBL})$	0.047	0.050	0.043
	$RC(L_{HBL})$	0.110	0.000	0.070

Both the results presented in Table 5.3 and in Table 5.4 show that, except for $RC(d_g)$ relative to SA4 (see Table 5.4), the relative change of each variable is in an acceptable range of variability. In fact, most of the changes are below 0.01 (i.e. 1%) and the greatest changes are around 0.1 (i.e. 10%). Results concerning the riverbed composition calculated using a different transport formula (i.e. $RC(d_g)$ relative to SA4), show that the riverbed composition at mobile-bed equilibrium is affected by the choice of the formula for the estimation of bedload transport. In particular, the Meyer-Peter and Müller (1948) formula extended to account for grainsize selectivity (i.e. eq. (5.21)) predicts finer riverbed compositions at mobile-bed equilibrium. In fact, with the Egiazaroff (1965) hiding function, the finest grain sizes of the riverbed material become less movable and are most likely to be overrepresented on the riverbed surface.

In Table 5.5, results of the four sensitivity analysis after 50 SBT operations are presented in terms of relative change of the deviatoric riverbed elevation $\Delta\eta$ as defined in eq. (5.32) on page 123, and relative change of the mean geometric size d_g of the riverbed

surface. They show similar trends to the ones relative to the mobile-bed equilibrium, in fact the greatest changes are due to the change of the formula for the estimation of bedload transport (SA4). In this case, a larger deposition results under OC1 and a smaller erosion results under OC2a as compared to the reference, while the riverbed surface results always finer than the reference. Note that the other two significant relative changes, i.e. concerning SA1 and SA2 for scenario II under OC1 ($RC(\Delta\eta)$ = 0.13 and $RC(\Delta\eta)$ = 0.36, respectively), represent a small absolute change. That is, the reference elevation difference is $\Delta\eta$ = -8 cm while it is $\Delta\eta$ = -7 cm in the first case (SA1), and $\Delta\eta$ = -11 cm in the second (SA2).

Table 5.5: Results of the sensitivity analysis concerning the relative change of the non-dimensional slope S^* and of the riverbed composition d_g^* at mobile-bed equilibrium for (i) a thinner active layer (SA1), (ii) a thicker active layer (SA2), (iii) a time-dependent Gauckler-Strickler parameter (SA3), and (iv) a different bedload transport formula (SA4).

		OC1			OC2a		
		SII	SIII	SIV	SII	SIII	SIV
SA1	$RC(\Delta\eta)$	0.130	0.002	0.002	0.022	0.054	0.019
	$RC(d_g)$	0.001	0.016	0.015	0.046	0.035	0.040
SA2	$RC(\Delta\eta)$	0.360	0.006	0.010	0.054	0.069	0.075
	$RC(d_g)$	0.012	0.006	0.027	0.021	0.060	0.068
SA3	$RC(\Delta\eta)$	0.000	0.000	0.000	0.000	0.000	0.000
	$RC(d_g)$	0.000	0.000	0.000	0.000	0.000	0.000
SA4	$RC(\Delta\eta)$	1.210	0.170	0.120	0.550	0.770	0.340
	$RC(d_g)$	0.160	0.140	0.190	0.090	0.0960	0.160

The results of the sensitivity analysis concerning the memory of the initial conditions are given in Figure 5.25, where results presented in Figure 5.20 (reference) are compared to the ones relative to the sensitivity analysis concerning the active layer thickness (SA1 and SA2). The cross-section located 10 km downstream of the inlet is the only one taken into account and it is considered as representative of the whole domain. Results

concerning SA3 and SA4 are not presented here since the active layer plays a major role in the speed of propagation of the sorting waves (Stecca *et al.*, 2014).

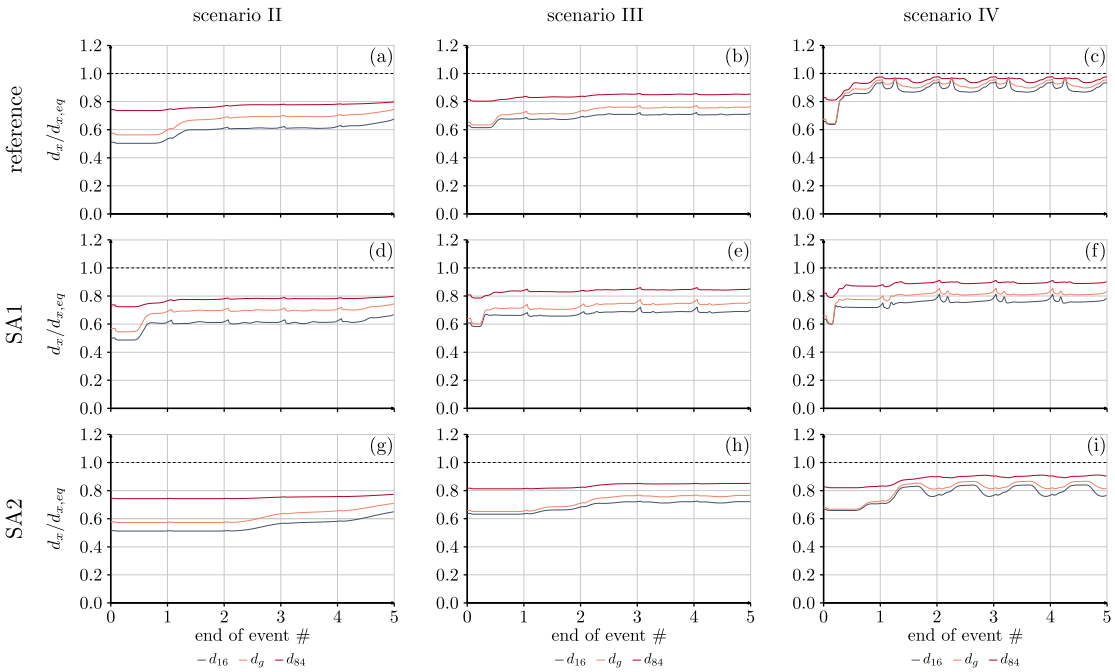

Figure 5.25: Non-dimensional diameter ratios ($d_x/d_{x,eq}$) relative to the sizes of the riverbed surface GSD such that 16% (blue-gray line) and 84% (red line) of the sediment is finer (d_{16} and d_{84}, respectively), and geometric geometric mean size d_g of the riverbed surface GSD (pink-orange line), plotted against the SBT operation number. Plots are relative to three runs (3, 7, and 11) belonging to three different scenarios (II, III, and IV, respectively) under OC1 and unarmored initial conditions 10 km downstream of the inlet for the two sensitivity analysis concerning the active layer thickness (SA1 and SA2).

Trends presented in Figure 5.25 show that the active layer thickness (Figure 5.25(d) to (i)) has an effect on the results. In fact, the initial rework of the riverbed surface composition, which is indicated by the first increase of $d_x/d_{x,eq}$, lasts shorter for a thinner active layer (SA1) and longer for a thicker one (SA2). For example, the initial reworking phase in Figure 5.25(a) lasts for 1 event, while the one of Figure 5.25(d) ca. half an event, and the one of Figure 5.25(g) ca. 2.5 events.

6 Conclusions and Outlook

6.1 Summary

To quantify downstream morphological effects of SBT operations, three modeling steps have been followed in this thesis (see Figure 1.1):

i) study of the real case of the Solis SBT at the Albula River (Canton of Grisons, Switzerland),

ii) development of a general framework for SBT operations,

iii) one dimensional numerical study of the morphological effects of SBT operations.

The field study on the real case of the Solis SBT in Canton of Grisons, Switzerland, has been conducted taking advantage of state-of-art technologies and methods for measuring the morphological modifications (bathymetric LiDAR), quantifying the uncertainty related to single measurements (spatially non-uniform error quantification by means of Fuzzy Inference Systems), and assessing the morphological changes occurring at reach-scale (DEM of Difference with statistic error propagation). The results show that in two years of SBT operations at the Solis SBT (Canton of Grisons, Switzerland) rather large volumes of sediment have been mobilized in the downstream reach and, in some areas, great morphological changes occurred. It seems that the alternation of bedload-laden and quasi bedload-free water releases from SBTs induces a pulse dynamics, where bedload-laden releases act as sediment source promoting sediment dispersion, while water releases promote sediment advection. Therefore, it can be inferred that SBTs exert a strong control on water and sediment fluxes being conveyed downstream of dams.

Before understanding in detail the possible morphological effects due to SBT operations, which crucially depend on how much water and sediment are released from the SBT, a general framework has been defined to describe SBT operational conditions (OCs). SBTs are designed to carry out a defined range of water discharges going from a minimum required to operate the SBT to a maximum design water discharge. Below the minimum water discharge the SBT is not operated and incoming water and sediment are stored and deposited inside the reservoir (Scenario I in Figure 4.6), respectively. In the design range concerning water discharges, what is transported in the upstream river reach is conveyed to the downstream reach through the SBT (Scenario II in Figure 4.6). If the design water discharge is exceeded, the surplus is diverted into the reservoir and stored or released through the dam outlets. However, SBTs are designed with a transport capacity that is higher than the one of the upstream river reach. Therefore, even if the SBT is operated at its design water discharge, while the water surplus is diverted inside the reservoir, more bedload can be diverted through the SBT (Scenario III in Figure 4.6). When the maximum transport capacity of the SBT is reached, i.e. in case of very large flood events, the exceeding sediment discharge is transported inside the reservoir where it is stored, while water can be diverted through the dam outlets to the downstream reach (Scenario IV in Figure 4.6). Worldwide experiences have shown that existing SBT operations are far from idealized conditions (OC1 in Figure 4.6), e.g. during the two years of operations at Solis bedload-laden and quasi bedload-free water releases were alternated (OC2 in Figure 4.6), while in Japan the coarsest fractions of the incoming sediment volume are generally mined upstream of the SBT inlet structure and only fines are carried out to the downstream reach (OC3 in Figure 4.6). Eventually, a reduced bypassing efficiency was also considered (OC4 in Figure 4.6) to account for possible flaws in SBT construction and/or operation.

The Operational Spaces (OS) defined in Chapter 4 serve also to quantify reliable boundary conditions for the numerical study of Chapter 5. Morphological effects of SBT operations were quantified both on the long- (at mobile-bed equilibrium) and on the short-term, considering all OCs defined in Chapter 5. The model results suggest that:

i) at mobile-bed equilibrium, riverbed grain size distribution (GSD) approaches a

static armor composition if only water is conveyed through the dam outlets (scenario I), while if the SBT is put in operation and delivers bedload-laden water to the downstream reach, the riverbed GSD approaches the feeding one, i.e. the riverbed becomes less armored with slight changes between different release conditions (scenario II, III, and IV). The equilibrium slope is smaller than the upstream one (i.e. the reference one) if only water is conveyed through the dam outlets (scenario I), while at a fixed bedload feed rate, the higher the ratio of bedload feed rate to channel transport capacity, the steeper the riverbed becomes (scenario II, III, and IV);

ii) the volume of sediment delivered to the downstream reach plays a role in changing the slope (the channel is steeper under OC1 compared to other OCs), while it does not significantly affect the armoring ratio of the riverbed surface;

iii) the disequilibrium between transport capacity and feed rate (see Figure 5.11) seems to be the main reason for the formation and persistence at mobile-bed equilibrium of a Hydrograph Boundary Layer (HBL) of defined length, where riverbed level and GSD fluctuate around the equilibrium state. The length of the HBL is in all cases less than 20% of the total domain length and the oscillations are more intense the higher the imbalance between transport capacity and feed rate. That is, for repeated and consecutive releases of bedload-laden water (i.e. OC1) the imbalance is only due to the different time distribution of the transport capacity and of the feed rate (see Figure 5.11), resulting in low-amplitude oscillations, i.e. smaller than the d_{90}. Differently, alternate bedload-laden and bedload-free water releases (OC2a, b, and c) result in larger oscillations exceeding the d_{90};

iv) the introduction of very fine material (OC3) has dramatic effects on the riverbed composition and reduces the riverbed slope to less than half of the reference one. By the same token, the introduction of only coarse material to the downstream reach might result in a very coarse riverbed surface GSD, which is an unwanted outcome of SBT operations;

v) riverbed level and composition evolve on different time scales, the first being very slow (thousands of operations) and the second very fast (about five operations).

Riverbed surface composition is already close to the equilibrium configuration after one SBT operation and is then reworked (i.e. the fractions of the single grain classes in the active layer change) at each operation. However, the lower the ratio of bedload feed rate to channel transport capacity, the more operations are needed to completely rework the surface layer. After the first dramatic change lasting a few events, the initial conditions do not play a role anymore and the riverbed surface converges to mobile-bed equilibrium together with the riverbed level, i.e. at a very slow pace;

vi) sediments released from SBTs behave like sediment pulses, i.e. they translate, disperse or a mix of the two depending on hydraulic conditions and sediment feed characteristics. When bedload-laden and bedload-free water releases to the downstream reach are alternating, the downstream reach experiences cycles of deposition and erosion with the sediment pulse showing an advective behavior during bedload-free water releases and a generally dispersive behavior during bedload-laden water releases;

vii) in most of the cases roughly 10^4 of SBT operations are needed to reach mobile-bed equilibrium, which is an unrealistic amount of time for physical processes connected to infrastructure that have a life-time of 80 to 100 years;

viii) on the short-term, SBT operations act as sudden disturbances, i.e. like sudden floods, which have the power to rework the riverbed surface. This can for instance enhance the hydrological continuum, i.e. the hyporheic exchange;

ix) the change in riverbed surface GSD caused by SBT operations can enhance fish habitat in the downstream reach.

Eventually, a sensitivity analysis was carried out to study the effects on the numerical results of: (i) a thinner active layer (SA1), (ii) a thicker active layer (SA2), (iii) a time-dependent roughness parameter (SA3), and (iv) the use of the Meyer-Peter and Müller (1948) formula for the estimation of bedload transport (SA4). Results are affected by the changes (i), (ii), and (iv) at the event-time scale, since the riverbed composition is reworked faster with a thinner active layer, and slower with a thicker active layer or

using the Meyer-Peter and Müller (1948) formula for bedload transport. Differently, the use of a time-dependent roughness parameter does not affect the results. Moreover, the riverbed composition at mobile-bed equilibrium results to be ca. 30% finer when using the Meyer-Peter and Müller (1948) formula instead of the Wilcock and Crowe (2003) formula, since the first is used in conjunction with the hiding function by Egiazaroff (1965) which makes the finer sediments of the riverbed surface less movable. Eventually, also on a shorter time-scale, i.e. after 50 SBT operations, only SA4 produces results that are significantly different from the presented ones.

6.2 Synthesis of research questions

Which are the volumes mobilized by two years of SBT operations at the Solis SBT and how do they affect river morphology?

In two years of SBT operations at the Solis SBT in the Canton of Grisons, Switzerland, a net volume of almost 6000 m^3 has been mobilized and sediment budget segregation reveals different trends in the downstream reach. That is, in the first 2.6 km deposition prevails, followed by 1 km of mainly erosion. From 3.6 to 5.0 km deposition prevails again, while downstream the trend is mixed. However, the eroded and deposited sediment volumes are mostly caused by relatively small elevation changes, i.e. confined between -1 m and +1 m (see Figure 3.20). Nevertheless, larger elevation changes might happen locally and are linked to the particular topography of some reaches. For example, the short reach right downstream of the first tributary show elevation changes larger than 1 m and a deposited volume of ca 600 m^3, which are probably caused by the mixed effect of SBT releases, sediment being transported by the tributary and the change of slope (see Figure 3.23).

How much sediment and water are released by the SBT to the downstream reach, under different operational conditions?

The main aim of SBTs is to prevent reservoir sedimentations, i.e. to avoid sediment to enter reservoirs. Therefore, they are built with higher transport capacity as compared with the upstream river reach. That is, the water discharge being equal, SBTs would

always transport more than the upstream river reach. Moreover, they are operated in a range of water discharges going from the minimum allowing for SBT operation to the design water discharge. Depending on the flood wave approaching the reservoir several scenarios might be defined and used to quantify the water and sediment discharges being carried to the downstream reach, where one should take into account the operational range of the SBT and the discrepancy between the SBT and the upstream transport capacity. Moreover, worldwide examples of SBTs have shown that: (i) bedload-laden and bedload-free water releases can be alternating, (ii) the coarsest part of the sediment being transported upstream might be mined before entering the SBT, and (iii) SBTs might not always work with an efficiency equal to 1. Under these assumptions, water and sediment discharges being released from SBTs can be quantified under different operational conditions.

Which are the morphological effects of repeated SBT operations on both short and long temporal scales from both a quantitative and qualitative perspective?

At mobile-bed equilibrium, i.e. after tens of thousands of SBT operations, the river reach might become steeper with an almost unarmored riverbed surface depending on the operational conditions of the SBT. On the contrary, releases of only fine material have dramatic effects on riverbed slope and composition. Moreover, the equilibrium reached is dynamic and allows for the formation of a short reach (its length being usually less than 1/5 of the total domain length), where riverbed level and composition fluctuate more strongly than downstream of this region. On a shorter time-scale, the riverbed slope evolves more slowly than the riverbed composition, which is reworked usually within less than 5 SBT operations. The initial conditions of the riverbed surface, i.e. the presence of a static armored or unarmored surface layer, do not play a major role in influencing this double-speed dynamic. This means that even after a few years of operations, a SBT might have the power to completely rework the riverbed composition, while still not affecting the riverbed slope dramatically. The alternation of bedload-laden and water releases makes the oscillations in the upstream region more intense, with cycles of deposition and erosion of remarkable magnitude.

6.3 Further research

The study of the morphological effects of SBT operations is still quite unexplored. This work provides objective, quantitative estimates that may be used in assessing potential future impacts of SBTs. Hereafter an outlook is provided and future challenges and potential successive research are proposed.

2D morphological variations induced by SBT operations

Results in Chapter 3 show that SBT-induced morphodynamics might be dependent on local topography and that two-dimensional effects might as well affect the morphodynamics of SBT-affected river reaches. Therefore a one-dimensional numerical study taking into account channel-width variations or a two-dimensional numerical study might help in understanding the dynamics described in Chapter 3. Moreover, extending the analysis presented in Chapter 5 is a stimulating challenge, since the pulse dynamics identified in 1D is also affected e.g. by river bars (e.g. Cui *et al.*, 2003a).

2D modeling of sediment transport inside the reservoir

A two-dimensional modeling of the sediment transport dynamics over a sedimentation body inside a reservoir might help in better understanding which sediments enter the SBT when the intake is built within the reservoir (e.g. Sumi *et al.*, 2012). Understanding the sorting processes occurring inside a reservoir might be of paramount importance to precisely evaluate the effects of SBT operations to the downstream reach.

Habitat modeling of SBT effects

A two-dimensional study of SBT-induced morphological changes might allow for the modeling of river habitats. Following a calibration, maps of river hydraulics might be used to assess the availability of fish habitat, as well as calculate hydraulic parameters to analyze the impacts of SBT operations on the macrobenthos community. Habitat modeling is a very active research field that has received a lot of attention in the last decades.

Further monitoring campaigns

At present, required monitoring of SBT projects is not detailed enough to provide meaningful data to interpret geomorphological impacts given the spatial and temporal variability in sediment supply to the downstream reach. The methodology proposed here should not supplant regular in-field monitoring, but allows for development of testable hypothesis that targeted monitoring can assess.

Bibliography

Albayrak, I.; Auel, C.; Boes, R.M.; Hagmann-Mueller, M. (2016). Mud Mountain Dam 9-foot Tunnel Re-armoring: Abrasion Calculations and Recommendations on the Invert Lining Concept. *Technical Report 4357*, Laboratory of Hydraulics, Hydrology and Glaciology (VAW), ETH Zurich, Switzerland.

An, C.; Fu, X.; Wang, G.; Parker, G. (2017a). Effect of Grain Sorting on Gravel-bed River Evolution Subject to Cycled Hydrographs: Bedload Sheets and Breakdown of the Hydrograph Boundary Layer. *Journal of Geophysical Research: Earth Surface*, Accepted. 21699003. http://dx.doi.org/10.1002/2016JF003994.

An, C.; Cui, Y.; Fu, X.; Parker, G. (2017b). Gravel-bed River Evolution in Earthquake-Prone Regions Subject to Cycled Hydrographs and Repeated Sediment Pulses. *Earth Surface Processes and Landforms*, Accepted. 01979337. http://dx.doi.org/10.1002/esp.4195.

Anderson, S.W.; Pitlick, J. (2014). Using repeat lidar to estimate sediment transport in a steep stream. *Journal of Geophysical Research: Earth Surface*, 119(3): 621–643. 21699011. http://dx.doi.org/10.1002/2013JF002933.

Annandale, G.W. (1987). Reservoir Sedimentation. *Elsevier*.

Annandale, G.W. (2011). Going Full Circle. *International Water Power and Dam Construction*, April: 30–34. http://www.waterpowermagazine.com/features/featuregoing-full-circle/.

Annandale, G.W. (2013). Quenching the Thirst – Sustainable Water Supply and Climate Change. *CreateSpace Indipendent Publication Platform*, Charleston, South Carolina, United States.

Asmal, K.; Blackmore, D.; Patkar, M.; Goldemberg, J.; Moore, D.; Veltrop, J.; Steiner, A.; Chand, J. L.; Henderson, J.; Lindahl, G.; Scudder, T.; Cariño, J. (2000). Chap. 3 – Ecosystems and Large Dams: Environmental Performance: 73–95. In: Dams and Development — A New Framework for Decision-making. *World Commission on Dams*.

Auel, C.; Berchtold, T.; Boes, R.M. (2010). Sediment Management in the Solis Reservoir Using a Bypass Tunnel. *Proc. Proceedings of the 8th ICOLD European Club Symposium*. Innsbruck: 438–443.

Auel, C.; Boes, R.M. (2011a). Sediment bypass tunnel design — hydraulic model tests. *Proc. Hydro 2011 - Practical solutions for a sustainable future. Aqua-Media International*.

Auel, C.; Boes, R.M. (2011b). Sediment bypass tunnel design — review and outlook. *Proc. ICOLD Symposium - Dams under changing challenges. Taylor & Francis*, London, UK.

Auel, C. (2014). Flow Characteristics, Particle Motion And Invert Abrasion In Sediment Bypass Tunnels. *PhD Thesis, VAW-Mitteilung 229* (R.M. Boes, ed.). Laboratory of Hydraulics, Hydrology and Glaciology (VAW), ETH Zurich, Switzerland.

Auel, C.; Kantoush, S.A.; Sumi, T. (2016). Positive effects of reservoir sedimentation management on reservoir life - Examples from Japan. *Proc. Proc. 84th ICOLD Annual meeting*. Johannesburg, South Africa: 4.11–14.20. ISBN 9780620710428.

Auel, C.; Kobayashi, S.; Sumi, T.; Takemon, Y. (2017). Effects of sediment bypass tunnels on sediment grain size distribution and benthic habitats. *Proc. 13th International Symposium on River Sedimentation*, S. Wieprecht; S. Haun; K. Weber; M. Noack; K. Terheiden (eds.). *CRC Press*, Stuttgart: 825–832. ISBN 9781138029453.

Bailly, J.S.; le Coarer, Y.; Languille, P.; Stigermark, C.J.; Allouis, T. (2010). Geostatistical estimations of bathymetric LiDAR errors on rivers. *Earth Surface Processes and Landforms*, 35(10): 1199–1210. 01979337. `http://dx.doi.org/10.1002/esp.1991`.

Bangen, S.; Hensleigh, J.; McHugh, P.; Wheaton, J.M. (2016). Error modeling of DEMs from topographic surveys of rivers using fuzzy inference systems. *Water Resources Research*, 52(2): 1176–1193. 00431397. http://dx.doi.org/10.1002/2015WR018299.

Bates, P.D.; Marks, K.J.; Horritt, M.S. (2003). Optimal use of high-resolution topographic data in flood inundation models. *Hydrological Processes*, 17(3): 537–557. 08856087. http://dx.doi.org/10.1002/hyp.1113.

Baumer, A.; Radogna, R. (2015). Rehabilitation of the Palagnedra sediment bypass tunnel (2011-2013). *Proc. First International Workshop on Sediment Bypass Tunnels*, R.M. Boes (ed.). *Laboratory of Hydraulics, Hydrology and Glaciology (VAW), ETH Zurich*, Switzerland: 235–245.

Bayley, P. B. (1995). Understanding Large River-Floodplain Ecosystems: Significant economic advantages and increased biodiversity and stability would result from restoration of impaired systems. *BioScience*, 45(3): 153–158.

Benger, W.; Ritter, M.; Heinzl, R. (2007). The Concepts of VISH. *Proc. 4th High-End Visualization Workshop*, W. Benger; R. Heinzl; W Kapferer; W Schoor; M Tyagi; S Venkataraman; G.H. Weber (eds.). *Lehmanns MediaLOB.de, Berlin*, Obergurgl Tyrol, Austria: 26–39.

Berchtold, T.; Mache, N.; Lais, A. (2008). Entlandung Stausee Solis — Hydraulische Modellversuche zum Variantenstudium ewz ('Counteracting Reservoir Sedimentation at Solis — Hydraulic modeling to study the variants proposed by ewz'). *Technical Report 4243*, Laboratory of Hydraulics, Hydrology and Glaciology (VAW), ETH, Zurich [unpublished, in German].

Bezak, N.; Grigillo, D.; Urbančič, T.; Mikoš, M.; Petrovič, D.; Rusjan, S. (2017). Geomorphic response detection and quantification in a steep forested torrent. *Geomorphology*, 291: 33–44. 0169555X. http://dx.doi.org/10.1016/j.geomorph.2016.06.034.

Bezzola, G.R. (2002). Fliesswiderstand und Sohlenstabilität natürlicher Gerinne unter besonderer Berücksichtigung des Einflusses der relativen Überdeckung ('Flow resistance and riverbed instability of natural channels with focus on the effect of the low submergence'). *PhD Thesis,VAW-Mitteilung 173* (H.-E. Minor, ed.). Laboratory of Hydraulics, Hydrology and Glaciology (VAW), ETH Zurich, Switzerland [in German].

Blair Greimann, A.M.; Randle, T.; Huang, J. (2006). Movement of finite amplitude sediment accumulations. *Journal of Hydraulic Engineering*, 132(7): 731–736.

Boes, R.M.; Auel, C.; Hagmann, M.; Albayrak, I. (2014). Sediment bypass tunnels to mitigate reservoir sedimentation and restore sediment continuity. *Reservoir Sedimentation 3* (A. J. Schleiss; G. de Cesare; M. J. Franca; M. Pfister, eds.). École Polytechnique Fédérale de Lausanne, Switzerland.

Boes, R.M. (2015). First International Workshop on Sediment Bypass Tunnels. *Laboratory of Hydraulics, Hydrology and Glaciology (VAW), ETH Zurich*, Switzerland VAW-Mitteilung 232.

Boes, R.M.; Beck, C.; Lutz, N.; Lais, A.; Albayrak, I. (2017). Hydraulics of water, air-water and sediment flow in downstream-controlled sediment bypass tunnels. *Proc. Proc. 2nd Intl. Workshop on Sediment Bypass Tunnels*, T. Sumi (ed.). Kyoto, Japan.

Brandt, S. A. (2000). Classification of geomorphological effects downstream of dams. *Catena*, 40(4): 375–401. 03418162. http://dx.doi.org/10.1016/S0341-8162(00)00093-X.

Brasington, J.; Rumsby, B.T.; McVey, R.A. (2000). Monitoring and modelling morphological change in a braided gravel-bed river using high resolution GPS-based survey. *Earth Surface Processes and Landforms*, 25(9): 973–990. 0197-9337. http://dx.doi.org/10.1002/1096-9837(200008)25:9<973::AID-ESP111>3.0.CO;2-Y.

Brasington, J.; Langham, J.; Rumsby, B. (2003). Methodological sensitivity of morphometric estimates of coarse fluvial sediment transport. *Geomorphology*, 53(3-4):

299–316. 0169555X. http://dx.doi.org/10.1016/S0169-555X(02)00320-3.

Brestolani, F.; Solari, L.; Rinaldi, M.; Lollino, G. (2015). Chap. 66: 319–322. In: G. Lollino; M. Arattano; M. Rinaldi; O. Giustolisi; J.-C. Marechal; G.E. Grant (eds.) On the Morphological Impacts of Gravel Mining: The Case of the Orco River. ISBN 978-3-319-09053-5. *Springer*, Cham, Switzerland. http://dx.doi.org/10.1007/978-3-319-09054-2_66.

Brewer, P.A.; Passmore, D.G. (2002). Sediment budgeting techniques in gravel-bed rivers. *Geological Society, London, Special Publications*, 191(June 2007): 97–113. 0305-8719. http://dx.doi.org/10.1144/GSL.SP.2002.191.01.07.

Bruno, M. C.; Maiolini, B.; Carolli, M.; Silveri, L. (2010). Short time-scale impacts of hydropeaking on benthic invertebrates in an Alpine stream (Trentino, Italy). *Limnologica - Ecology and Management of Inland Waters*, 40(4): 281–290. 00759511. http://dx.doi.org/10.1016/j.limno.2009.11.012.

Buffington, J.M. (2012). Gravel-bed Rivers VII: Processes, Tools, Environments (Biron P. Roy A. Church M., ed.). 433–463. ISBN 9781119952497.

Bunte, K. (2004). Gravel mitigation and augmentation below hydroelectric dams: a geomorphological perspective. *Technical Report*, Stream Systems Technology Center, USDA Forest Service.

Cao, Z.; Day, R.; Egashira, S. (2002). Coupled and Decoupled Numerical Modeling of Flow and Morphological Evolution in Alluvial Rivers. *Journal of Hydraulic Engineering*, 128(3): 306. 07339429. http://dx.doi.org/10.1061/(ASCE)0733-9429(2002)128:3(306).

Cavalli, M.; Goldin, B.; Comiti, F.; Brardinoni, F.; Marchi, L. (2017). Assessment of erosion and deposition in steep mountain basins by differencing sequential digital terrain models. *Geomorphology*, 291: 4–16. 0169555X. http://dx.doi.org/10.1016/j.geomorph.2016.04.009.

Chen, Y.; Syvitski, J.P.M.; Gao, S.; Overeem, I.; Kettner, A.J. (2012). Socio-economic Impacts on Flooding: A 4000-Year History of the Yellow River, China. *Ambio*, 41(7): 682–698. 0044-7447. http://dx.doi.org/10.1007/s13280-012-0290-5.

Chu, S.; Majumdar, A. (2012). Opportunities and challenges for a sustainable energy future. *Nature*, 488(7411): 294–303. 1476-4687. http://dx.doi.org/10.1038/nature11475.

Church, M.; Haschenburger, J.K. (2017). What is the "active layer"? *Water Resources Research*, 53(1): 5–10. http://dx.doi.org/10.1002/2016WR019675.

Croke, J.; Todd, P.; Thompson, C.; Watson, F.; Denham, R.; Khanal, G. (2013). The use of multi temporal LiDAR to assess basin-scale erosion and deposition following the catastrophic January 2011 Lockyer flood, SE Queensland, Australia. *Geomorphology*, 184: 111–126. 0169555X. http://dx.doi.org/10.1016/j.geomorph.2012.11.023.

Cui, Y.; Parker, G.; Lisle, T.E.; Gott, J.; Hansler-Ball, M.E.; Pizzuto, J.E.; Allmendinger, N.E.; Reed, J.M. (2003a). Sediment pulses in mountain rivers: 1. Experiments. *Water Resources Research*, 39(9). 00431397.

Cui, Y.; Parker, G.; Pizzuto, J.E.; Lisle, T.E. (2003b). Sediment pulses in mountain rivers: 2. Comparison between experiments and numerical predictions. *Water Resources Research*, 39(9). 00431397.

Cui, Y.; Parker, G. (2005). Numerical model of sediment pulses and sediment-supply disturbances in mountain rivers. *Journal of Hydraulic Engineering*, 131(8): 646–656.

De Cesare, G.; Manso, P.; Daneshvari, M.; Schleiss, A.J. (2015). Laboratory research: Bed load guidance into sediment bypass tunnel inlet. *Proc. First International Workshop on Sediment Bypass Tunnels*, R. M. Boes (ed.). *Laboratory of Hydraulics, Hydrology and Glaciology (VAW), ETH Zurich*, Switzerland: 169–179.

Die Moran, A.; El Kadi Qbderrezzak, K.; Mosselman, E.; Habersack, H.; Lebert, F.; Aelbrecht, D.; Laperrousaz, E. (2013). Physical model experiments for sediment

supply to the old Rhine through induced bank erosion. *International Journal of Sediment Research*, 28(4): 431–447. 10016279. http://dx.doi.org/10.1016/S1001-6279(14)60003-2.

Dietrich, W.E.; Kirchner, J.W.; Ikeda, H.; Iseya, F. (1989). Sediment supply and the development of the coarse surface layer in gravel-bedded rivers. *Nature*, 342: 215–217. 0028-0836. nature.vol.342.30nov1989, http://dx.doi.org/10.1038/340301a0.

Dincer, I. (2000). Renewable energy and sustainable development: a crucial review. *Renewable and Sustainable Energy Reviews*, 4(2): 157–175. 13640321. http://dx.doi.org/10.1016/S1364-0321(99)00011-8.

Dobler, W.; Baran, R.; Steinbacher, F.; Ritter, M. (2014). (A. J. Schleiss; G. De Cesare; M. J. Franca; M. Pfister, eds.). Lausanne, 1995–2001. ISBN 9781138026742.

Dufour, S.; Piégay, H. (2009). From the myth of a lost paradise to targeted river restoration: forget natural references and focus on human benefits. *River research and applications*, 25(5): 568–581. <null>. http://dx.doi.org/10.1002/rra.

Egiazaroff, V.I. (1965). Calculation of non-uniform sediment concentrations. *Journal of the Hydraulic Division - ASCE*, 91(4): 225–247.

European Union (2000). Directive 2000/60/EC (2000) of the European Parliament and of the Council of 23 October 2000 establishing a framework for Community action in the field of water policy (Water Framework Directive). *Official Journal of the European Communities*, 43(L327).

Facchini, M.; Siviglia, A.; Boes, R.M. (2015). Downstream morphological impact of a sediment bypass tunnel – preliminary results and forthcoming actions. *Proc. First International Workshop on Sediment Bypass Tunnels*, R. M. Boes (ed.). *Laboratory of Hydraulics, Hydrology and Glaciology (VAW), ETH Zurich*, Switzerland: 137–146.

Ferrer-Boix, C.; Martín-Vide, J.P.; Parker, G. (2014). Channel evolution after dam removal in a poorly sorted sediment mixture: Experiments and numerical model. *Wa-*

ter Resources Research, 50(11): 8997–9019. http://dx.doi.org/10.1002/2014WR015550.Received.

Ferrer-Boix, C.; Hassan, M.A. (2015). Channel adjustments to a succession of water pulses in gravel bed rivers. *Water Resources Research*, 51(11): 8773–8790. 00221694. 2014WR016527, http://dx.doi.org/10.1002/2014WR016259.

Fukuda, T.; Yamashita, K.; Osada, K.; Fukuoka, S. (2012). Study on Flushing Mechanism of Dam Reservoir Sedimentation and Recovery of Riffle-Pool in Downstream Reach by a Flushing Bypass Tunnel. *Proc. International Symposium on Dams for a Changing World*. 2185-467X: 6.

Fuller, I.C.; Large, A.R.G.; Charlton, M.E.; Heritage, G.L.; Milan, D.J. (2003). Reach-scale sediment transfers: An evaluation of two morphological budgeting approaches. *Earth Surface Processes and Landforms*, 28(8): 889–903. 01979337. http://dx.doi.org/10.1002/esp.1011.

Goudie, A.S. (2004). Encyclopedia of geomorphology. Volume 1. ISBN 0–415–32737–7. arXiv:1011.1669v3, http://dx.doi.org/10.1017/CBO9781107415324.004.

Gran, K.B.; Czuba, J.A. (2017). Sediment pulse evolution and the role of network structure. *Geomorphology*, 277: 17–30. 0169555X. http://dx.doi.org/10.1016/j.geomorph.2015.12.015.

Grant, G.E. (2012). (M. Church; P. M. Biron; A. G. Roy, eds.). Chichester, West Sussex (UK), 165–181. ISBN 9780470688908. http://dx.doi.org/10.1002/9781119952497.ch15.

Guney, M. S.; Bombar, G.; Aksoy, A. O. (2013). Experimental Study of the Coarse Surface Development Effect on the Bimodal Bed-Load Transport under Unsteady Flow Conditions. *Journal of Hydraulic Engineering*, 139(1): 12–21. http://dx.doi.org/10.1061/(ASCE)HY.1943-7900.0000640..

Hagmann, M.; Albayrak, I.; Boes, R.M. (2015). Field research : Invert material resistance and sediment transport measurements. *Proc. First International Workshop on Sediment Bypass Tunnels*, R. M. Boes (ed.). *Laboratory of Hydraulics, Hydrology and Glaciology (VAW), ETH Zurich*, Switzerland: 123–136.

Hassan, M.A.; Egozi, R.; Parker, G. (2006). Experiments on the effect of hydrograph characteristics on vertical grain sorting in gravel bed rivers. *Water Resources Research*, 42(9): 1–15. 00431397. http://dx.doi.org/10.1029/2005WR004707.

Heckmann, T.; Haas, F.; Abel, J.; Rimböck, A.; Becht, M. (2017). Feeding the hungry river: Fluvial morphodynamics and the entrainment of artificially inserted sediment at the dammed river Isar, Eastern Alps, Germany. *Geomorphology*, 291: 128–142. 0169555X. http://dx.doi.org/10.1016/j.geomorph.2017.01.025.

Hilldale, R.C.; Raff, D. (2008). Assessing the ability of airborne LiDAR to map river bathymetry. *Earth Surface Processes and Landforms*, 33(5): 773–783. 01979337. bhmic00033, http://dx.doi.org/10.1002/esp.1575.

Hirano, M. (1971). River bed degradation with armoring. *Transactions of the Japan Society of Civil Engineers*, 3(2): 194–195.

Hirano, M. (1972). Studies on variation and equilibrium state of a river bed composed of nonuniform material. *Transactions of the Japan Society of Civil Engineers*, 4: 128–129.

Humphries, R.; Venditti, J.G.; Sklar, L.S.; Wooster, J.K. (2012). Experimental evidence for the effect of hydrographs on sediment pulse dynamics in gravel-bedded rivers. *Water Resources Research*, 48(1). 0043-1397.

ICOLD (2009). Sedimentation and Sustainable Use of Reservoirs and River Systems. *Technical Report*, Paris.

ICOLD (2016). Role of dams.

Junk, W. J.; Bayley, P. B.; Sparks, R.E. (1989). The flood pulse concept in river-floodplain systems. *Proc. Large River Symposium - Canadian special publication of fisheries and aquatic sciences*, D. P. Dodge (ed.). 19326203: 110–127. ISBN 0-660-13259-1. http://dx.doi.org/10.1371/journal.pone.0028909.

Kantoush, S.A.; Sumi, T.; Murasaki, M. (2011). Evaluation of Sediment Bypass Efficiency By Flow Field and Sediment Concentration Monitoring Techniques. *Journal of Japan Society of Civil Engineers, Ser. B1 (Hydraulic Engineering)*, 67(4): I_169–I_174. http://dx.doi.org/10.2208/jscejhe.67.I_169.

Khosronejad, A.; Le, T.; DeWall, P.; Bartelt, N.; Woldeamlak, S.; Yang, X.; Sotiropoulos, F. (2016). High-fidelity numerical modeling of the Upper Mississippi River under extreme flood condition. *Advances in Water Resources*, 98: 97–113. 03091708. http://dx.doi.org/10.1016/j.advwatres.2016.10.018.

Kinzel, P.J.; Wright, C.W.; Nelson, J.M.; Burman, A.R. (2007). Evaluation of an Experimental LiDAR for Surveying a Shallow, Braided, Sand-Bedded River. *Journal of Hydraulic Engineering*, 133(7): 838–842. 0733-9429. http://dx.doi.org/10.1061/(ASCE)0733-9429(2007)133:7(838).

Kirchner, J.W. (2001). Data Analysis Toolkits (J.W. Kirchner, ed.). Berkeley, California, USA.

Klir, G.J.; Yuan, B. (1995). Fuzzy sets and fuzzy logic, theory and applications. ISBN 0-13-101171-5. *Prentice Hall*, Upper Saddle River, NJ.

Kondolf, G.M.; Wolman, M.G. (1993). The sizes of salmonid spawning gravels. *Water Resources Research*, 29(7): 2275–2285. 19447973. http://dx.doi.org/10.1029/93WR00402.

Kondolf, G.M.; Wilcock, P.R. (1996). The flushing flow problem: Defining and evaluating objectives. *Water Resource Research*, 32(8): 2589–2599.

Kondolf, G.M. (1997). Hungry water: Effects of dams and gravel mining on river channels. *Environmental Management*, 21(4): 533–551. 0364152X. http://dx.doi.org/10.1007/s002679900048.

Kondolf, G.M.; Gao, Y.; Annandale, G.W.; Morris, G.L.; Jiang, E.; Zhang, J.; Cao, Y.; Carling, P.; Fu, K.; Guo, Q.; Hotchkiss, R.H.; Peteuil, C.; Sumi, T.; Wang, H.-W.; Wang, Z.; Wei, Z.; Wu, B.; Wu, C.; Yang, C.T. (2014). Sustainable sediment management in reservoirs and regulated rivers: Experiences from five continents. *Earth' s Future*, 2(5): 256–280. 2328-4277. http://dx.doi.org/10.1002/2013EF000184.of.

Lane, S.N.; Chandler, J. H.; Richards, K. S. (1994). Developments in monitoring and modelling small-scale river bed topography. *Earth Surface Processes and Landforms*, 19(4): 349–368. 10969837. http://dx.doi.org/10.1002/esp.3290190406.

Lane, S.N.; Westaway, RiM.; Hicks, D.M. (2003). Estimation of erosion and deposition volumes in a large, gravel-bed, braided river using synoptic remote sensing. *Earth Surface Processes and Landforms*, 28(3): 249–271. 01979337. http://dx.doi.org/10.1002/esp.483.

Lichti, D.D.; Gordon, S.J.; Tipdecho, T. (2005). Error Models and Propagation in Directly Georeferenced Terrestrial Laser Scanner Networks. *Journal of Surveying Engineering*, 131(4): 135–142. 0733-9453. http://dx.doi.org/10.1061/(ASCE)0733-9453(2005)131:4(135).

Lisle, T.E.; Cui, Y.; Parker, G.; Pizzuto, J.E.; Dodd, A.M. (2001). The dominance of dispersion in the evolution of bed material waves in gravel-bed rivers. *Earth Surface Processes and Landforms*, 26(13): 1409–1420. 0197-9337.

Madej, M.A. (2001). Development of channel organization and roughness following sediment pulses in single-thread, gravel bed rivers. *Water Resources Research*, 37(8): 2259–2272.

Mandlburger, G.; Hauer, C.; Höfle, B.; Habersack, H.; Pfeifer, N. (2009). Optimisation of LiDAR derived terrain models for river flow modelling. *Hydrology and Earth System Sciences*, 13(8): 1453–1466. 1607-7938. http://dx.doi.org/10.5194/hess-13-1453-2009.

Mandlburger, G.; Hauer, C.; Wieser, M.; Pfeifer, N. (2015). Topo-bathymetric LiDAR for monitoring river morphodynamics and instream habitats-A case study at the Pielach River. *Remote Sensing*, 7(5): 6160–6195. 20724292. http://dx.doi.org/10.3390/rs70506160.

Mao, L. (2012). The effect of hydrographs on bed load transport and bed sediment spatial arrangement. *Journal of Geophysical Research: Earth Surface*, 117(3): 1–16. 21699011. http://dx.doi.org/10.1029/2012JF002428.

Martín, E.J.; Doering, M.; Robinson, C.T. (2017). Ecological assessment of a sediment by-pass tunnel on a receiving stream in Switzerland. *River Research and Applications*, (published online). http://dx.doi.org/10.1002/rra.3145.

Martin, R.L.; Jerolmack, D.J. (2013). Origin of hysteresis in bedform response to unsteady flows. *Water Resources Research*, 49(3): 1314–1333. 00431397. http://dx.doi.org/10.1002/wrcr.20093.

Maturana, O.; Tonina, D.; Mckean, J.A.; Buffington, J.M.; Luce, C.H.; Caamaño, D. (2014). Modeling the effects of pulsed versus chronic sand inputs on salmonid spawning habitat in a low-gradient gravel-bed river. *Earth Surface Processes and Landforms*, 39(7): 877–889. 10969837. http://dx.doi.org/10.1002/esp.3491.

Meyer-Peter, E.; Müller, R. (1948). Formulas for Bed-Load Transport. *Proc. Proceedings of the 2nd Meeting of the International Association of Hydraulic Research*. Stockholm, Sweden: 39–64. http://dx.doi.org/1948-06-07.

Milan, D.J.; Heritage, G.L.; Large, A.R.G.; Fuller, I.C. (2011). Filtering spatial error from DEMs: Implications for morphological change estimation. *Geomorphology*, 125(1): 160–171. 0169555X. http://dx.doi.org/10.1016/j.geomorph.2010.09.012.

Milan, D.J. (2012). Geomorphic impact and system recovery following an extreme flood in an upland stream: Thinhope Burn, northern England, UK. *Geomor-*

phology, 138(1): 319–328. 0169555X. http://dx.doi.org/10.1016/j.geomorph.2011.09.017.

Morris, G.L.; Fan, J. (1998). Reservoir Sedimentation Handbook: Design and Management of Dams, Reservoirs and Watersheds for Sustainable Use. ISBN 9788578110796. *McGraw-Hill Book Co.*, New York. arXiv:1011.1669v3, http://dx.doi.org/10.1017/CBO9781107415324.004.

Morris, G.L. (2015). Management Alternatives to Combat Reservoir Sedimentation. *Proc. First International Workshop on Sediment Bypass Tunnels*, R.M. Boes (ed.). *Laboratory of Hydraulics, Hydrology and Glaciology (VAW), ETH Zurich*, Switzerland: 181–192.

Mueller-Hagmann, M. (2018). Hydroabrasion in high speed flows at sediment bypass tunnels. *PhD Thesis, VAW-Mitteilung 239* (R.M. Boes, ed.). Laboratory of Hydraulics, Hydrology and Glaciology (VAW), ETH Zurich, Switzerland.

Muth, R. T.; Crist, L. W.; LaGory, K. E.; Hayse, J. W.; Bestgen, K. R.; Ryan, T. P.; Lyons, J. K.; Valdez, R. A. (2000). Flow and Temperature Recommendations for Endangered Fishes in the Green River Downstream of Flaming Gorge Dam. *Technical Report*, Upper Colorado River Endangered Fish Recovery Program Project FG-53.

Nagrodski, A.; Raby, G. D.; Hasler, C. T.; Taylor, M. K.; Cooke, S. J. (2012). Fish stranding in freshwater systems: sources, consequences, and mitigation. *Journal of environmental management*, 103: 133–41. 1095-8630. http://dx.doi.org/10.1016/j.jenvman.2012.03.007.

Nelson, A.; Dubé, K. (2016). Channel response to an extreme flood and sediment pulse in a mixed bedrock and gravel-bed river. *Earth Surface Processes and Landforms*, 41(2): 178–195. 01979337. http://dx.doi.org/10.1002/esp.3843.

Nilsson, C.; Reidy, C.A.; Dynesius, M.; Revenga, C. (2005). Fragmentation and Flow Regulation of the World's Large River Systems. *Science*, 308(5720): 405–408. 0036-8075. http://dx.doi.org/10.1126/science.1107887.

Oertli, C.; Auel, C. (2015). Solis sediment bypass tunnel: First operation experiences. *Proc. First International Workshop on Sediment Bypass Tunnels*, R. M. Boes (ed.). *Laboratory of Hydraulics, Hydrology and Glaciology (VAW), ETH Zurich*, Switzerland: 223–233.

Pace, K.M.; Tullos, D.D.; Walter, C.; Lancaster, S.T.; Segura, C. (2017). Sediment pulse behaviour following dam removal in gravel-bed rivers. *River research and applications*, 33(1): 102–112. <null>. http://dx.doi.org/10.1002/rra.

Parker, G.; Klingeman, P.C.; McLean, D.G. (1982). Bedload and size distribution in paved gravel-bed streams. *Journal of the Hydraulic Division - ASCE*, 108(HY4): 544–571.

Parker, G.; Klingeman, P.C. (1982). On why gravel bed streams are paved. *Water Resources Research*, 18(5): 1409–1423.

Parker, G.; Sutherland, A.J. (1990). Fluvial armor. *Journal of Hydraulic Research*, 28(5): 529–544. 0022-1686.

Parker, G.; Toro-Escobar, C.M. (2002). Equal mobility of gravel in streams: The remains of the day. *Water Resources Research*, 38(11). 00431397. http://dx.doi.org/10.1029/2001WR000669.

Parker, G. (2004). 1D Sediment transport morphodynamics with applications to rivers and turbidity currents. http://hydrolab.illinois.edu/people/parkerg//morphodynamics_e-book.htm.

Parker, G.; Hassan, M.A.; Wilcock, P.R. (2007). Adjustment of the bed surface size distribution of gravel-bed rivers in response to cycled hydrographs. *Gravel-bed Rivers VI: From Process Understanding to River Restoration 10* (H. Habersack; H. Piégay; M. Rinaldi, eds.). New York, 241–285.

Petts, G.E. (1984). Impounded Rivers: Perspectives for Ecological Management. *John Wiley & Sons, Ltd*, Chichester, West Sussex (UK).

Podolak, C.J.P.; Wilcock, P.R. (2013). Experimental study of the response of a gravel streambed to increased sediment supply. *Earth Surface Processes and Landforms*, 38(14): 1748–1764. 01979337. http://dx.doi.org/10.1002/esp.3468.

Poff, N.L.; Allan, J.D.; Bain, M.B.; Karr, J.R.; Prestegaard, K.L.; Richter, B.D.; Sparks, R.E.; Stromberg, J.C. (1997). The Natural Flow Regime. *BioScience*, 47(11): 769–784. 00063568. http://dx.doi.org/10.2307/1313099.

Poff, N.L.; Hart, D. D. (2002). How Dams Vary and Why It Matters for the Emerging Science of Dam Removal. *BioScience*, 52(8): 659–668. 0006-3568. http://dx.doi.org/10.1641/0006-3568(2002)052[0659:HDVAWI]2.0.CO;2.

Preisendorfer, R.W. (1986). Secchi disk science: Visual optics of natural waters. *Limnology and Oceanography*, 31(5): 909–926. 0024-3590. http://dx.doi.org/10.4319/lo.1986.31.5.0909.

Reid, I.; Frostick, L. E.; Layman, J. T. (1985). The incidence and nature of bedload transport during flood flows in coarse-grained alluvial channels. *Earth Surface Processes and Landforms*, 10(1): 33–44. 01979337. http://dx.doi.org/10.1002/esp.3290100107.

Ribberink, J. S. (1987). Mathematical modelling of one-dimensional morphological changes in rivers with non-uniform sediment. *PhD Thesis*, Delft University of Technology.

Rickenmann, D.; Turowski, J. M.; Fritschi, B.; Wyss, C.; Laronne, J.; Barzilai, R.; Reid, I.; Kreisler, A.; Aigner, J.; Seitz, H.; Habersack, H. (2014). Bedload transport measurements with impact plate geophones: Comparison of sensor calibration in different gravel-bed streams. *Earth Surface Processes and Landforms*, 39(7): 928–942. 10969837. http://dx.doi.org/10.1002/esp.3499.

Rickenmann, Di.; Antoniazza, G.; Wyss, C.R.; Fritschi, B.; Boss, S. (2017). Bedload transport monitoring with acoustic sensors in the Swiss Albula mountain river. *Proceedings of the International Association of Hydrological Sciences*, 375: 5–10. 2199-899X. http://dx.doi.org/10.5194/piahs-375-5-2017.

Rinaldi, M.; Amponsah, W.; Benvenuti, M.; Borga, M.; Comiti, F.; Lucía, A.; Marchi, L.; Nardi, L.; Righini, M.; Surian, N. (2016). An integrated approach for investigating geomorphic response to extreme events: Methodological framework and application to the October 2011 flood in the Magra River catchment, Italy. *Earth Surface Processes and Landforms*, 41(6): 835–846. 10969837. http://dx.doi.org/10.1002/esp.3902.

Robinson, C.T.; Uehlinger, U.; Monaghan, M.T. (2003). Effects of a multi-year experimental flood regime on macroinvertebrates downstream of a reservoir. *Aquatic Sciences*, 65(3): 210–222. 10151621. http://dx.doi.org/10.1007/s00027-003-0663-8.

Robinson, C.T.; Uehlinger, U.; Monaghan, M.T. (2004). Stream ecosystem response to multiple experimental floods from a reservoir. *River Research and Applications*, 20(4): 359–377. 15351459. http://dx.doi.org/10.1002/rra.743.

Robinson, C.T. (2012). Long-term Changes in Community Assembly, Resistance and Resilience following Experimental Floods. *Ecological Applications*, 22(7): 1949–1961. 1051-0761. http://dx.doi.org/10.1890/11-1042.1.

Schleiss, A.J.; De Cesare, G.; Althaus, J.J. (2010). Verlandung der Stauseen gefährdet die nachhaltige Nutzung der Wasserkraft. *Wasser Energie Luft*, 102(1): 31.

Schleiss, Anton J; Franca, Mário J; Juez, Carmelo; De Cesare, Giovanni (2016). Reservoir sedimentation. *Journal of Hydraulic Research*, 54(6): 595–614. 0022-1686. http://dx.doi.org/10.1080/00221686.2016.1225320.

Shaw, J.; Kellerhals, R. (1982). The composition of recent alluvial gravels in Alberta river beds. *Technical Report 41*, Alberta Research Council, Edmonton, Alberta, Canada..

Siviglia, A.; Stecca, G.; Blom, A. (2017). Chap. 26 – Modelling of Mixed-Sediment Morphodynamics in Gravel-Bed Rivers Using the Active-Layer Approach: 703–728. In: D. Tsutsumi; J.B. Laronne (eds.) Gravel-Bed Rivers: Process and Disasters. ISBN

978-1-118-97140-6. *Wiley-Blackwell*, Chichester, UK. http://dx.doi.org/10.1002/9781118971437.ch26.

Sklar, L.S.; Fadde, J.; Venditti, J.G.; Nelson, P.A.; Wydzga, M.A.; Cui, Y.; Dietrich, W.E. (2009). Translation and dispersion of sediment pulses in flume experiments simulating gravel augmentation below dams. *Water Resources Research*, 45(8). 00431397.

Sloff, C. J.; Jagers, H. R. A.; Kitamura, Y.; Kitamura, P. (2001). 2D Morphodynamic modelling with graded sediment. *Proc. 2nd IAHR Symposium on River, Coastal and Estuarine Morphodynamics*. Obihiro, Japan.

Smart, G.M.; Jaeggi, M.N.R. (1984). Sediment Transport Formula for Steep Channels. *Journal of Hydraulic Engineering*, 110(3): 267–276. 0733-9429. http://dx.doi.org/10.1061/(ASCE)0733-9429(1984)110:3(267).

Stecca, G.; Siviglia, A.; Blom, A. (2014). Mathematical analysis of the Saint-Venant – Hirano model for mixed-sediment morphodynamics. *Water Resources Research*, 50(10): 7563–7589. 1944-7973. http://dx.doi.org/10.1002/2014WR015251.Received.

Steinbacher, F.; Pfennigbauer, M.; Ullrich, A.; Aufleger, M. (2010). Airborne hydromapping area-wide surveying of shallow water areas. *Wasserwirtschaft*, 99(12): 10–14.

Sumi, T.; Okano, M.; Takata, Y. (2004). Reservoir sedimentation management with bypass tunnels in Japan. *Proc. Ninth International Symposium on River Sedimentation*: 1036–1043.

Sumi, T.; Kantoush, S.A. (2011). Comprehensive Sediment Management Strategies in Japan: Sediment bypass tunnels in Japan. *Proc. 34th IAHR World COngress - Balance and Uncertainty*, Engineers Australia (ed.). *IAHR*, Brisbane: 1803–1810. ISBN 9780858258686.

Sumi, T.; Kantoush, S.A.; Suzuki, S. (2012). Performance of Miwa Dam sediment bypass tunnel: evaluation of upstream and downstream state and bypassing efficiency.

Proc. International Symposium on Dams for a Changing World. International COmmission on Large Dams (ICOLD), Kyoto, Japan: 576 – 596.

Sumi, T. (2015). Comprehensive reservoir sedimentation countermeasures in Japan. *Proc. First International Workshop on Sediment Bypass Tunnels*, R. M. Boes (ed.). *Laboratory of Hydraulics, Hydrology and Glaciology (VAW), ETH Zurich*, Switzerland: 9–28.

Sumi, T. (2017). Proceedings of the second International Workshop on Sediment Bypass Tunnels. *DPRI, University of Kyoto*, Kyoto, Japan.

Surian, N.; Rinaldi, M. (2003). Morphological response to river engineering and management in alluvial channels in Italy. *Geomorphology*, 50(4): 307–326. 0169555X. `http://dx.doi.org/10.1016/S0169-555X(02)00219-2`.

Sutherland, D.G.; Hansler-Ball, M.E.; Hilton, S. J.; Lisle, T.E. (2002). Evolution of a landslide-induced sediment wave in the Navarro River, California. *Geological Society of America Bulletin*, 114(8): 1036–1048. 00167606.

Swiss Federal Council (1998). 814.201 Waters Protection Ordinance of 28 October 1998 (WPO).

Syvitski, J.P.M.; Kettner, A.J.; Overeem, I.; Hutton, E.W.H.; Hannon, M.T.; Brakenridge, G.R.; Day, J.; Vörösmarty, C.J.; Saito, Y.; Giosan, L.; Nicholls, R.J. (2009). Sinking deltas due to human activities. *Nature Geoscience*, 2(10): 681–686. `http://dx.doi.org/10.1038/ngeo629`.

Tockner, K.; Malard, F.; Ward, J. V. (2000). An Extension of the Flood Pulse Concept. *Hydrological Processes*, 14(16-17): 2861–2883.

Toro, E. F. (2009). Riemann Solvers and Numerical Methods for Fluid Dynamics: A Practical Introduction. *Springer*, Heidelberg, Germany.

Toro-Escobar, C.M.; Paola, C.; Parker, G. (1996). Transfer function for the deposition of poorly sorted gravel in response to streambed aggradation. *Journal of Hy-*

draulic Research, 34(1): 35–53. 0022-1686. http://dx.doi.org/10.1080/00221689609498763.

Vanzo, D.; Siviglia, A.; Carolli, M.; Zolezzi, G. (2016). Characterization of sub-daily thermal regime in alpine rivers: Quantification of alterations induced by hydropeaking. *Hydrological Processes*, 30(7): 1052–1070. 10991085. http://dx.doi.org/10.1002/hyp.10682.

Venditti, J.G.; Dietrich, W.E.; Nelson, P.A.; Wydzga, M.A.; Fadde, J.; Sklar, L.S. (2010). Effect of sediment pulse grain size on sediment transport rates and bed mobility in gravel bed rivers. *Journal of Geophysical Research*, 115(F3). 0148-0227.

Venditti, J.G.; Nelson, P.A.; Minear, J. T.; Wooster, J.K.; Dietrich, W.E. (2012). Alternate bar response to sediment supply termination. *Journal of Geophysical Research*, 117(F2). 0148-0227.

Vetsch, D.; Siviglia, A.; Ehrbar, D.; Facchini, M.; Kammerer, S.; Koch, A.; Peter, S.; Vanzo, D.; Vonwiller, L.; Gerber, M.; Volz, C.; Farshi, D.; Mueller, R.; Rousselot, P.; Veprek, R.; Faeh, R. (2017a). BASEMENT — Basic Simulation Environment for Computation of Environmental Flow and Natural Hazard Simulation.

Vetsch, D.; Siviglia, A.; Ehrbar, D.; Facchini, M.; Kammerer, S.; Koch, A.; Peter, S.; Vonwiller, L.; Gerber, M.; Volz, C.; Farshi, D.; Mueller, R.; Rousselot, P.; Veprek, R.; Faeh, R. (2017b). System Manuals of BASEMENT, Version 2.7. *Laboratory of Hydraulics, Glaciology and Hydrology (VAW). ETH Zurich*.

Viparelli, E.; Gaeuman, D.; Wilcock, P.R.; Parker, G. (2011). A model to predict the evolution of a gravel bed river under an imposed cyclic hydrograph and its application to the Trinity River. *Water Resources Research*, 47(2). 00431397.

Vischer, D.L.; Hager, W.H.; Casanova, C.; Joos, B.; Lier, P.; Martini, O. (1997). Bypass Tunnels to Prevent Reservoir Sedimentation. *Proc. International Congress on large Dams. International COmmission on Large Dams (ICOLD)*, Florence, Italy: 605 – 624.

Vörösmarty, C.J.; Meybeck, M.; Fekete, B.; Sharma, K.; Green, P.; Syvitski, J.P.M. (2003). Anthropogenic sediment retention: major global impact from registered river impoundments. *Global and Planetary Change*, 39(1-2): 169–190. 09218181. http://dx.doi.org/10.1016/S0921-8181(03)00023-7.

Ward, J. V.; Stanford, J. A. (1979). The Ecology of Regulated Streams. ISBN 1468486136. *Plenum Press*, New York. http://dx.doi.org/10.1007/978-1-4684-8613-1.

Waters, K.A.; Curran, J.C. (2015). Linking bed morphology changes of two sediment mixtures to sediment transport predictions in unsteady flows. *Water Resource Research*, 51(4): 1–18. 00431397. http://dx.doi.org/10.1002/2014WR016083.Received.

Wechsler, S.P.; Kroll, C.N. (2006). Quantifying DEM Uncertainty and its Effect on Topographic Parameters. *Photogrammetric Engineering & Remote Sensing*, 72(9): 1081–1090. 0099-1112. http://dx.doi.org/10.14358/PERS.72.9.1081.

Wheaton, J.M. (2008). Uncertainty in morphological sediment budgeting of rivers. *PhD Thesis*, University of Southampton.

Wheaton, J.M.; Brasington, J.; Darby, S. E.; Sear, D.A. (2010). Accounting for uncertainty in DEMs from repeat topographic surveys: Improved sediment budgets. *Earth Surface Processes and Landforms*, 35(2): 136–156. 01979337. http://dx.doi.org/10.1002/esp.1886.

Wilcock, P.R.; Crowe, J. C. (2003). Surface-based transport model for mixed-size sediment. *Journal of Hydraulic Engineering*, 129(2): 120–128.

Williams, G.P.; Wolman, M.G. (1984). Downstream effects of dams on alluvial rivers. *Technical Report*. http://dx.doi.org/10.1126/science.277.5322.9j.

Wohl, E.; Angermeier, P.L.; Bledsoe, B.P.; Kondolf, G.M.; MacDonnell, L; Merritt, D.M; Palmer (2005). River restoration. *Water Resources Research*, 41(10): 1–12. 00431397. http://dx.doi.org/10.1029/2005WR003985.

Wohl, E.; Lane, S.N.; Wilcox, A.C. (2015). The science and practice of river restoration. *Water Resources Research*, 51(8): 5974–5997. 19447973. 2014WR016527, http://dx.doi.org/10.1002/2014WR016874.

Wong, M.; Parker, G. (2006). One-dimensional modeling of bed evolution in a gravel bed river subject to a cycled flood hydrograph. *Journal of Geophysical Research: Earth Surface*, 111(3). 21699011. http://dx.doi.org/10.1029/2006JF000478.

Wootton, J. T.; Parker, M. S.; Power, M. E. (1996). Effects of Disturbance on River Food Webs. *Science*, 273(5281): 1558–1561.

Zolezzi, G.; Siviglia, A.; Toffolon, M.; Maiolini, B. (2011). Thermopeaking in alpine streams: Event characterization and time scales. *Ecohydrology*, 4(4): 564–576. 19360584. http://dx.doi.org/10.1002/eco.132.

Zunka, J. P. P.; Tullos, D.D.; Lancaster, S.T. (2015). Effects of sediment pulses on bed relief in bar-pool channels. *Earth Surface Processes and Landforms*, 40(8): 1017–1028. 10969837. http://dx.doi.org/10.1002/esp.3697.

List of Acronyms

ALS	Airborne Laser Scanning
BASEMENT	Basic Simulation Environment
BRC	Bedload Rating Curve
BRC_{SBT}	Bedload Rating Curve of the SBT
BRC_{us}	Bedload Rating Curve of the upstream river reach
CED	Cumulative Elevation Difference
CI	Confidence Interval
CIR	Capacity-Inflow Ratio
DEM	Digital Elevation Model
DoD	DEM of Difference
DSM	Digital Surface Model
DTM	Digital Terrain Model
ED	Elevation Difference
FIS	Fuzzy Inference System
GCD	Geomorphic Change Detection
GSD	Grain Size Distribution
GSD_{red}	Grain Size Distribution reduced of its coarsest part
HBL	Hydrograph Boundary Layer
LiDAR	Light Detection And Ranging
LMS	Laser Measurement System
minLoD	minimum Level of Detection
nCED	normalized Cumulative Elevation Difference

OC	Operational Condition
OS_{SBT}	Operational Space of the SBT
PDE	Partial Differential Equation
pts	Points
SBL	Sedimentograph Boundary Layer
SBT	Sediment Bypass Tunnel
SCI	Spatial Contiguity Index
SWE	Shallow-Water Equations
UTM	Universal Transverse Mercator
WGS	World Geodetic System

List of Symbols

Latin Symbols

b_t SBT width

h_t SBT height

D_t SBT diameter

L length

L_{tot} total length of the domain

L_{HBL} length of the hydrograph boundary layer

A_{HBL} amplitude of the hydrograph boundary layer

S riverbed slope

S_{ref} reference riverbed slope

S^* non-dimensional riverbed slope

d_{90} riverbed surface grain size such that 90% of the material is finer

d_{16} riverbed surface grain size such that 16% of the material is finer

d_{30} riverbed surface grain size such that 30% of the material is finer

d_{50} riverbed surface grain size such that 50% of the material is finer

d_{84} riverbed surface grain size such that 84% of the material is finer

H_{crit} critical thresholded error

$p(A|E_j)$ probability of the j-th cell of being erosional

$p(A|D_j)$ probability of the j-th cell of being depositional

Q_w water discharge

Q_b bedload discharge

$Q_{w,us}$ water discharge in the upstream river reach

$Q_{b,us}$ bedload discharge in the upstream river reach

$Q_{w,SBT}$ water discharge carried by the SBT

$Q_{b,SBT}$ bedload discharge carried by the SBT

$Q_{w,ds}$ water discharge in the downstream river reach

$Q_{b,ds}$ bedload discharge in the downstream river reach

$Q_{w,m,SBT}$ minimum water discharge needed for operating the SBT

$Q_{w,d,SBT}$ SBT design water discharge

$Q_{w,M}$ water discharge needed for carrying out $Q_{b,M,SBT}$

Q_w^* non-dimensional water discharge

$Q_{b,m,SBT}$ minimum bedload discharge carried by the SBT

$Q_{b,d,SBT}$ design bedload discharge carried by the SBT

$Q_{b,M,SBT}$ maximum bedload discharge carried by the SBT

$Q_{b,peak}$ bedload discharge at the sedimentograph peak

e_{SBT} efficiency of the SBT

t time

x longitudinal direction

h water depth

q_w flow discharge per unit width

g acceleration due to gravity

S_f dimensionless friction slope

k_s Gauckler-Strickler coefficient

C_h dimensionless Chezy coefficient

h_{C_h} Chezy constant

d_m median grain size of the riverbed GSD

h_R height of the roughness sublayer

q_b total sediment discharge per unit width

$q_{b,k}$ sediment discharge per unit width relative to the kth grain class

N_{gc} number of grain classes

d_k diameter representative of the kth grain class

d_g mean geometric size

$d_{g,f}$ mean geometric size of the feeding

$d_{g,eq}$ mean geometric size at the equilibrium

d_g^* dimensionless mean geometric size

L_a active layer thickness

$F_{a,k}$ volume fraction in the active layer of the kth grain class

$f_{s,k}$ volume fraction in the substrate layer of the kth grain class

$M_{a,k}$ sediment mass per surface area in the active layer of the kth grain class divided by sediment density

$M_{s,k}$ sediment mass per surface area in the substrate layer of the kth grain class divided by sediment density

f_k^I volume content of the kth fraction at the interface between the active layer and the substrate

$p_{b,k}$ volume fraction of bedload in the kth grain class

u_* shear velocity

W_k^* dimensionless bedload transport rate

Greek Symbols

λ_{pts} point density

ε_{ALS} accuracy of the ALS system

ε_{geo} georeferencing error

ε_{aln} stripes alignment error

$\delta\eta$ DEM uncertainty

$\delta\eta_{new}$ new DEM uncertainty

$\delta\eta_{old}$ old DEM uncertainty

$\delta\eta_{DoD}$ propagated DoD uncertainty

σ standard deviation

λ_p bed porosity

η riverbed elevation

η_0 constant reference riverbed elevation

$\Delta\eta$ deviatoric riverbed level variation (elevation difference)

$\Delta\eta_{eq}$ deviatoric riverbed level variation (elevation difference) at equilibrium

δ_k ratio of d_k to d_g

ψ base-2 logarithmic scale to specify grain sizes

λ^* speed of the sorting wave

α pre-factor of the Meyer-Peter and Müller formula

β exponent of the Meyer-Peter and Müller formula

ρ_w water density

ρ_s sediment density

Δ submerged specific gravity of the sediment

θ shear stress relative to the mean size d_m

θ_c critical Shields number

τ_s boundary shear stress at the bed

ϕ_k ratio of the shear stress to the reference shear stress of the size fraction k

$\theta_{s,g}$ shear stress relative to the mean geometric size d_g

$\theta_{ssr,g}$ reference Shields number for the mean geometric size d_g

σ_g geometric standard deviation of the GSD